Measurement of beam asymmetries in the reaction $\gamma p \rightarrow p\pi^0\eta$ with the Crystal Barrel/TAPS experiment at ELSA

Dissertation

zur

Erlangung des Doktorgrades (Dr. rer. nat.)

der

Mathematisch-Naturwissenschaftlichen Fakultät

der

Rheinischen Friedrich-Wilhelms-Universität

Bonn

vorgelegt von

Eric Paul-Maria Gutz

aus

Villingen-Schwenningen

Bonn, Oktober 2010

Angefertigt mit Genehmigung der
Mathematisch-Naturwissenschaftlichen Fakultät der
Rheinischen Friedrich-Wilhelms-Universität Bonn

Diese Dissertation ist auf dem Hochschulschriftenserver der ULB Bonn
http://hss.ulb.uni-bonn.de/diss_online elektronisch publiziert.

1. Referent:	Prof. Dr. U. Thoma
2. Referent:	Prof. Dr. Ch. Weinheimer
Tag der Promotion:	20. Dezember 2010
Erscheinungsjahr:	2011

Abstract

The photoproduction of mesons off the nucleon provides an excellent tool to gain further insight into the structure of baryons and their excitation spectrum. A large number of final states yielding various resonance contributions are accessible in photoproduction experiments. Especially in the regime of high-lying resonances, the photoproduction of multi-meson final states is of increasing importance, giving access to sequential decays of such resonances via e.g. $\Delta(1232)P_{33}$ or $\mathrm{N}(1535)S_{11}$ in the intermediate state. For a complete understanding of the processes involved, however, it is insufficient to measure only unpolarized total and differential cross sections. The extraction of polarization observables from data obtained using polarized beams and targets is mandatory to constrain theoretical models and analyses and to uniquely determine the amplitudes participating in a given process.

This work presents the analysis of data taken with the Crystal Barrel/TAPS experiment at the accelerator facility ELSA in Bonn, using a linearly polarized photon beam impinging on a liquid hydrogen target. The detector system is optimized for the detection of multi-photon final states. The data has been selected for the reaction $\gamma\mathrm{p} \to \mathrm{p}\pi^0\eta \to \mathrm{p}4\gamma$ for an incoming photon energy range of 970 MeV to 1650 MeV. In this range, photon polarizations of up to 50% have been achieved.

From this data, all polarization observables accessible with a linearly polarized photon beam and an unpolarized target have been extracted. This includes the beam asymmetry Σ, determined as a function of various invariant masses and angles using a quasi two-body approach, along with the three-body asymmetries I^c and I^s. The latter two observables are unique to the acoplanar kinematics of multi-meson final states and have been measured for the first time within this work. The comparison of the results to solutions derived from various theoretical frameworks demonstrates the sensitivity of the observables to the contributing resonances and their decays.

Main results of this work have already been published in [GSvP$^+$08] and [GSvP$^+$10].

Zusammenfassung

Die Photoproduktion von Mesonen am Nukleon ist hervorragend dazu geeignet, ein besseres Verständnis der Struktur der Baryonen und ihres Anregungsspektrums zu gewinnen. In Photoproduktionsexperimenten ist eine Vielzahl von Endzuständen zugänglich, zu denen verschiedene Resonanzen auf unterschiedliche Weise beitragen. Insbesondere im Bereich höherliegender Anregungsenergien gewinnt hierbei die Multi-Meson-Produktion an Bedeutung und erlaubt den Zugang zu sequentiellen Resonanzzerfällen, z.B. über Zustände wie $\Delta(1232)P_{33}$ oder $\mathrm{N}(1535)S_{11}$. Für ein umfassendes Verständnis der beteiligten Prozesse ist allerdings die reine Messung von totalen und differenziellen Wirkungsquerschnitten unzureichend. Für die eindeutige Bestimmung der an einem Prozess beteiligten Amplituden ist zudem die Extraktion von Polarisationsobservablen unabdingbar. Hierzu sind Experimente unter Verwendung polarisierter Photonstrahlen und polarisierter Targets notwendig.

In der vorliegenden Arbeit wird die Analyse von Daten präsentiert, die mit dem Crystal-Barrel/TAPS-Experiment an der Bonner Beschleunigeranlage ELSA gewonnen wurden. Hierbei kam ein linear polarisierter Photonenstrahl, der auf ein Flüssigwasserstoff-Target traf, zum Einsatz. Das Detektorsystem ist auf den Nachweis von Viel-Photonen-Endzuständen optimiert. Die Daten wurden für einen Energiebereich der einlaufenden Photonen von 970 MeV bis 1650 MeV im Hinblick auf die Reaktion $\gamma\mathrm{p} \to \mathrm{p}\pi^0\eta \to \mathrm{p}4\gamma$ selektiert. In diesem Bereich konnten Polarisationsgrade von bis zu 50% erreicht werden.

Aus diesen Daten wurden sämtliche Polarisationsobservablen extrahiert, die mittels linear polarisierter Photonen und einem unpolarisierten Target zugänglich sind. Dies beinhaltet die Quasi-Zweikörper-Strahlasymmetrie Σ, die als Funktion verschiedener invarianter Massen und Winkel bestimmt wurde. Zudem wurden zum ersten Mal die Dreikörper-Asymmetrien I^c und I^s gemessen, die einzig in der akoplanaren Kinematik von Multi-Mesonen-Endzuständen auftreten. Der Vergleich der gewonnenen Daten mit Ergebnissen verschiedener theoretischer Ansätze zeigt die Sensitivität der Observablen auf die beitragenden Resonanzen und ihre Zerfälle.

Wesentliche Ergebnisse dieser Arbeit wurden bereits in [GSvP$^+$08] und [GSvP$^+$10] veröffentlicht.

Contents

1 Outline of this work

This work is structured as follows: The next chapter gives a brief introduction to the field of hadrons as composite systems of strongly interacting constituents in general and the excitation spectrum of baryons in particular.
In chapter 3 the motivation for the determination of polarization observables in pseudoscalar meson photoproduction is given. The significance of the $p\pi^0\eta$ final state in particular is discussed along with an overview of the available data and theoretical models for this reaction.
The following chapter introduces the experimental facilities and techniques used to obtain the data relevant for this work. This includes the production of linearly polarized photons from the primary electron beam delivered by the Electron Stretcher Accelerator ELSA, and the setup of the Crystal Barrel/TAPS experiment, a high acceptance calorimeter arrangement optimized for the detection of multi-photon final states.
Chapter 5 gives an outline of the calibration and reconstruction methods applied to the detector system. Here the electronic signals provided by the various components are translated to physical quantities like time and energy and correlated to the actual particles creating the detector signals in the first place.
The datasets used in this analysis and the identification of the $p\pi^0\eta$ final state are the topics of chapter 6. Here the basic considerations for the selection process are illustrated and the cuts applied on the data are described along with the application of a kinematic fit.
Chapter 7 focuses on the extraction of the polarization observables from the selected data sample in a quasi two-body and a full three-body approach. The resulting beam asymmetries are shown as functions of various quantities along with invariant mass distributions and Dalitz plots, illustrating the different contributions to $\pi^0\eta$-photoproduction.
The discussion of the results in comparison to other published data and in the context of the Bonn-Gatchina partial wave analysis, the Fix isobar model and the Valencia chiral unitary framework is topic of chapter 8, leading to an interpretation of the data with respect to the participating excited states and their decay couplings.
The experimental findings within the framework of this analysis and their interpretation are summarized in chapter 9 and the current and future experimental program of the

Crystal Barrel/TAPS experiment is presented briefly.
The tabular presentation of the results is given in the appendices, along with additional spectra, some technical information, and a list of publications and conference contributions based on this work.

2 Introduction

2.1 Hadrons and the quark model

Starting with experiments utilizing high-energy cosmic rays in the 1930s and culminating in the use of the first particle accelerators in the following decades, a multitude of seemingly elementary particles were discovered, a situation referred to as the *particle zoo*. It was not until the 1960s that a successful classification scheme was devised, introducing elementary particles, the *quarks*, as constituents of composite systems, the *hadrons*. This classification scheme, the quark model, developed independently by Murray Gell-Mann and George Zweig[1], allowed for a comprehensive description of the properties of the two classes of hadrons, the *mesons* and the *baryons*.

2.1.1 Properties of quarks

It is now known that in nature six versions of quarks, so called *flavors*, exist, named *up* (u), *down* (d), *charm* (c), *strange* (s), *top* (t) and *bottom* (b), along with their corresponding antiparticles. In the following some of the main properties of the quarks are summarized.
The quarks are, like the leptons, spin $s = 1/2$ particles and come in two (electrical) charge states with $\Delta q = 1$, $q = +2/3$ and $q = -1/3$. This suggests a classification scheme in three generations, analogous to the six leptons (ν_e, e), (ν_μ, μ), and (ν_τ, τ), with increasing masses [A$^+$08b]:

$$\begin{pmatrix} q = +\frac{2}{3} \\ q = -\frac{1}{3} \end{pmatrix} \begin{pmatrix} u,\ m = 1.5 - 3.3\,\mathrm{MeV} \\ d,\ m = 3.5 - 6.0\,\mathrm{MeV} \end{pmatrix} \begin{pmatrix} c,\ m = 1.27^{+0.07}_{-0.11}\,\mathrm{GeV} \\ s,\ m = 104^{+26}_{-34}\,\mathrm{MeV} \end{pmatrix} \begin{pmatrix} t,\ m = 171.2 \pm 2.1\,\mathrm{GeV} \\ b,\ m = 4.20^{+0.17}_{-0.07}\,\mathrm{GeV} \end{pmatrix}.$$

The masses of the three light flavors, u, d, and s, are orders of magnitude smaller than for the other three, with the quarks within the first generation being approximately mass-degenerate. This situation is reflected in the proton and the neutron, which are

[1] The term *quarks* was introduced by Gell-Mann, Zweig referred to the constituents as *aces*, assuming there were four of them.

also (nearly) mass-degenerate states differing only in electrical charge. This suggests the identification of these particles as two states of the same particle, the nucleon, and the introduction of a new quantum number associated with this behavior, the isospin I, defined analogously to the spin of a particle, introducing an $SU(2)$ symmetry. Accordingly, the isospin is a conserved quantity with respect to the strong interaction[2]. In this framework the quarks composing the nucleon, u and d, form a doublet with isospin 1/2, differing in the third component I_3, being 1/2 for the u- and $-1/2$ for the d-quark. In general, particles of given isospin I occur in $2\mathsf{I}+1$ charge states. Other quark-flavors than u and d carry isospin 0, but here additional flavor quantum numbers such as strangeness S arise.

The comparably light masses of the three flavors u, d, and s suggest an extension of the $SU(2)_{\text{isospin}}$ symmetry to include the strange flavor. This (approximate) $SU(3)_{\text{flavor}}$ symmetry will be addressed in section 2.1.2. These masses however might seem incongruous at first, knowing that e.g. the proton with a mass of $m_{\text{p}} = 938.272\,\text{MeV}$ consists of two u and one d quark (see 2.1.2). This apparent discrepancy can be resolved by acknowledging the complicated structure of the interaction between the quarks confined in a hadron. It gives rise to a sea of gluons, the mediators of the strong interaction, and quark-antiquark-pairs generated within e.g. the proton, contributing to its effective mass. It is therefore convenient to introduce the *constituent quark mass* which takes these effects into account, as opposed to the *current quark masses* stated above. In this framework, the constituent masses of up and down quarks amount to $m_u \approx m_d \approx 350\,\text{MeV}$ and for the strange quark to $m_s \approx 500\,\text{MeV}$.

The source of the strong interaction between the quarks is the color charge. The concept has been introduced to address a problem posed by the existence of the Δ^{++}-baryon. The quark content of the Δ^{++} is $|uuu\rangle$ with spin $S = 3/2$, Isospin $\mathsf{I} = 3/2$, and vanishing angular orbital momentum $L = 0$ between the quarks. Therefore, the decomposition of the wavefunction for this state in its components

$$|uuu\rangle = |\text{space}\rangle_{\text{S}}\,|\text{spin}\rangle_{\text{S}}\,|\text{flavor}\rangle_{\text{S}}, \tag{2.1}$$

contains only symmetrical terms. The Pauli exclusion principle however states that the total wavefunction of a system of fermions has to be antisymmetric. The introduction of a new quantum number, color, solves this by extending the wavefunction by an antisymmetrical term:

$$|uuu\rangle = |\text{space}\rangle_{\text{S}}\,|\text{spin}\rangle_{\text{S}}\,|\text{flavor}\rangle_{\text{S}}\,|\text{color}\rangle_{\text{A}}. \tag{2.2}$$

[2] According to Noether's theorem, every symmetry transformation implies a corresponding conservation law.

The quarks are assigned three different color charges, called *red* (R), *green* (G), and *blue* (B), respectively, generating again an $SU(3)$ symmetry, here an exact symmetry, $SU(3)_{\text{color}}$. Antiquarks carry the respective anticolors *anti-red* ($\bar{R}$), *anti-green* ($\bar{G}$) and *anti-blue* ($\bar{B}$). Up to now only colorless particles and especially no free quarks have been observed. This leads to the conclusion that quarks are confined to colorless, composite systems, the most simple of which would be composed of either a quark-antiquark pair $|q\bar{q}\rangle$ or three quarks $|qqq\rangle$, the mesons and baryons. For a three-quark system, like the Δ^{++}, the color wave function reads:

$$|\text{color}\rangle_{\text{A}} = \frac{1}{\sqrt{6}}(RGB - RBG + BRG - BGR + GBR - GRB). \tag{2.3}$$

In case of the mesons, the color singlet state is symmetrical and reads:

$$|\text{color}\rangle_{\text{S}} = \frac{1}{\sqrt{3}}(R\bar{R} + G\bar{G} + B\bar{B}). \tag{2.4}$$

2.1.2 Mesons and baryons

The considerations stated above now make it possible to classify the multitude of discovered particles in terms of their quark content and quantum numbers. Figure 2.1 shows such an ordering scheme for mesons using the strangeness S and the third component of the isospin $\mathsf{I_3}$ as ordering parameters. These *multiplets* arise when grouping the mesons according to their total angular momentum $J = L + S$ and parity $P = (-1)^{L+1}$. Here the lightest ground state ($L = 0$) mesons form nonets with $J^P = 0^-$ ($S = 0$), the *pseudoscalar* mesons, and $J^P = 1^-$ ($S = 1$), the *vector* mesons.
The three lightest quarks form a representation of the special unitary group $SU(3)$, $\mathbf{3}$, and the according antiquarks form the conjugate representation $\bar{\mathbf{3}}$. The combination of both yields:

$$\mathbf{3} \otimes \bar{\mathbf{3}} = \mathbf{8} \oplus \mathbf{1}, \tag{2.5}$$

so these nonets are in fact a combination of an octet and a singlet[3]. For the baryons the ordering scheme is similar, their nature of being qqq states however gives rise to more complex configurations. The description of the three quarks within their $SU(3)_{\text{flavor}}$

[3] Actually two isosinglets with identical quantum numbers exist in the nonet. Therefore a mixing between these states is possible. In case of the pseudoscalar mesons, these states, the η_1 $SU(3)$-singlet and the η_8 $SU(3)$-octet state, mix in such a way that $\eta_1 \approx \eta'$ and $\eta_8 \approx \eta$. In case of the vector mesons the situation is less clear due to the maximal mixing of the ω and ϕ. See e.g. [Gri08] for details.

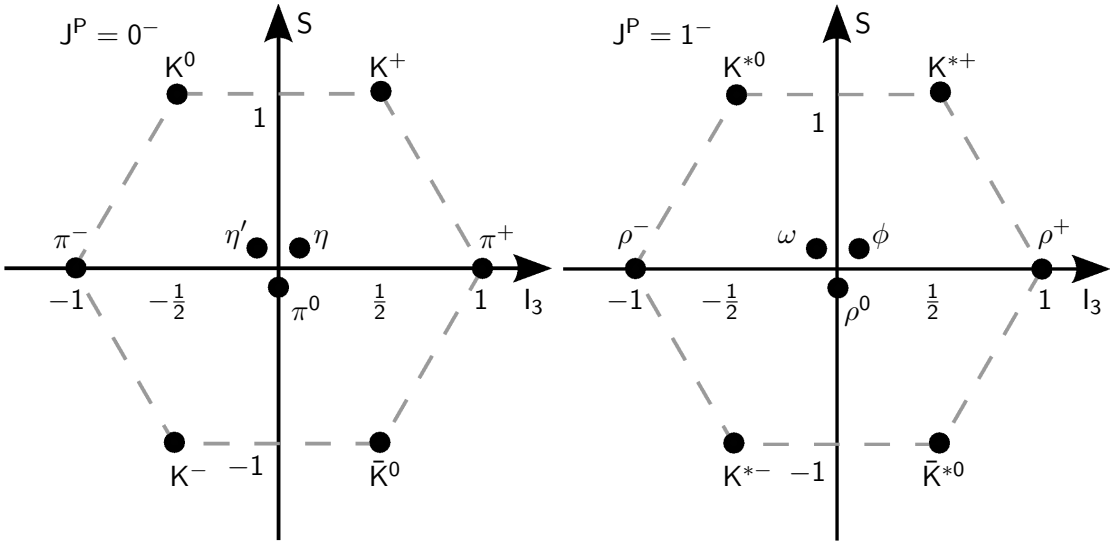

Figure 2.1: **Pseudoscalar and vector meson nonets.** The mesons are ordered by their strangeness S (vertical) and third component of the isospin I_3 (horizontal). Using this scheme, particles with the same electrical charge fall on the same diagonal. Left: Pseudoscalar mesons ($J^P = 0^-$), Right: Vector mesons ($J^P = 1^-$).

representation yields:

$$\mathbf{3} \otimes \mathbf{3} \otimes \mathbf{3} = \mathbf{10}_S \oplus \mathbf{8}_{MS} \oplus \mathbf{8}_{MA} \oplus \mathbf{1}_A, \tag{2.6}$$

where the subscripts refer to the symmetry properties under the exchange of quarks. This translates to one completely symmetric (S) decuplet, one octet with mixed symmetry (symmetric under exchange of the first two quarks, MS), one octet with mixed antisymmetry (antisymmetric under exchange of the first two quarks, MA) and one completely antisymmetric singlet. Considering spin in addition leads, using the $SU(2)$ representation, to the following configurations:

$$\mathbf{2} \otimes \mathbf{2} \otimes \mathbf{2} = \mathbf{4}_S \oplus \mathbf{2}_{MS} \oplus \mathbf{2}_{MA}. \tag{2.7}$$

The combination of (2.6) and (2.7) leads to

$$\mathbf{6} \otimes \mathbf{6} \otimes \mathbf{6} = \mathbf{56}_S \oplus \mathbf{70}_{MS} \oplus \mathbf{70}_{MA} \oplus \mathbf{20}_A. \tag{2.8}$$

These multiplets can be subdivided into:

$$\begin{aligned} \mathbf{56} &= {}^4 10 +^2 8 \\ \mathbf{70} &= {}^2 10 +^4 8 +^2 8 +^2 1 \\ \mathbf{20} &= {}^2 8 +^4 1. \end{aligned}$$

The superscript denotes the number of possible spin orientations within the multiplet, $2S+1$. The requirement for an antisymmetric wavefunction for the baryons now leads to two multiplets, the $J^P = 1/2^+$ octet and the $J^P = 3/2^+$ decuplet, shown in figure 2.2, again arranged by their strangeness S and third component of the isospin I_3.

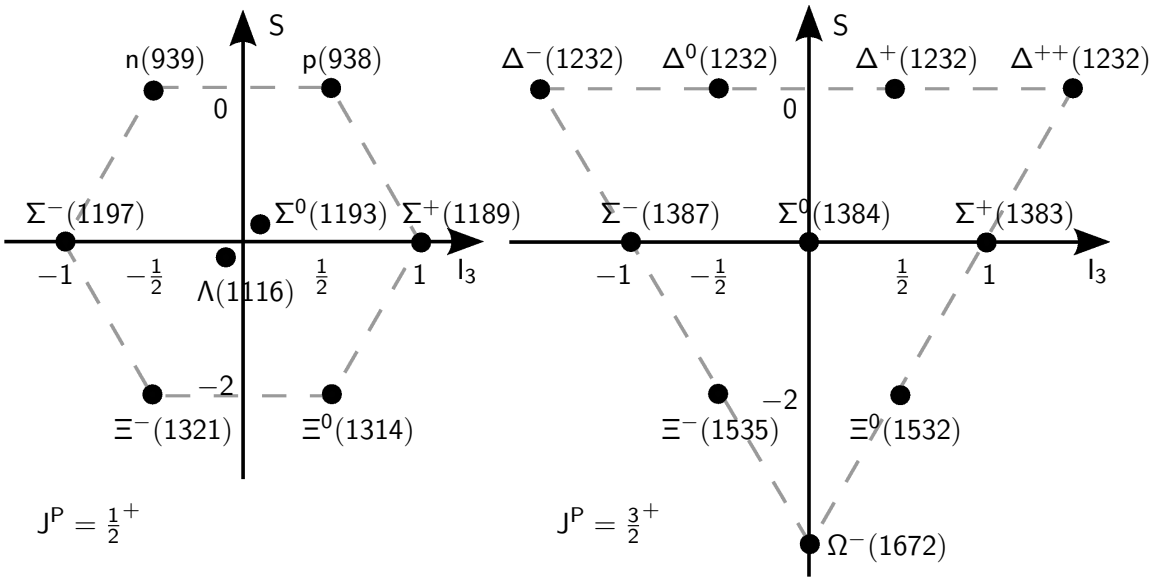

Figure 2.2: **Baryon octet and decuplet.** The baryons are ordered by their strangeness S (vertical) and third component of the isospin I_3 (horizontal). Using this scheme, particles with the same electrical charge fall on the same diagonal. Left: $J^P = 1/2^+$ octet, Right: $J^P = 3/2^+$ decuplet.

2.2 Excitation spectrum

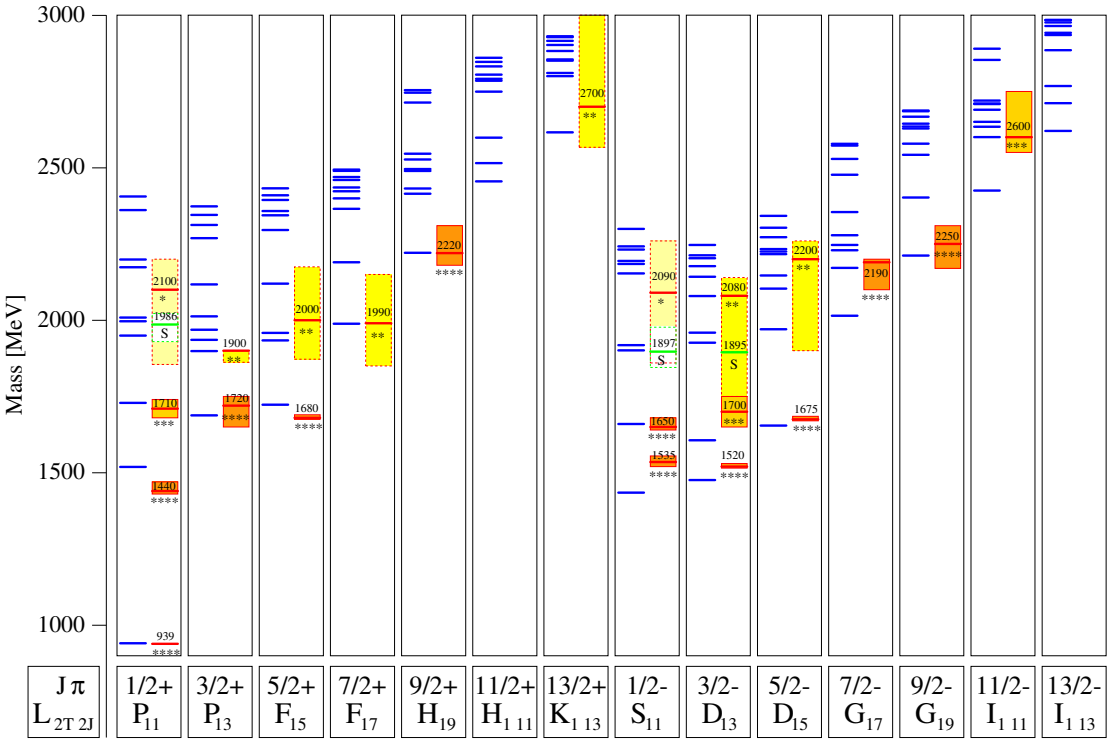

Figure 2.3: **Nucleon excitation spectrum.** Shown are the excited states of the nucleon ordered by their masses (vertical) and their total angular momentum and parity, J^P. Each column shows on the left the predictions by the Bonn-constituent-quark-model [LMP01] in blue and on the right the experimental findings with the uncertainties in their masses (colored boxes) and PDG classification (stars) [A$^+$08b].

The nature of baryons as composite systems allows for their excitation and thereby the formation of new states. The structure of *Quantum Chromodynamics* (QCD), the theory of the strong interaction, does not allow for the calculation of such states[4]; *constituent quark models* are used to describe the excitation spectra of hadrons. Such models assume constituent quarks as introduced in the previous section, bound by a confinement potential. One difference between these respective modern quark models is the parametrization of the residual interaction between the quarks. Figure 2.3 shows the excitation spectrum of the nucleon as predicted within the framework of the Bonn-model [LKMP01, LMP01] as blue lines on the left for each J^P combination, compared to

[4] In the energy regime of baryons, the strong coupling constant α_s approaches 1, ruling out a pertubative treatment of the system.

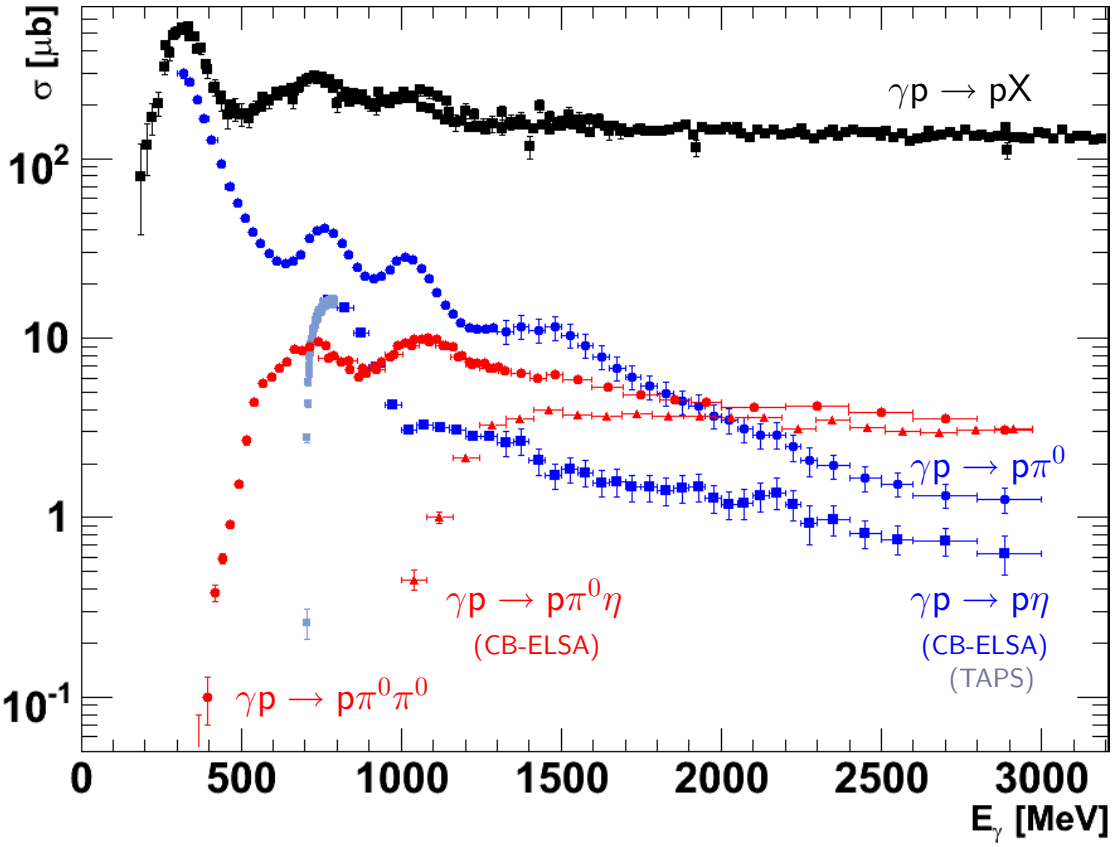

Figure 2.4: **Photoabsorption cross section on the proton.** Shown is the world data on the total photoabsorption cross section on the proton ([BLACK]) along with selected single- ([BLUE]) and double-meson ([RED]) production cross sections.

the experimental findings on the right (red lines with colored boxes denoting the uncertainties in their masses). While at low excitation energies the agreement between model and experiment is qualitatively reasonable, starting at masses of about 1900 MeV major discrepancies are observed. The model predicts a multitude of states for which few to no experimental findings are reported. Assuming the premise of three constituent quarks being the effective degrees of freedom for baryon excitation is correct, this presents an experimental challenge.

Nearly all of the experimental data shown in figure 2.3 has been obtained in pion-nucleon-scattering experiments. Should the *missing states* couple only weakly to Nπ, they might have escaped detection in the experiments, an interpretation supported by calculations, see e.g. [CR93, CR94, LKMP01]. Photoproduction experiments, investigating final states different from Nπ, therefore have a big discovery potential. Figure 2.4

shows the total photoabsorption cross section on the proton along with selected final states. It is obvious that a direct determination of the excited states from this spectrum, like in atomic spectroscopy, is not possible. Excited states in baryon spectroscopy exhibit large decay widths[5], and are energetically close, leading to an overlap of the states. Different structures in the cross sections have been observed, depending on the final state under investigation, however for a detailed identification of states contributing to a specific reaction a more refined analysis technique is necessary, the partial wave analysis (PWA). In a PWA, states contributing to different partial waves are parametrized in a K-matrix formalism in case of strongly overlapping resonances or as relativistic Breit-Wigner amplitudes. The superposition of these states, along with non-resonant background amplitudes, then results in the cross section. An example is shown in figure 2.5 for the total cross section in η-photoproduction. The three partial waves, with $J^P = 1/2^-$, $3/2^+$, and $5/2^-$, which are strongly contributing to the reaction, are depicted, along with contributions due to ρ- and ω-exchange, as calculated within the framework of the Bonn-Gatchina partial wave analysis (BnGa-PWA) [ASB$^+$05], a coupled channel analysis in which the positions, total and partial widths and relative strengths of the contributing states are calculated and fitted to different data sets in parallel. The information contained in total and differential cross sections however does not sufficiently constrain the fit, ambiguous solutions describing the data with equal quality can occur. This problem can be countered by the measurement of a set of observables that unambiguously fixes the amplitudes for a given reaction, leading to a unique partial wave decomposition. This set of measurements, the *complete experiment* is in part the topic of the next chapter.

[5] Excited, non-strange baryonic states decay via the strong interaction, resulting in lifetimes of the order of 10^{-23} s. The lifetime τ and the width Γ of a state are correlated due to Heisenberg's uncertainty principle: $\tau = \hbar/\Gamma$.

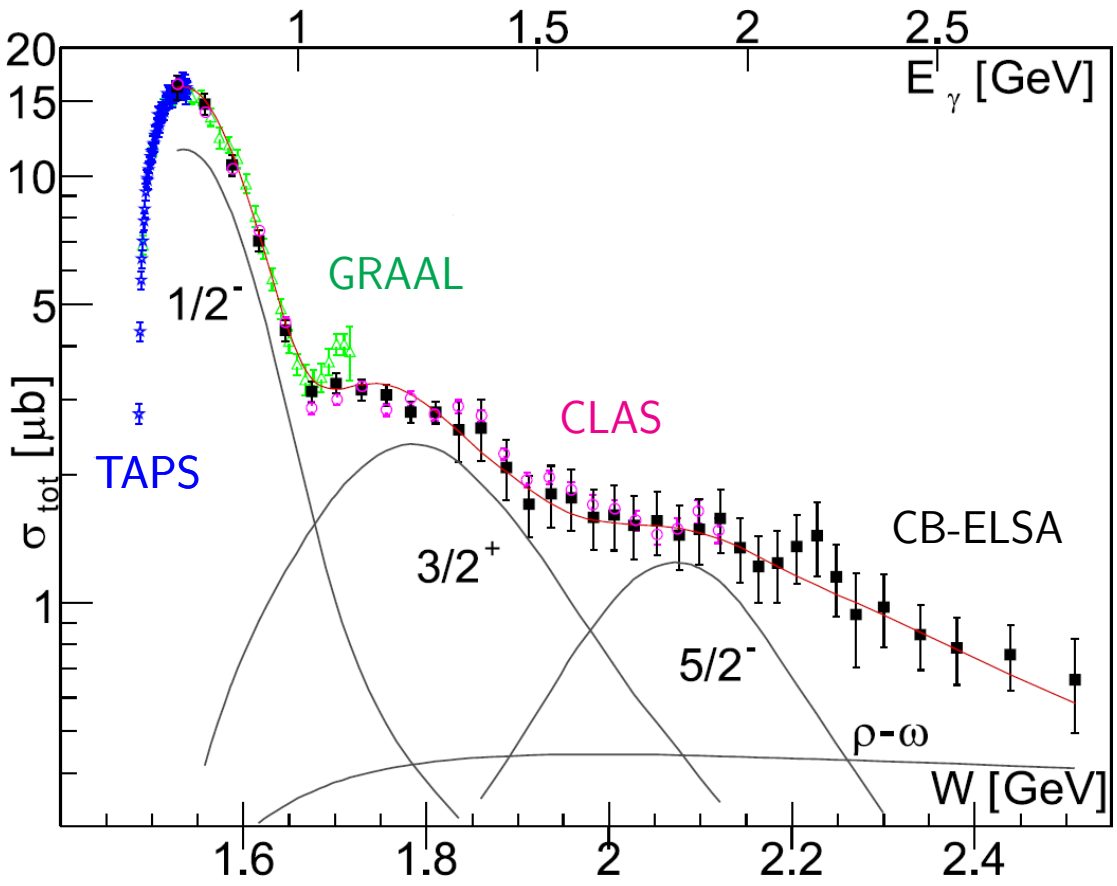

Figure 2.5: **Total cross section for η-photoproduction.** Given are the dominating partial waves ($1/2^-$, $3/2^+$, $5/2^-$) along with t-channel ρ-/ω-exchange contributions as derived from a BnGa-PWA fit (red line) [ASB+05].

3 Motivation

3.1 Polarization observables and complete experiment

The term *complete experiment* refers to a set of measurements that uniquely fixes the four (eight) complex helicity or transversity amplitudes of a given single meson (meson-pair) photoproduction reaction [BDS75, RO05]. The unpolarized cross section, obtained already in experiments without defined incoming photon beam or target polarization only provides information on the sum of the absolute squares of these amplitudes. Single, double and in the case of meson-pair production also triple polarization measurements are necessary to fulfill the constraints posed by the complete experiment to allow for the extraction of the real and imaginary parts of the amplitudes independently[1]. For the field of pseudoscalar meson production these constraints will be introduced in the following pages.

3.1.1 Single pseudoscalar meson production

For the photoproduction of a single pseudoscalar meson the total cross section including all polarization observables reads [SHKL09]:

$$\begin{aligned}\sigma = \sigma_{\mathbf{0}}(1 \quad &- \quad \delta_l \mathbf{\Sigma} \cos 2\phi + \Lambda_y \mathbf{T} + \Lambda_{y'} \mathbf{P} \\ &- \quad \delta_\odot \Lambda_z \mathbf{E} + \delta_l \Lambda_z \mathbf{G} \sin 2\phi + \delta_\odot \Lambda_x \mathbf{F} + \delta_l \Lambda_x \mathbf{H} \sin 2\phi \\ &+ \quad \delta_\odot \Lambda_{x'} \mathbf{C}_{\mathbf{x}'} + \delta_\odot \Lambda_{z'} \mathbf{C}_{\mathbf{z}'} + \delta_l \Lambda_{x'} \mathbf{O}_{\mathbf{x}'} \sin 2\phi + \delta_l \Lambda_{z'} \mathbf{O}_{\mathbf{z}'} \sin 2\phi \\ &+ \quad \Lambda_z \Lambda_{x'} \mathbf{L}_{\mathbf{x}'} + \Lambda_z \Lambda_{z'} \mathbf{L}_{\mathbf{z}'} + \Lambda_x \Lambda_{x'} \mathbf{T}_{\mathbf{x}'} + \Lambda_x \Lambda_{z'} \mathbf{T}_{\mathbf{z}'}).\end{aligned} \tag{3.1}$$

Here δ_l ($\delta_\odot$) denotes the degree of linear (circular) photon polarization, $\Lambda_{x,y,z}$ ($\Lambda_{x',y',z'}$) the polarization of the target (recoiling) baryon along the respective axis. In the case of recoil polarization, the direction of the recoiling baryon is $-\hat{z}'$. ϕ is the angle of the photon polarization vector with respect to the $(\hat{x},\hat{z})$-plane, the incoming photon direction

[1] In fact the polarization observables can be expressed as the real (imaginary) part of linear combinations of bilinears formed from these amplitudes.

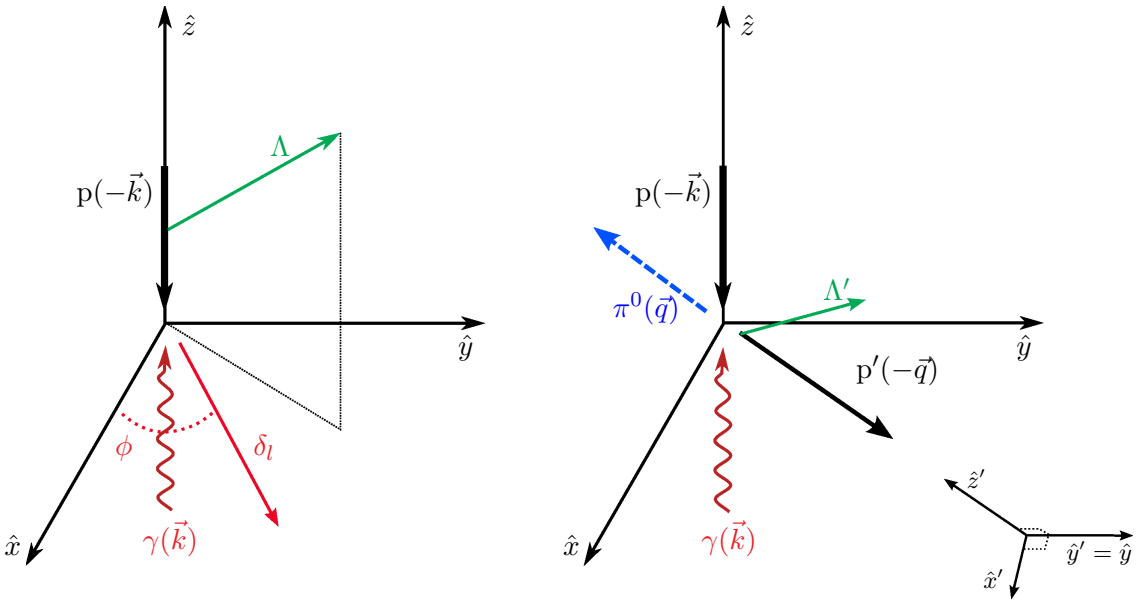

Figure 3.1: **Coordinate systems in single meson production.** The center-of-momentum coordinate systems used in (3.1) for the reaction $\gamma(\vec{k}, \delta_l) + \mathrm{p}(-\vec{k}, \Lambda) \rightarrow \pi^0(\vec{q}) + \mathrm{p}(-\vec{q}, \Lambda')$. Left: Initial γp-system, right: Final pπ^0-system [SHKL09].

is $\hat{z}$ (see figure 3.1). A total of 16 observables arise. These are, in the first line of (3.1), the unpolarized cross section σ_0 along with three single polarization observables, the beam asymmetry Σ, the target asymmetry T and the recoil asymmetry P. Combining beam- and target polarization (BT), beam- and recoil polarization (BR) and target- and recoil polarization (TR), four more observables are accessible for each combination. A complete experiment now requires the measurement of a selected set of eight of these, exploiting certain identities of combinations of the observables. This set is not arbitrary but requires the determination of the unpolarized cross section and the three single-polarization observables along with four well chosen double-polarization observables. An overview of the sets constituting a complete experiment and the respective identities can be found in [CT97].

3.1.2 Pseudoscalar meson-pair production

When dealing with two pseudoscalar mesons in the final state, a first step to the determination of polarization observables is the treatment of the reaction in a quasi two-body kinematic, e.g. $X\eta$ instead of p$\pi^0\eta$, with $X \rightarrow \mathrm{p}\pi^0$. Such an ansatz has the advantage

that the formalism introduced in the previous section can be applied to such three-body reactions just the same. Allowing for an additional final state particle however introduces additional degrees of freedom to the reaction which is reflected in the cross section. In case of a linearly or circularly polarized beam and without target- or recoil-polarization measurement for example, the cross section for two-meson production reads, within the framework introduced in [RO05],

$$\begin{aligned} \sigma = \sigma_{\mathbf{0}}(1 \quad &+ \quad \delta_{\odot}\mathbf{I}^{\odot} \\ &- \quad \delta_l(\mathbf{I^s}\sin 2\phi + \mathbf{I^c}\cos 2\phi). \end{aligned} \tag{3.2}$$

In this configuration alone already four observables arise, where in single meson production only two, σ_0 and Σ, are accessible. Taking target- and recoil-polarization and their combinations (BT, BR, TR and BTR) into account, a total of 64 observables appear in the cross section. As for the single-meson production, using a set of identities, the number of measurements for a complete experiment in pseudoscalar meson-pair production can be derived, leading to a set of 15 observables to be determined. The possible sets, for examples see [RO05], consist of the unpolarized cross section along with single-double- and triple-polarization observables.

Here the problem inherent to the quasi two-body approach becomes apparent. In this framework only 16 observables are accessible in general, none of which occur due to triple-polarization experiments. While the measurements of such observables still yields valuable information for the interpretation of the reactions, a full three-body approach to the photoproduction of pseudoscalar meson-pairs is indispensable for a complete description of the processes. In the example given in (3.2) for instance, additional information is contained in the polarization observables I^s and I^c which would be reduced to one single observable Σ in a quasi two-body approach, using linearly polarized photons (cf. chapter 7); using circularly polarized photons without defined target polarization, no information in addition to the unpolarized cross section would be obtained.

For the reaction $\gamma N \rightarrow N\pi\pi$, data on the helicity asymmetry $I^{\odot}$ (see (3.2)) has been published in [S$^+$05a, KZF$^+$09] and an analysis with respect to the beam asymmetries I^s and I^c will be presented in [Sok10]. For the reaction $\gamma N \rightarrow N\pi\eta$ however, prior to this thesis, no data has been published in a full three-body framework, apart from the results presented in this work.

3.2 $\pi^0\eta$-photoproduction off the proton

The photoproduction of $\pi^0\eta$-pairs is a comparably young field of research with the first experimental data published in 2006 [N$^+$06]. This is, among other constraints such as incoming beam energy, most likely due to the high demands posed by this reaction concerning geometrical acceptance and photon detection efficiency of the experimental setup. The study of the reaction $\gamma p \rightarrow p\pi^0\eta$ does, however, give the opportunity to address some intriguing questions in the field of hadron physics, as shown below.

Missing resonances As can be seen in figure 2.4, with increasing incoming photon energy the cross sections for production of meson-pairs exceed the ones for the single mesons. This is particularly interesting, since the open question of the missing resonances predicted by constituent quark models arises in this high-energy region. Such high-lying resonances may not decay directly to the nucleon ground-state via emission of a single meson, but rather via a sequential decay chain, e.g.

$$X \rightarrow Y\eta \rightarrow p\pi^0\eta. \tag{3.3}$$

Such a process not only provides independence from the πN couplings mentioned in section 2.2 due to the photoproduction mechanism, but is also independent of the photon coupling of the state Y.
In addition to the general advantages of meson-pair production, the $p\pi^0\eta$ final state is particularly attractive due to its isospin-selectivity. The η-meson is an isoscalar, so in the example given in (3.3), the states X and Y have the same isospin. This allows for the distinct study of excited Δ-states via the cascade

$$\Delta^* \rightarrow \Delta\eta \rightarrow p\pi^0\eta. \tag{3.4}$$

Negative-parity Δ-states Figure 3.2 shows the Δ excitation spectrum, in the same way as for the nucleon in section 2.2 as a comparison of the experimental findings to predictions by the Bonn model [LMP01]. Apart from the missing resonances also predicted in this isospin channel, a second distinct feature is apparent, a triplet of negative-parity states with masses of $\approx 1900\,\text{MeV}$. Not only is the existence of these states, $\Delta(1900)S_{31}$, $\Delta(1940)D_{33}$, $\Delta(1920)S_{35}$, less well established, as denoted by the number of stars, than for their positive-parity counterparts $\Delta(1910)P_{31}$, $\Delta(1920)P_{33}$, and $\Delta(1905)F_{35}$, but also the quark model predictions for the two parity states exhibit large discrepancies.

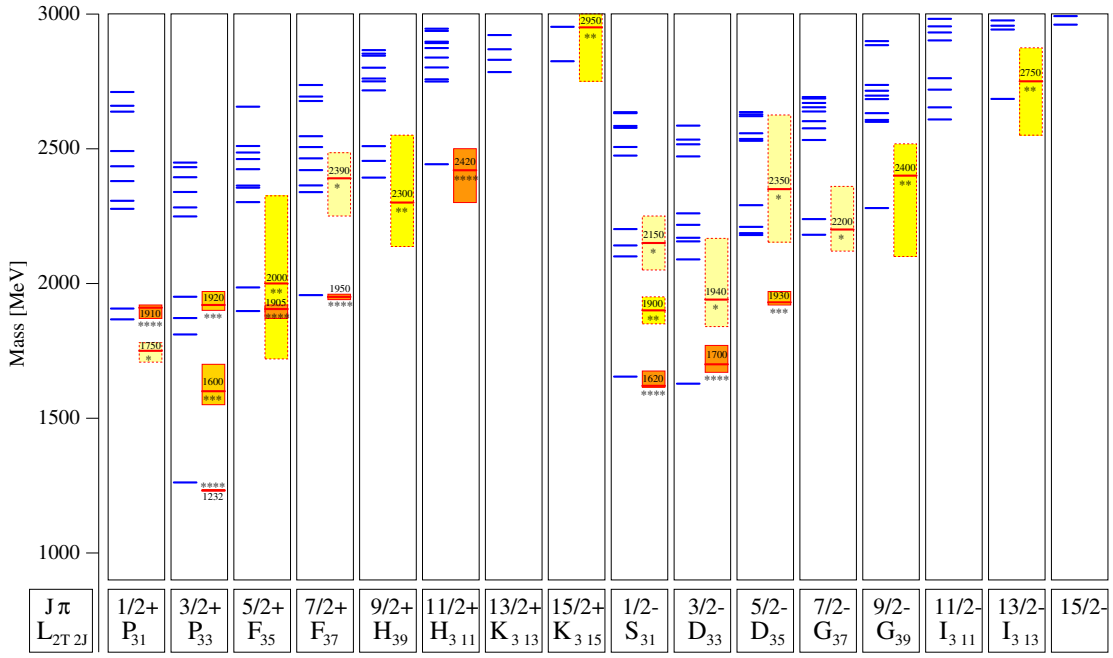

Figure 3.2: **Δ excitation spectrum.** Shown are the Δ-resonances, ordered by their masses (vertical) and their total angular momentum and parity, J^P (horizontal). Each column shows on the left the predictions by the Bonn-constituent-quark-model [LMP01] in blue and on the right the experimental findings with their uncertainties (colored boxes) and PDG classification (stars) [A$^+$08b].

While in case of the positive parity states these predictions describe the experimental findings quite accurately, the negative parity states are all predicted with masses of about 150-250 MeV higher than observed[2]. Additionally, further experimental evidence for the existence of such parity doublets is much needed for their interpretation with respect to quark dynamics or chiral symmetry restoration [Glo00, Kle03].

Resonance decays other than $\Delta\eta$ The decay chain (3.3) is only an example of the possible cascades occurring for high-lying resonances. Couplings to N(1535)$S_{11}\pi^0$ or p$a_0(980)$[3] are by no means forbidden but widely neglected in theoretical models (see chapter 8). Here the $\pi^0\eta$-photoproduction presents a unique tool for the further investigation of resonance decays via higher-mass baryons or mesons.

[2] A similar point concerning the mass predictions can be made for the $\Delta(1600)P_{33}$. This state can be seen as the first radial excitation of the Δ ground state, analogue to the N(1440)P_{11} *Roper*-resonance in the nucleon spectrum (see e.g. [CG98, FK09]), which is predicted equally too high (c.f. fig. 2.3).
[3] The scalar meson $a_0(980)$ dominantly decays to $\pi^0\eta$ [A$^+$08b].

3.2.1 Existing data

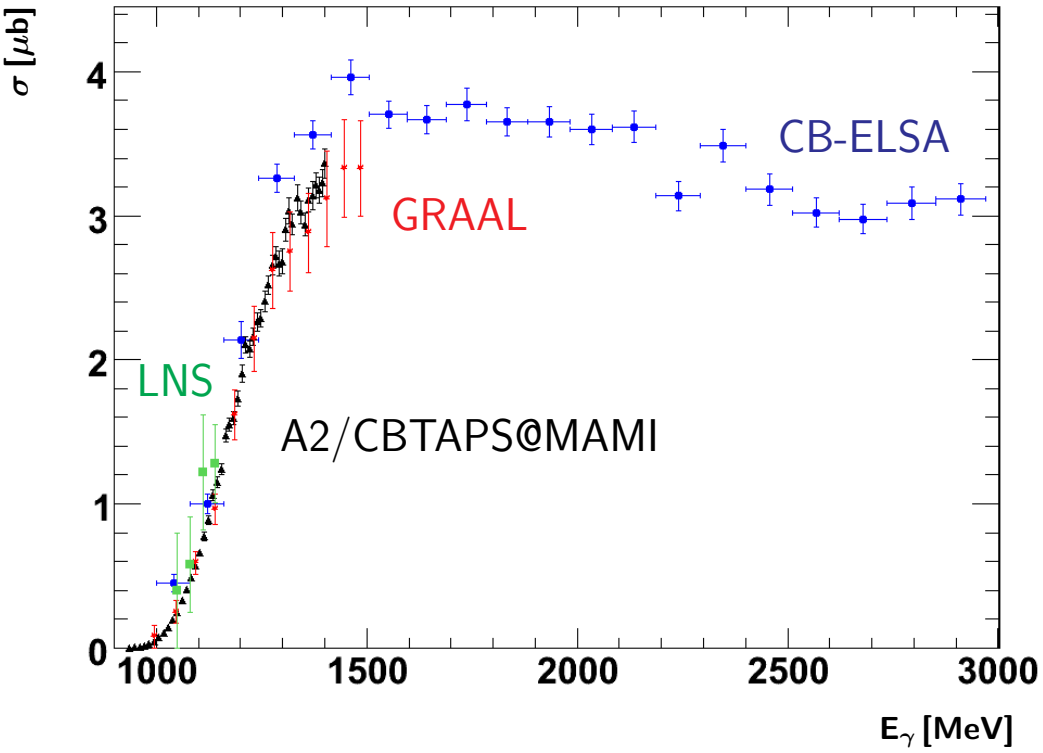

Figure 3.3: **Experimental data on the $\gamma p \rightarrow p\pi^0\eta$ total cross section.** Data taken from [N$^+$06, H$^+$08a, A$^+$08a, KF$^+$09].

As mentioned before, the reaction $\gamma p \rightarrow p\pi^0\eta$ is a comparably new field of study, and therefore the available data is rather sparse. In figure 3.3 all published data on the total cross section for $\pi^0\eta$-production off the proton is compiled.
The first analysis has been conducted by Nakabayashi et al. in 2006 [N$^+$06], who published four datapoints for the total cross section from threshold up to an incoming photon energy of $E_\gamma = 1150\,\text{MeV}$ along with some angular- and momentum distributions.
In 2008 the first Crystal Barrel data has been published by Horn et al. [H$^+$08a, H$^+$08b], extending the energy range for the total cross section to $E_\gamma = 3000\,\text{MeV}$ and also including differential cross sections $\mathrm{d}\sigma/\mathrm{d}\Omega$ and $\mathrm{d}\sigma/\mathrm{d}M$.
As the first data obtained using linearly polarized photons, parts of the results of the analysis presented in this work have been presented at the NSTAR 2007 conference [NST08] and published in the following year [GSvP$^+$08] at the same time as data obtained by the GRAAL collaboration [A$^+$08a]. Both publications feature the quasi

two-body beam asymmetry Σ. The GRAAL data, determined for an energy range of $E_\gamma = 1100 - 1500\,\mathrm{MeV}$, is shown in figure 3.4. Within this analysis, the total and mass-differential cross sections have also been extracted.

The latest data on the unpolarized cross section, obtained with the Crystal Ball/TAPS experiment at MAMI, has been published in 2009 by Kashevarov et al. [KF$^+$09]. Here, the total cross section along with angular- and invariant mass distributions has been determined from threshold up to $E_\gamma = 1400\,\mathrm{MeV}$.

In 2010, again parts of the results of this work, the first measurement of the beam asymmetries I^s and I^c, have been published [GSvP$^+$10].

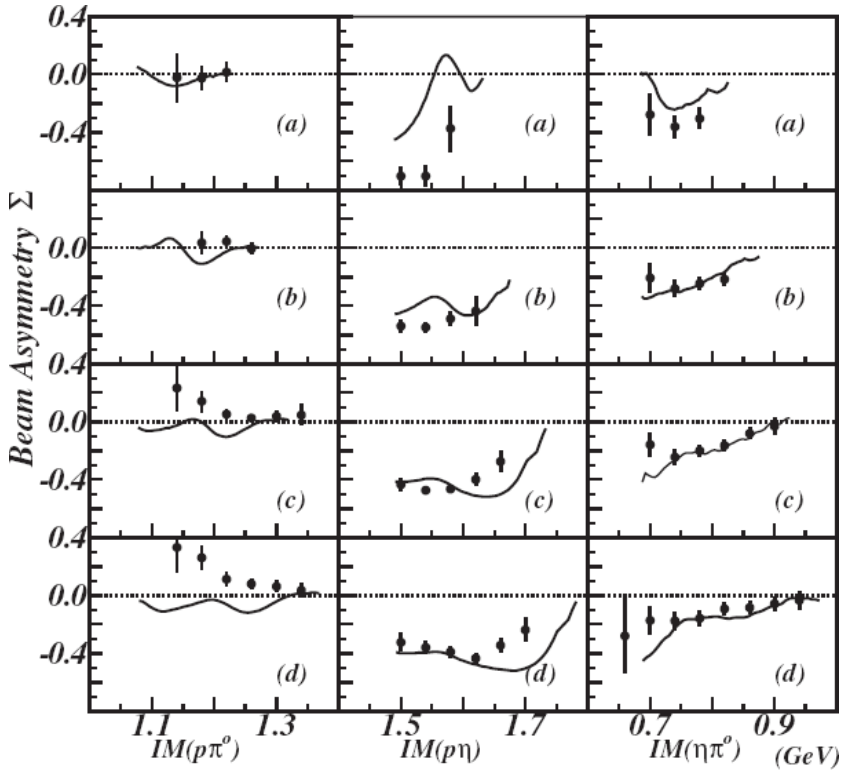

Figure 3.4: **Beam asymmetry Σ as published by the GRAAL collaboration.** Beam asymmetries for the incoming photon energy ranges $E_\gamma = 1050 \pm 50\,\mathrm{MeV}$ (a), $E_\gamma = 1250 \pm 50\,\mathrm{MeV}$ (b), $E_\gamma = 1350 \pm 50\,\mathrm{MeV}$ (c), $E_\gamma = 1450 \pm 50\,\mathrm{MeV}$ (d) as function of two-body invariant masses; solid curves: Valencia chiral unitary framework [A$^+$08a].

3.2.2 Theoretical frameworks

The photoproduction of the $p\pi^0\eta$ final state is studied theoretically within various frameworks. Most prominently, three approaches have to be noted, the partial wave analysis of the data within the BnGa-PWA [H$^+$08b], the chiral unitary framework developed by Döring et al. [DOS06, DOM10] and the isobar model by Fix et al. [FOT08, FKLO10]. The prerequisites of these and the differences in terms of resonant contributions and their decay couplings is the topic of chapter 8, where the application of the different frameworks to the results of this work and the implications thereof are discussed.

4 Experimental setup

This chapter gives an overview over the experimental facility used to take the data presented in this thesis. This includes the **EL**ectron **S**tretcher **A**ccelerator ELSA [Hil06] as well as the setup of the Crystal Barrel/TAPS experiment during the data taking period 2001-2003. After a description of the accelerator facility and its capabilities along with the production of a photon beam off the primary electron beam, the various detectors included in the experimental setup will be discussed, closing with the trigger system used to select the events during data taking.

4.1 Primary electron beam

4.1.1 ELSA

The Electron Stretcher Accelerator ELSA at the *Physikalisches Institut* of the university of Bonn is a three stage facility consisting of a linear accelerator, a booster synchrotron and a stretcher ring. ELSA is able to accelerate an electron beam up to energies of 3.5 GeV. This beam can then be extracted to two different experimental areas. Figure 4.1 gives an overview over the facility. The three accelerator stages are:

- **Electron source and linear accelerator (LINAC)**
  In the data taking period relevant to this work, electrons from a 48 keV thermal source were accelerated to 26 MeV by LINAC2 before being injected into the booster synchrotron. Additionally a second electron source is available, producing polarized electrons via photoemisson induced by a circularly polarized laser beam incident on a GaAs-like crystal. These electrons carry a degree of polarization of approx. 80%.

- **The booster synchrotron**
  The pre-accelerated electron beam is injected into the booster synchrotron [A$^+$68] where it is typically accelerated further up to an energy of 1.2 GeV. It is then

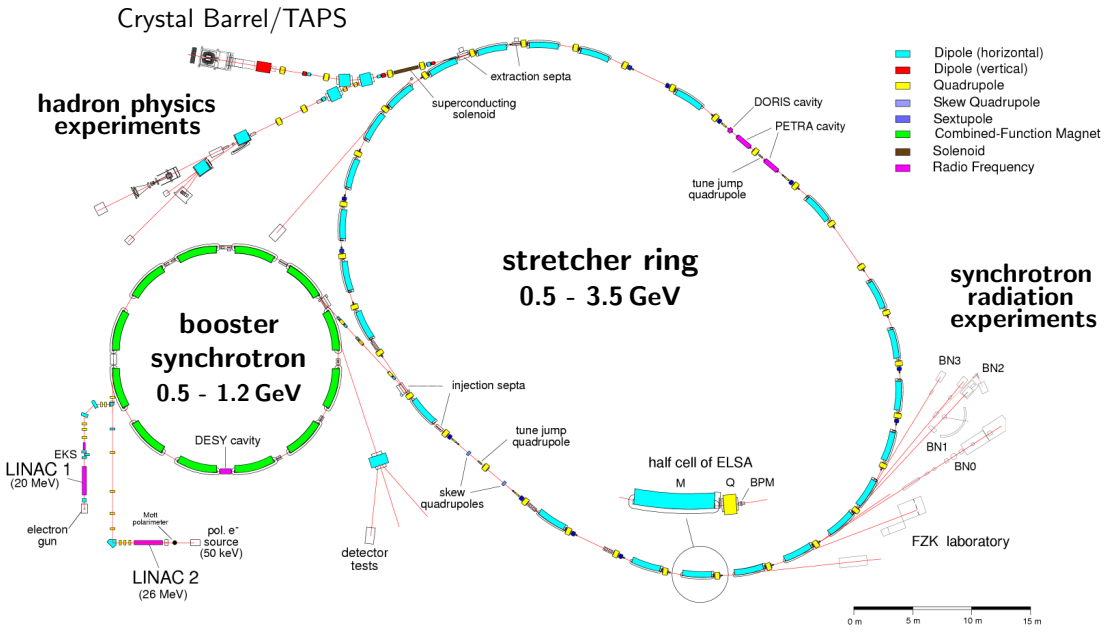

Figure 4.1: **The ELSA accelerator facility at the university of Bonn.** In a three stage system consisting of LINAC, booster synchrotron and stretcher ring electrons up to an energy of 3.5 GeV can be delivered to two experimental areas suitable for medium energy physics experiments (upper left).

extracted into the stretcher ring as a pulsed beam with an extraction rate of 50 Hz.

- **The stretcher ring**
  The stretcher- or storage ring can be operated in one of three different modes, depending on the requirements of the respective experiment:

  1. *Stretcher mode*
     In this mode of operation the electron beam is not further accelerated, so the maximum extraction energy caps at the maximum energy of the booster synchrotron. This beam, however, can be extracted to the experimental areas quasi-continuously for the time between two injections using slow extraction.

  2. *Post-accelerator mode*
     In this mode of operation several injections are accumulated and accelerated further in the stretcher ring, so energies up to 3.5 GeV can be provided. Since it is not possible to extract the electrons with a defined energy during the

post-acceleration phase, the extraction lasts for 1 to 30 s, depending on the extracted current, followed by a pause of about 1 s. Design values are 3 nA for an extraction time of 10 s, resulting in a duty factor of 50-90% [Hof01]. For the Crystal Barrel/TAPS experiment, ELSA was operated in this mode.

3. *Storage ring for synchrotron-radiation experiments*
   When used purely as a storage ring, the electron beam is stored at a constant energy for up to six hours. Due to the high beam currents this mode is mainly used for the production of high energetic synchrotron radiation which can be utilized by experiments at six dedicated beamlines.

4.2 Photon beam

The aim of the Crystal Barrel/TAPS experiment is the investigation of photon-induced reactions on the nucleon. For this, photons within the energy range of interest have to be produced from the primary electron beam. In general, two main procedures to achieve this are laser backscattering [D^+00] as used for instance in the GRAAL experiment [Sch92], and the utilization of the bremsstrahlung process. In case of linearly polarized photons, Compton-backscattering of polarized laser light yields linear photon beam polarizations up to 100%, but it limits the achievable luminosity as well as the maximum photon energy [San95]. In the Crystal Barrel/TAPS experiment the bremsstrahlung method is applied using a diamond radiator for the production of linearly polarized photons.

4.2.1 Bremsstrahlung

When passing through matter, electrons lose energy by three processes: ionization, radiation of bremsstrahlung, and Møller scattering. The relative strengths of these contributions are functions of the incoming electron energy as depicted in figure 4.2. While the contribution of Møller scattering is generally low, ionization is the leading process in the low energy regime and bremsstrahlung dominates above 10 MeV. The *critical energy*, E_c, is defined as the incoming electron energy at which the energy losses due to ionization and bremsstrahlung are equal; it can be approximated by [BS64]:

$$E_c = \frac{800\,\mathrm{MeV}}{Z + 1.2},$$

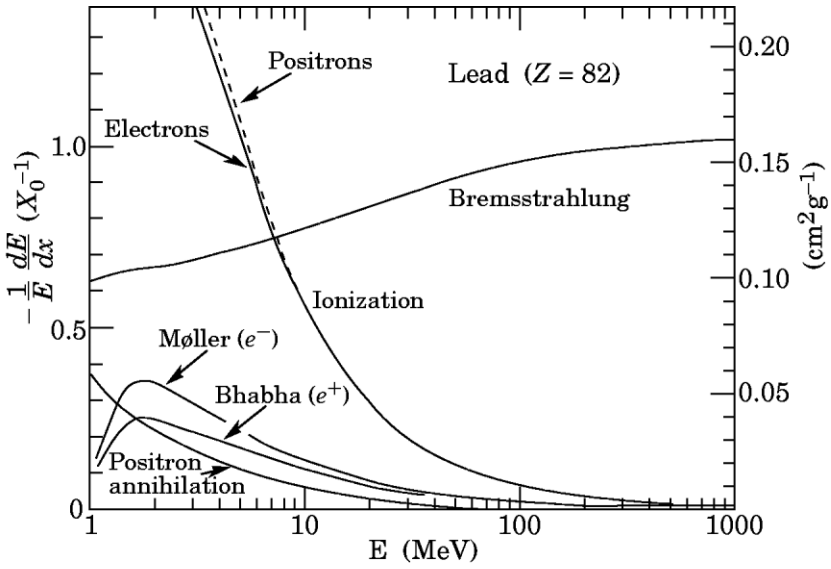

Figure 4.2: **Fractional energy loss per radiation length in lead as a function of e^+/e^- energy.** At low energies the primary process of energy loss for electrons in matter is ionization with contributions from bremsstrahlung and Møller scattering. Above 1 GeV of incoming electron energy, the region in which the ELSA accelerator operates, bremsstrahlung clearly dominates [A+08b].

leading to critical energies of $E_c \approx 26.5\,\mathrm{MeV}$ for copper and $E_c \approx 111\,\mathrm{MeV}$ for carbon (diamond), the two radiator materials used in the Crystal Barrel/TAPS experiment. These numbers are well below the primary electron beam energy of 3200 MeV at which the Crystal Barrel/TAPS experiment operated. It is therefore safe to assume that, for electrons interacting with the radiator target, bremsstrahlung is the relevant process.

Incoherent bremsstrahlung

Bremsstrahlung can be characterized as the radiation of one or more real photons with energy k by an electron with initial momentum $\vec{p}_e$, accelerated in the Coulomb field of an atomic nucleus:

$$e^- + N \rightarrow e^- + N + \gamma.$$

Conservation of 4-momentum dictates that the scattering nucleus has to take the recoil momentum, $\vec{q}$:

$$\vec{q} = \vec{p}_e - \vec{p}_{e'} - \vec{k}, \tag{4.1}$$

with $\vec{p}_{e'}$ being the momentum of the outgoing electron.
The differential cross section of the bremsstrahlung process is given by:

$$d\sigma = \frac{|S_{fi}|^2}{t \cdot N_{e^-}}, \tag{4.2}$$

with S_{fi} the transition matrix element, t the time and N_{e^-} the flux of the primary electron beam [Jac98]. Taking a pointlike charge distribution, in momentum space given by the Fourier transformed Coulomb potential:

$$V(\vec{q}) = \frac{-Ze4\pi}{\vec{q}^2}, \tag{4.3}$$

the Born approximation leads to a bremsstrahlung cross section:

$$d\sigma \propto |V(\vec{q})|^2 \propto \frac{1}{|\vec{q}|^2}. \tag{4.4}$$

Accordingly, processes with small momentum transfers $\vec{q}$ are preferred. The energy distribution of the bremsstrahlung process is described by the Bethe-Heitler cross section [Hei54] and yields, after integration [LBP82]:

$$d\sigma_{B.H.} = 4Z^2\alpha {a_0}^2 \frac{dk}{k} \frac{E}{E_0} \left[\frac{E_0}{E} + \frac{E}{E_0} - \frac{2}{3}\right] \left[\ln\left(\frac{2E_0E}{k}\right) - \frac{1}{2}\right] \tag{4.5}$$

with α being the fine structure constant, a_0 the Bohr radius, E_0 and E the energies of incoming and outgoing electron and k the energy of the bremsstrahlung photon. Thus, the bremsstrahlung spectrum follows approximately a $\frac{1}{k}$ shape.
For an amorphous radiator the scattering centers are isotropically distributed and there is on average no preferred planar relation between the incoming electron and the outgoing photon. As a result, the orientation of the electric field vectors is statistically random and the photons effectively unpolarized.

Coherent bremsstrahlung

The use of a crystal as a radiator target leads to additional effects due to its periodic lattice structure. Depending on the orientation of the crystal lattice and the kinematic conditions, it is possible to get constructive interference of the various bremsstrahlung amplitudes from single atoms. Additionally, the recoil momentum $\vec{q}$ of the bremsstrahlung process can be absorbed by the whole crystal lattice, rendering it effectively recoilless. The term *coherent* reflects the fact that the bremsstrahlung photons are created in a pro-

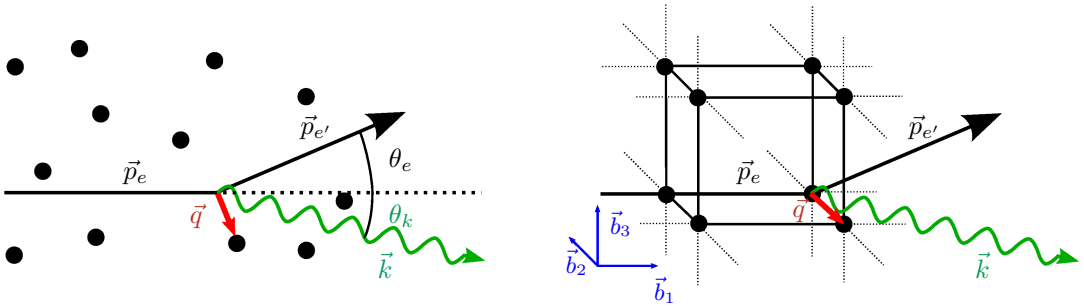

Figure 4.3: **Recoil momentum transfer in incoherent and coherent bremsstrahlung.** Left: Incoherent process, the recoil momentum is transferred to a single atom. Right: Coherent process, the recoil momentum is transferred to the crystal lattice. Notation according to (4.1).

cess in which many indistinguishable atoms are participating. Coherent bremsstrahlung only occurs under the condition that the transferred recoil momentum $\vec{q}$ coincides with a reciprocal lattice vector $\vec{g}$ [1] of the crystal. Accordingly, only discrete recoil momenta

$$\vec{q} = n \cdot \vec{g} \tag{4.6}$$

can be transferred to the lattice as a whole (see figure 4.3), fixing the orientation of the scattering plane spanned by the incoming electron and the recoil momentum. This yields a fixed plane of the electric field vector of the bremsstrahlung photon and produces linearly polarized photons. The following kinematic constraints for the longitudinal (q_l) and transversal (q_t) momentum transfers can be derived [Pal68]:

$$\delta + \frac{q_t^2}{2E_0} \leq \quad q_l \quad \leq \frac{\delta}{x} \tag{4.7}$$

$$0 \leq \quad q_t \quad \lesssim 1 \tag{4.8}$$

with $\delta = \frac{1}{2E_0}\frac{x}{1-x}$ and $x = \frac{k}{E_0}$. This selects a kinematic region, the so-called *pancake* [Ü56], in momentum-space in which momentum transfer is allowed (see figure 4.4). Only one defined reciprocal lattice vector should fall into the allowed region to avoid destructive interference of polarization contributions from perpendicular scattering planes. This can be achieved by proper alignment of the crystal radiator with respect to the incoming electron beam. For the incoherent process, where momentum transfer occurs on individual atoms, an increase in x and therefore a shift of the pancake in momentum

[1] The reciprocal lattice is a representation of the crystal lattice in Fourier space. The components of reciprocal lattice vectors are given by the Miller indices h_i: $\vec{g} = \sum_{i=1}^{3} h_i \vec{b}_i$ [Kit04].

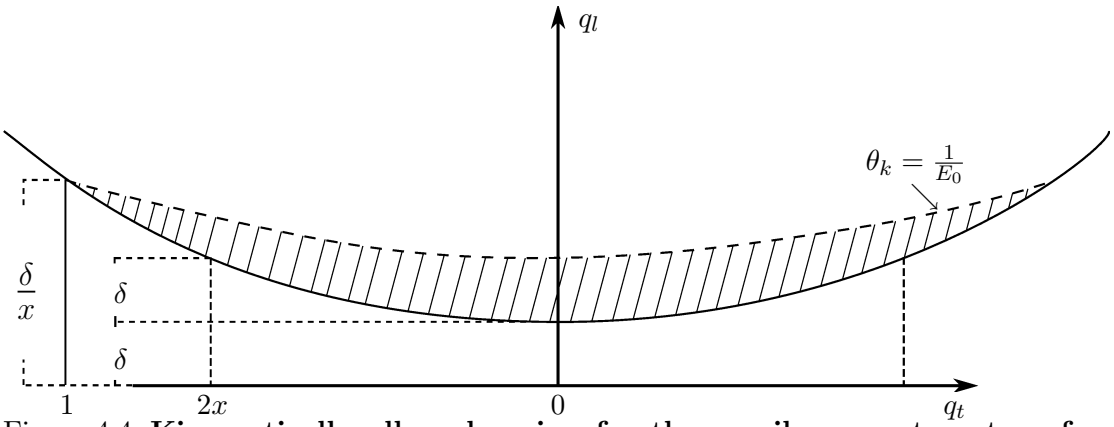

Figure 4.4: **Kinematically allowed region for the recoil momentum transfer.** The hatched area denotes the *pancake* region defined by (4.7).

space leads to the $\frac{1}{k}$ shape of the bremsstrahlung spectrum mentioned above. For the coherent process however, momentum transfer has to fulfill (4.6) so only reciprocal lattice vectors within the pancake region contribute to the coherent cross section. Once x reaches a certain value, the vector leaves the pancake, resulting in an acute drop in the cross section, a discontinuity referred to as *coherent edge* as visible in figure 4.5. Since real crystals are not completely periodical due to thermal motion of the participating atoms, it is still possible to transfer the recoil momentum to single atoms leading to a fraction of incoherent processes. Accordingly the cross section for the production of bremsstrahlung off a crystal consists of two parts:

$$d\sigma_{\text{crystal}} = d\sigma_{\text{coh.}} + d\sigma_{\text{incoh.}}. \tag{4.9}$$

Figure 4.5 shows a typical bremsstrahlung spectrum obtained with the Crystal Barrel/TAPS experiment using a diamond crystal as a radiator, after normalization on the incoherent spectrum.

The degree of linear polarization of the photons is defined as the ratio of coherent to incoherent processes. It can be improved by reducing the incoherent contribution in the bremsstrahlung spectrum. Seeing that coherent and incoherent processes have different angular distributions [Els07], collimation of the photon beam is one option to do so.

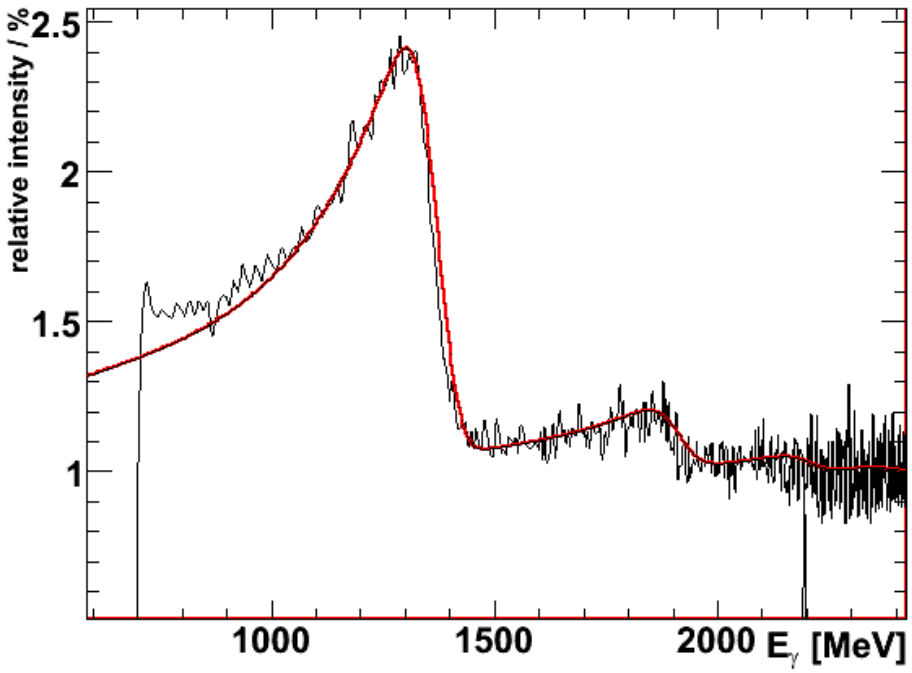

Figure 4.5: **Relative intensity of coherent bremsstrahlung.** The spectrum was obtained with the tagging system of the Crystal Barrel/TAPS experiment (see section 4.2.3) and a diamond crystal radiator (section 4.2.2) and normalized to the corresponding incoherent spectrum [E$^+$09]. The enhancements due to coherent processes are clearly visible. Solid line: ANB calculation [NGH$^+$03, Els07].

4.2.2 Goniometer and radiator targets

Goniometer

A variety of radiators are accessible to produce bremsstrahlung photons off the primary electron beam, along with means for beam diagnosis. These are mounted on a 5-axis goniometer contained in a vacuum tank (Figure 4.6, far left). Figure 4.7 shows a schematic view of the goniometer. It is possible to precisely align the crystal radiator, located at the intersection of the three rotatory axes, to fulfill the requirements for coherent bremsstrahlung stated in section 4.2.1. The other radiators are mounted on an aluminum disc and can be positioned in the beam via translation along the x-axis and rotation in ϕ.

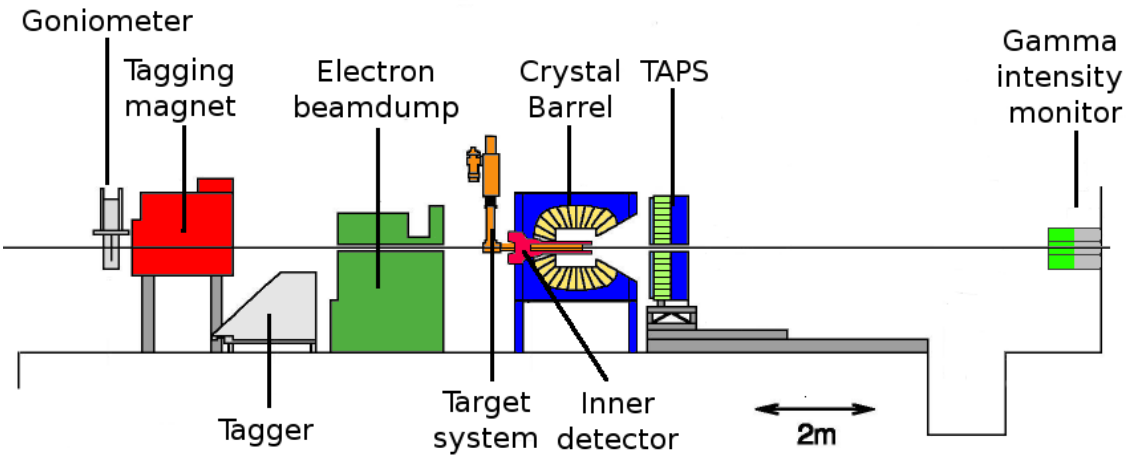

Figure 4.6: **Schematic overview of the beamline of the Crystal Barrel/TAPS experiment.** Electron beam entering from the left. Descriptions of the different components: see text.

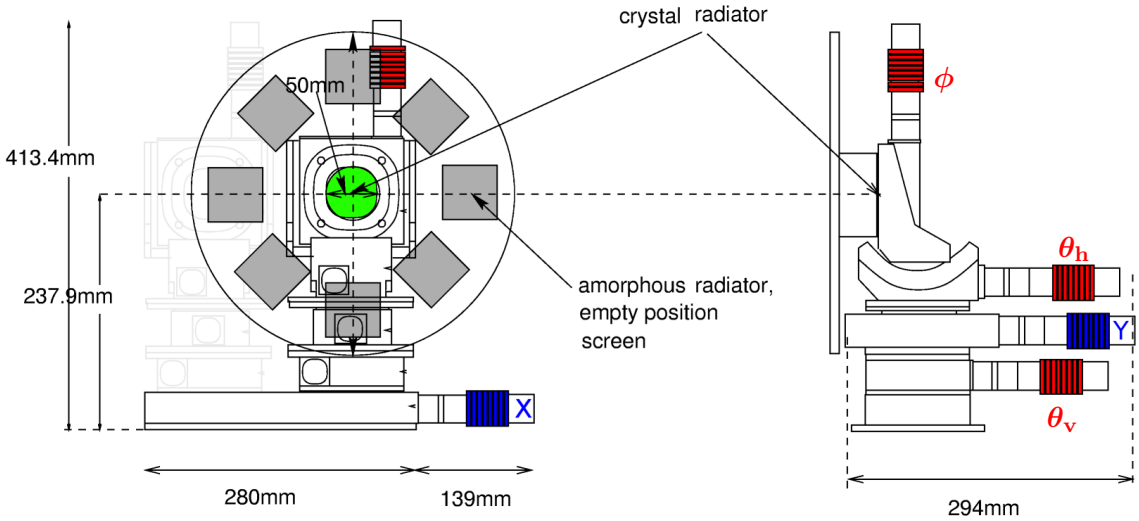

Figure 4.7: **Schematic view of the goniometer.** The goniometer disc contains carriers for amorphous radiators and tools for beam diagnostics ([GRAY]) along with the diamond radiator mounting ([GREEN]). The five axes of the goniometer are divided in two translational axes (perpendicular to beam direction, [BLUE]) and three rotatory axes ($\theta_{\text{horizontal}}$, θ_{vertical}, ϕ, [RED]).

Crystal radiator

A diamond crystal for the production of linearly polarized bremsstrahlung photons is glued on a 12.5 μm thick Kapton foil in the center of the goniometer. The diamond itself has a face plane of 4 mm × 4 mm and a thickness of 500 μm. This corresponds to 1/243 of the radiation length[2] of diamond, $X_0 = 12.13$ cm, and is chosen to match the effective thickness of one of the amorphous radiators most commonly used (see table 4.1 for details). The diamond is cut in a way that the reciprocal lattice vector [100] is perpendicular to its face plane [Els07].

Material	*Density* [g/cm^3]	*Radiation Length* X_0 [g/cm^2]	[cm]	*Thickness* X [μm]	X/X_0
Copper	8.96	12.86	1.43	15	$1.05 \cdot 10^{-3}$
				50	$3.50 \cdot 10^{-3}$
				150	$1.05 \cdot 10^{-2}$
Carbon (diamond)	3.52	42.70	12.13	500	$4.12 \cdot 10^{-3}$

Table 4.1: **Bremsstrahlung radiators used in the Crystal Barrel/TAPS experiment.** Given are the key characteristics to be considered for the production of bremsstrahlung off the radiators [A$^+$08b].

Amorphous radiators

Three copper radiators are mounted radially on the goniometer disc, allowing for the incoherent production of bremsstrahlung photons for unpolarized measurements and normalization purposes. These are 4 mm wide copper strips with thicknesses of 15 μm, 50 μm, and 150 μm, respectively. These thicknesses correspond to approximately 1/1000, 3/1000 and 1/100 of the radiation length of copper ($X_0 = 1.43$ cm, see table 4.1 for details). Only the two thinnest radiators have been used under experimental conditions to avoid multiple scattering in the radiator material and the resulting uncertainty in the energy measurement (see section 4.2.3).

[2] The radiation length is the mean distance in matter over which an electron loses all but $1/e$ of its energy by bremsstrahlung. For photons it is equal to 7/9 of the mean free path for pair production [A$^+$08b].

Beam diagnostics

Two different means of control and optimization for the electron beam position and shape are implemented in the goniometer. A *Chromox*[3] luminescence screen is viewed by a camera and yields basic information about the position and extension of the beam. To precisely measure not only the position and size but also the relative intensity distribution, two individual iron wires of about 1 mm thickness are mounted horizontally and vertically on the goniometer disc. When passing the beam, the bremsstrahlung events produced off the wire are measured by the tagging system, leading to an intensity profile of the beam in x- and y-direction. A non-invasive method for beam diagnostics during data taking is given by monitoring the position of the coherent edge which is very sensitive to the beam position (see section 4.2.1).

4.2.3 Tagging system

In order to determine the energy of the incident photon and thereby the center-of-mass energy of a hadronic reaction, the energy loss of the primary electrons after the bremsstrahlung process is measured:

$$E_\gamma = E_0 - E_{e^-}, \tag{4.10}$$

with E_0 being the incident electron energy and E_{e^-} the measured electron energy after the bremsstrahlung process. This is achieved by the tagging system, consisting of two parts, the tagging dipole magnet and the tagging detector (see figure 4.8). After passing the radiator target, the electron and photon beams enter the tagging magnet, where the electrons are deflected according to their momentum:

$$p_{e^-} = E_{e^-} = eBr \quad \text{for} \quad p_{e^-} \gg m_{e^-},\ c \equiv 1, \tag{4.11}$$

with bending radius r and magnetic field strength B. Most of the electrons do not participate in the bremsstrahlung process due to the relatively small cross section for bremsstrahlung. The electrons with energy E_0 have to be diverted into the electron beam dump (section 4.2.4). For the data presented in this work, a primary beam energy of 3176 MeV and an according dipole field of 1.413 T has been used[4].

[3] Chromium-doped Al_2O_3

[4] The mentioned relations base on the assumption of a constant magnetic field over the full flight path of the electrons. In reality variations of the field have to be taken into account for a reliable reconstruction. This is addressed in chapter 5

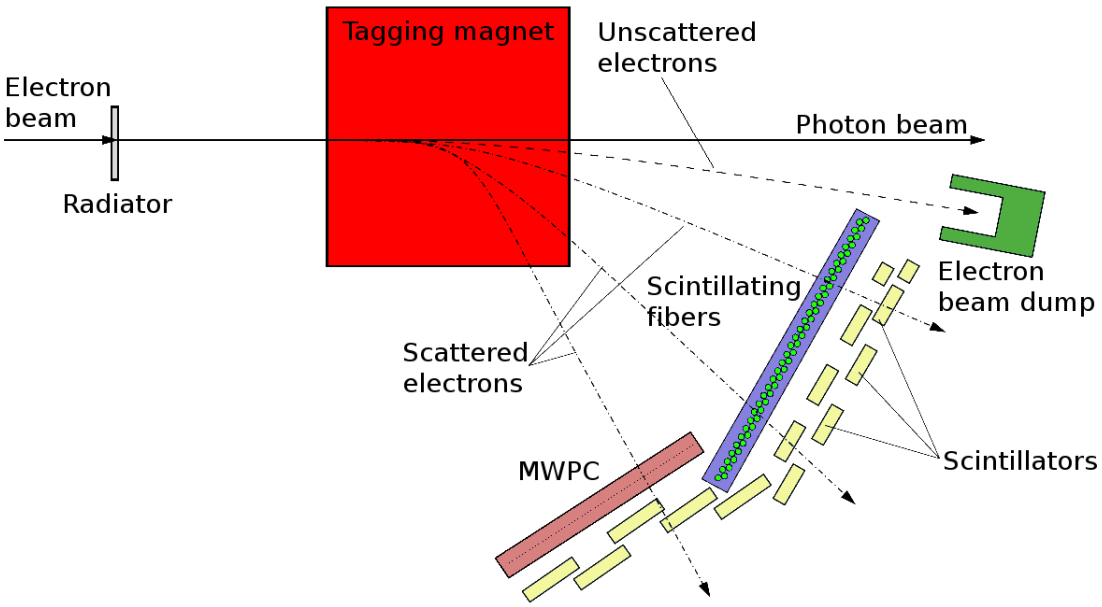

Figure 4.8: **Schematic view of the tagging system.** After passing the radiator target the incoming electron beam is diverted by the dipole field in the gap of the tagging magnet ([RED]). Unscattered electrons hit the electron beam dump ([GREEN], see section 4.2.4) while electrons having undergone a bremsstrahlung process are detected in a tagging detector system consisting of three parts of varying granularity: 14 plastic scintillator bars ([YELLOW]), a 208-wire proportional chamber ([RED]), and a hodoscope consisting of 480 scintillating fibers ([BLUE]).

Electrons that have produced a bremsstrahlung photon are detected in a three-part detector system, depicted in figure 4.8. 14 slightly overlapping scintillator bars of 4 cm thickness, and widths varying according to the expected rate. The uppermost bar, exposed to the highest rates, has a width of 30.5 mm, the lowermost bar, corresponding to the highest photon energies, of 208.3 mm. Together the bars cover an energy region of 22% to 92% of the primary electron beam energy with resolutions varying from 0.5 MeV to 30 MeV from lowest to highest electron energies[5]. The scintillator bars are read out by two photomultipliers each whose signals are processed by TDCs[6] and QDCs[7] and counted by scalers.

[5] Values correspond to a primary beam energy of 3200 MeV.
[6] **T**ime-to-**D**igital **C**onverter
[7] Charge(**Q**)-to-**D**igital **C**onverter

To improve the spatial resolution and with that the energy resolution, a second layer of detector components supplements the system. The high photon energy range of 80% to 92% of the incoming beam energy is covered by a 208-wire proportional chamber (MWPC). Since the energy region covered by the MWPC is outside the region of interest for this work, this component will not be used in the analysis.
The photon energy range of 18%[8] up to 80% of incoming beam energy is covered by a scintillating-fiber hodoscope. The hodoscope comprises a total of 480 fibers, 2 mm in diameter, arranged in two layers in such a way that 2/3 of each fiber from one layer overlap with two fibers from the other layer. The fibers are read out by multi-anode photomultipliers in sets of 16, whose signals are then processed by multi-hit TDCs and counted by scalers. The TDCs have a time resolution of 64 ps per channel, the energy resolution of the fibers varies due to dispersion between 2 MeV and 13 MeV.

4.2.4 Electron beam dump

High energy electrons, mainly the unscattered part of the primary beam, are deflected towards the electron beam dump by the tagging magnet. This beam dump, located between the tagger and the Crystal Barrel calorimeter, consists of lead and iron interrupted by layers of boron carbide and polyethylene. The construction is such that outside the beam dump neither electromagnetic radiation nor neutrons should occur. No additional background should be introduced in the surrounding detectors. Data analysis shows however distinct background patterns in the Crystal Barrel calorimeter as well as an increased background rate in the tagger, both of which has been found to stem from leakage from the electron beam dump (see chapter 6).
Embedded in the photon beam line running through the beam dump are two iron collimators of 20 cm length and inner radii of 11.9 mm and 16,0 mm, respectively. The setup also contains two sweeping dipoles to divert electron-positron-pairs created off the collimators into the lead end-wall of the beam dump. An insufficient alignment of the collimators however can introduce additional background in the upstream part of the Crystal Barrel, as shown in chapter 6.

4.2.5 γ-intensity monitor

On the far end of the beamline (far right in figure 4.6) a γ-intensity monitor, consisting of nine PbF_2 crystals arranged in a 3x3-matrix and read out by photomultipliers,

[8] Only 450 of the 480 fibers actually overlap with the scintillator bars, thus the whole taggable range is 18% to 80% of the primary electron energy.

measures the total photon flux on the target. Photons entering the detector produce an electromagnetic shower and are detected by the Čerenkov light emitted by the shower particles. The segmentation of the detector, in combination with certain weighting algorithms for the energy deposition also gives the option to use the γ-intensity monitor for the determination of the photon beam position (see [Kon01] for details).

4.3 Reaction target and detector components

4.3.1 Reaction target

Located in the center of the Crystal Barrel calorimeter is a 5.275 cm long, cylindrical target cell [Kop02] with a diameter of 3 cm. The cell itself consists of a 125 μm thick Kapton cylinder with endcaps of 80 μm thickness. It can be filled with either liquid hydrogen or liquid deuterium, cooled down by a separate liquid hydrogen circuit joined to the target circuit by a heat-exchanger. With the low density of Kapton ($\rho = 1.4\,\mathrm{g/cm^2}$) and its large radiation length of $X_0 = 28.6\,\mathrm{cm}$, the target cell in combination with the surrounding vacuum pipe (1 mm Al) ending in a 625 μm Kapton window yields a sufficiently low material budget around the reaction vertex to allow the decay products to reach the detector components almost undisturbed.

4.3.2 Inner detector

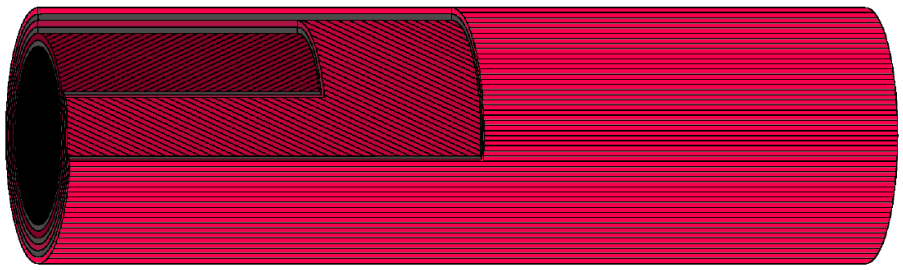

Figure 4.9: **Schematic view of the inner detector.** Visible are the three layers of a total of 513 scintillating fibers with their respective angles to the photon beamline. See text for details.

The target cell is surrounded by a cylindrical scintillating fiber detector sensitive to charged reaction products, covering the angular range of $28° \leq \theta \leq 172°$ (see figure 4.10)

[Fös01, Bog02]. This inner detector consists of a total of 513 scintillating fibers, 2 mm in diameter. They are arranged in three layers on carbon fiber cylinders of 40 cm length, and stabilized by an inner aluminum cylinder of 1.8 mm thickness. The fibers of the inner detector are connected via lightguides in sets of 16 to multi-anode photomultipliers outside of the Crystal Barrel calorimeter, providing a fast timing signal. In the outer layer the scintillating fibers are aligned parallel to the beam axis while the middle and inner layer are oriented at angles $+25.7°$ and $-24.5°$, respectively (see figure 4.9). This arrangement, with the fibers of the rotated layers circling only half of the cylinder, allows for the reconstruction of a charged hit if two of the three layers detect the particle, the efficiency of which is 98.4% (77.6% for the detection of a three-layer hit). The overall angular resolution for this detector amounts to $0.4°$ in ϕ and up to $0.1°$ in θ, respectively [S$^+$05b].

4.3.3 Crystal Barrel calorimeter

The central part of the experimental setup is the Crystal Barrel calorimeter, consisting of 1290 CsI(Tl) modules pointing towards the target center and covering a polar angular range of $30° \leq \theta \leq 168°$ and the full azimuthal angle. Figure 4.10 shows the arrangement of these modules in 23 rings around the beam axis. Rings of type 1 - 10 consist of 60 crystals per ring with angular coverages of $\Delta\phi = 6°$ and $\Delta\theta = 6°$, whereas the last three rings in the upstream direction (types 11 - 13) consist of 30 crystals each, covering $\Delta\phi = 12°$ and $\Delta\theta = 6°$ per module. Photons entering the calorimeter deposit their energy via electromagnetic showers, the depth and width of which are constrained by the characteristics of the absorbing material. Table 4.2 gives an overview over the main features of CsI(Tl). The crystal length of 30 cm corresponds to 16 radiation lengths, leading to an almost complete deposit of the shower energy of a 2 GeV photon within the calorimeter. This energy deposit however encompasses a number of crystals due to the transversal extent of the shower, given by its energy and the *Molière radius*[9] of CsI(Tl). An energy weighted reconstruction of such clusters allows for an improvement of the effective angular resolution with respect to the granularity down to 1°-1.5°, depending on the energy of the incident photon (see 5.2.2). The energy resolution of the calorimeter scales with the deposited energy like [A$^+$92]

$$\frac{\sigma(E)}{E} = \frac{2.8\%}{\sqrt[4]{E[\mathrm{GeV}]}}. \tag{4.12}$$

[9]The Molière radius R_M defines a cylinder in which 90% of the shower energy is deposited. Its dependence on the radiation length approximates to $R_M = 0.0265 X_0 (Z + 1.2)$ [A$^+$08b].

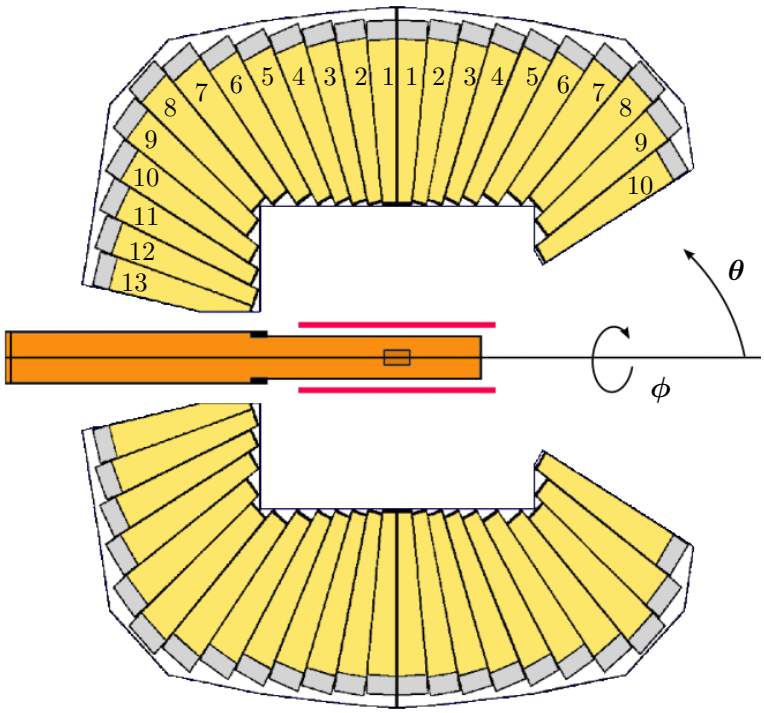

Figure 4.10: **Schematic view of the Crystal Barrel calorimeter.** The photon beam enters from the left. Numbers denote ϕ-symmetric rings of identical module types. Also visible are the position of the inner detector ([RED]) and the LH_2 target cell surrounded by the beam pipe ([ORANGE]).

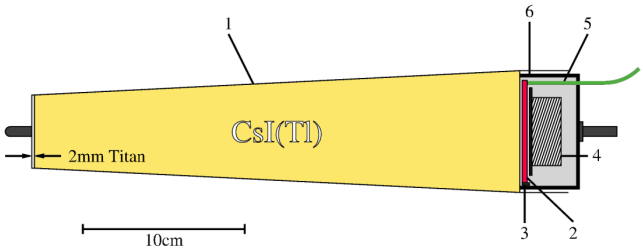

Figure 4.11: **Schematic view of a CsI(Tl) module.** 1: Titanium casing, 2: Wavelength-shifter, 3: Photodiode, 4: Preamplifier, 5: Optical fiber, 6: Electronics casing.

Figure 4.11 shows the layout of a CsI(Tl) module in detail. The scintillation light produced within the CsI(Tl) crystal is shifted in wavelength towards the region of maximum

sensitivity of the photodiode used for readout. Since the output signal of photodiodes is rather weak, a preamplification of the signal has to take place before transmission to the readout electronics located outside the experimental area. These signals are then shaped and read out by 12-bit dual-range ADCs[10]. For monitoring and calibration purposes light of defined relative intensities can be introduced directly to the wavelength shifter via an optical fiber connected to a lightpulser system [Bar00, Bös06] (see 5.1.2).

Scintillator	Density ρ	Radiation length X_0	Molière radius R_M	Energy loss rate dE/dx	Maximum of emission $\lambda_{\max}$	Decay time τ_{decay}
CsI(Tl)	$4.53\,\text{g/cm}^3$	1.86 cm	3.8 cm	5.6 MeV/cm	550 nm	7.0 μs 0.9 μs
BaF_2	$4.89\,\text{g/cm}^3$	2.03 cm	3.1 cm	6.6 MeV/cm	220 nm 300 nm	0.9 ns 630 ns

Table 4.2: **Main properties of the calorimeter crystals [A$^+$92, A$^+$08b].**

4.3.4 TAPS

The TAPS calorimeter complements the Crystal Barrel in forward direction, covering the polar angular range from 30° down to 5.8°. It consists of 528 hexagonal BaF_2 modules in a forward wall setup (see figure 4.12), 1.18 m from the target center. According to [G$^+$94], the energy resolution of the calorimeter for an incoming photon energy range of 45 - 790 MeV using a collimated beam is

$$\frac{\sigma(E_\gamma)}{E_\gamma} = \frac{A}{\sqrt{E_\gamma}} + B, \tag{4.13}$$

with $A = 0.79\%$ and $B = 1.80\%$ for the fast component of the scintillation light and $A = 0.59\%$ and $B = 1.91\%$ for the total light output, respectively. Figure 4.13 shows a detailed view of one BaF_2 module used in the TAPS calorimeter. A hexagonal BaF_2 crystal with a height of 59 mm and a length of 115 mm, corresponding to 12 radiation lengths (see table 4.2 for details), ending cylindrically with a diameter of 54 mm is attached to a photomultiplier. The front of the crystal is covered by a separate, 5 mm thick plastic scintillator for the identification of charged particles. These *charged particle vetos* [Jan98] are read out via optical fibers connected to multi-anode photomultipliers.

[10] **A**nalog-to **D**igital **C**onverter

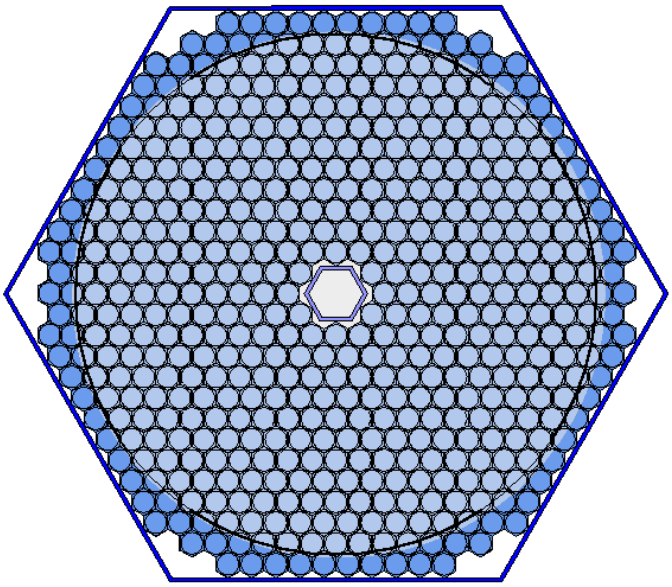

Figure 4.12: **Schematic view of the TAPS calorimeter.** Hexagonal forward wall setup of 528 BaF_2 modules. The light blue area represents the 30° opening left by the Crystal Barrel calorimeter.

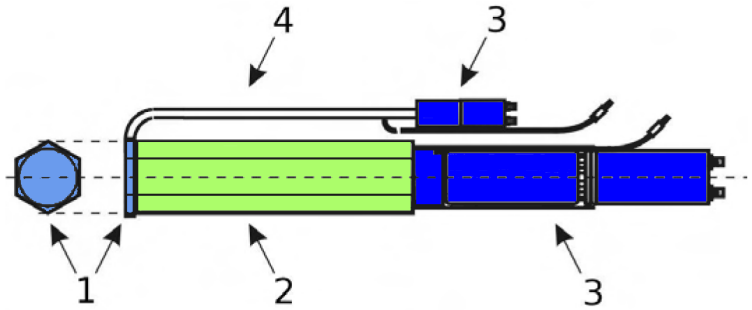

Figure 4.13: **Schematic view of a BaF_2 module.** 1: Plastic scintillator, 2: BaF_2 crystal, 3: Photomultiplier, 4: Optical fiber.

The readout of the BaF_2 modules with photomultipliers allows for signal processing without the use of additional preamplifiers or shapers and can be used not only for energy but also timing information. The signals of each module are split and processed by constant-fraction discriminators (CFDs, see chapter 5) and leading-edge discriminators (LEDs) for trigger purposes as described in the next paragraph.

4.4 Trigger system

Since the hadronic cross section is orders of magnitude smaller than the electromagnetic cross section, the detector responses during data taking have to be prefiltered online according to specific topologies to ensure the taken data mainly consists of events due to the desired reactions. In the Crystal Barrel/TAPS experiment a two-level trigger system is implemented which generates a signal depending on the fulfillment of previously set trigger conditions [JG04]. On the first level a fast decision is made whether a digitization of all measured values by the detectors should be started. The decision time for this level is determined by the time it takes for the analog signals from the detectors to reach the readout electronics and can be set using delay lines. For the data taking periods relevant for this work, this time was fixed by the TAPS detector whose signal propagation time has been 300 ns. This timeframe only allows for rather simple trigger logic derived from the fast detector signals. If the first-level trigger condition is met and the digitization is started, the second-level trigger decides whether the event should be written out. For the second level trigger, more complex logics can be applied since the digitization time is in the order of 1 ms. In particular, the comparably slow signals of the Crystal Barrel calorimeter[11] can be used in this stage.

4.4.1 First-level trigger

In the data taking periods used in this work, only the signals of the TAPS calorimeter have been considered for the first-level trigger decision. The trigger signals of the TAPS calorimeter are generated by two leading-edge discriminators (LEDs) connected to each BaF_2 module. The thresholds for the two discriminators are set to different values, referred to as *LED High* and *LED Low*, to allow for more complex trigger conditions[12]. The thresholds are set individually for each ring of the calorimeter, with the innermost thresholds being at the highest possible value of approx. 1 GeV (see 5.1.1) in order to suppress electromagnetic background. Figure 4.14 shows the segmentation of the calorimeter surface with respect to the generation of the LED High and LED Low trigger signals. For each threshold set, the calorimeter is subdivided into eight segments consisting of 64 modules each[13]. The signals from the individual modules of

[11] The necessary pre-amplification and shaping of the Crystal Barrel signals results in a risetime of the order of 2 μs.

[12] Due to the limited number of available LED modules, the trigger signals of the LED High segments G and H are generated by the LED Low modules.

[13] The 4×4 modules not assigned to a trigger segment (white modules at the edge in figure 4.14) show a considerably reduced efficiency and are therefore not used during data taking.

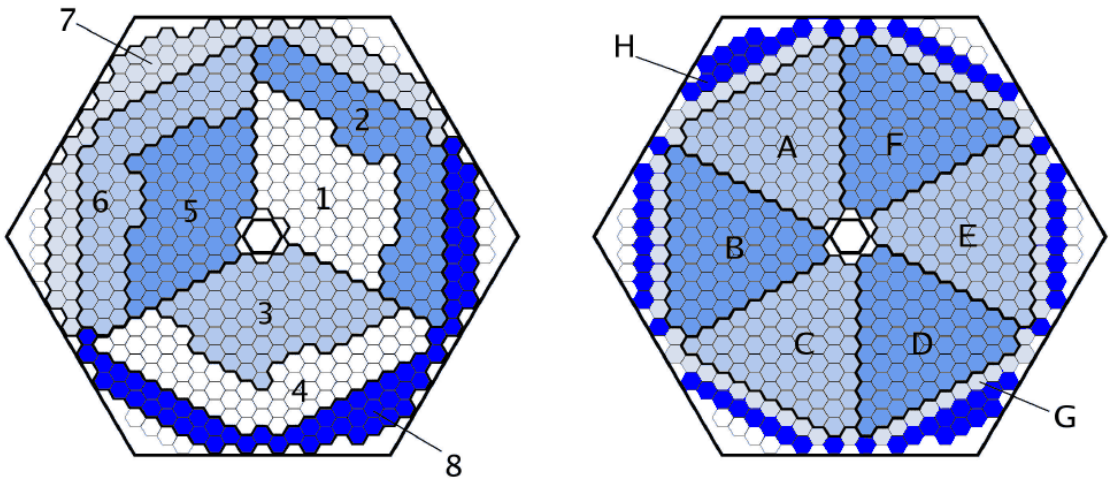

Figure 4.14: **Trigger segmentation of the TAPS calorimeter.** Trigger segments for the LED Low (left, numbered) and LED High (right, lettered) trigger conditions.

each segment are passed through a logical OR unit, thus generating one trigger signal per segment for each LED setting. The different layout of the LED Low trigger segmentation was chosen to limit the probability that e^+e^--pairs created by photon conversion hit two different segments, fulfilling trigger condition B described below.

4.4.2 Second-level trigger

The available time for the second-level trigger decision is sufficient to take the hits detected in the Crystal Barrel calorimeter into account. The corresponding trigger signal is created by the FAst Cluster Encoder (FACE), a clusterfinder based on a cellular logic [Fle01]. A cluster is in this case defined as a contiguous group of detector modules containing energy of the electromagnetic shower created by the incident photon[14]. The time for the logic to determine the number of clusters in a given event is on the order of 6 - 10 μs, depending on the number of participating crystals. The trigger signal itself, based on a predefined minimum number of clusters to be detected, then either acknowledges or interrupts the digitization of the detector information started by the first-level trigger.

[14] For the TAPS calorimeter the issue of online cluster detection is circumvented by the introduction of trigger segments.

4.4.3 Trigger conditions

During the data taking periods relevant for this work the trigger *facetest2new* was used, comprising two conditions based on the two trigger levels introduced above:

- **Condition A:** At least one hit in the TAPS calorimeter above the LED high threshold (LED-High OR), accompanied by at least two separate clusters in the Crystal Barrel calorimeter identified by the FACE.
- **Condition B:** Two hits in the TAPS calorimeter in separate LED Low trigger segments over their according thresholds. The second-level FACE decision is bypassed in this case.

Other triggers have been used for calibration and monitoring purposes, most importantly the *Tagger-OR* trigger, whose only condition is a hit in one of the scintillator bars of the tagging hodoscope. Data taken with this trigger is mandatory for the determination of the photon flux as well as the monitoring of the photon polarization.

4.4.4 Trigger simulation

The hardware trigger has also been implemented in the offline analysis by means of a trigger simulation package [JG04]. The concept is based on the binary nature of trigger conditions; either a given combination of conditions (i.e. detector signals) is fulfilled or not. The trigger conditions are therefore formulated as a 16-bit binary trigger word, where each bit represents a possible trigger signal. During analysis of an event, the same pattern is generated from the respective detector responses and compared to the pre-loaded trigger condition. Trigger thresholds, scaling factors and arbitrary trigger conditions can be set by means of initialization files.
The simulation is applied to both the experimental data, e.g. for threshold adjustment purposes (see section 5.1.1) and Monte Carlo simulations (section 6.1) to e.g. reproduce trigger acceptances in the simulated data. For further information on the trigger simulation as well as the trigger logic of the Crystal Barrel/TAPS experiment and other trigger conditions used during data taking, see [JG04].

5 Calibration and reconstruction

The experimental setup described in the previous chapter provides digital information obtained by a variety of detectors. To use this information in terms of physical quantities like time or energy, the data has to be calibrated accordingly. The next step is then to correlate the calibrated information with the actual particles which created the detector signals, a process referred to as reconstruction.

5.1 Subdetector calibration

5.1.1 TAPS calibration

Time calibration

The time calibration of the TAPS calorimeter consists of two parts, the determination of the gain (time/channel) of the TDC-modules and the correction of offsets due to varying cable lengths and signal propagation delays within the electronics. To measure the gain, pulses of different, known frequencies are fed into the TDCs resulting in a series of sharp signals in each time spectrum. The relative position of these peaks allows for the calculation of the gain-factor for each module. The time offset between the individual modules is determined using the decay photons of a π^0 event, both of which are detected in the TAPS calorimeter. The central crystal for each photon-cluster gives the time for the particle, and the time difference between all possible pairs of particles is entered into two histograms, one for each central module. Should, due to defects, no timing signal be available for a module, it is assigned the time of a neighboring module belonging to the same cluster, the signal of which stems from the same incident photon. The offset of the modules is now corrected in such a way that the time signals are at the same position, 0 ns. This process is done iteratively, since only the central crystal timing is corrected in each pass. Figure 5.1 shows the resulting spectra.

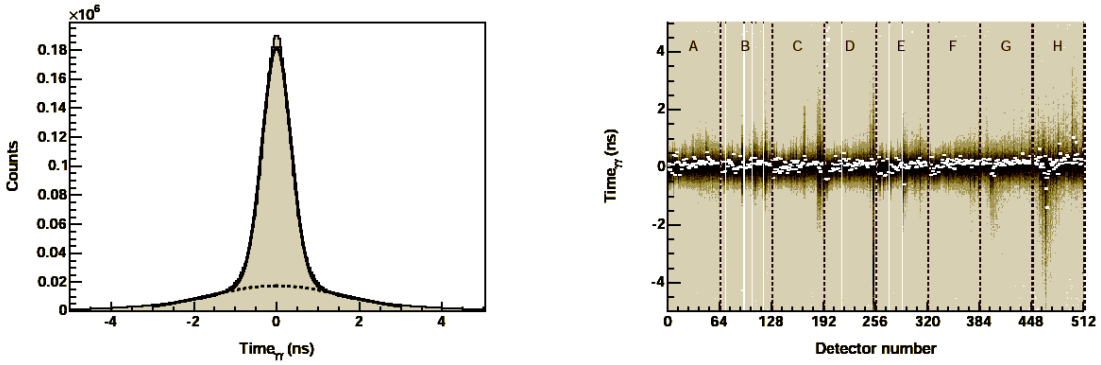

Figure 5.1: **Calibrated relative timing of TAPS modules.** The time difference between two photons from a π^0 decay detected in the TAPS calorimeter. Left: Summed over all BaF_2 modules. Right: As a function of the module number. White points denote peak positions, empty channels correspond to modules with bad timing signals [Cas06]. For the beamtimes subject to this work, a time resolution of $\sigma = 0.39\,\mathrm{ns}$ has been achieved.

Energy calibration

The energy calibration of the TAPS calorimeter is a three-stage process. In the first stage, the linear relation between deposited energy and QDC channel number is exploited [G$^+$94]. A first calibration point is obtained using a pedestal pulser, resulting in a sharp peak in the QDC spectrum (see figure 5.2), corresponding to 0 MeV energy deposit. The second point needed for a linear extrapolation is given by the response of the BaF_2 modules to cosmic muons. Since all TAPS modules are identical in shape and orientation, the energy deposition of cosmic muons is the same for each crystal, namely 38.9 MeV[1] (cf. figure 5.2). This calibration is sufficient for control purposes during data taking. In the second step of the process, the decay photons of the π^0 meson, detected in the TAPS calorimeter are used, analogous to the time calibration. For all possible pairs of hits, the invariant $\gamma\gamma$-mass is calculated as

$$M_{\gamma 1\gamma 2} = \sqrt{2E_{\gamma 1}E_{\gamma 2}(1 - \cos(\theta_{\gamma 1\gamma 2}))} \tag{5.1}$$

where $E_{\gamma i}$ are the measured energies of the photons and $\theta_{\gamma 1\gamma 2}$ their respective opening angle. This invariant mass is histogrammed for both of the central modules of the electromagnetic showers. The difference between the position of the π^0 peak in the invariant mass spectrum to its nominal mass of 134.98 MeV [A$^+$08b] results in a correction factor

[1] Assuming perpendicular entry to the flat side of a crystal of 5.9 cm thickness and $\mathrm{d}E/\mathrm{d}x = 6.6\,\mathrm{MeV/cm}$.

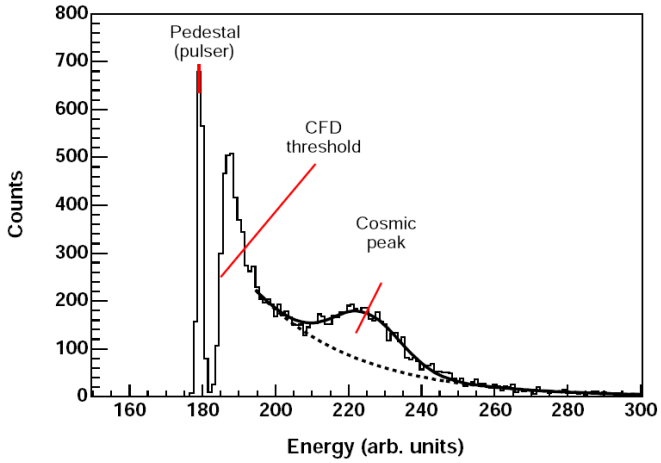

Figure 5.2: **Example cosmic ray spectrum for a TAPS BaF_2 module [Cas06].**

for the corresponding central module. The module detecting the second decay photon is arbitrary, so its effect on the calibration of the first detector cancels out on average. As for the time calibration, this process is done iteratively. The overall π^0 peak as well as the peak positions for the individual detector modules after calibration are shown in figure 5.3. One complication arises due to the fact that the outermost parts of the TAPS calorimeter are shadowed by the Crystal Barrel, so that only few π^0 events hit this region. For the according modules, an overall correction factor, the average of all detectors, is applied and these modules are rejected in the data analysis as central detectors for electromagnetic showers.

A cross-check of the calibration at this point, using the invariant mass of the η meson, reconstructed from its $\gamma\gamma$-decay as described above for the π^0, yields a mass-shift of about 5 to 10 MeV towards higher masses. This can be explained by the fraction of energy loss for the respective clusters due to modules with energy deposits below the CFD threshold. This effect, for the π^0 corrected by a factor as described above, is energy-dependent [Kot01]. The decay photons of the η meson have in general higher energies than for the π^0, so the influence of the CFD thresholds is less, since more modules participate in a cluster; the η mass is overcorrected. Since the statistics for η events, due to cross section, opening angle and branching ratio restrictions, is significantly lower than for the π^0, a different approach has to be taken. Additionally, only the η mass has to be corrected and the π^0 has to stay untouched, since it is already set to the correct position. Using the peak positions of the respective meson masses in the invariant $\gamma\gamma$-mass spectrum as reference and assuming that the decay photons have the

same energy, a correction function of the form

$$E_{new} = a + b \cdot E_{old} + c \cdot E_{old}^2, \tag{5.2}$$

is used. The zero point of the calibration is fixed by the pedestal, so the parameter a has to be zero. The parameters b and c are then determined by

$$b = \frac{m_\pi}{m_\pi^{\gamma\gamma}} - c \cdot E_\pi \tag{5.3}$$

$$c = \left(\frac{m_\eta}{m_\eta^{\gamma\gamma}} - \frac{m_\pi}{m_\pi^{\gamma\gamma}} \right) \Big/ (E_\eta - E_\pi). \tag{5.4}$$

Here (m_π, m_η) are the nominal meson masses, $(m_\pi^{\gamma\gamma}, m_\eta^{\gamma\gamma})$ the reconstructed peak positions in the invariant $\gamma\gamma$-mass spectrum and (E_π, E_η) the mean reconstructed energies of the respective mesons. For the data presented here, the parameters have been determined to $b = 1.0165$; $c = -5.6715 \cdot 10^{-5}$ within this work (cf. figure 5.4).

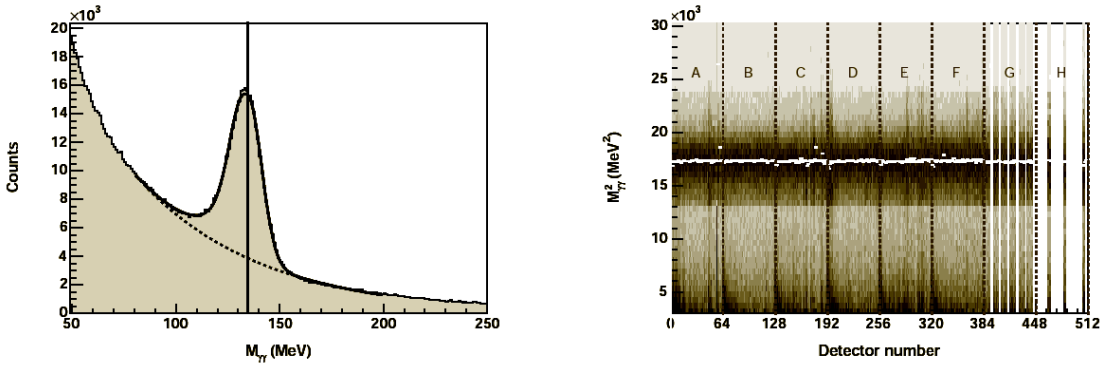

Figure 5.3: **Calibrated π^0 mass reconstructed in the TAPS calorimeter.** Left: Invariant mass of two photons detected in the TAPS calorimeter, summed over all BaF_2 modules. Right: As a function of the module number. White points denote peak positions, empty channels correspond to the parts of the detector shadowed by the Crystal Barrel [Cas06].

LED calibration and threshold determination

As described in 4.4, the TAPS calorimeter creates two trigger signals depending on two thresholds set for the leading-edge discriminator (LED) for each detector module, *LED High* and *LED low*. To ensure a reliable, reproducible situation for each data taking period, the according discriminators have to be calibrated. This calibration is done

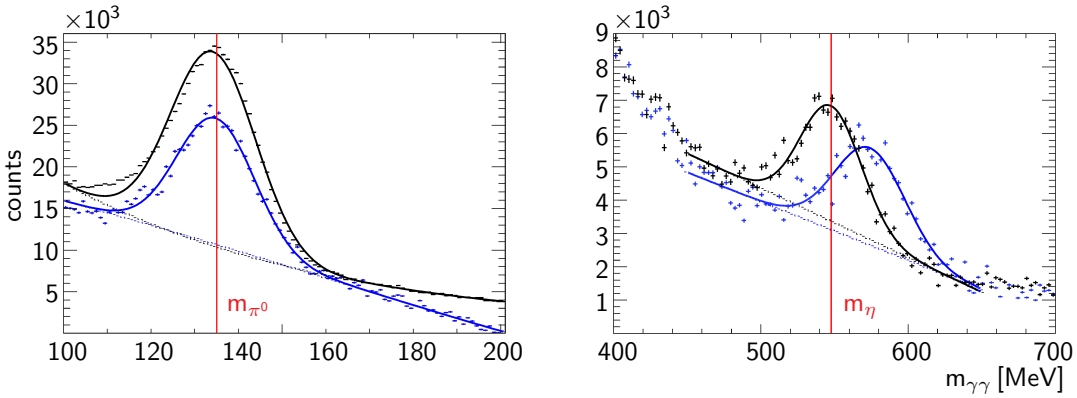

Figure 5.4: **Effect of the energy-dependent calibration.** Reconstructed π^0- [LEFT] and η-mass [RIGHT] before [BLUE] and after [BLACK] application of the correction function (5.2) (using different data samples, counts refer to uncorrected spectra). The peak positions, as derived from a fit assuming a Gaussian signal (solid line) and polynomial background (dashed) show virtually no change for the π^0 (134.8 MeV to 134.2 MeV) while the position of the η-signal changes from 574.0 MeV to 547.6 MeV.

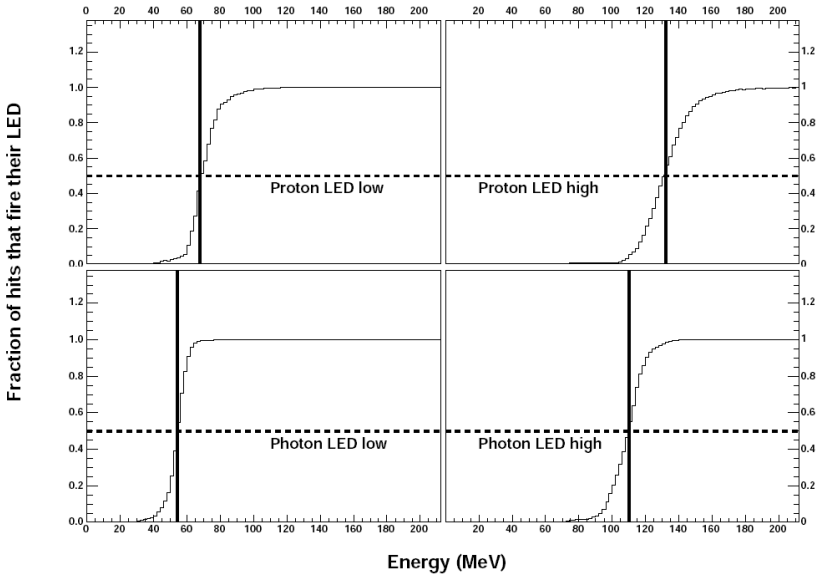

Figure 5.5: **TAPS LED thresholds for photons and protons.** Ratio of energy spectra taken under the condition that the LED has fired and without any condition. Left: LED low, right: LED high. The threshold is defined as the center of the arising edge (vertical line). Due to their different pulse shape, protons [TOP] and photons [BOTTOM] exhibit different threshold characteristics [Cas06].

using data taken at three different LED voltage settings. For each setting two energy spectra are recorded for each module, one only with entries for which the corresponding LED has given a signal and one without any condition (raw spectrum). From the ratio of these spectra the thresholds can be determined either in units of QDC channels or, after energy calibration, in MeV. Figure 5.5 shows the resulting ratios.
The thresholds were set to the same value for each ring of the TAPS detector with values increasing with decreasing polar angle to reduce the effects of e^+e^- pair production off the primary photon beam. It is also possible to set slightly higher thresholds than the hardware settings artificially in the offline analysis to compensate for variations occurring during data taking e.g. due to thermal shifts in the electronics. In order to determine such variations, which may have an influence on the resulting angular distributions, the same method as for the LED calibration is used during data analysis. The threshold values used in this analysis are given in appendix D. The same values are also used in the analysis of Monte Carlo simulations.
For a more detailed description of the calibration process for the TAPS calorimeter, see [Cas06].

5.1.2 Crystal Barrel calibration

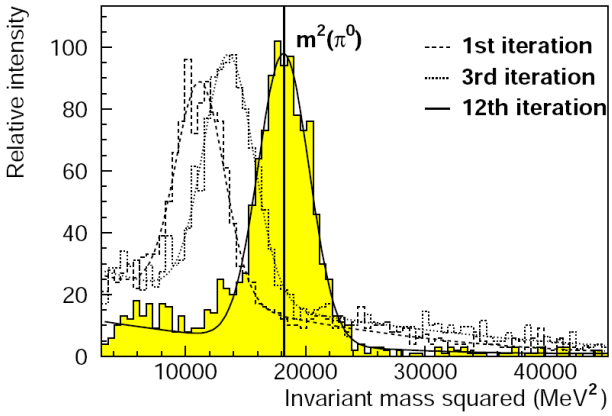

Figure 5.6: **Squared π^0 mass for the Crystal Barrel after calibration.** π^0 peak used for calibration for one CsI(Tl) module in various stages of the calibration [Jun00].

The calibration process for the Crystal Barrel calorimeter is handled in the same way as the second step of the TAPS energy calibration, using π^0 events with both decay photons detected in the Crystal Barrel. For each CsI(Tl) module the position of the π^0 peak is

iteratively compared to its nominal mass, resulting in a calibration factor. The central module of the second electromagnetic shower is again arbitrary so that effects from the second module cancel out in average. A cross-check of this calibration using the η-mass as described above does not show the need for an additional energy-dependent correction. This is partially due to the comparably low single crystal thresholds of 1 MeV, because of which modules with energy deposits below this threshold do not influence the π^0-calibration as much as for the TAPS calorimeter. Additionally, a different means of energy- and angle-dependent correction is applied during reconstruction (see 5.2.2).
In contrast to the TAPS calorimeter, the Crystal Barrel utilizes 12bit *dual-range* ADCs. The two ranges are realized by splitting the signal at the ratio of 8:1:1, feeding 8/10 to the *low range* and 1/10 to the *high range* input of the ADC. The remaining 1/10 is fed to a reference channel and used for an internal pedestal correction. The logic of the ADC, using two internal discriminators, decides which channel to digitize, resulting in a low energy, high resolution range for energies up to ~ 130 MeV and the lower resolution, high-energy range covering energies up to ~ 1100 MeV. The π^0 calibration method is used to fix the gain for the high resolution, low range of the ADCs. A second means of calibration, covering both the low and the high range of the ADCs is given by a lightpulser system [Bar00].
This system feeds lightpulses matching the spectral distribution of the CsI(Tl) scintillating light directly into the wavelengthshifter of each module. The intensity of the pulses can be varied using different filters, thus mimicking the CsI(Tl) response to different energy deposits. Using the proportionality of ADC response and energy known from the π^0 calibration this allows for a continuous calibration over both energy ranges [Bös06]. A detailed description of the calibration of the Crystal Barrel calorimeter is given in [Jun00].

5.1.3 Tagging hodoscope calibration

Time calibration

The time of an event is given by the trigger which in the given case is created by the TAPS calorimeter with its excellent timing resolution (cf. 5.1.1). Accordingly, the time calibration of the fiber hodoscope is done with respect to this detector. Once the calibration for TAPS is finished, the mean time between two photons from the decay of a π^0 serves as a timing reference. The tagging hodoscope calibration itself is now conducted in such a way that the time difference between the 480 individual fibers,

registering the incident electron for each π^0 event, and the TAPS reference time is zero. Figure 5.7 shows the resulting spectra.

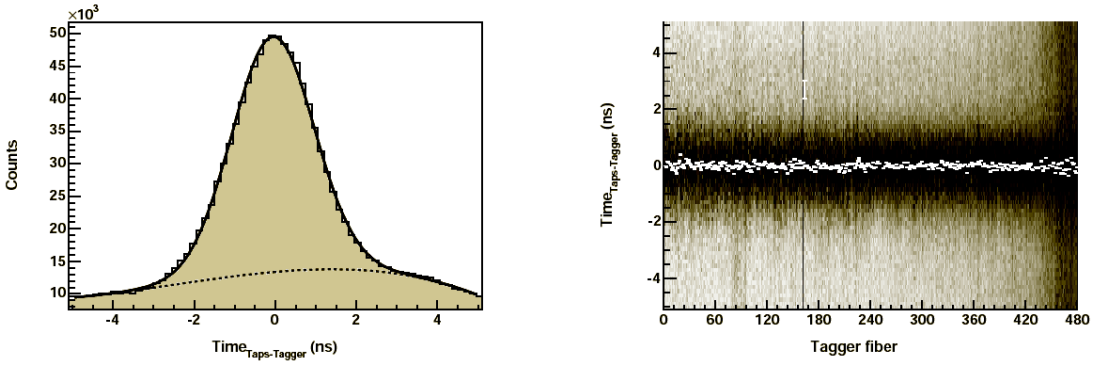

Figure 5.7: **Calibrated relative timing between the tagging hodoscope and TAPS.** The time difference between the mean time of two photons from a π^0 decay detected in the TAPS calorimeter and the associated electron in the tagging hodoscope after the calibration process. Left: Sum over all fibers of the tagging hodoscope. Right: As a function of the fiber number [Cas06]. For the beamtimes subject to this work, a relative time resolution between the tagging hodoscope and TAPS of 0.69 ns has been achieved.

Energy calibration

Goal of the energy calibration of the tagging system is the assignment of a distinct electron - and therefore photon - energy to each of the 480 fibers of the hodoscope for a given setting of primary electron beam energy and field strength of the tagging dipole. In a first step, a fifth degree polynomial expressing this correlation has been calculated using the field map of the dipole and the known spatial positions of the fibers [Hor04]. In a second step, a low rate primary electron beam is varied in energy and is deflected by a constant field of the tagging dipole directly into the tagging hodoscope (*direct injection*). In this way four measurements, using primary electron energies of 680 MeV, 1300 MeV, 1800 MeV, and 2050 MeV at a dipole field strength of $B = 1.413\,\mathrm{T}$, have been conducted [Kle10]. This data has then been used to correct the polynomial (see figure 5.8). For the presented data, taken using primary electrons with an energy of 3176 MeV, the final polynomial reads:

$$\begin{aligned} E = Pol(x)|_{3.2\,\mathrm{GeV}} &= 2533.81 - 190.67 \cdot 10^{-2}x + 28.86 \cdot 10^{-4}x^2 \\ &- 34.43 \cdot 10^{-6}x^3 + 95.59 \cdot 10^{-9}x^4 - 12.34 \cdot 10^{-11}x^5, \end{aligned} \tag{5.5}$$

with E being the photon energy in MeV and x the fiber index. For a different primary beam energy, E_2, and thus a different field strength of the dipole (see 4.2.3), this polynomial is scaled using the ratio of the energies:

$$Pol(x)|_{E_2} = \frac{3.2\,\mathrm{GeV}}{E_2} \cdot Pol(x)|_{3.2\,\mathrm{GeV}}\,. \tag{5.6}$$

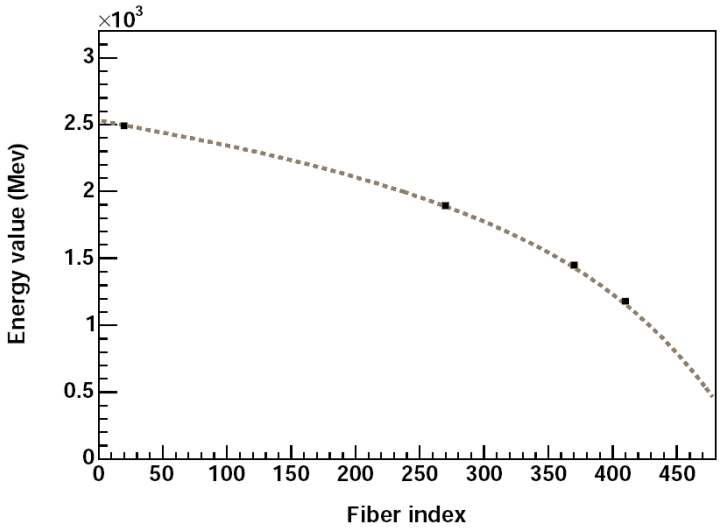

Figure 5.8: **Relation between photon energy and fiber number.** Dashed line: Tagger polynomial (5.5), points: Data obtained by direct injection method [Kle10].

5.2 Subdetector reconstruction

In order to process a recorded event with respect to a certain hadronic reaction, information about the initial and final state particles has to be obtained. This requires knowledge of the energy of the incoming photon and the four-vectors of the outgoing decay products. The former can be calculated from the information generated by the tagging system. For the latter, the energy and direction of the final state photons can be obtained from the response of the calorimeters. In the case of protons, only the direction can be derived from detector information, since they mainly only deposit part of their energy in the calorimeter crystals. The full energy of the protons has to be calculated from energy-momentum-conservation.

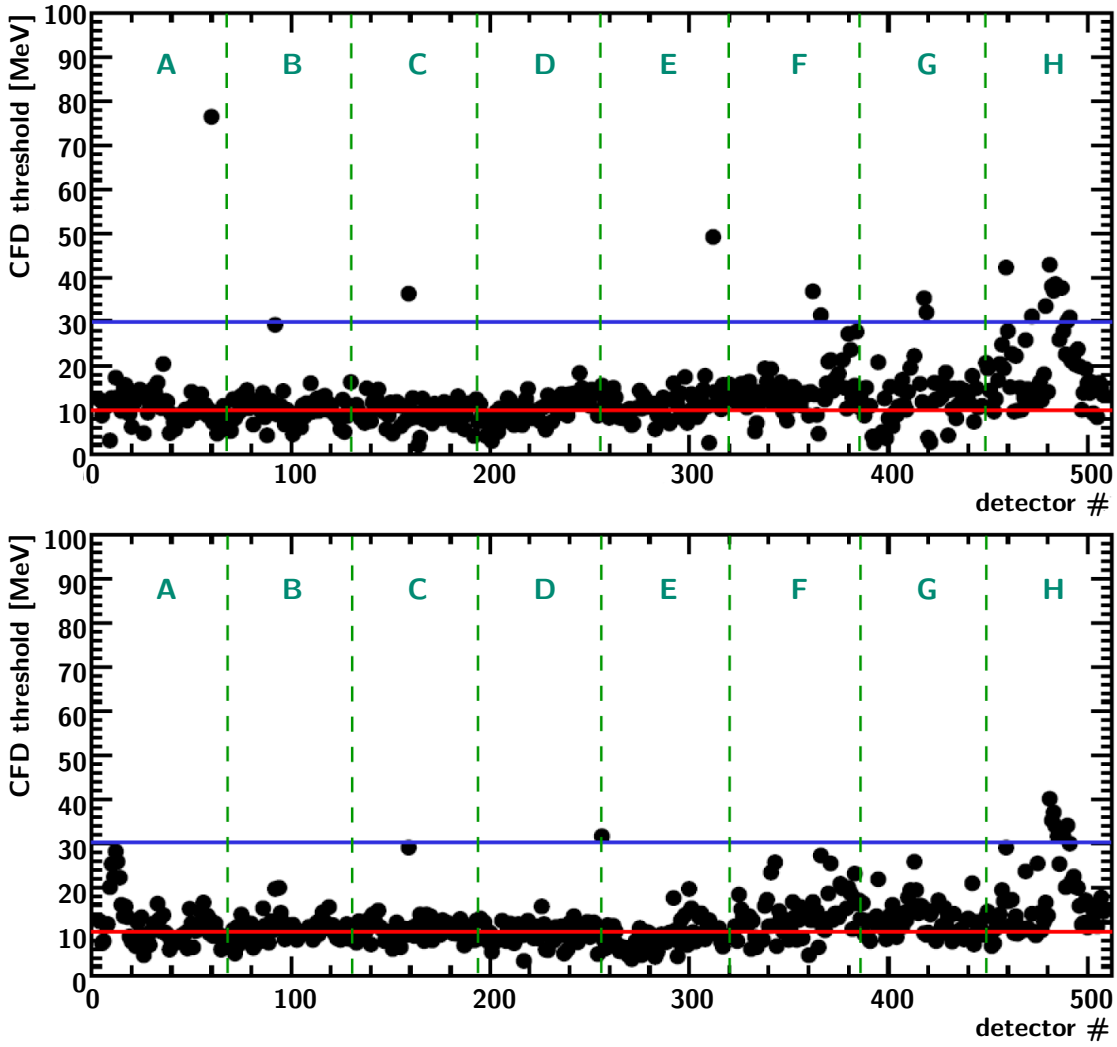

Figure 5.9: **CFD thresholds for the March and May 2003 beamtimes.** The thresholds have been determined from the data for the March ([TOP]) and May ([BOTTOM]) 2003 beamtimes [Nan06, Jae06]. Lower ([RED]) line: Hardware threshold setting (10 MeV). Upper ([BLUE]) line: Software threshold setting (30 MeV). Vertical ([GREEN]) lines: TAPS LED High segmentation (see figure 4.14).

In the following, the reconstruction of final state photons in the TAPS and Crystal Barrel calorimeters along with the reconstruction of the incoming photon energy will be discussed.

5.2.1 TAPS reconstruction

In general, photons do not deposit their energy in just one crystal but instead form electromagnetic showers spanning multiple detector modules. This is accounted for by a cluster-finding algorithm implemented in the TAPS reconstruction. A cluster is defined as any contiguous group of BaF_2 crystals registering an energy deposit above the threshold of their respective constant-fraction discriminators (CFDs).
For the beamtimes relevant to this work the hardware CFD thresholds had been set to 10 MeV. Independent analyses of the data [Nan06, Jae06] however showed a significant spread over a wide energy range. Figure 5.9 shows the distributions of the CFD thresholds for the March and May 2003 beamtimes as extracted from the data. Since the larger variations in the CFD thresholds led to artificial asymmetries in the data analysis, the data has been recalibrated using a software threshold setting of 30 MeV.
The energy of a cluster is then calculated as the sum of the energies detected in the participating modules, the module with the highest entry is treated as the center of the shower.
The timing information available for each BaF_2 module gives an additional constraint on the reconstruction of clusters. All signals of one cluster have to be coincident within 5 ns with the central module to assure the energy deposits originate from the same incident photon. Should, due to inefficiencies, no timing signal be available for the central module, the one with the next highest energy deposit is used as reference for the cluster. Modules without timing information are then assigned a mean time derived from all TAPS detectors. Modules belonging to a cluster, but having a relative timing outside of the coincidence window are discarded.
The spacial distribution of an electromagnetic shower allows for a reconstruction of the position of the incident particle with a resolution better than the inherent resolution due to the granularity of the calorimeter. This is achieved by means of a weighted sum of the x and y coordinates of the individual members of a cluster:

$$X = \frac{\sum_i w_i x_i}{\sum_i w_i}, \quad Y = \frac{\sum_i w_i y_i}{\sum_i w_i}, \tag{5.7}$$

where:

$$w_i = \max\left\{0; W_0 + \ln\frac{E_i}{\sum_i E_i}\right\}. \tag{5.8}$$

This logarithmic weighting yields a significantly better description of the energy deposition than e.g. a linear weighting [AOP+92]. The value of the constant $W_0 = 4$ has been determined by GEANT simulations [Cas06]. This method of position reconstruc-

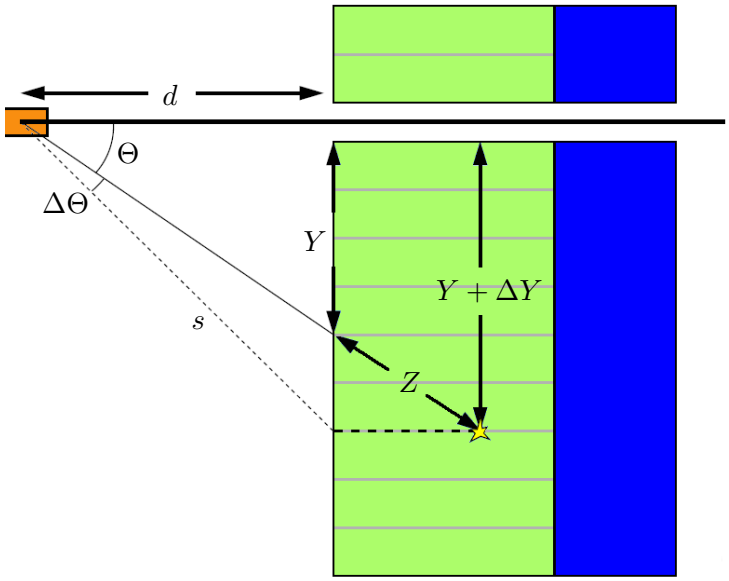

Figure 5.10: **Shower depth correction for the TAPS calorimeter.** See text for details.

tion assumes that electromagnetic showers start at the front face of the BaF_2 modules, neglecting the penetration depth of the photon into the detector before the shower is formed. This method leads to an error in the position reconstruction of the incident photon as illustrated in figure 5.10. To account for this, the travel length Z of the photon in the detector material has to be calculated [A$^+$08b]:

$$Z = X_0 \left(\ln \frac{E}{E_c} + C_\gamma \right), \tag{5.9}$$

with the radiation length of BaF_2, $X_0 = 2.03\,\text{cm}$, incident photon energy, E, and the critical energy for the crystal, $E_c = 12.78\,\text{MeV}$ (see chapter 4.2.1). The constant C_γ is given in [A$^+$08b] as $C_\gamma = 0.5$. This value however has been found by Monte Carlo simulations to be too small. Figure 5.11 shows the difference of the generated and reconstructed polar angle for photons in the TAPS calorimeter, using three different values for C_γ. In the analysis presented in this work, a value of $C_\gamma = 2.0$ has been used. With this information the position corrections ΔX and ΔY can be approximated by [Hej98]:

$$\frac{\Delta X}{X} = \frac{\Delta Y}{Y} = \left(\frac{s}{Z} + 1 \right)^{-1}. \tag{5.10}$$

Using these methods a polar angular resolution for photons of less than 1.3° can be achieved [Cas06].

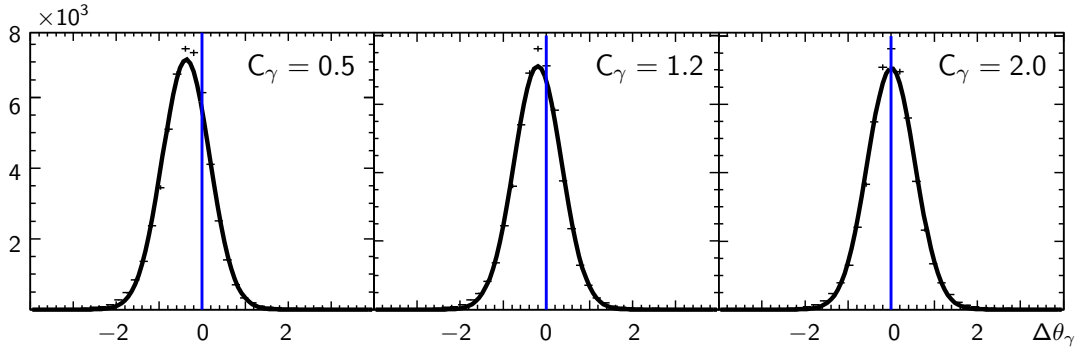

Figure 5.11: **Polar angle reconstruction in the TAPS calorimeter.** Difference between the generated and reconstructed polar angle for photons in the TAPS calorimeter. Left to right: $C_\gamma = 0.5$, $C_\gamma = 1.2$, $C_\gamma = 2.0$ (see (5.9)).

5.2.2 Crystal Barrel reconstruction

The reconstruction methods applied to the Crystal Barrel are very similar to those described above for the TAPS calorimeter. Here, a cluster is defined as any contiguous group of CsI(Tl) modules with an individual energy deposit of at least 1 MeV (single-crystal threshold) and a total energy sum of at least 20 MeV (cluster threshold). This cluster threshold is applied to reduce the influence of shower fluctuations (*split-offs*). Split-offs can occur when the energy deposit in a module belonging to a cluster is below the single crystal threshold, thus breaking the single contiguous group of modules into two, the main one and a small, low energetic one split off from it. This can lead to a wrong multiplicity in the calorimeter, since the one photon creating the split-off would be counted as two[2].

It is possible for a cluster to be formed by more than one incident particle due to overlapping electromagnetic showers. This is accounted for by scanning the participating crystals for local maxima in the deposited energy. Such a maximum is considered as the central crystal of the cluster if its energy deposit exceeds 13 MeV (central crystal threshold). In case of clusters containing only one such maximum, they are identified with one incident particle, forming a *PED*[3] and the PED energy is equal to the energy sum of the participating modules:

$$E_{\mathrm{PED}} = E_{\mathrm{cl}} = \sum_i E_i. \tag{5.11}$$

In case of more than one local maximum, the energy reconstruction is somewhat more

[2]This applies - to a lesser extent - also for the 30 MeV cluster threshold for the TAPS calorimeter.
[3]Particle Energy Deposit

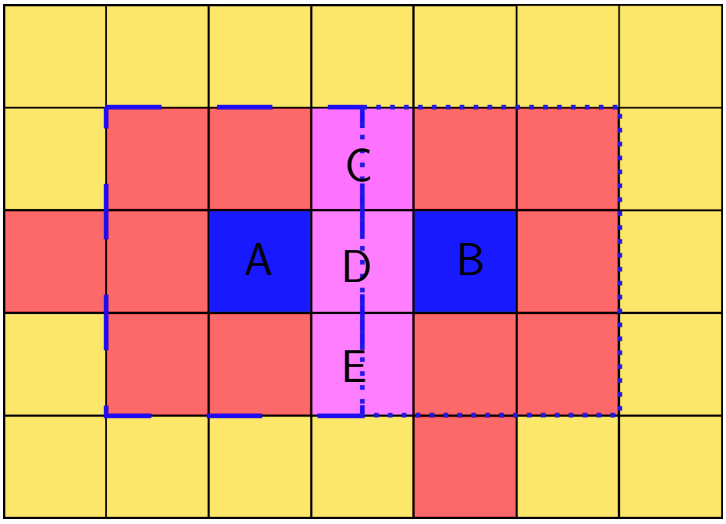

Figure 5.12: **A cluster containing 2 PEDs.** CsI(Tl)-modules with an energy deposit exceeding the single crystal threshold are colored red, central crystals blue. The dashed (dotted) line denotes the crystals relevant for the nine-energy of central crystal A (B). The energy deposit in detectors neighboring both central crystals (C-E, magenta) is split between the two nine-energies according to (5.13).

complicated, since the energy of the cluster has to be distributed among the incident particles. In a first step, the energy sum of each central crystal k and its eight neighbors, the so called *nine-energy* E_9, is calculated:

$$E_9^k = E_{\text{cen}}^k + \sum_{j=1}^{8} E_j. \tag{5.12}$$

If a crystal is adjacent to more than one central crystal, only a fraction of its energy is added to the corresponding nine-energies. Let crystal i be neighbor to j local maxima. Then the fraction of its energy E_i that enters the nine-energy of central crystal k, E_{9k}^i, is calculated as:

$$E_{9k}^i = \frac{E_{\text{cen}}^k}{\sum\limits_j E_{\text{cen}}^j} \cdot E_i. \tag{5.13}$$

In the example illustrated in figure 5.12, this translates to e.g.:

$$E_{9\mathsf{A}}^{\mathsf{D}} = \frac{E_{\mathsf{A}}}{E_{\mathsf{A}} + E_{\mathsf{B}}} \cdot E_{\mathsf{D}}.$$

The energy of each PED is now the cluster energy, weighted with the nine-energies:

$$E^i_{\mathrm{PED}} = \frac{E^i_9}{\sum\limits_k E^k_9} \cdot E_{\mathrm{cl}}. \tag{5.14}$$

As for the clusters, the PED energies have to exceed a threshold of 20 MeV to be accepted as a particle in the reconstruction.
The PED energy calculated as described above is however not equal to the energy of the incident photon, since parts of the electromagnetic shower are not detected due to insensitive material between the CsI(Tl)-crystals or leakage at the edges of the calorimeter. These effects vary with the true energy and therefore shower size as well as with the polar angle. This is accounted for by the application of an energy- and angle-dependent correction function of the form [Jun00]:

$$E^{\mathrm{corr}}_{\mathrm{PED}} = \left(a(\theta) + b(\theta) \cdot e^{-c(\theta)\cdot E_{\mathrm{PED}}}\right) \cdot E_{\mathrm{PED}}. \tag{5.15}$$

Typical values for the coefficients used in this work are $a \approx 1.05$, $b \approx 0.05$, and $c \approx 0.007$.
The position reconstruction for 1-PED cluster in the Crystal Barrel calorimeter is carried out similar to the TAPS reconstruction using a weighted sum of the crystals participating in the cluster. In this case however instead of the Cartesian coordinates in (5.7) the polar and azimuthal angles of the crystal centers, θ_i and ϕ_i are used:

$$\theta_{\mathrm{PED}} = \frac{\sum_i w_i \theta_i}{\sum_i w_i}, \quad \phi_{\mathrm{PED}} = \frac{\sum_i w_i \phi_i}{\sum_i w_i}. \tag{5.16}$$

The weighting factors are defined as in (5.8) with a constant $W_0 = 4.25$. In case of multi-PED clusters, only the central crystal and its direct neighbors can be used for the position reconstruction, so the sum over all crystal energies, $\sum_i E_i$, in (5.8) is replaced by the nine-energy (5.12). This leads to a spatial resolution for photons of $1^\circ - 1.5^\circ$ in θ_{lab} and ϕ_{lab}, depending on the energy and polar angle of the incident photon [Jun05]. The CsI(Tl) modules of the Crystal Barrel are pointing towards the target center, so a correction due to the penetration depth of electromagnetic showers is not necessary.

5.2.3 Tagging hodoscope reconstruction

The reconstruction of the incident photon energy for each event implies the determination of the position of the incident electron within the fiber hodoscope of the tagging system. A fiber is considered as hit by an electron once the corresponding multi-hit

TDC shows at least one entry for the given event. Since an electron can produce a signal in more than one fiber, such hits in the hodoscope have to be clustered according to their spatial and timing information. In the given analysis, any contiguous group recording a hit in their corresponding TDCs within 2 ns of each other is regarded as a cluster. Should one fiber adjacent to two signaling ones not record a hit, this is still considered a cluster to account for inefficiencies. To obtain the energy value corresponding to a cluster, the fiber numbers are averaged and the tagger polynomial (see 5.1.3) is calculated for the resulting average number.
The readout of the fibers via multi-hit TDCs allows for the possibility of more than one hit being registered per event. The determination of the correct hit associated with the hadronic event under consideration is part of the selection process and is described in detail in chapter 6.

The energy region of interest for this work, with respect to the extraction of polarization observables, was covered completely by the fiber hodoscope of the tagging system. Therefore the calibration and reconstruction of the wire chamber has been omitted in this chapter. The scintillator bars and the γ-intensity monitor, which are mainly used for the photon flux determination, have also been left out since an absolute normalization is not needed in the presented analysis.
The use of the charge-sensitive subdetectors of the Crystal Barrel/TAPS experiment has also been avoided for efficiency reasons explained in the following chapter. For further information on these components, see e.g. [Cas06].

6 Selection of the reaction $\gamma p \rightarrow p\pi^0\eta$

In this chapter the relevant datasets are introduced and the selection of events with respect to the $p\pi^0\eta$ final state is described. The latter comprises cuts on timing information and kinematic constraints, as well as the application of a kinematic fit.

6.1 Monte Carlo

In order to understand possible background contributions to the data and for acceptance and efficiency determination, 3 million Monte Carlo events of the type

$$\gamma p \rightarrow p\pi^0\eta \rightarrow p4\gamma$$

were generated for a photon energy range from threshold to 3.175 GeV. This set, produced using the GEANT3 based CBGEANT [Cre01] simulation package, has been subjected to the same analysis chain as the data, allowing for a cross-check of each step.
The experimental setup described in chapter 4 is realized in the simulation package as accurately as possible, including all detector components as well as insensitive material placed in the path of the reaction products, such as holding structures. The simulation starts, however, at the target point; the incoming photon beam, tagging system and beam dump are not included. The desired reaction products are produced by an event generator according to the available phasespace, taking into account energy- and momentum-balance. Dynamical effects, like the formation of resonant states, are not simulated. Next the created particles are tracked through the insensitive material and detector components in small steps and their interactions calculated on a statistical basis. Possible processes include ionization, Coulomb-scattering, shower formation and decays. The results of the simulation are then digitized based on the properties of the sensitive detector components and stored in the same format as the real experimental data, allowing for the use of the same analysis framework for data and simulation. Additionally, the Monte Carlo data has also been subjected to the trigger simulation [JG04] (see chapter 4.4).

6.2 Datasets

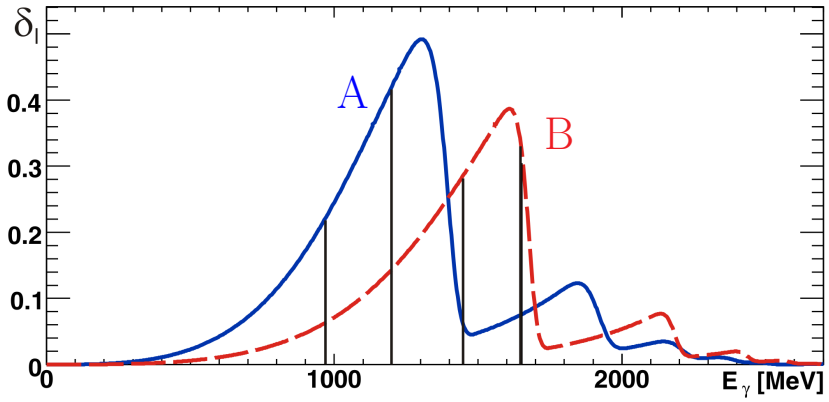

Figure 6.1: **Degree of linear polarization for the two beamtimes.** The highest polarizations were 49.2% at $E_\gamma = 1305\,\text{MeV}$ (A, March) and 38.7% at 1610 MeV (B, May), respectively (see [E$^+$09] for details). Vertical lines indicate the three energy ranges chosen for the extraction of polarization observables.

The selection procedure derived in this chapter and the results presented in chapter 7 are based on data taken with the Crystal Barrel/TAPS experiment in March and May 2003. Figure 6.1 shows the polarization settings for these data taking periods. In both cases the linearly polarized photons were produced via coherent bremsstrahlung off a diamond radiator, using a primary electron beam with an energy of 3.2 GeV. The measurements were performed using a liquid hydrogen target. For the March beamtime the coherent edge position was set to 1350 MeV, resulting in a maximum degree of polarization of 49.2% at a photon energy of 1300 MeV; for the May 2003 beamtime the coherent edge was set to 1650 MeV, leading to a maximum polarization of 38.7% at a photon energy of 1600 MeV. The data taken during these beamtimes amounts to a total of 160 hours and 245 million events of raw data on disk[1].

The two datasets were subdivided into three energy ranges for the determination of the polarization observables, $E_\gamma = 1085 \pm 115\,\text{MeV}$, $1325 \pm 125\,\text{MeV}$, and $1550 \pm 100\,\text{MeV}$ respectively, as indicated by the vertical lines in Fig. 6.1. The low energy range consists solely of data taken with the polarization setting A (March), and the high energy range of data taken only with setting B (May), to guarantee a sufficiently high degree of polarization. Both datasets were combined for the intermediate energy range. The spectra shown in this chapter are, unless stated otherwise, integrated over the energy

[1] Due to a problem with the trigger settings, parts of the May beamtime had to be excluded from the analysis, resulting in the given numbers.

range of 970 to 1650 MeV.
The photon energy range of 900 MeV, slightly below the $\pi^0\eta$ production threshold, to 2500 MeV, corresponding to the lower end of the tagging hodoscope, has also been selected for analysis to perform further cross-checks of the data. A selection of the resulting invariant mass distributions and Dalitz plots is shown in chapter 7, and the full set is shown in appendix C.

6.3 Preselection

Meson	Decay mode	Branching ratio
π^0	$\gamma\gamma$	$(98.798 \pm 0.032)\%$
η	$\gamma\gamma$	$(39.31 \pm 0.20)\%$
	$\pi^0\pi^0\pi^0$	$(32.56 \pm 0.23)\%$
	$\pi^+\pi^-\pi^0$	$(22.73 \pm 0.28)\%$
	$\pi^+\pi^-\gamma$	$(4.60 \pm 0.16)\%$

Table 6.1: **Dominant decay modes of π^0 and η mesons.** Values taken from [A$^+$08b].

Particle multiplicity Table 6.1 gives an overview of the dominant decay modes of the π^0 and η mesons. Since the Crystal Barrel and TAPS calorimeters are designed for the detection of photons, decay modes involving charged particles will not be taken into account for further analysis. This poses no limitation in case of the π^0, since its neutral decay $\pi^0 \to \gamma\gamma$ has a branching ratio[2] of $\approx 98.8\%$. In case of the η this constraint leaves the two decay modes $\eta \to \gamma\gamma$ and $\eta \to \pi^0\pi^0\pi^0$, whose combined branching ratio is $\approx 72\%$. These considerations lead to two possible final states to be measured by the detector system, the proton along with 4 photons ($\eta \to \gamma\gamma$) and the proton plus eight photons ($\eta \to \pi^0\pi^0\pi^0$). The latter state however poses the problem of a significant decrease in acceptance and a dramatic increase in combinatorial background. Therefore this analysis is limited to data preselected for five distinct hits in the calorimeters (PEDs), identified as described in chapter 5.
The initial state of the reaction is completely known kinematically (incoming photon momentum, proton mass and momentum), so it is generally possible to reconstruct

[2]The branching ratio is defined as the ratio of the decay width of the given decay mode to the total decay width: $BR = \Gamma_i/\Gamma \cdot 100\%$

the final state even if one of the particles escaped detection. This option is not used however, since no significant signal for the $p\pi^0\eta$ final state could be distinguished from the background for such 4-PED events.

Charge identification The main goal of this work is the determination of asymmetries in the ϕ-distributions of the final state particles (see 3.1), so it has to be ensured that no artificial asymmetries are introduced by detector inefficiencies. While for the calorimeters the efficiencies are well known and under control [Jun05, Cas06], this is not necessarily the case for the charge sensitive inner detector and the TAPS vetos. Here uncertainties in the determination of the efficiencies exist and inefficient channels would lead to the omittance of events in certain proton-angles, thus leading to artificial asymmetries. This is illustrated in figure 6.2. Shown are in the upper row the reconstructed ϕ-θ-distributions of the proton, determined as described below, for the incoming photon energy range $E_\gamma = 1325 \pm 125\,\mathrm{MeV}$, once with a cut on exactly one charged particle (left) and once with a cut on one or no charged particle in the final state (right). The comparison shows distinct areas of less statistics in the spectrum cut on exactly one charged particle, for example at $(\phi, \theta) \approx (60°, 10°)$ (A) or $(\phi, \theta) \approx (-160°, 24°)$ (B). Here inefficient TAPS veto-scintillators lead to the omission of otherwise good events. For example A this is further illustrated in the bottom row of figure 6.2. On the left side the projections on the ϕ-axis of the ϕ-θ-distributions are shown for a θ region of $1° - 15°$. The area of less statistics in the spectrum cut on exactly one charged particle (solid line) is clearly seen in comparison to the cut on one or no charged particle (dashed line) as a dip at $\phi \approx 60°$. This is also reflected in the ratio of the distributions shown in the bottom right. The binning for the projections has been chosen according to the binning of the ϕ-distributions later used for the extraction of the polarization observables (see chapter 7). The difference in statistics between the two variants is approx. 10%.
The data has therefore, in addition to the selection of five PEDs mentioned above, been selected for events where not more than one of these PEDs has been identified as charged, allowing for five "neutral" particles in the final state. Additionally, charge information, where available, will not be used in the further analysis. Effectively, all five final state particles are regarded as photons and the proton will be determined via the kinematic constraints posed on the fourvectors. The analysis is carried out in such a way that each of these five "photons" is left out of the analysis loop once, leaving five 4-photon combinations. These are then tested for compatibility with the assumption that the left out particle is the proton. This leads to five individual analyses for each event to ascertain the correct proton out of the five particles.

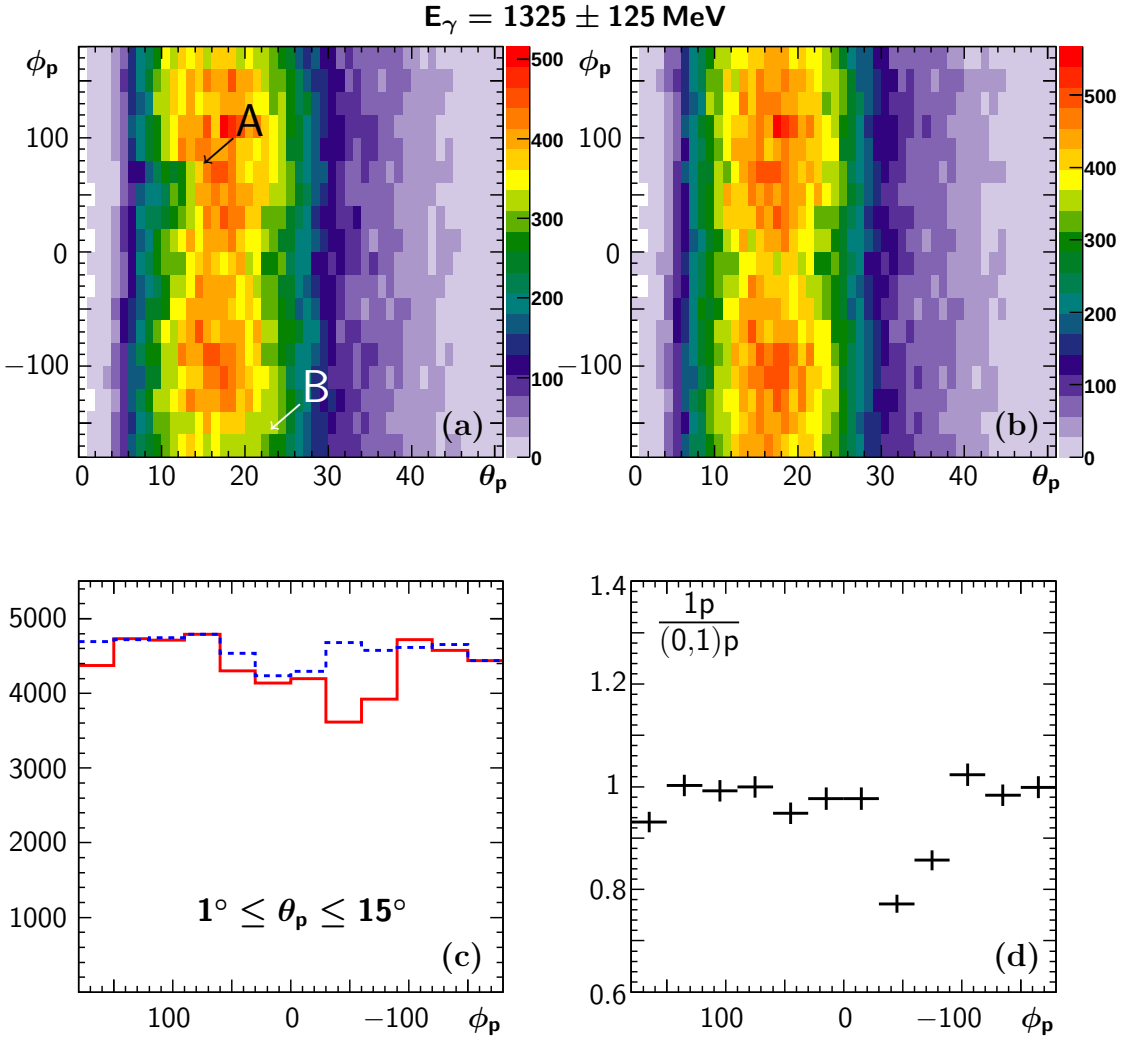

Figure 6.2: **Charge identification efficiency.** Top row: Reconstructed ϕ-θ-distribution of the proton, identified by combinatorics using all cuts described in the following sections with the exception of the kinematic fit, for a preselection of the data requiring (a) exactly one charged particle and (b) one or no charged particle in the final state. Already in this picture detection inefficiencies are visible for the cut on exactly one charged particle (A, B). Bottom row: (c) ϕ-projections of the distributions (a) and (b), integrated over $1° \leq \theta \leq 15°$. ϕ-binning according to the distributions later used for the extraction of polarization observables. Solid ([RED]) line: Cut on exactly one charged particle, dashed ([BLUE]) line: Cut on less or equal one charged particle. The dip around $\phi = 60°$ corresponds to structure A in (a). (d) Ratio of the projections in (c).

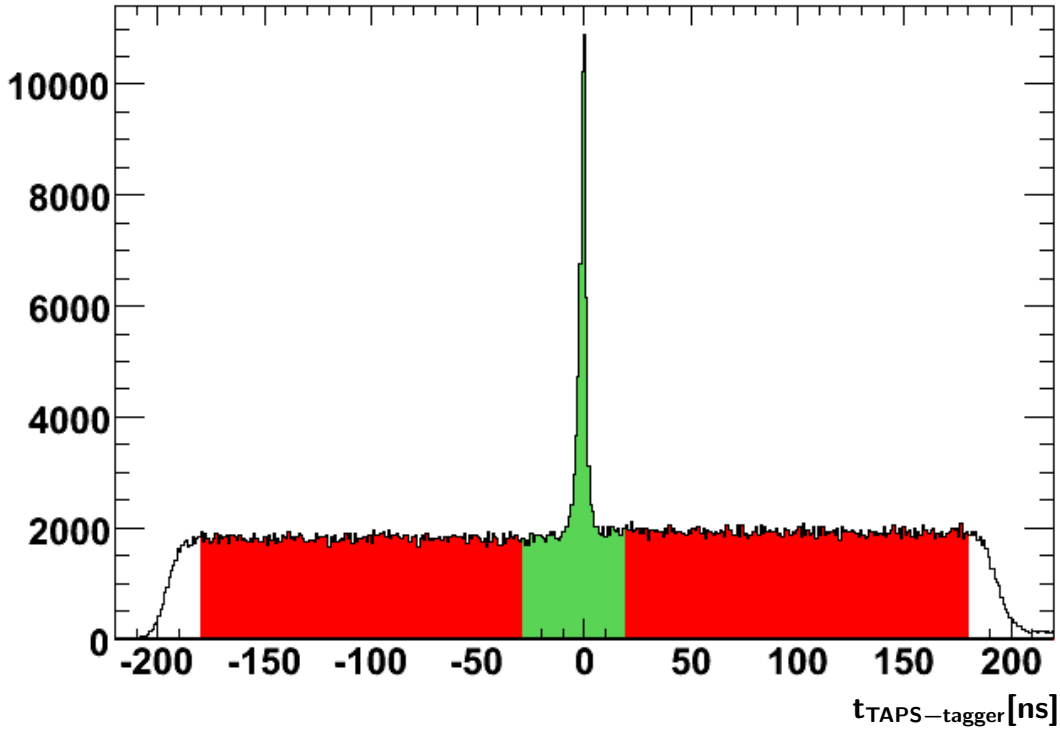

Figure 6.3: **TAPS-tagger time spectrum.** Background events in the signal region ([GREEN]) are accounted for by sideband subtraction using events from the uniform part in the random background region ([RED]). The signal region is chosen asymmetrically to account for timing signals produced by protons in the TAPS calorimeter.

Timing information The tagging system of the Crystal Barrel/TAPS experiment operated with rates of about 10^7 Hz in combination with multi-hit TDCs (see chapter 5). Therefore multiple hits in the tagging system are recorded for each event. This can be treated up to a certain extent by using the reconstruction methods described in 5.2.3, but still multiplicities as high as 15 per event can occur. Each of these hits has to be processed individually, always yielding the same topology in the other detectors, but with a different energy for the incoming photon. For further analysis however, it is necessary to have complete, unique information about the initial state, for example for missing mass calculations. The Crystal Barrel/TAPS experiment has two subdetectors defining the timing of an event, the tagging system and the TAPS calorimeter (see chapter 5). For the beamtimes used in this work, TAPS triggered the readout for an event, giving a distinct time reference. Only those hits in the tagger that, after calibration,

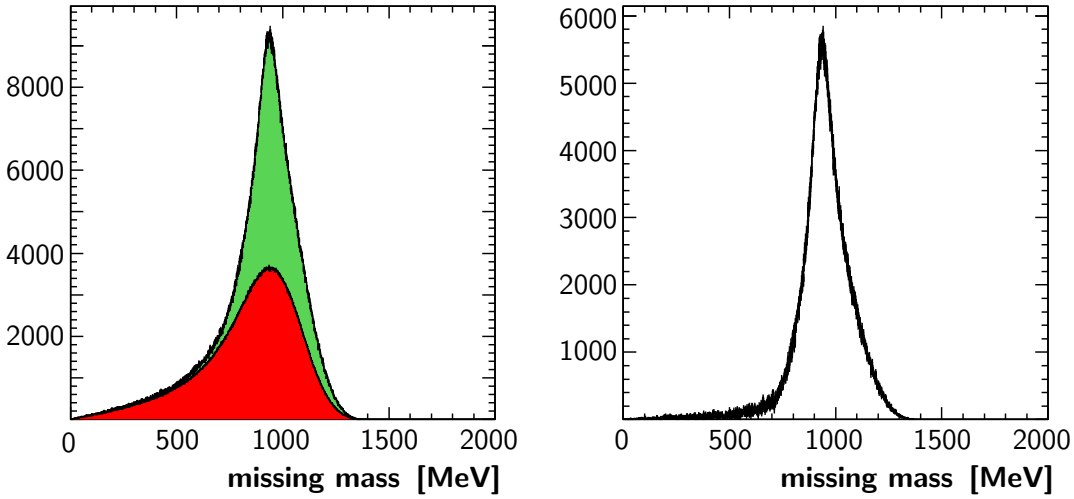

Figure 6.4: **Example for the time-background subtraction.** Shown is the 4γ-missing mass (described below) for an incoming photon energy range of $970\,\text{MeV} \leq E_\gamma \leq 1650\,\text{MeV}$. In this spectrum, cuts on the masses of the final state mesons are already applied. Left: Missing mass of events in the signal region (figure 6.3, [GREEN]) and the corresponding random time-background as determined from the sidebands and scaled accordingly ([RED]). Right: Subtracted spectrum.

are coincident with this trigger signal of TAPS can be correlated to the actual event. Figure 6.3 shows an example of a TAPS-tagger timing spectrum. A sharp coincidence signal is visible on top of a flat, uncorrelated background. The coincidence signal is not symmetric around zero since not only photons but also protons can produce trigger signals in the TAPS calorimeter. The signal is therefore a superposition of the fast photon and the slower proton timing signals, leading to an asymmetric broadening of the peak. It is not sufficient to just cut the data with respect to the coincidence peak, since there is still a considerable amount of background located underneath. This background, however, is uniformly distributed, so it is possible to subtract it using events from the sidebands. This is done by performing all further analysis steps in parallel for events in the coincident, "signal" region (green area in figure 6.3) and events in the uniform part of the uncorrelated region (shaded red). Each histogram is then filled once with the signal events and once with the uncorrelated events, scaled in such a way that the integral of uncorrelated events in figure 6.3 matches the number of background events below the coincidence peak[3], assuming a uniform distribution. In the end, the

[3] In the given analysis, a time window of $\pm 180\,\text{ns}$ is used with a coincidence window of $[-30; +20]$, leading to a scaling factor of $\frac{5}{31}$.

weighted background histogram is subtracted from the signal spectrum. This procedure is illustrated in figure 6.4 using the example of the 4γ-missing mass as described in the next paragraph. Shown is the missing mass of four photons with respective invariant $\gamma\gamma$-masses compatible with one π^0 and one η meson (see *Meson masses* below). No other cuts have been applied to the spectrum. The colors in the left spectrum correspond to those in figure 6.3, the green distribution being the missing mass calculated from events in the signal region. The red distribution has been calculated from events in the random background region and scaled to match the background below the coincidence peak. It is notable that the timing-background peaks at the proton-mass, meaning that a cut on this spectrum without the background subtraction would lead to a contamination by uncorrelated events. Also, the lineshape is affected by the subtraction, since the low-mass part in the signal distribution is dominated by such uncorrelated events, as is clearly visible in the subtracted spectrum. Additional examples for the effects of the time-background subtraction will be given in the following sections.

6.4 Kinematic cuts

The selection of the $p\pi^0\eta$ final state from the preselected data described above exploits certain kinematical constraints posed by energy-momentum-conservation as well as by the knowledge of the masses of the particles involved. The according kinematic variables are introduced in the following and the application of cuts based on their distributions is described.

6.4.1 Kinematic variables

Missing mass A first constraint to be imposed on the five 4-photon combinations per event is that their *missing mass* has to be compatible with the mass of the proton, $m_p = 938.272\,\mathrm{MeV}$ [A+08b]. The missing mass is calculated according to:

$$m_{\mathrm{miss}} = \sqrt{(E_{f,\mathrm{miss}}, \vec{p}_{f,\mathrm{miss}})^2} = \sqrt{\left(\sum (E_i, \vec{p}_i) - \sum (E_{f,\mathrm{meas}}, \vec{p}_{f,\mathrm{meas}})\right)^2}, \tag{6.1}$$

with $(E_i, \vec{p}_i)$ and $(E_{f,\mathrm{meas}}, \vec{p}_{f,\mathrm{meas}})$ being the fourvectors of the initial and measured final state particles, respectively.

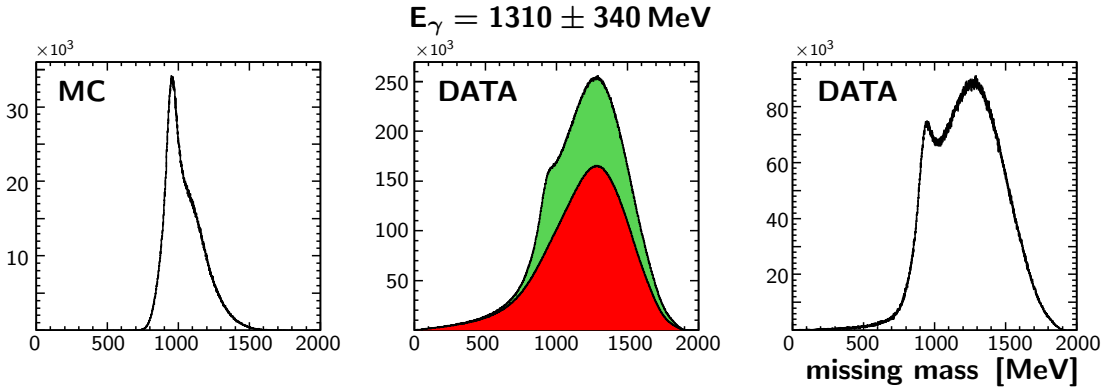

Figure 6.5: **4-particle missing mass distribution.** Shown is the calculated missing mass for five combinations per preselected event without any further cuts. Signals at the position of the proton mass are seen above combinatorial background in the Monte Carlo simulation ([LEFT]) as well as a shoulder in the non background subtracted data spectrum ([CENTER, GREEN]). The uncorrelated timing-background ([CENTER, RED]) however shows no distinct feature at the proton mass. After subtraction, a clearer signal for the proton is visible above combinatorial and other background ([RIGHT]).

Figure 6.5, shows the missing mass distribution for the incoming photon energy range of 970 MeV to 1650 MeV for the Monte Carlo simulation of the reaction $\gamma p \rightarrow p\pi^0\eta \rightarrow p4\gamma$ in the left panel. A signal at the correct proton mass can be seen on top of combinatorial background. In the central panel the according spectrum for the data is shown, once for the complete signal region without random background subtraction (green, cf. figure 6.3) and once for the uncorrelated timing-background (red). A shoulder at the correct position is visible for the uncorrected signal events, whereas the timing-background shows no distinct features. In the subtracted spectrum, shown in the right panel of figure 6.5, a peak at the proton mass is visible more clearly, however on top of a significant background. Unlike in the Monte Carlo simulation, this background is not just combinatorial, but comprises events from competing reactions where for example particles escaped detection, as well as non-hadronic contributions, detailed in the following paragraphs. All events enter the histograms five times due to the process of proton determination described above, so signatures not simulated but present in the data impair the signal-to-background ratio excessively, compared to the Monte Carlo simulation.

Meson masses An additional constraint for the identification of the $p\pi^0\eta$ final state is posed by knowledge of the meson masses,

$$m_{\pi^0} = 134.6799 \pm 0.0006\,\text{MeV} \quad \text{and} \quad m_\eta = 547.853 \pm 0.024\,\text{MeV}\ [\text{A}^+08\text{b}].$$

Only events for which the invariant mass of either pair of photons is independently compatible with these masses are to be considered for further analysis:

$$m_{\gamma\gamma} = \sqrt{((E_{\gamma_1}, \vec{p}_{\gamma_1}) + (E_{\gamma_2}, \vec{p}_{\gamma_2}))^2} = m_M, \tag{6.2}$$

with m_M being the mass of the respective meson and $m_{\gamma\gamma}$ the *invariant mass* of the two photons γ_1 and γ_2. In order to reconstruct two mesons out of the four measured photons, $\binom{4}{2} = 6$ combinations have to be processed for each proton candidate in each event, leading to 30 entries per event entering the according histogram shown in figure 6.6. The fact that the final state comprises two different mesons that have to be reconstructed concurrently reduces the number of $\gamma\gamma$-combinations by a factor of 2, but this is canceled by the fact that each $m_{\gamma\gamma}$-$m_{\gamma\gamma}$-pairing is entered twice - (m_1, m_2) and (m_2, m_1) - for symmetry reasons. While in the Monte Carlo simulation the signal at (m_π, m_η) and (m_η, m_π), corresponding to the simulated reaction $\gamma p \rightarrow p\pi^0\eta$, is clearly visible on top of combinatorial background, for the data the predominant feature is the signal at

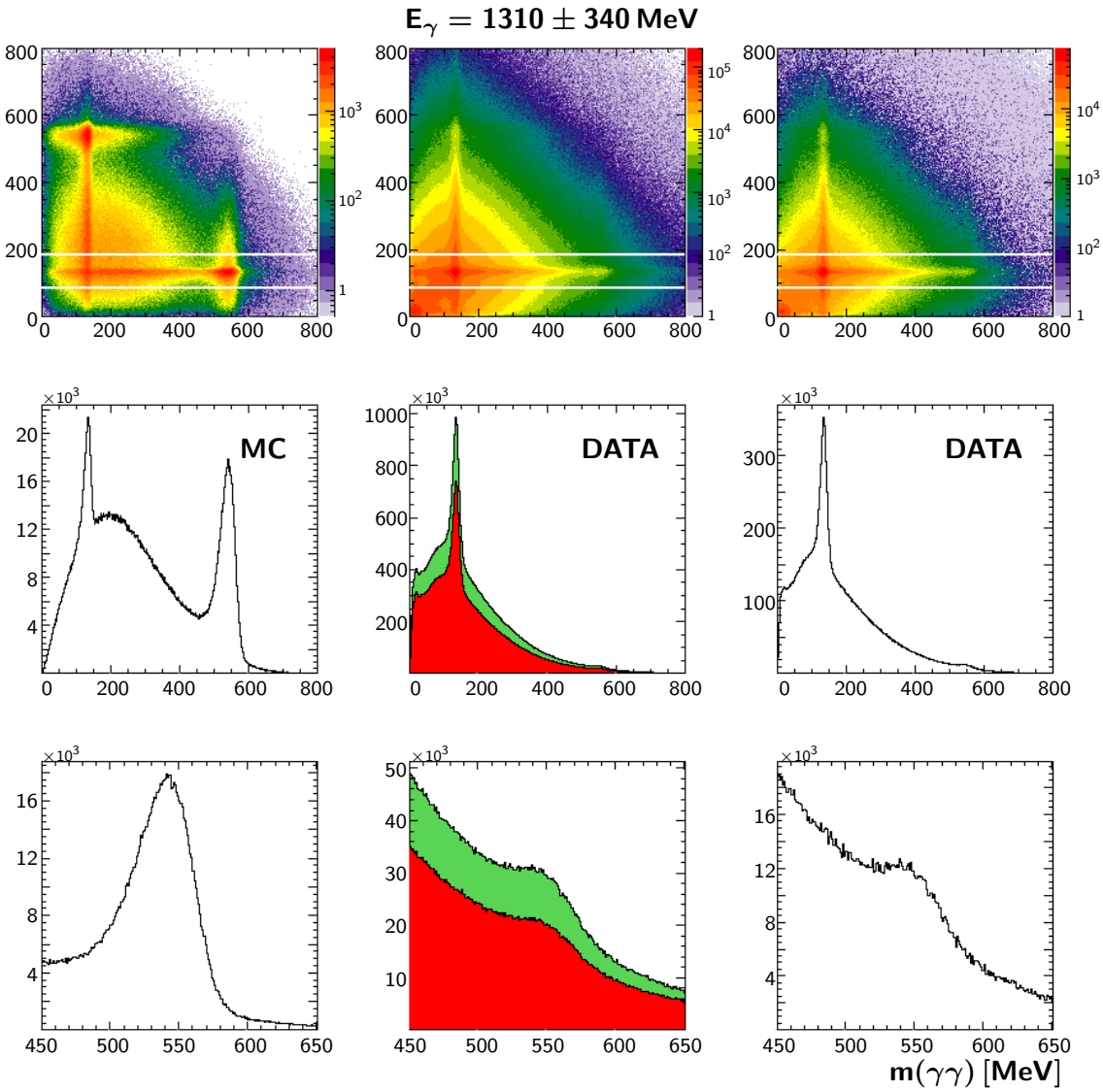

Figure 6.6: **Invariant $\gamma\gamma$-mass.** Top row: Invariant $\gamma\gamma$-mass of one photon-pair versus the invariant mass of the other pair for all five combinations per event, entered symmetrically, for the Monte Carlo simulation ([LEFT]) and the data without ([CENTER]) and with time-background subtraction ([RIGHT]). Lines denote the region used for the projections below. Clear signals are visible at (m_π, m_η) and (m_η, m_π) above combinatorial background for the Monte Carlo simulation, while the data is dominated by $2\pi^0$-production. Center row: Projections from 85 MeV to 185 MeV of the two-dimensional spectra above. Bottom row: Zoom on the η-mass range. Central panels: Projections of the coincident events ([GREEN]) and uncorrelated background ([RED]).

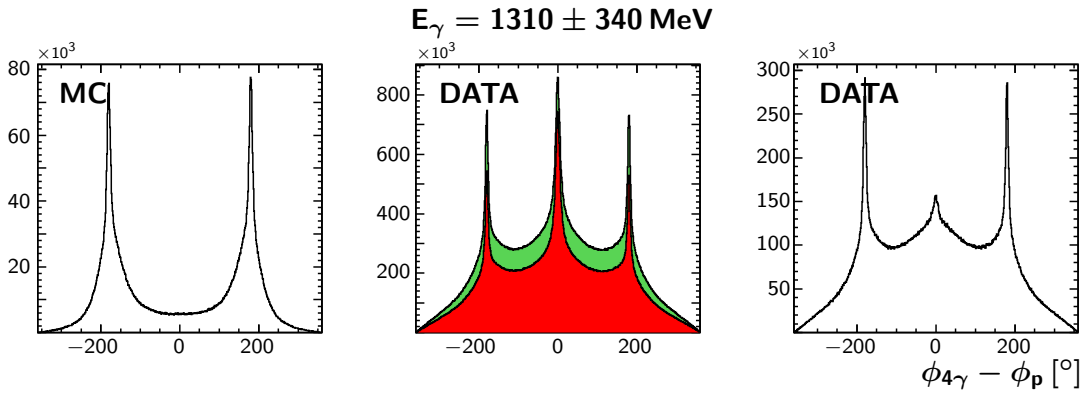

Figure 6.7: **ϕ-difference between the 4γ-system and the proton candidate.** Shown is the difference for five combinations per preselected event without any further cuts. Distinct coplanarity peaks at $\pm 180°$ are seen above combinatorial background in the Monte Carlo simulation ([LEFT]) as well as in the data ([CENTER, RIGHT]). In the data however, an additional signal at 0° is visible, dominating in the uncorrelated timing-background ([CENTER, RED]), but still being present in the background subtracted spectrum ([RIGHT]). These events are caused by leakage from the electron beam dump. See text, figure 6.8 for details.

(m_π, m_π), stemming from the competing reaction $\gamma p \rightarrow p\pi^0\pi^0$. In the energy region $E_\gamma = 1310 \pm 340\,\text{MeV}$ the cross section for this reaction is up to a factor 3 larger than for $\pi^0\eta$-production (cf. figure 2.4) and its branching ratio to 4γ of 97.6% highly exceeds that of the $\pi^0\eta$ final state of 38.8% (cf. table 6.1). The signal for $\pi^0\eta$-production is however visible in the data as well, especially in the projection zoomed in on the η mass region (figure 6.6, bottom right). The separation of the two final states poses no problem due to the comparably high mass of the η meson, as will be shown below.

Coplanarity The sum of the three-momenta of the outgoing particles for any given final state has to equal zero in the center of momentum frame, as dictated by energy-momentum-conservation. This means in particular that the difference between the azimuthal angle ϕ of the proton and of the meson system comprising the π^0 and η has to be 180°[4]. The latter is at the given stage represented by the sum of the four photons, since the final state mesons are yet to be identified. Figure 6.7 depicts the difference of the azimuthal angle of the proton candidate and the sum of the remaining four particles, again for the Monte Carlo simulation and for the data. As expected, distinct peaks at $\pm 180°$ are visible on top of combinatorial background. The data however shows another signal around $\Delta\phi = 0°$, dominated by random timing background but still discernible

[4]Since the azimuthal angle is Lorentz-invariant, this condition holds also true in the laboratory frame.

after the background subtraction (central panel).
Figure 6.8 illustrates the signature of these background events. Panel (a) shows the θ-ϕ-distribution for events in the region of the $\Delta\phi = 0$ peak from figure 6.7. A heightened intensity in the negative ϕ-region, corresponding to the lower halves of the calorimeters, is visible, starting at $\theta \approx 156°$ and extending throughout the whole Crystal Barrel up to the lower part of TAPS. Panel (b) shows the ϕ-difference between the 4γ-system and the proton candidate as function of the azimuthal angle of the proton candidate. It is clearly visible that the additional intensity around $\Delta\phi = 0°$ is confined to the lower half of the calorimeter system. An additional feature of these events is the number of reconstructed PEDs per cluster for the proton candidate, as shown in panels (c) and (d) of figure 6.8. Panel (c) shows the ϕ-distribution of proton candidates for events with a $\Delta\phi$ within $\pm 20°$. Again for the lower half of the setup, a tendency towards higher numbers of PEDs per cluster, up to four, is visible. This is confirmed in panel (d) where the $\Delta\phi$-distribution is shown as function of the number of PEDs. An explanation for this type of signal lies in the general setup of the experiment, especially the position of the electron beam dump (cf. section 4.2.4). Should particles like neutrons be able to escape the beam dump, they would enter the Crystal Barrel in the region of ring 11, corresponding to $\theta \approx 156°$. They would then deposit energy all throughout the calorimeter, fluctuations in the deposition leading to the reconstruction of multiple PEDs within one large cluster, and finally reach TAPS, triggering the event. Since the data shown has been preselected for five PEDs, the PED multiplicity per cluster caps at 4, the fifth PED being the one in TAPS. All these PEDs are created by a single particle traversing the detector setup in a straight line, thus having all the same azimuthal angle, leading to the peak at $\Delta\phi = 0°$ in figure 6.7. This background is, however, easily separable, due to its distinct signature, as can be seen in figure 6.8 (b). The considerations concerning momentum conservation also allow for the calculation of the polar angle of the proton from the fourvectors of the photon system. Figure 6.9 shows the difference between the polar angle of the missing particle for all 4γ-combinations per event and the measured angle of the fifth PED, both in the laboratory frame. A signal around $\Delta\theta = 0°$, above a background distribution[5], is seen in the Monte Carlo simulation as well as in the data. Two distinct features are apparent in the data, however, that do not appear in the simulation, at $\Delta\theta \approx -30°$ (A) and $\approx -160°$ (B). Both signals are also prominent in the random timing background (shaded red in the central panel in figure 6.9), but stay visible even after background subtraction (right panel). Figure 6.10 shows, in the upper row, again the $\Delta\theta$-distributions for the Monte Carlo simulation and

[5]The distribution is asymmetric because due to the Lorentz boost the proton has to go in forward directions while photons are reconstructed over the full θ range.

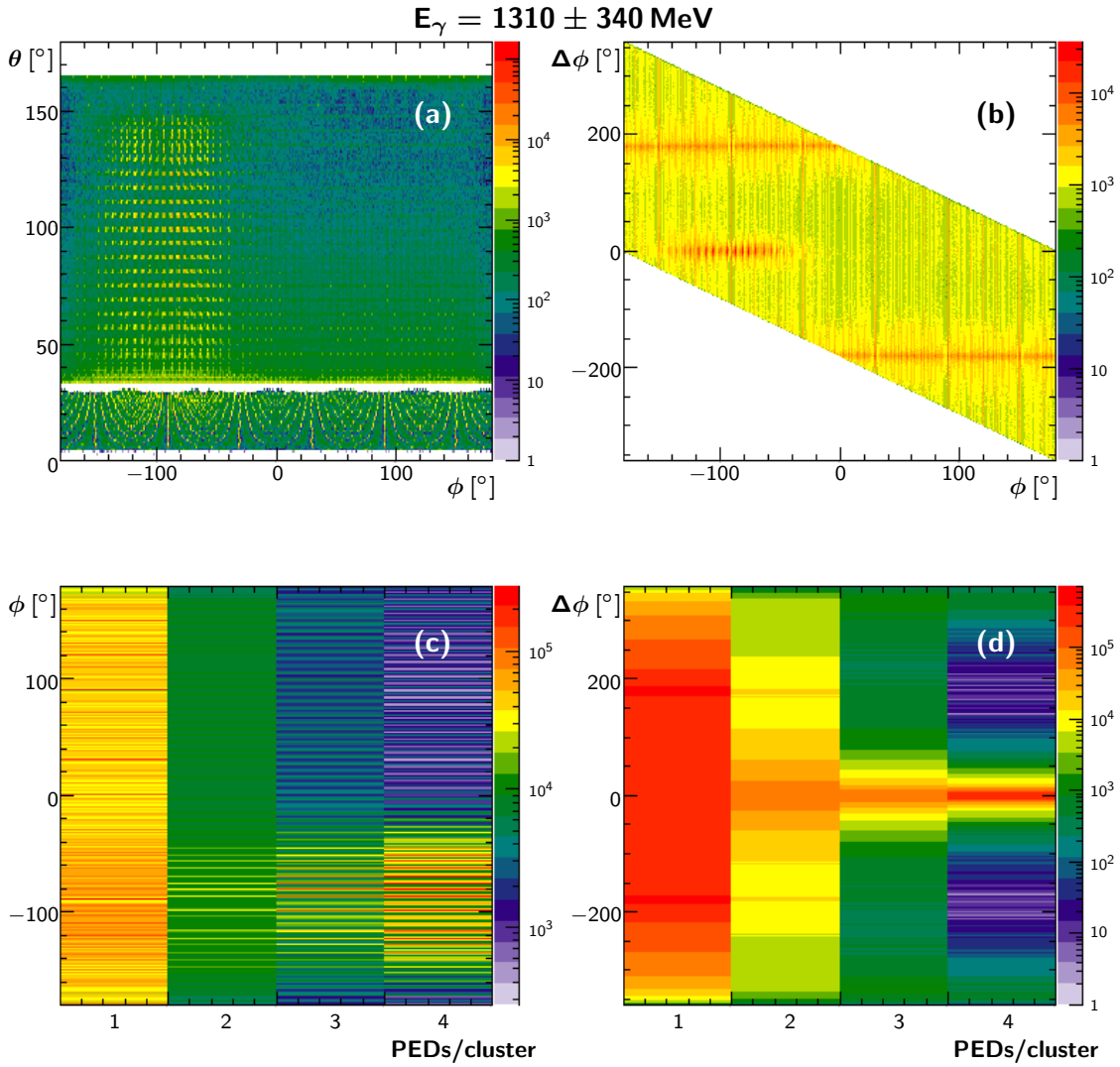

Figure 6.8: **Signature of background events stemming from beam dump leakage.** (a) θ-ϕ-distribution of events with a $\Delta\phi$ within $\pm 20°$ (see figure 6.7). A distinct accumulation of events in the lower half of the Crystal Barrel (negative ϕ-values) is visible, starting at $\theta \approx 156°$, corresponding to ring 11 in the upstream half of the calorimeter and extending up to the lower part of TAPS at $\theta \approx 30°$. (b) $\Delta\phi$-distribution (figure 6.7) as function of the azimuthal angle. The background events clustering at $\Delta\phi = 0°$ are again visible in the lower part of the detector system. (c) ϕ-distribution of particles as function of the number of PEDs reconstructed per cluster for the $\Delta\phi$-region $\pm 20°$. Events in the lower half of the detector system tend to have higher numbers of PEDs. (d) $\Delta\phi$-distribution as function of the number of PEDs per cluster. The higher numbers of PEDs accumulate in the region of the background events at $\Delta\phi = 0°$. See text for details.

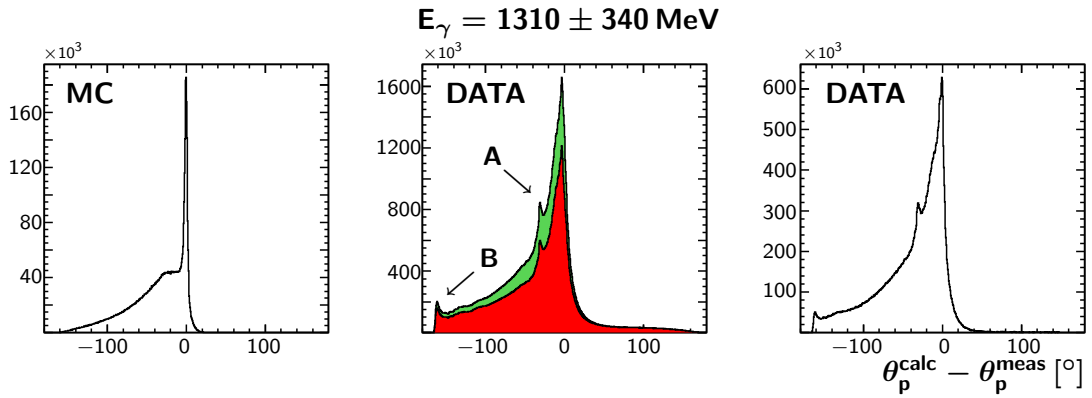

Figure 6.9: **θ-difference between calculated and measured proton candidate in the laboratory frame.** Shown is the difference for five combinations per preselected event without any further cuts. A peak at $\Delta\theta = 0°$ is seen above combinatorial background in the Monte Carlo simulation ([LEFT]) as well as in the data ([CENTER, RIGHT]). In the data however additional features at $\Delta\theta \approx -30°$ (A) and $\approx -160°$ are visible (B), also pronounced in the random timing background ([CENTER, RED]). These can by identified with a heightened background contribution in the Crystal Barrel caused by leakage from the electron beam dump (A) and $e^{\pm}$-pairs created at the collimator and diverted into the last ring of the Crystal Barrel calorimeter by the sweeping magnet (B). See text, figure 6.10 for details.

the background subtracted data, this time separated for combinations for which the proton candidate was detected in the TAPS (blue) and Crystal Barrel (red) calorimeter. The TAPS calorimeter covers polar angles up to 30°, so the maximum (negative) difference between calculated and measured proton candidate is −30°, from this point on all measured PEDs are detected in the Crystal Barrel. The enhancement in intensity at $\Delta\theta \approx -30°$ in the overall spectrum is therefore not due to a distinct signal but the result of an overall heightened background in the Crystal Barrel. This additional background can be identified with the events caused by leakage of the beam dump mentioned before, as shown in the ϕ-dependence of the polar angle difference in figure 6.10 (c). Figure 6.10 (d) shows the ϕ-distribution of the measured proton candidates in the $\Delta\theta$-region around −160°. Here, additional intensity is visible at $\phi \approx \pm 100°$, responsible for feature B in the projection (fig. 6.10 (b)). A likely explanation for this signature is the production of $e^{\pm}$-pairs by the primary photon beam off the collimators, the positions of which were not exactly determined [Wal10]. Under certain conditions it is possible that such $e^{\pm}$-pairs were deflected by the sweeping magnets (cf. section 4.2.4) in such a way that they could be detected in the innermost ring of the upstream half of the Crystal

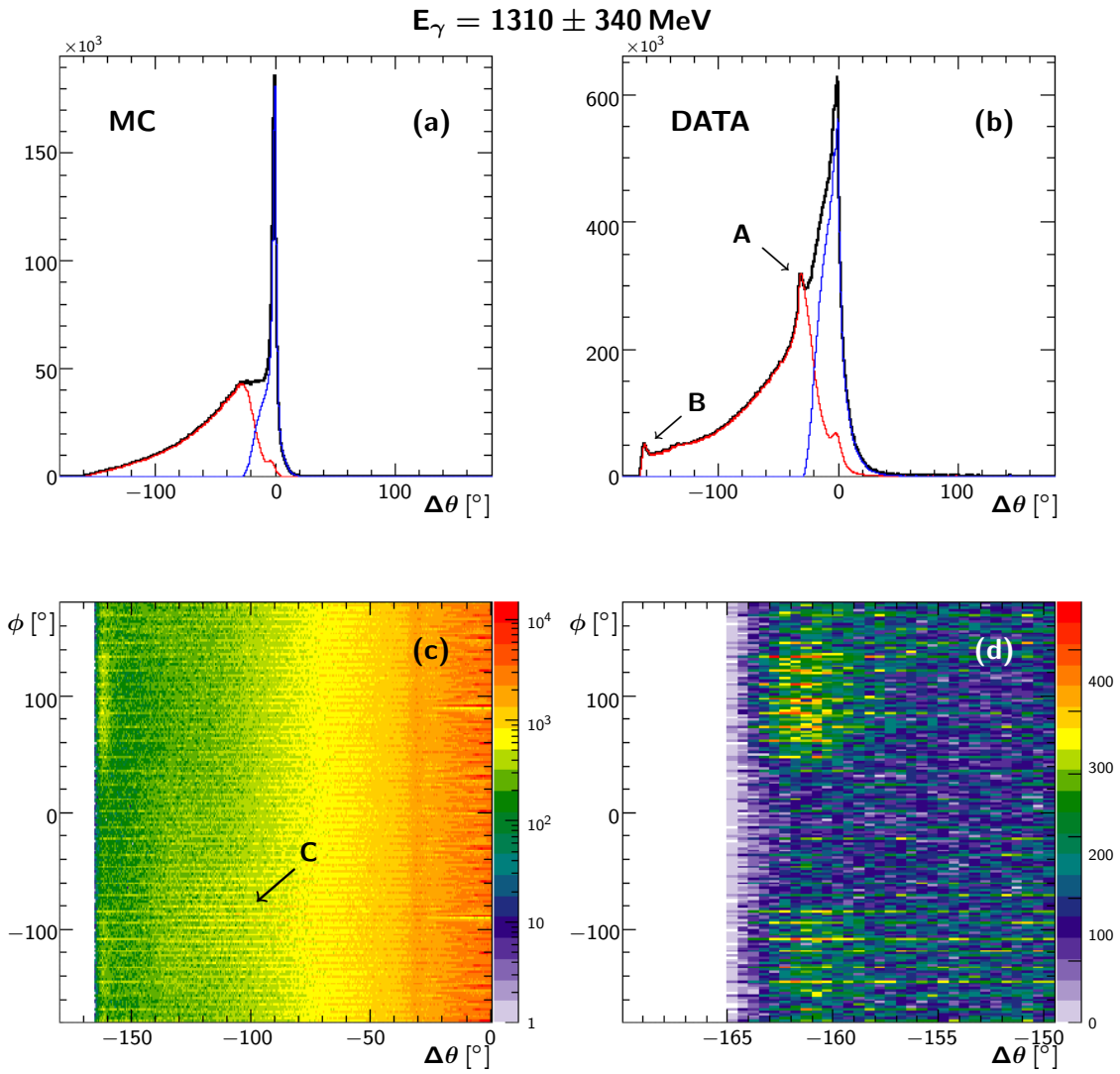

Figure 6.10: **Background features in $\Delta\theta$.** Top row: θ-difference from figure 6.9, separated for combinations with the proton candidate detected in the Crystal Barrel ([RED]) and TAPS ([BLUE]) calorimeter. (a) Monte Carlo simulation, (b) preselected data, after random background subtraction. The signal at $\Delta\theta \approx -30°$ (A) is due to the overall heightened background in the Crystal Barrel calorimeter, due to events stemming from beam dump leakage. (c) ϕ-$\Delta\theta$-distribution for the data. Background events from the beam dump are visible as increased intensity around $\phi = -90°$ (C). (d) Zoom of (c) to the $\Delta\theta$-region of signal B. Regions of increased intensity are visible around $\phi \approx \pm 100°$. Their origin is most likely $e^{\pm}$-pairs created by the primary photon beam off a collimator and bent by the sweeping magnets towards ring 13 of the Crystal Barrel calorimeter [Wal10]. See text for details.

Barrel, ring 13 (see figure 4.10), covering $168^\circ \leq \theta \leq 162^\circ$[6]. Since this background is always present, these hits lead to an enhancement in the $\Delta\theta$-distribution. The separation of these events, however, again poses no problem due to their distinct signature.

6.4.2 Application of the cuts

The determination of the widths of the cuts on the kinematic variables introduced above is an iterative process. Beginning with wide cuts and observing their effects on the according spectra, the cuts are optimized over various iterations until a reasonable signal-to-background ratio is achieved. It is to be kept in mind that the selection process for the data does not end at this point, but the application of a kinematic fit, as described in the next section, further refines the data. Table 6.2 summarizes the cuts

Variable	Fit function	Mean [MeV]	σ [MeV]	Cut width
Missing mass	Gaussian + 3rd order pol.	936.403	31.761	$\pm$123.55 MeV
m($\gamma\gamma$), π^0	Gaussian + 3rd order pol.	135.261	8.640	$\pm$33.61 MeV
m($\gamma\gamma$), η	Gaussian + 1st order pol.	548.159	20.920	$\pm$81.38 MeV
$\Delta\phi$	–	$\pm180^\circ$	–	$\pm10^\circ$
$\Delta\theta$	–	0°	–	$\pm15^\circ$ (CB)
				$\pm5^\circ$ (TAPS)

Table 6.2: **Width of the kinematic cuts.** The cuts on the missing mass and the $\gamma\gamma$ invariant masses have been determined using a fit assuming a Gaussian signal on a polynomial background. The resulting width of the cuts applied is 3.89σ, translating to a net loss of the integrated signal intensity of not more than 10^{-4} (see for example the *Statistics* section in [A$^+$08b]). In case of the angular differences, conservative cuts have been applied derived from the according distributions. The different cuts on $\Delta\theta$ take the different granularity of the calorimeters into account.

finally used in the selection process before applying the kinematic fit. The missing- and invariant mass distributions have been fitted assuming a Gaussian signal and polynomial background. The effective cut width has been set to 3.89 times the σ of the Gaussian. This is consistent with a net loss of signal of not more than 10^{-4} or a confidence interval of 99.99% (see for example the *Statistics* section in [A$^+$08b]). These rather wide cuts

[6] An additional slight tilt of the collimator probably leads to the intensity showing at $\phi \approx \pm100^\circ$ instead of $\pm90^\circ$.

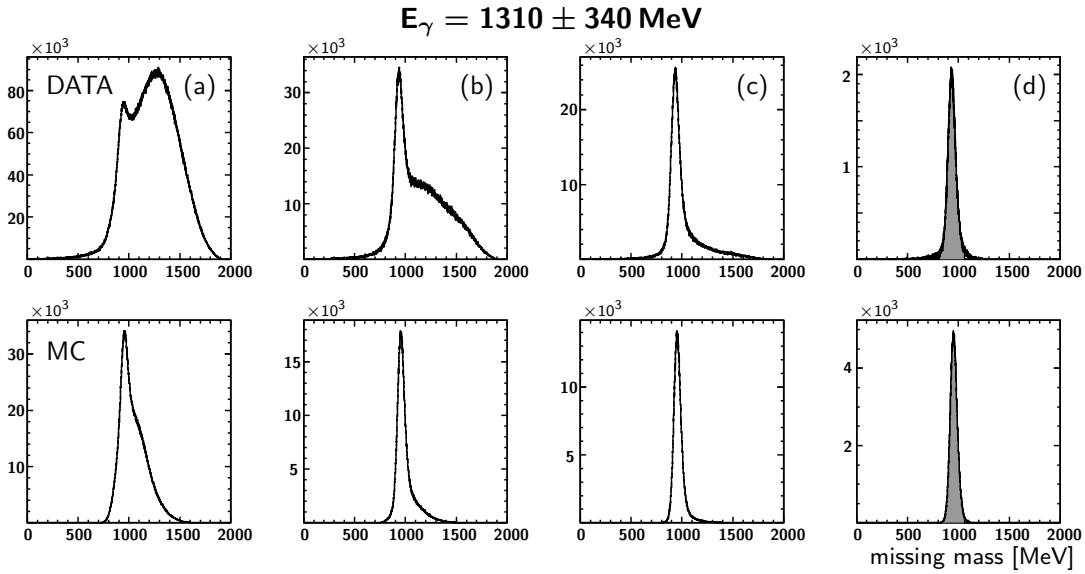

Figure 6.11: **Missing mass after cuts.** Evolution of the missing mass signal after the application of the cuts on the other variables. Top row: Data, bottom row: Monte Carlo. Left to right: Uncut spectrum, after background subtraction (a), cut on $\Delta\theta$ (b), additional cut on $\Delta\phi$ (c), additional cut on the meson masses (d). The shaded area denotes the width of the cut applied on this spectrum. See text for details.

accommodate the fact that the masses enter the kinematic fit applied in the next step as direct constraints.

The cuts on the angular differences between the measured and calculated proton candidate have been fixed in a more conservative manner. Here the cut widths have been estimated such that at least 2σ of the signal is included. In case of the $\Delta\theta$-distribution, the different granularities of the calorimeters have been taken into account by applying separate cuts for proton candidates measured in the Crystal Barrel or in TAPS. The effects of the cuts are shown in figures 6.11-6.16 and described below.

Missing mass spectrum Figure 6.11 shows the evolution of the missing mass distribution after time-background subtraction and the application of the cuts on the other variables introduced above. In the uncut spectrum for the data, only a small signal at the mass of the proton is visible on top of a substantial background (a). This background is greatly reduced by the application of the cut on the θ-difference between the calculated and measured proton candidate for each combination per event (b). This reduction is on the one hand due to the elimination of combinatorial background, as can be seen in comparison to the according Monte Carlo spectrum. Additionally, this

cut eliminates misinterpreted 4-PED events, where a fifth PED is mimicked by the $e^{\pm}$ signals in ring 13 of the Crystal Barrel calorimeter (see figure 6.10), as well as the better part of background due to beam dump leakage (see *Coplanarity* below). A subsequent cut on the ϕ-difference between the 4γ-system and the proton candidate for the remaining combinations again reduces combinatorial background as well as it removes residual events stemming from the beam dump (see figure 6.8). The main effect of the cut on the masses of the final state mesons (d) in the data is a substantial reduction in statistics due to the elimination of the competing reaction $\gamma p \rightarrow p\pi^0\pi^0$, along with a further elimination of combinatorial background. The shaded area in figure 6.11 (d) corresponds to the cut on this spectrum of 3.89σ of the Gaussian signal, translating to $\pm 135.55\,\mathrm{MeV}$, as stated above.

Meson masses Figure 6.12 shows the invariant $\gamma\gamma$-mass of one photon-pair versus the other for all five combinations per event and entered symmetrically, after time-background subtraction (a). In comparison to the Monte Carlo simulation it is to be noted that in the data the signature of $\pi^0\pi^0$-events dominates the spectra, while the simulation only contains $\pi^0\eta$-events. The cuts on the θ- (b) and ϕ-differences (c) mainly just improve the overall signal-to-background ratio for the $\pi^0\pi^0$- and $\pi^0\eta$-events in the data, since the specific background contributions from pair-production and beam bump leakage do not show as prominent features in this spectrum. The final cut on the missing mass (d) then predominantly eliminates background intensity at very low invariant $\gamma\gamma$-masses.
Figures 6.13 and 6.14 show the same distributions, projected over a mass range of 85 MeV to 185 MeV, as denoted by the lines in figure 6.12, for illustration purposes. The width of the cuts on the meson masses is determined from the signal at (m_π, m_η), cut on the width of the π^0 and projected on the η mass range, and vice versa. The resulting widths of the cuts are denoted by the shaded areas and translate to $\pm 33.61\,\mathrm{MeV}$ for the π^0 and ± 81.38 MeV for the η, respectively.

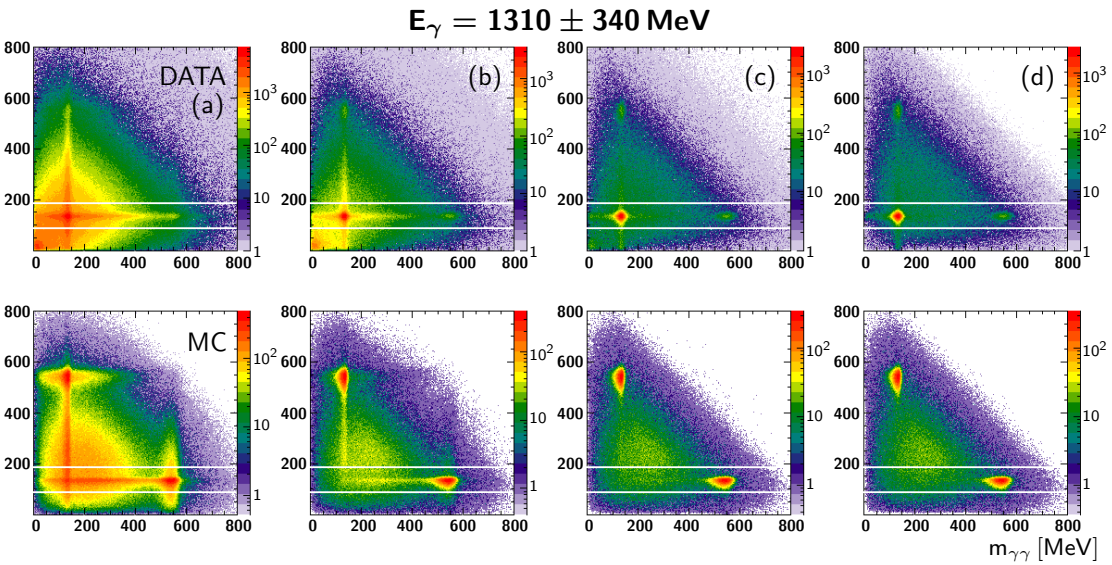

Figure 6.12: **Invariant $\gamma\gamma$-mass after cuts.** Evolution of the invariant $\gamma\gamma$-mass after the application of the cuts on the other variables. Top row: Data, bottom row: Monte Carlo. Left to right: uncut spectrum, after background subtraction (a), cut on $\Delta\theta$ (b), additional cut on $\Delta\phi$ (c), additional cut on the missing mass (d). Lines denote the region used for the projections shown in figures 6.13, 6.14. See text for details.

Coplanarity Figure 6.15 shows the evolution of the ϕ-difference between the 4γ-system and the proton candidate after time-background subtraction (a) and the application of the cuts on the other variables (b - d). The cut on the θ-difference between the calculated and measured proton candidate for each combination per event reduces the combinatorial background considerably (b). It also eliminates most of the events due to beam dump leakage which by definition cannot fulfill coplanarity (see previous section). The additional cut on the missing mass further reduces combinatorics (c) while the cut on the meson masses (d) predominantly reduces statistics due to the removal of the $p\pi^0\pi^0$ final state. For the final cut on the ϕ-difference, a conservative width of $\pm 10°$, as denoted by the shaded areas in figure 6.15 (d), has been chosen. It stands to reason that background contributions in the angular variables influence the result of the kinematic fit more than in case of the masses, which enter the fit as direct constraints (see next section).

The effects of the cuts on the θ-difference between the calculated and measured proton candidate, shown in figure 6.16, are mainly concurrent to what has been stated before in case of the ϕ-difference. Here the cut on $\Delta\phi$ takes the place of the $\Delta\theta$-cut, again eliminating combinatorial background and events stemming from the beam dump. This

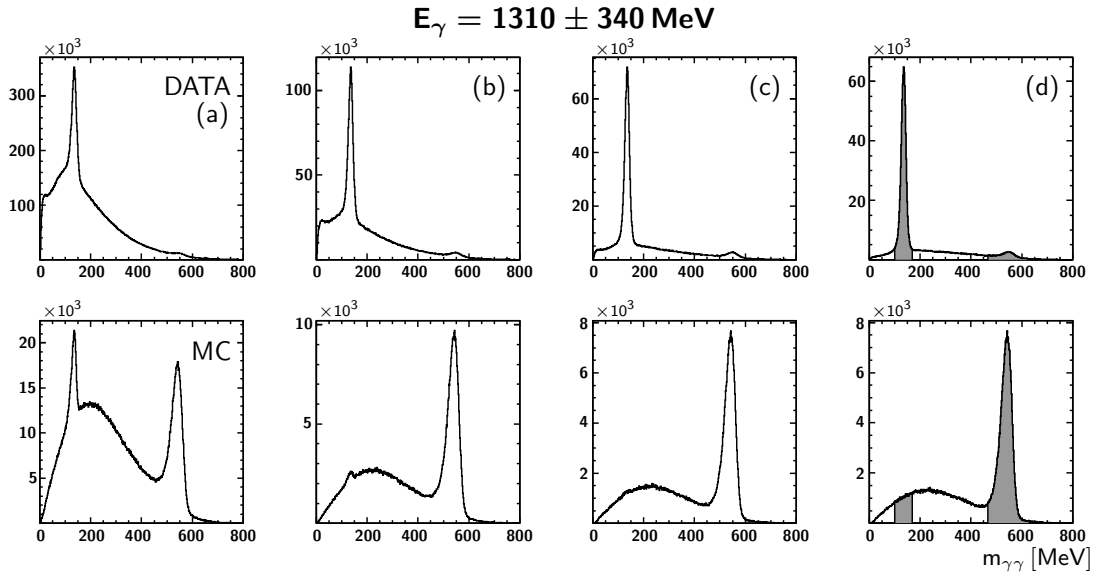

Figure 6.13: **Projection of the invariant $\gamma\gamma$-mass after cuts.** Same as figure 6.12, projected from 85 MeV to 185 MeV. The shaded areas denote the width of the cuts applied on the meson masses. Note that the data at this point is still dominated by the reaction $\gamma p \rightarrow p\pi^0\pi^0$, which is not present in the simulation.

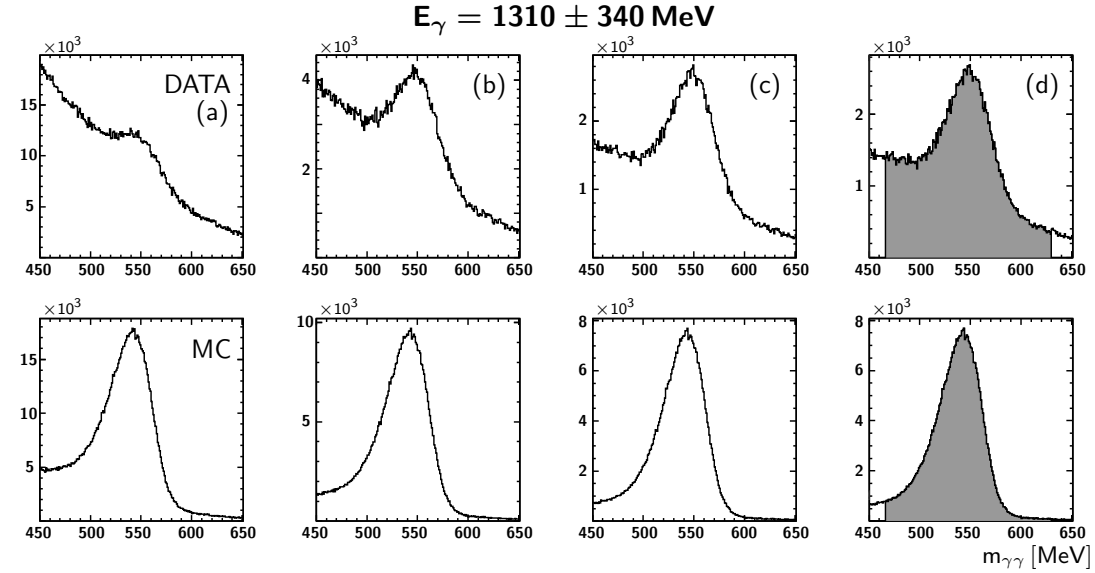

Figure 6.14: ***η*-signal after cuts.** Zoom of figure 6.13 to the η mass region. The shaded area denotes the width of the cut on the η-mass.

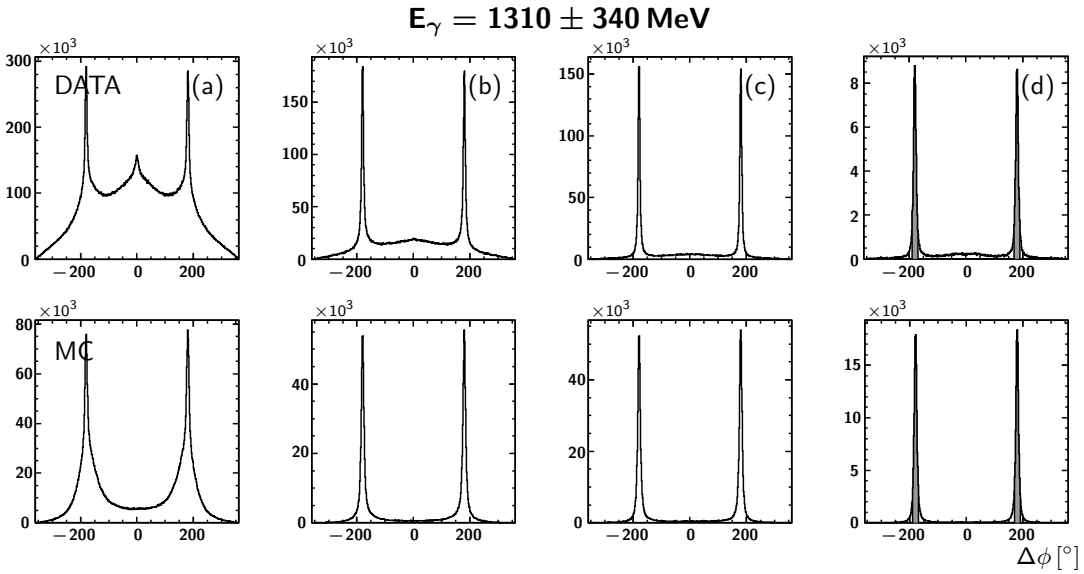

Figure 6.15: **ϕ-difference after cuts.** Evolution of the ϕ-difference between the 4γ-system and the proton candidate after the application of the cuts on the other variables. Top row: Data, bottom row: Monte Carlo. Left to right: uncut spectrum, after background subtraction (a), cut on $\Delta\theta$ (b), additional cut on the missing mass (c), additional cut on the meson masses (d). The shaded regions denote the width of the cuts applied on this spectrum. See text for details.

can clearly be seen in the substantial reduction of background for combinations where the proton candidate has been detected in the Crystal Barrel calorimeter (red distribution in figure 6.16), in accordance with the argumentation stated before. In case of the widths of the cuts on the θ-difference, the different granularities of the calorimeters have to be taken into account. Therefore, and following the same reasoning as for the ϕ-difference, a cut of $\pm 5°$ has been chosen for TAPS (shaded blue in figure 6.16 (d)) and $\pm 15°$ for the Crystal Barrel (shaded red).

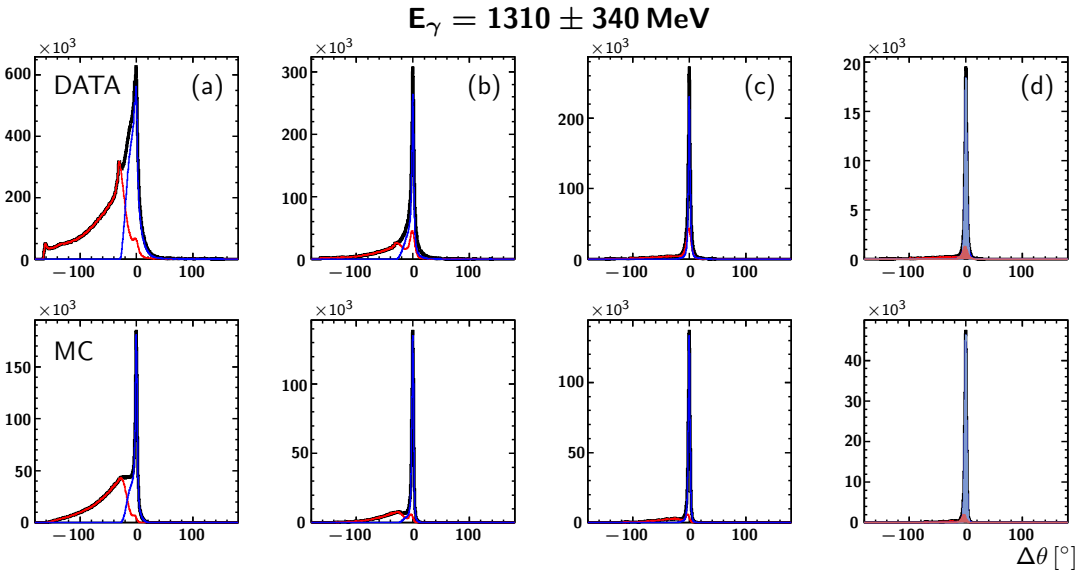

Figure 6.16: **θ-difference after cuts.** Evolution of the θ-difference between the calculated and measured proton candidate in the laboratory frame after the application of the cuts on the other variables. Top row: Data, bottom row: Monte Carlo, both separated for combinations with the proton candidate detected in the Crystal Barrel ([RED]) and TAPS ([BLUE]) calorimeter. Left to right: uncut spectrum, after background subtraction (a), cut on $\Delta\phi$ (b), additional cut on the missing mass (c), additional cut on the meson masses (d). The shaded regions denote the width of the cuts applied on this spectrum. See text for details.

6.5 Kinematic fit

A kinematic fit [vP03] is applied to the data in two steps after the selection of the $\pi^0\eta$ final state by kinematic cuts. The energy- and momentum-values used in the reconstruction and selection are not error-free due to uncertainties given for example by the detector resolution. Therefore, energy-momentum-conservation is in general not fulfilled exactly. The kinematic fit varies the measured quantities within their error margins event by event to achieve energy-momentum-conservation using a χ^2-test. Additionally, it is possible, even after the selection process described above, that more than one combination of four "photons" and one proton candidate per event pass the cuts. This issue is also addressed using the kinematic fit, ascertaining the one combination with the highest probability for further analysis.

6.5.1 Basic principle

The kinematic fit is an event-based, least-squares fit with constraints, using the measured parameters of the reaction, such as the energies and angles of the particles. If n values were measured, this can be written in terms of an n-dimensional vector $\vec{y}$. The measured values differ from the exact ones $\vec{\eta}$ within their error margins $\vec{\epsilon}$:

$$\vec{y} = \vec{\eta} + \vec{\epsilon}. \tag{6.3}$$

The constraints, posed by conservation laws and the known masses of intermediate and final state particles, can be used to calculate r not measured parameters, as long as the number of constraints m is larger or equal to the number of unmeasured quantities. Let $\vec{x}$ be the r-dimensional vector of parameters to be calculated. Then the m conservation laws can be written in the form:

$$f_{1\ldots m}(\vec{x}, \vec{\eta}) = f_{1\ldots m}(\vec{x}, \vec{y} - \vec{\epsilon}) = 0. \tag{6.4}$$

Here the estimated error margins $\vec{\epsilon}$, in which the measured values are allowed to vary, are an input to the fit. The set of constraints is referred to as the *hypothesis* of the fit. Solutions for $\vec{x}$ and $\vec{y}$ are those values, for which

$$M = \vec{\epsilon}^T C_y^{-1} \vec{\epsilon} \tag{6.5}$$

is minimal, while the constraints are fulfilled exactly. Here C_y is the covariance matrix of the measured quantities. The resulting values for M follow a χ^2-distribution $f(\chi^2)$

with $m - r$ degrees of freedom.
If no systematic errors in the measured values are present, the difference between the measured and the fitted values should form a distribution centered at zero, since the fit will just as likely increase a specific value as decrease it. A systematic error, not accounted for in the error margins handed to the fit, will cause a shift in the distribution to either positive or negative values. A normalization of this distribution to the error should result in a Gaussian distribution with $\sigma = 1$. Such a distribution is called the *pull* of a measured quantity y_i:

$$pull(y_i) = \frac{\eta_i - y_i}{\sqrt{\sigma^2(\eta_i) - \sigma^2(y_i)}}. \tag{6.6}$$

Any deviation of these pulls from $\sigma = 1$ points towards a wrong estimation of the errors passed to the fit. A narrower distribution means that the fit did not use the full range of the error margins passed to it, the errors have been estimated too high. Analogously, errors which are too small lead to a broader distribution. Figure 6.17 shows such pull-distributions using the example of the $\gamma p \to x p\, n\gamma$ hypothesis. The *xp* denotes a *missing proton*-fit, meaning the proton is treated as a not measured particle, consistent with the selection criteria described before. Without any further mass-constraints this constitutes a fit using four constraints from energy- and momentum-conservation. The coordinate system used for the kinematic fit is based on the energy, and the polar and azimuthal angles of the particles, $(\sqrt{E}, \theta, \phi)$[7], leading to three unmeasured quantities for the final state proton. This is called a one-constraint (1C) fit. The errors for the measured quantities are estimated for the incoming beam photon and the final state photons, dependent on the calorimeter in which they were detected. These errors have to be estimated for each hypothesis, for data and Monte Carlo, independently in an iterative process. The distributions shown in figure 6.17 fulfill the requisites stated above, suggesting a correct estimation and no systematic effects.
A means to quantify the quality of the fit bases on the fact that the minimized quantity M in (6.5) follows a χ^2-distribution. If all errors are properly estimated and no systematic effects are present, $f(\chi^2)$ should follow the standard χ^2-distribution $f_{st}(\chi^2)$, obtained by adding $m - r$ Gaussians with $\mu = 0$ and $\sigma = 1$. The distribution for events that do not fulfill the requirements imposed by the constraints will peak at higher or lower $f(\chi^2)$ values than $f_{st}(\chi^2)$. In practice, the quantity used for control purposes is

[7] Previous investigations have shown that using the square root of the energy leads to a better description of the errors in terms of a Gaussian distribution than using the energy linearly [vP03].

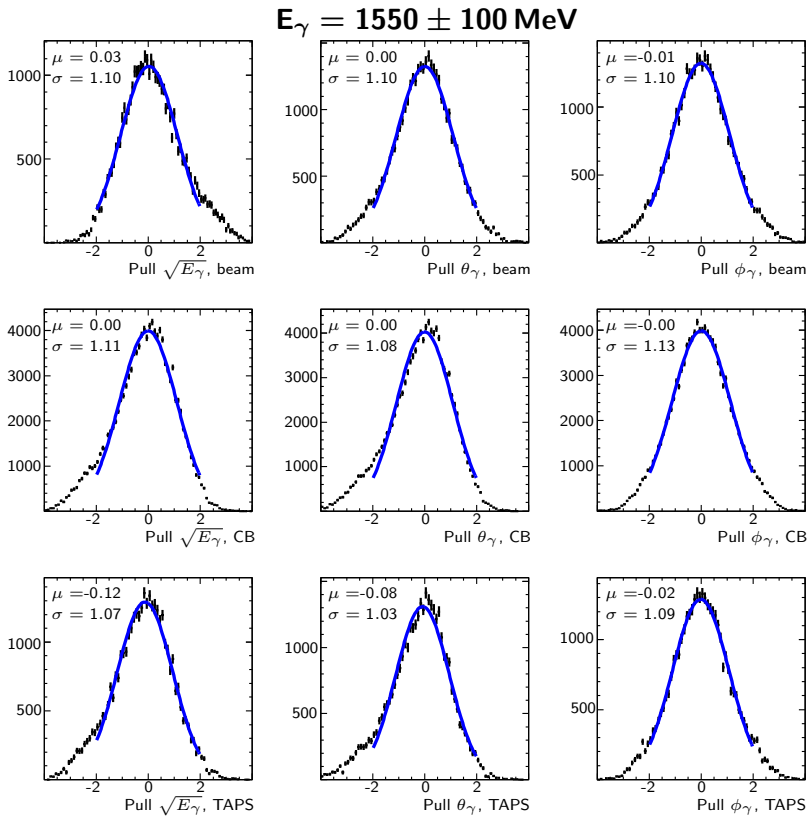

Figure 6.17: **Pull-distributions for the hypothesis $\gamma p \rightarrow xp\ n\gamma$, data.** Top to bottom: Pull distributions for the incoming photon, photons in the Crystal Barrel calorimeter, photons in TAPS. Left to right: Pull distribution for $\sqrt{E_\gamma}$, θ_γ, ϕ_γ. Blue line: Gaussian fit from -2 to 2. Mean and standard deviation of the fit are given in each panel.

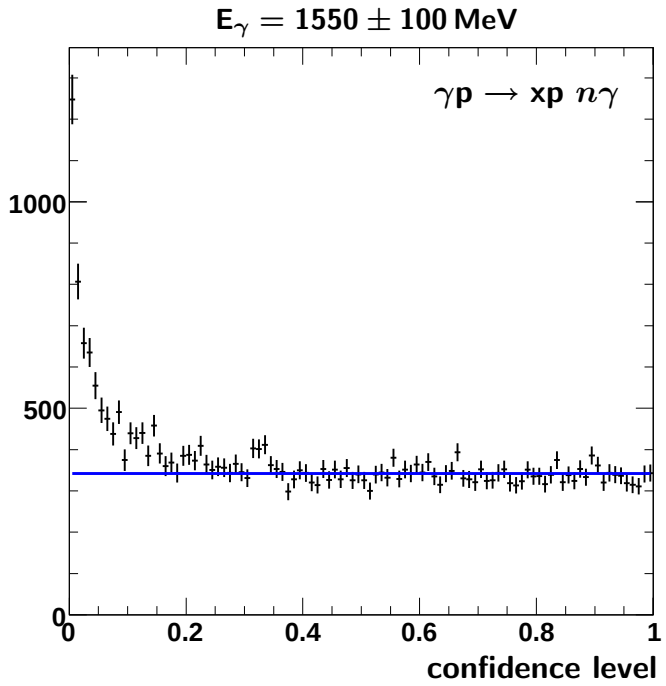

Figure 6.18: **CL-distribution for the hypothesis $\gamma p \rightarrow xp\ n\gamma$, data.** Blue line: Constant fit from 0.2 to 1. The peaking of the distribution towards low probabilities is due to background events not fulfilling the constraints posed by the hypothesis.

the *confidence level* (CL), a function varying between 0 and 1:

$$CL = 1 - \left(\int_0^{\chi^2} f_{st}(\chi^2) d\chi^2 \right). \tag{6.7}$$

The distribution function $f(CL) = f(\chi^2)/f_{st}(\chi^2)$ should accordingly be flat, if the measured values are distributed according to a Gaussian distribution around the fitted values and the input errors have been estimated correctly. It is however safe to assume that background events result in much higher χ^2- and therefore lower CL-values than events fulfilling the constraints. Therefore a cut on the confidence level, selecting events above a certain CL-value, can be used to dramatically reduce the background with little loss of good events. Figure 6.18 shows the confidence level distribution for events subjected to the $\gamma p \rightarrow xp\ n\gamma$ 1C-fit described before. The flat distribution of probabilities again demonstrates the correct estimation of the errors, as visualized by a constant fit, using a fit range from 0.2 to 1. As stated above, background events which do not fulfill the constraints posed by the hypothesis cause a steep rise of the distribution towards low

probabilities. In the given example, a cut on $CL > 0.1$ would eliminate nearly all of the background events but would only lead to a loss of 10% of the valid events.

6.5.2 Application to the data

In the given analysis, the data and the Monte Carlo simulation have been subjected to four differently constrained fit hypotheses:

$$\begin{aligned} \gamma p &\rightarrow xp4\gamma \text{ (1C)} \\ \gamma p &\rightarrow xp\pi^0\gamma\gamma \text{ (2C)} \\ \gamma p &\rightarrow xp\pi^0\eta \text{ (3C)} \\ \gamma p &\rightarrow xp\pi^0\pi^0 \text{ (3C).} \end{aligned} \tag{6.8}$$

The first two hypotheses are tested just for control purposes, seeing that the two three-constraint hypotheses include both the energy-momentum-balance and the π^0 mass-constraint[8].
In a first step, the problem of multiple combinations per event passing the kinematic cuts is addressed by subjecting the selected data sample to the $\gamma p \rightarrow xp\pi^0\eta$-fit. Here the only condition to be met is the convergence of the fit. Should an event enter the fit more than once, due to ambiguities in the proton determination, only that combination with the highest probability (confidence level, CL) is retained. This way all residual combinatorial background in the event sample is eliminated.
In the next step the cleaned event sample is subjected to the fit hypotheses given in (6.8). The events that are to be retained for the final extraction of the observables have to exceed a probability of 10^{-2}% in case of the 1C-fit and 8% in case of the 2C-$\pi^0\gamma\gamma$-fit. As stated before, these cuts however pose no real restriction with respect to the results. Regarding the hypotheses imposing two meson mass-constraints, it is in general possible that a given event is identified both as a $p\pi^0\eta$ and a $p\pi^0\pi^0$ final state. Therefore a naive cut on just the confidence level of the $xp\pi^0\eta$ hypothesis might leave a contamination by events passing the $xp\pi^0\eta$ hypothesis with a high probability. Figure 6.19 shows the according confidence levels in a two-dimensional histogram for an incoming photon energy range of $E_\gamma = 1325 \pm 125\, MeV$, confirming this assumption. Both in the Monte Carlo simulation and especially in the data, events with high probabilities for both hypotheses are observed. Therefore, to avoid the contamination of the final sample

[8] It is possible that the hypothesis including both meson mass constraints selects different final state photons for the π^0 than the $\pi^0\gamma\gamma$ hypothesis. This does, however, not pose a problem with respect to the assessment of the statistics and background contamination of the final event sample.

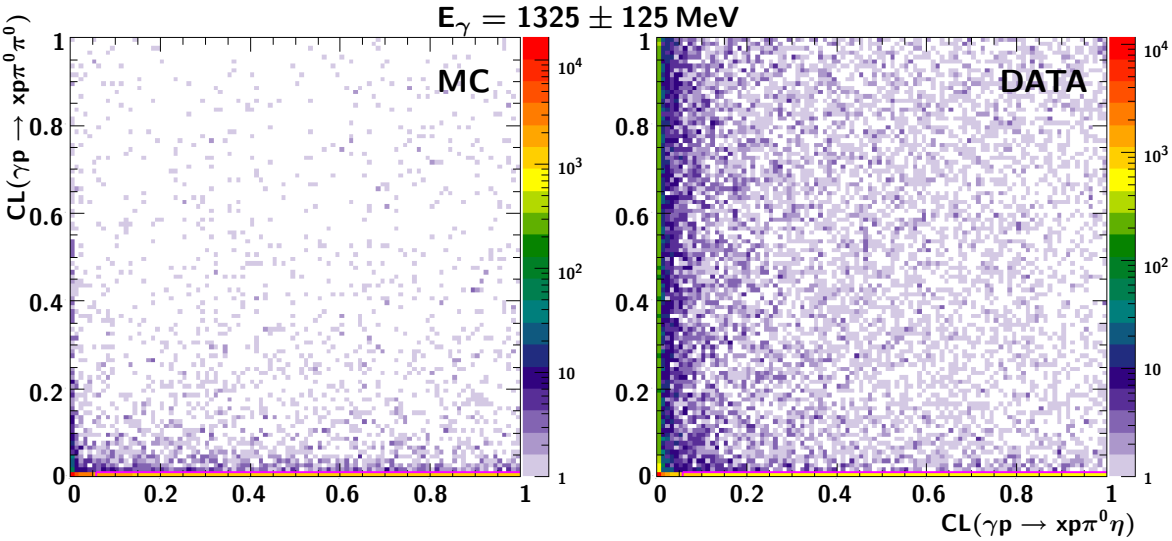

Figure 6.19: **Confidence levels of the three-constraint fit hypotheses, 2D.** Shown is the confidence level distribution for the $\gamma p \to x p \pi^0 \pi^0$ hypothesis versus the distribution for the $\gamma p \to x p \pi^0 \eta$ hypothesis for the Monte Carlo simulation ([LEFT]) and the data ([RIGHT]). Magenta lines denote the cuts on the respective CLs of < 0.01 for the $\pi^0\pi^0$ hypothesis and > 0.06 for the $\pi^0\eta$ hypothesis (see also figure 6.20). See text for details.

by probable $\pi^0\pi^0$-events, the following cuts on the confidence levels have been chosen, denoted by the magenta lines in figure 6.19 and the shaded areas in figure 6.20:

$$\begin{aligned} \mathrm{CL}(\gamma p \to x p \pi^0 \eta) &> 6\% \\ \mathrm{CL}(\gamma p \to x p \pi^0 \pi^0) &< 1\%. \end{aligned} \tag{6.9}$$

This is also illustrated in figure 6.20, showing the one-dimensional confidence level distributions for the respective hypotheses. Here the shaded areas denote the probabilities that have to be met by events to be retained. Note that while the Monte Carlo sample consists solely of simulated $p\pi^0\eta$-events, $p\pi^0\pi^0$-probabilities up to 100% occur. In the final step, a cross-check between the reconstruction and the kinematic fit is performed by comparing the direction of the proton identified using the kinematic cuts described before and the direction of the proton resulting from the kinematic fit, imposing the $\gamma p \to x p \pi^0 \eta$ hypothesis, for events passing the confidence level cuts. This is done by calculating the azimuthal and polar angle-difference between the respective fourvectors, as shown in figure 6.21. In case of the θ-difference, this check is again performed independently for protons detected in the Crystal Barrel or TAPS calorimeter.

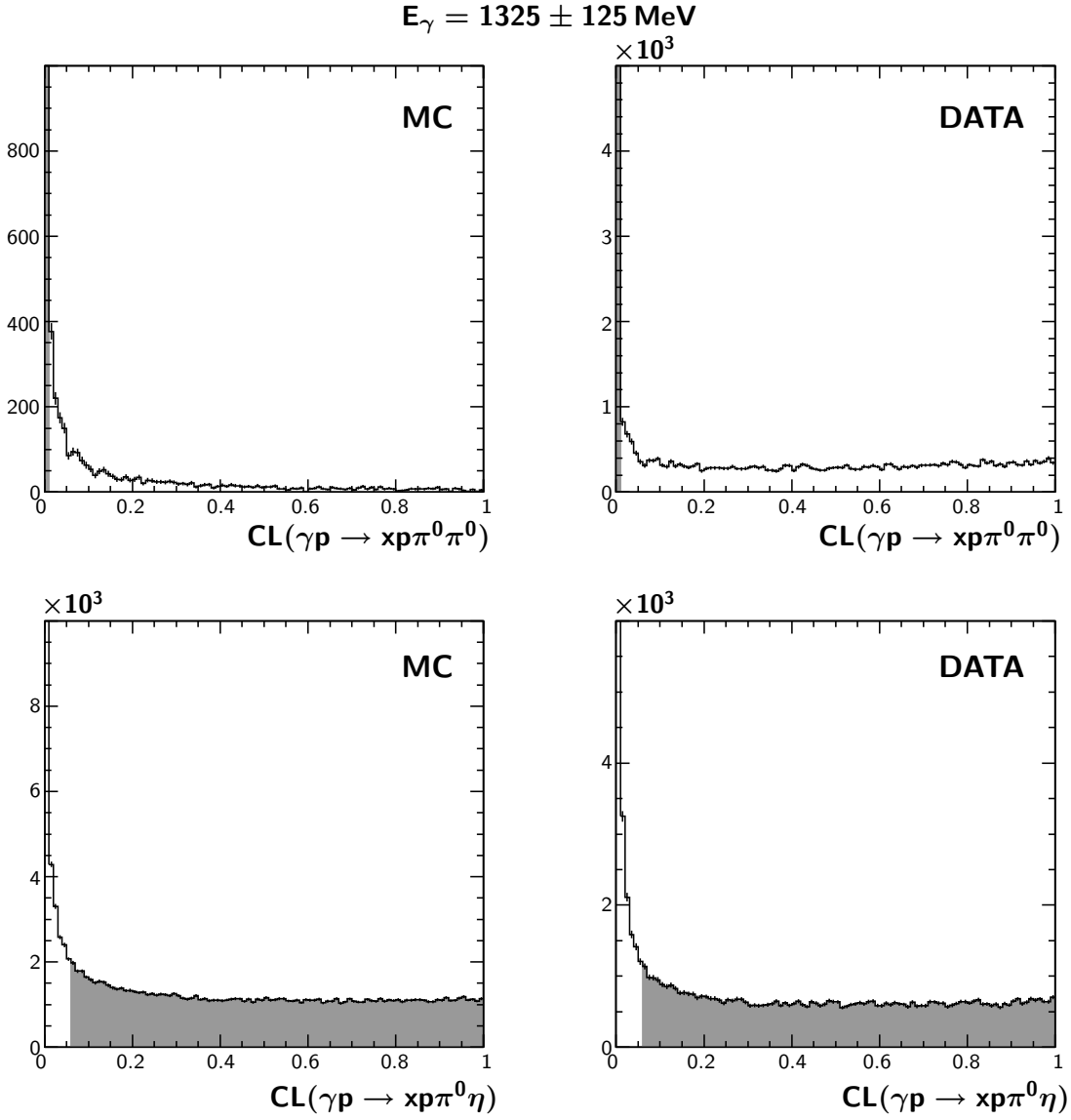

Figure 6.20: **Confidence levels of the three-constraint fit hypotheses, 1D.** Shown are the confidence level distributions for the $\gamma p \rightarrow xp\pi^0\pi^0$- ([TOP]) and the $\gamma p \rightarrow xp\pi^0\eta$ hypothesis ([BOTTOM]) for the Monte Carlo simulation ([LEFT]) and the data ([RIGHT]). Shaded areas denote the probabilities which have to be met by each event to be retained for further analysis.

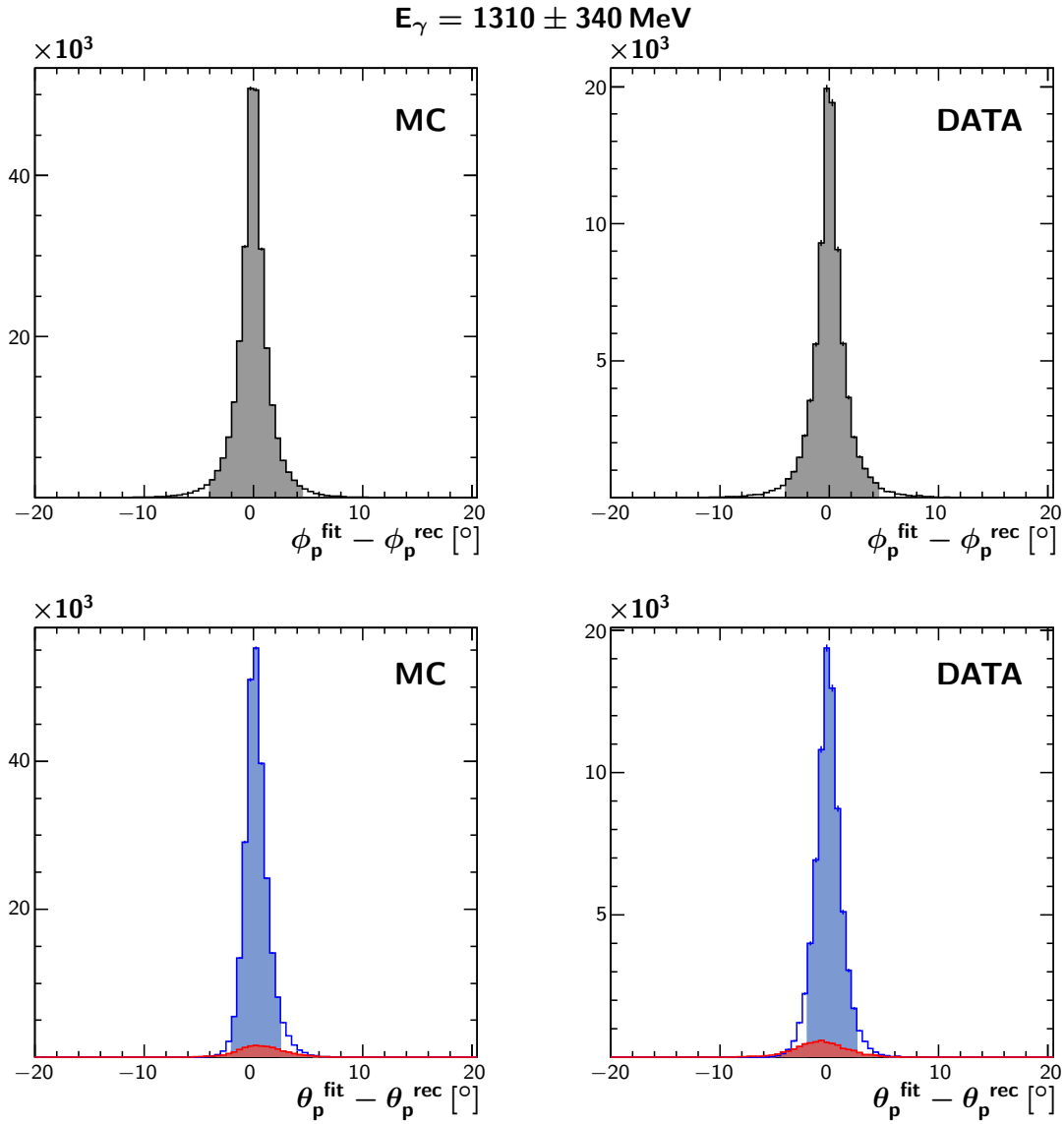

Figure 6.21: **Matching of fitted and reconstructed proton.** Shown are the differences in the azimuthal ([TOP]) and polar angle ([BOTTOM]) between the particle identified as proton using kinematic cuts and using the kinematic fit for the Monte Carlo simulation ([LEFT]) and the data ([RIGHT]). In case of the θ-difference, the distributions are separated for particles detected in the Crystal Barrel ([RED]) and TAPS ([BLUE]) calorimeter. The shaded areas denote the width of the cuts applied. See text for details.

In general, much narrower distributions are obtained than when comparing measured and calculated proton candidates during the determination of the kinematic cuts (cf. figures 6.15, 6.16). The distributions however do exhibit tails towards higher angular

differences, corresponding to events for which the kinematic fit had to overly adjust the proton direction. While this is perfectly within the margins passed to the fit, it might point towards a mismatch between the reconstruction and the fit which, especially with respect to the extraction of asymmetries in the ϕ-distributions of the final state particles, can affect the results. Therefore, following the reasoning presented for the application of the cuts on the angular differences between the measured and the calculated proton before, the following cuts, denoted by the shaded areas in figure 6.21:

$$\begin{aligned} \Delta\phi &= 0^\circ \pm 4^\circ \\ \Delta\theta_{\text{ CB}} &= 0^\circ \pm 5^\circ \\ \Delta\theta_{\text{ TAPS}} &= 0^\circ \pm 2^\circ. \end{aligned} \tag{6.10}$$

For the final assessment of the background contamination of the event sample used for the extraction of the observables described in the next chapter, the invariant mass of the two free photons from the $\gamma\text{p} \rightarrow \text{xp}\pi^0\gamma\gamma$ fit in the η mass range is studied. Figure 6.22 shows the according distribution for the incoming photon energy range $E_\gamma = 1310 \pm 340\,\text{MeV}$ after the application of all cuts mentioned before with the exception of the cut on the confidence level of the $\gamma\text{p} \rightarrow \text{xp}\pi^0\eta$ fit. A fit assuming a Gaussian signal on a linear background leads to a total of 68,514 (226,249) events in the data (Monte Carlo), including background, translating to a signal-to-background ratio of 17.5 : 1 (18.9 : 1) in a mass range of $m_\eta \pm 3.89\sigma$. The cut on the $\pi^0\eta$ confidence level rejects 3083 (9856) of these events, leading to a final background contamination of 624 (1516) events or 0.95% (0.99%).

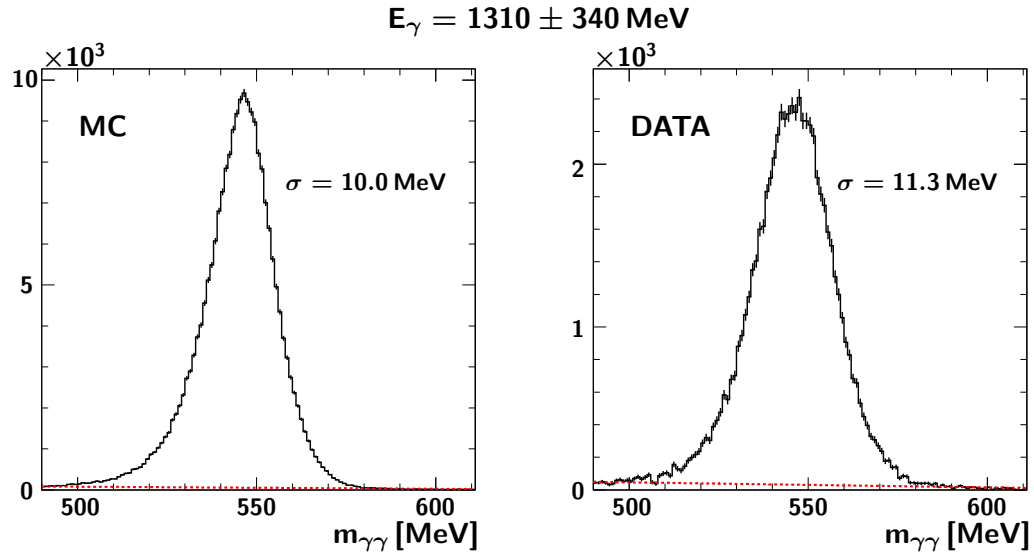

Figure 6.22: ***η*-signal after the kinematic fit.** Invariant mass of the free $\gamma\gamma$-pair after the $\gamma p \rightarrow xp\pi^0\gamma\gamma$ (CL $> 8\%$) fit. A cut on the confidence level of the $\gamma p \rightarrow xp\pi^0\pi^0$ (CL $< 1\%$) fit is applied, as well as on the reconstructed and fitted proton direction. This yields a total number of 68514 (226249) events including the linear background (dashed line) for the data (Monte Carlo). An additional cut on the $\gamma p \rightarrow p\pi^0\eta$ fit (CL $> 6\%$) rejects 3083 (9856) events, retaining 624 (1516) background events ($\approx 1\%$).

7 Results

In the previous chapters the process of selecting the $p\pi^0\eta$ final state from raw information obtained with the Crystal Barrel/TAPS experiment has been introduced. In this chapter the extraction of polarization observables from this data will be described and the obtained beam asymmetries Σ, I^c and I^s will be presented. The latter two observables have been extracted for the first time in the framework of this analysis. This has been done, using a full three-body approach never before utilized in linearly polarized photoproduction data.
Additionally, invariant mass distributions and Dalitz plots will be presented, illustrating the various physics contributions to the data, later addressed in chapter 8 in the context of different theoretical frameworks.

7.1 Polarization observables in quasi two-body kinematics

Prior to the analysis presented in this work, the only polarization observable investigated in the photoproduction of non-strange pseudoscalar mesons using linearly polarized photons and an unpolarized target was the beam asymmetry Σ. While this observable already occurs in single meson production (see for example [E^+07, E^+09]), it is also accessible in meson-pair production by restricting the kinematics to a quasi two-body final state (for example [A^+08a, $GSvP^+08$]). This is achieved by adding two of the three fourvectors of the final state particles. For the $p\pi^0\eta$ final state this translates to the three quasi two-body reactions:

$$\begin{aligned}
\gamma p &\rightarrow pX, \text{ with } X \rightarrow \pi^0\eta, \\
\gamma p &\rightarrow \eta Y, \text{ with } Y \rightarrow p\pi^0, \\
\gamma p &\rightarrow \pi^0 Z, \text{ with } Z \rightarrow p\eta.
\end{aligned}$$

The cross section for such two-body final states can be written as [Wor72]:

$$\frac{d\sigma}{d\Omega} = \left(\frac{d\sigma}{d\Omega}\right)_0 (1 + \delta_l \Sigma \cos 2\phi), \tag{7.1}$$

where $\left(\frac{d\sigma}{d\Omega}\right)_0$ is the unpolarized cross section and δ_l the degree of linear polarization. In this work the angle ϕ is defined as depicted in figure 7.1. Two planes are relevant for

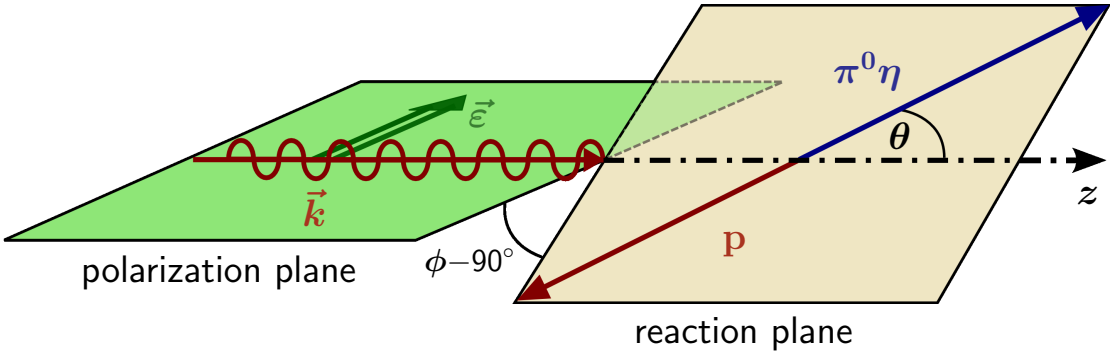

Figure 7.1: **Angle definitions in the quasi two-body approach.** The relevant planes in the center-of-momentum frame are spanned by the incoming photon $\vec{k}$ and its polarization vector $\vec{\varepsilon}$ (polarization plane) and by the incoming photon and one of the final state particles recoiling against the remaining two-particle system, respectively (reaction plane). ϕ is the angle of the reaction plane with respect to the normal of the polarization plane, θ is measured against the z-axis defined by the incoming photon direction.

the kinematics of the process in the center-of-momentum frame, the polarization plane spanned by the incoming photon and its polarization vector and the reaction plane spanned by the incoming photon and one of the final state particles recoiling against the combination of the other two. In this framework, ϕ is the azimuthal angle of the reaction plane with respect to the normal to the polarization plane.

The unpolarized cross section is independent of the azimuthal angle, so according to (7.1), the ϕ-distribution of any final state particle should exhibit a $\cos 2\phi$-modulation on top of a flat, unpolarized contribution. The amplitude of the modulation is then given by the degree of polarization and the beam asymmetry Σ. Such a ϕ-distribution, using the example of the final state π^0, recoiling against the pη-system, is depicted in figure 7.2. The ϕ-distribution is shown in five bins in $\cos\theta_\pi$, and also integrated over all $\cos\theta_\pi$ for the energy range $E_\gamma = 1325 \pm 125\,\text{MeV}$. The full set of ϕ-distributions is given in appendix B.

A distinct $\cos 2\phi$-modulation is visible over the full range. The distributions were fitted according to the cross section given in (7.1) with the expression:

$$f(\phi) = A + P \cdot B \cdot \cos 2\phi. \tag{7.2}$$

The polarization degree is determined for each event individually, using a modified version of the ANalytic Bremsstrahlungs Calculation software ANB [NGH+03]. This pack-

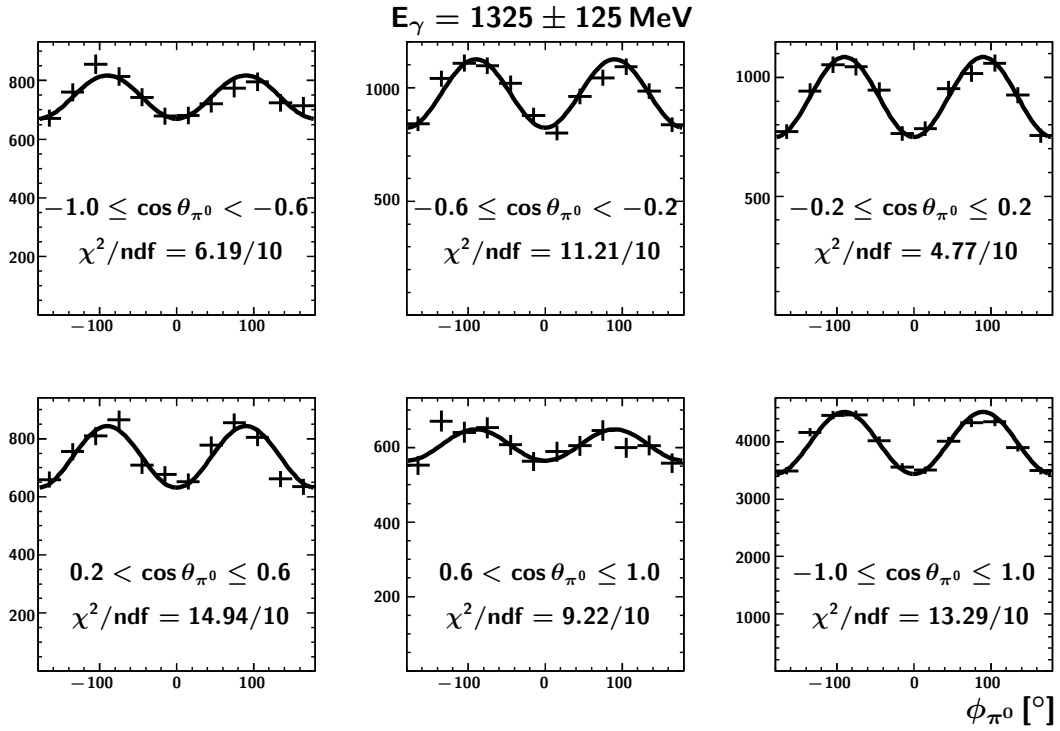

Figure 7.2: **ϕ-distributions for the final state π^0.** Shown are the ϕ-distributions with respect to the final state π^0 recoiling against the pη-system in the energy range $E_\gamma = 1325 \pm 125\,\mathrm{MeV}$ for five bins in $\cos\theta_{\pi^0}$ along with the spectrum integrated over all $\cos\theta$. The data is not polarization-weighted. Solid line: Fit according to (7.2).

age, developed at the university of Tübingen, calculates the photon polarization based on a parametrization of the properties of the incoming electron beam, type, orientation, thickness, and temperature of the radiator as well as collimation. The analytical results are in excellent agreement with the experimental data (see figure 4.5). For a more detailed description see [Els07].

In the analysis, each histogram used for the extraction of the beam asymmetry, for example ϕ versus $\cos\theta$, is filled twice, once with the polarization as weight and once without. For each $\cos\theta$-bin, both distributions are then integrated over ϕ and the ratio of the integrals enters the fit (7.2) as the average polarization P. The ratio of the fit-parameters B/A then translates to the beam asymmetry Σ and is shown in figure 7.4 for the three energy ranges under consideration and all three final state particles. Asymmetries of the order of 50% and higher can be observed as well as distinct differences in the sign of the asymmetry in case of the η recoiling compared to the proton and π^0, respectively.

Figure 7.6 shows again the beam asymmetry Σ, determined in the same way as described, but for each recoiling particle as a function of the invariant mass of the other two particles. Similar features as stated above are apparent, along with a distinct energy-dependence, especially noticeable in the $p\pi^0$ invariant mass. Asymmetry data for the $p\pi^0\eta$ final state as function of invariant masses has also been measured by the GRAAL collaboration [A$^+$08a] and is in good agreement with the results presented here. In their work however a finer energy binning was used which, applied to this analysis, leads to a substantial increase in the statistical error. The according distributions are shown in chapter 8 together with the data published by the GRAAL collaboration.
Detection efficiencies should not influence the result since they cancel out in the asymmetry determination using the method described above, assuming a phase space binning reasonably small compared to variations in efficiency. Yet, due to geometrical limitations present in every experimental setup, the phase space is not covered completely, leading to areas of vanishing acceptance. Attempts at a full acceptance correction of the data using the ratio of reconstructed and generated Monte Carlo events failed due to the amount of diskspace and computing power necessary to cover the five-dimensional phasespace with sufficient statistics and in a reasonable binning (see [Sok10] for details). Two different methods have been applied to the data, however, to estimate the influence of acceptance variations and other systematic effects on the results. In a first step, the two-dimensional acceptance has been determined for the three energy ranges separately as function of ϕ of the recoiling particle and the variable intended for binning the polarization observable. The data has been corrected for this acceptance, determining the resulting change in the observables for each bin. Figure 7.3 shows this acceptance using $\cos\theta$ of the respective recoiling particle as the second variable. The absolute value of the change in Σ due to the correction of the data for this acceptance is shown in figure 7.4 as blue bars. The same has been done using the invariant mass of the respective two-body system the particle is recoiling against as the second variable. The according acceptances are shown in figure 7.5, and the influence on the observables in figure 7.6.
In the second step, the Bonn-Gatchina partial wave analysis, described in the next chapter, has been implemented. Here, the lack of statistics for a five-dimensional determination of the acceptance is treated by extrapolating into the uncovered regions using the predictions of the PWA solution. A weighting factor, derived from the solution for each phasespace bin, similar to the procedure derived in [Fuc05], is applied to generated and reconstructed Monte Carlo events. The resulting five-dimensional distributions are then, binned in energy and for example $\cos\theta$, integrated and normalized to the number of events, resulting in a one-dimensional ϕ-distribution from which the polarization observables are extracted. In the case of the generated Monte Carlo set the obtained

distributions represent the original prediction from the PWA solution, and the results derived from the reconstructed set are additionally convoluted with the geometrical acceptance and detection efficiencies of the experiment. Here again the differences in terms of the observables are calculated and their absolute value entered as the red bars in figures 7.4, 7.6.
In both cases, the obtained estimates for the systematic uncertainties due to the acceptance and detection efficiency of the experiment and the reconstruction are comparable to or less than the statistical errors. Larger deviations are only seen for the systematics derived using the two-dimensional acceptance correction in the invariant mass binning. This is due to the strongly varying statistics over the given mass ranges, as can be seen in the invariant mass distributions shown in section 7.3.1.

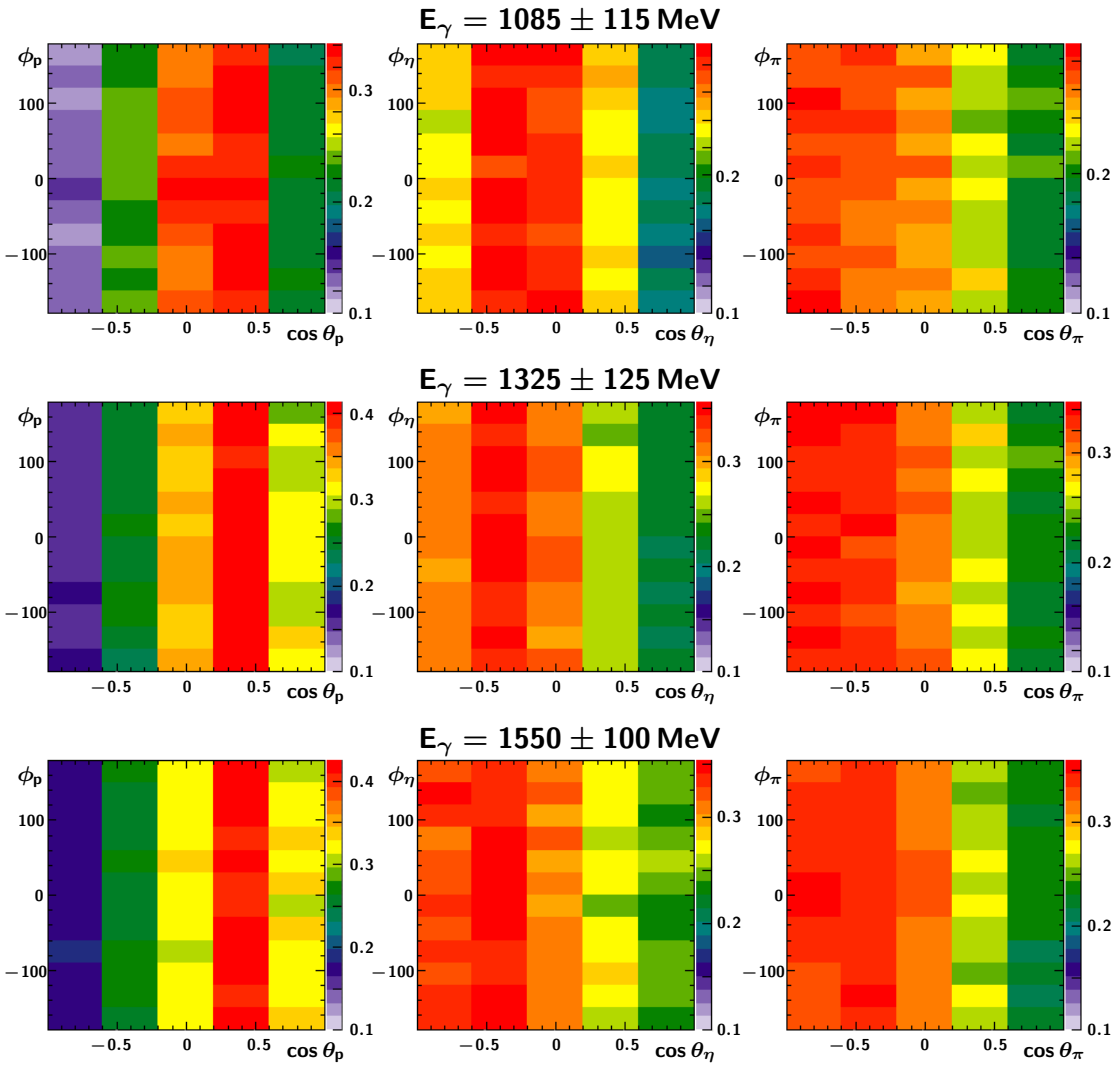

Figure 7.3: **Acceptance, ϕ versus $\cos\theta$.** Shown are the ratios of reconstructed to generated Monte Carlo events, binned in the azimuthal angle ϕ and $\cos\theta$ of each of the three recoiling particles (left to right: p, η, π^0) for the three energy ranges used for the extraction of the polarization observables (top to bottom).

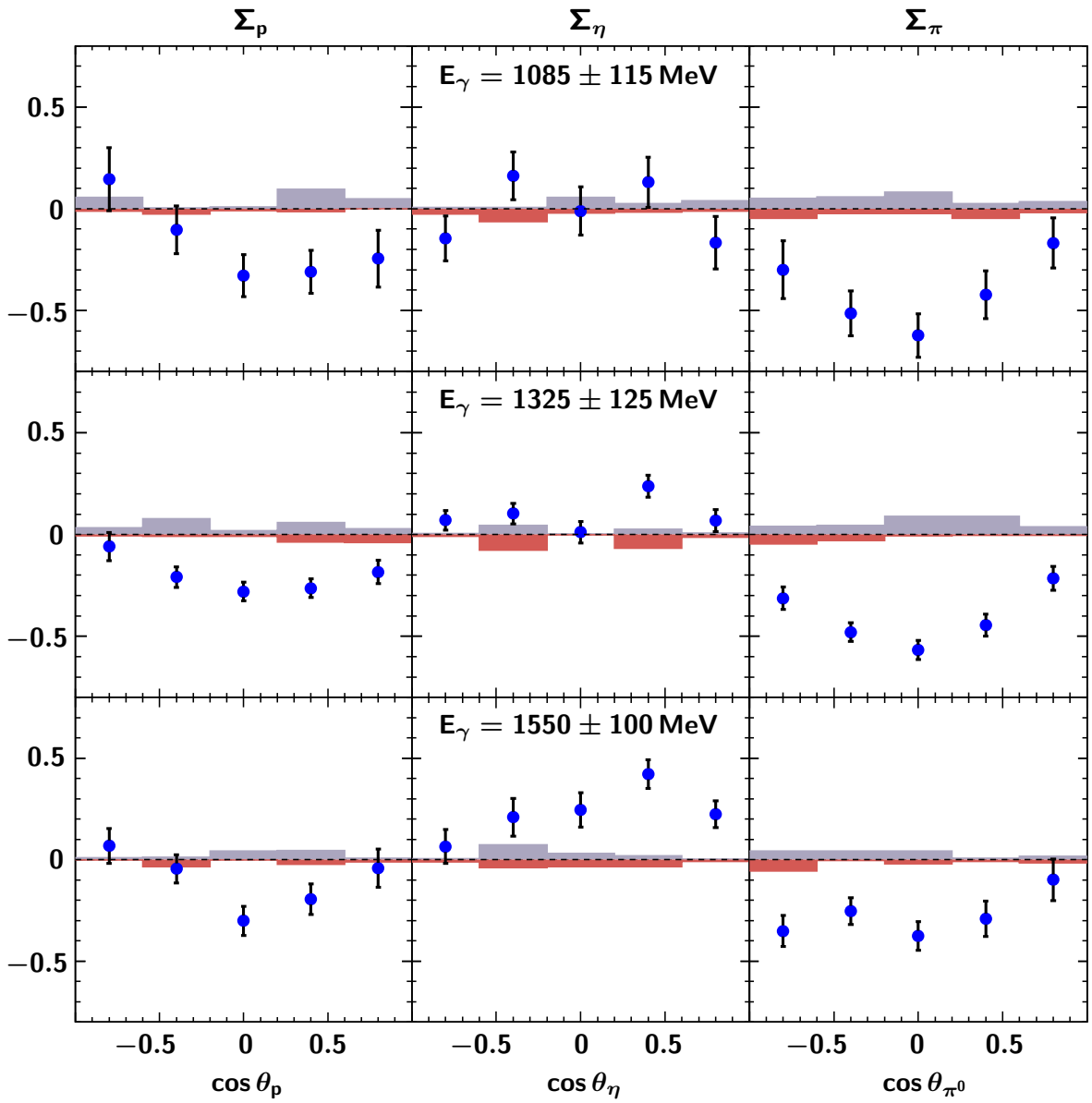

Figure 7.4: **Beam asymmetry Σ as function of $\cos\theta$.** Left to right: Beam asymmetries derived from the ϕ-distribution of the final state proton, η, and π^0, respectively, as functions of the corresponding $\cos\theta$ in the center-of-momentum frame (see figure 7.1). Bar graphs represent the systematic error estimate derived from acceptance correction ([BLUE], positive) and PWA phasespace-weighting ([RED], negative). See text for details.

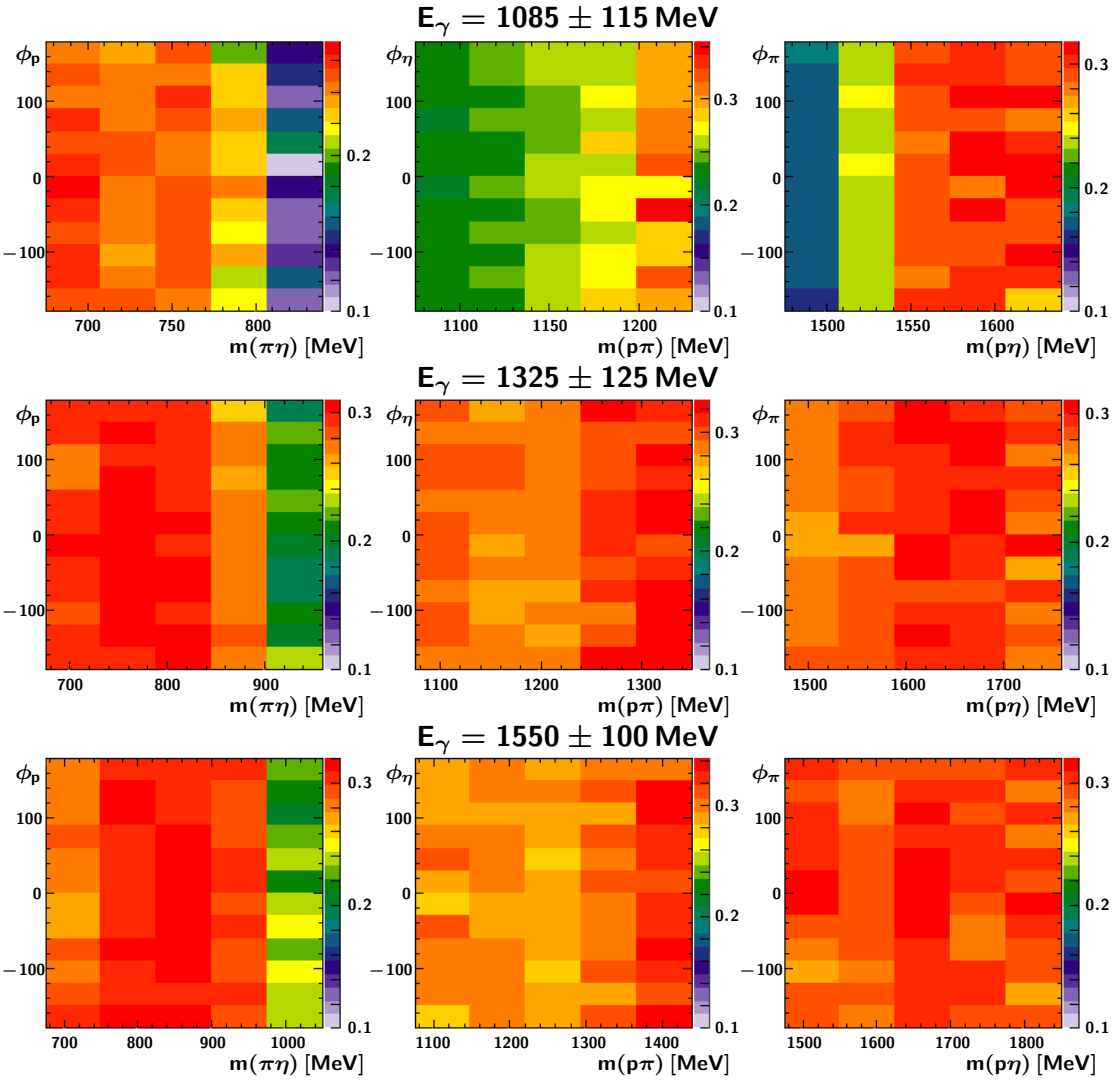

Figure 7.5: **Acceptance, ϕ versus invariant masses.** Shown are the ratios of reconstructed to generated Monte Carlo events, binned in the azimuthal angle ϕ of each of the three recoiling particles (left to right: p, η, π^0) and the invariant mass of the remaining two-particle system for the three energy ranges used for the extraction of the polarization observables (top to bottom).

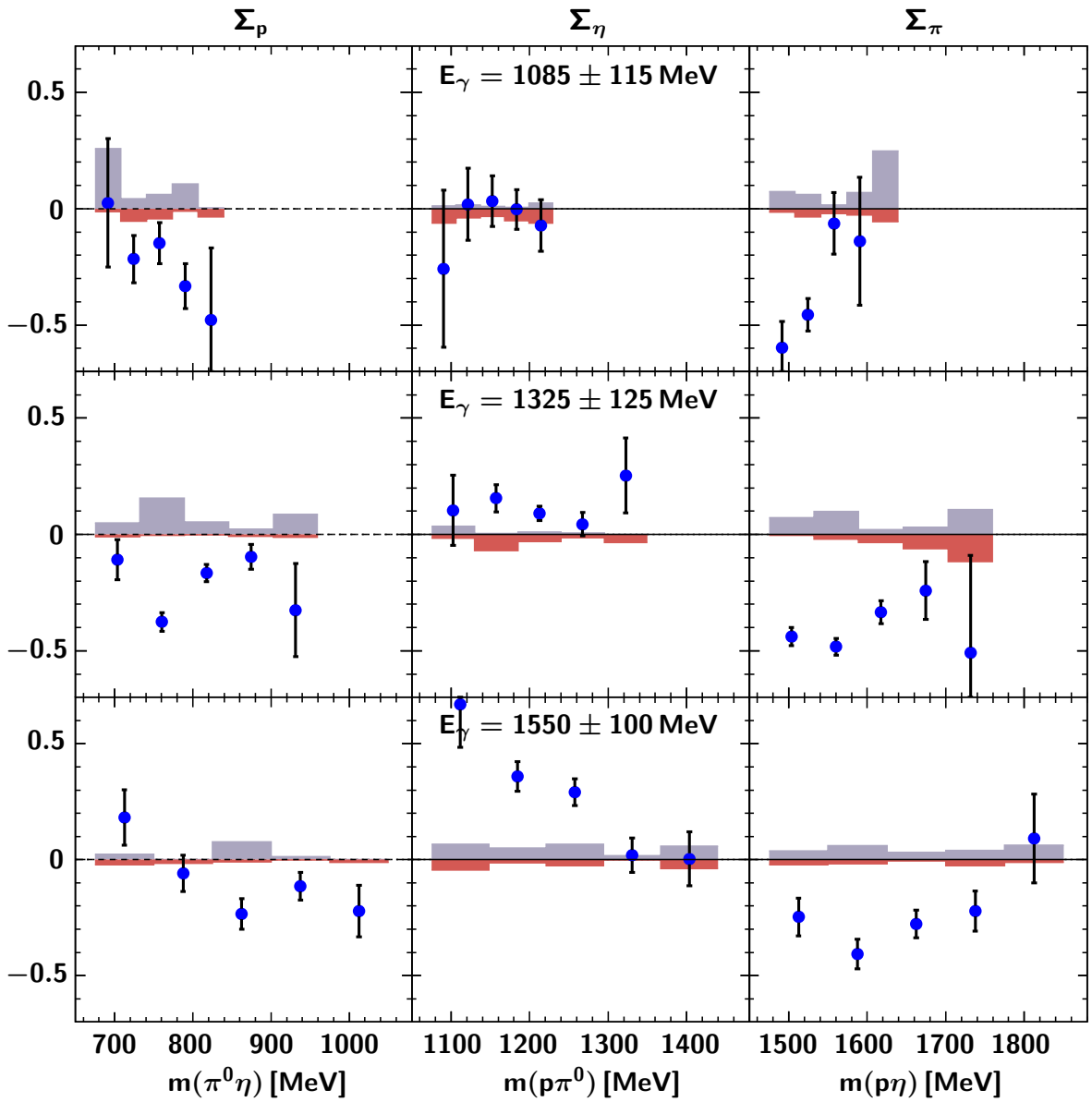

Figure 7.6: **Beam asymmetry Σ as function of invariant mass.** Left to right: Beam asymmetries derived from the ϕ-distribution of the final state proton, η and π^0, respectively, as functions of the invariant mass of the remaining two final state particles. Bar graphs represent the systematic error estimate derived from acceptance correction ([BLUE], positive) and PWA phasespace-weighting ([RED], negative). See text for details.

7.2 Polarization observables in full three-body kinematics

In the quasi two-body approach described in the previous section, the number of degrees of freedom for meson-pair production is artificially decreased by restricting the three-body final state to three, two-body final states. In general, the three outgoing particles and the incoming photon are not coplanar but another plane occurs spanned by the final state particles, being at an angle to the reaction plane as defined before. Figure 7.7 illustrates this situation. The occurrence of this additional angle ϕ^* between the reaction

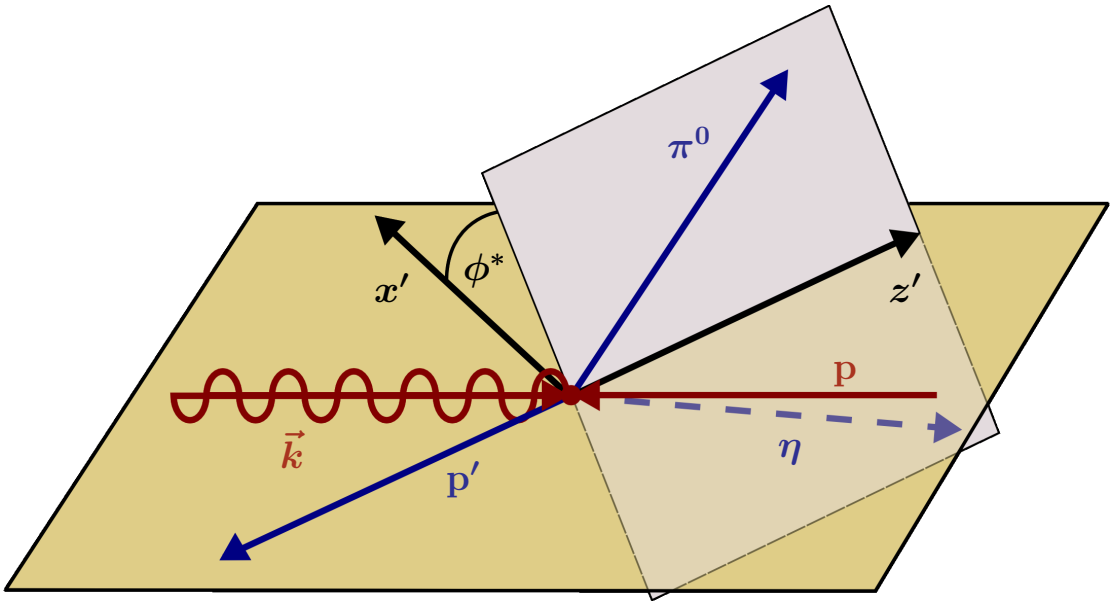

Figure 7.7: **Angle definitions in the three-body approach.** The angle ϕ^* occurs as an additional degree of freedom due to the general acoplanarity of the final state particles and the incoming photon momentum $\vec{k}$. It is defined as the angle between the reaction plane (see figure 7.1) and the decay plane spanned by the three final state particles. It is identical to the polar angle in the rest frame of the $\pi^0\eta$-system (in this example) with the z'-axis in the direction of the total momentum of this system (helicity frame).

plane and the newly defined decay plane leads to a modification of the cross section [RO05]:

$$\frac{\mathrm{d}\sigma}{\mathrm{d}\Omega} = \left(\frac{\mathrm{d}\sigma}{\mathrm{d}\Omega}\right)_0 \left(1 + \delta_l \left(I^c(\phi^*)\cos 2\phi + I^s(\phi^*)\sin 2\phi\right)\right). \tag{7.3}$$

Here, two polarization observables arise, I^c and I^s, defining the amplitudes of a $\cos 2\phi$- and an additional $\sin 2\phi$-modulation, respectively.

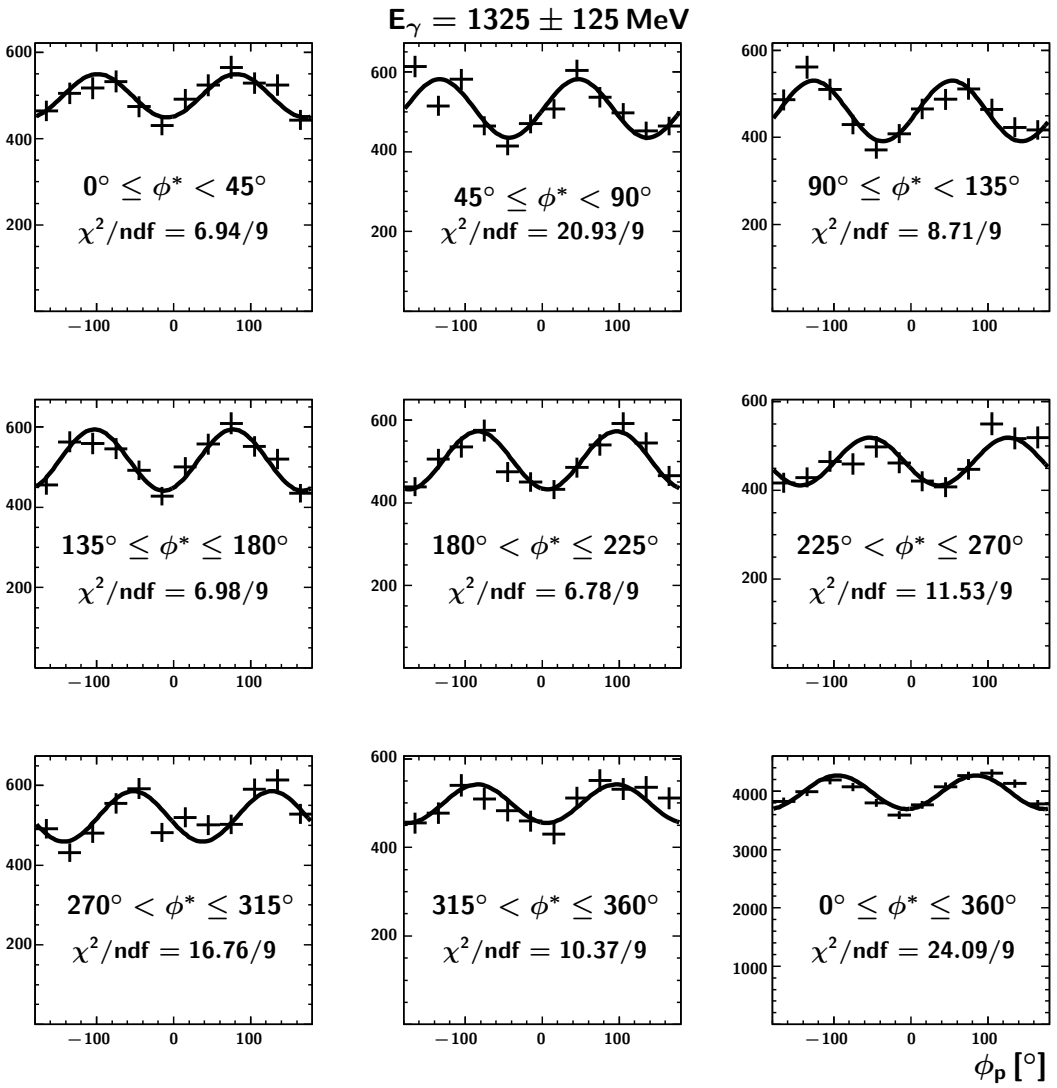

Figure 7.8: **ϕ-distributions for the final state proton.** Shown are the ϕ-distributions with respect to the final state proton recoiling against the $\pi^0\eta$-system in the energy range $E_\gamma = 1325 \pm 125\,\mathrm{MeV}$ for eight bins in ϕ^* as defined in figure 7.7 along with the spectrum integrated over all ϕ^*. The data is not polarization-weighted. Solid line: Fit according to (7.11).

Figure 7.8 shows the ϕ-distribution of the final state proton for eight ϕ^*-bins for the energy bin 1200 MeV to 1450 MeV (see appendix B for the full set of distributions). The effect of both asymmetries is clearly visible in the superposition of the $\cos 2\phi$ and $\sin 2\phi$-modulations, both varying in amplitude as function of ϕ^*. For the calculation of this angle from the scalar product of the normals to the corresponding planes, this work follows the angle definitions for the determination of helicity asymmetries in $2\pi^0$-production using circularly polarized photons as described in [Roc05]. In the example of the reaction plane being spanned by the recoiling proton momentum $\vec{p'} = -\vec{q}$, $\vec{q} = \vec{p}_{\pi^0} + \vec{p}_\eta$, and incoming photon momentum $\vec{k}$ (figure 7.7), the definition reads:

$$\begin{aligned} \cos\phi^* &= \frac{(\vec{k}\times\vec{q})\cdot(\vec{q}\times\vec{p}_{\pi^0})}{|\vec{k}\times\vec{q}|\cdot|\vec{q}\times\vec{p}_{\pi^0}|} \\ &= \frac{(\vec{k}\times\vec{p'})\cdot(\vec{p}_{\pi^0}\times\vec{p}_\eta)}{|\vec{k}\times\vec{p'}|\cdot|\vec{p}_{\pi^0}\times\vec{p}_\eta|} \end{aligned} \tag{7.4}$$

and

$$\begin{aligned} \sin\phi^* &= -1\cdot\frac{\Big((\vec{k}\times\vec{q})\times\vec{q}\Big)\cdot(\vec{q}\times\vec{p}_{\pi^0})}{|(\vec{k}\times\vec{q})\times\vec{q}|\cdot|\vec{q}\times\vec{p}_{\pi^0}|} \\ &= \frac{\Big((\vec{k}\times\vec{p'})\times\vec{p'}\Big)\cdot(\vec{p}_{\pi^0}\times\vec{p}_\eta)}{|(\vec{k}\times\vec{p'})\times\vec{p'}|\cdot|\vec{p}_{\pi^0}\times\vec{p}_\eta|}. \end{aligned} \tag{7.5}$$

Therefore:

$$\phi^* = \begin{cases} \arccos(\phi^*) & \text{for} \quad \sin(\phi^*) > 0 \\ 2\pi - \arccos(\phi^*) & \text{else.} \end{cases} \tag{7.6}$$

In the case of one of the mesons being the recoiling particle, the momenta of the proton and the respective meson are interchanged in (7.4) and (7.5).
As visible in figure 7.8, the amplitudes of the modulations of the cross section vary with ϕ^*, so the beam asymmetries themselves are functions of this angle. Taking the definitions in figure 7.7 into account, the following constraints can be derived:

- In coplanar kinematics, meaning for $\phi^* = 0, \pi, 2\pi$, the situation is indistinguishable from the one presented for the quasi two-body approach, where no $\sin 2\phi$-modulation is present in the cross section. Therefore I^s has to vanish for these configurations: $I^s(\phi^* = 0) = I^s(\phi^* = \pi) = I^s(\phi^* = 2\pi) = 0$.

- The transition $\phi^* \to 2\pi - \phi^*$ is equivalent to a mirror operation of the system with respect to the reaction plane. The polarization plane is thereby mirrored as well, leading to the transition $\phi \to 2\pi - \phi$ (see figure 7.1). Since $\sin(2\cdot(2\pi-\phi)) =$

$-\sin(2\phi)$ and $\cos(2\cdot(2\pi-\phi)) = \cos(2\phi)$, (7.3) yields:

$$I^s(2\pi-\phi^*) = -I^s(\phi^*) \text{ and} \tag{7.7}$$

$$I^c(2\pi-\phi^*) = I^c(\phi^*). \tag{7.8}$$

Taking these considerations into account, the asymmetries can be expanded in a series of sine and cosine functions,

$$I^s(\phi^*) = \sum_{n=0} a_n \sin(n\phi^*) \text{ and} \tag{7.9}$$

$$I^c(\phi^*) = \sum_{n=0} a_n \cos(n\phi^*). \tag{7.10}$$

In this ansatz, the relation between I^c and the two-body asymmetry Σ becomes clear. The transition from the three-body approach to the quasi two-body situation effectively implies an integration over the angle ϕ^*. For the expansions of the observables (7.9), (7.10), this means that I^s vanishes, as expected regarding the absence of a $\sin 2\phi$-modulation in the two-body cross section. In case of I^c however only higher terms in the expansion vanish and the integration leaves the constant term which then corresponds to Σ. The two asymmetries are therefore not identical, but I^c contains Σ along with additional information from higher terms in the expansion.
Figures 7.10 and 7.11 show the asymmetries as functions of ϕ^*, derived from a fit to the according ϕ-distributions in the same way as described before, using the function:

$$f(\phi) = A + P\cdot[B\cdot\cos(2\phi) + C\cdot\sin 2\phi)]. \tag{7.11}$$

The solid symbols show the observables themselves determined as stated above. The open symbols have been obtained by exploiting the relations given in (7.7), (7.8), performing the transition $\phi^* \rightarrow 2\pi - \phi^*$ and changing the sign in the case of I^s. The symmetry properties imposed by these relations are clearly visible in the data, and the sporadic deviations are consistent with statistics. This demonstrates the comparably small uncertainties due to systematic effects. As for the quasi two-body asymmetry Σ, these effects were studied further, determining the two-dimensional acceptance, here as function of the variables ϕ and ϕ^* as shown in figure 7.9, and using the PWA phasespace-weighting technique. Again, large asymmetries in the order of up to 50% can be observed for all recoiling particles with systematic uncertainties in the order of, or well below the statistical errors. The symmetry constraints imposed by the expansions (7.9), (7.10) are clearly fulfilled as shown by the associated second order fits applied to the observable

distributions (solid lines in figures 7.10 and 7.11). The correspondence between I^c and the two-body beam asymmetry Σ is visible in the baseline shift of the cosine series, especially in the case of the recoiling η.

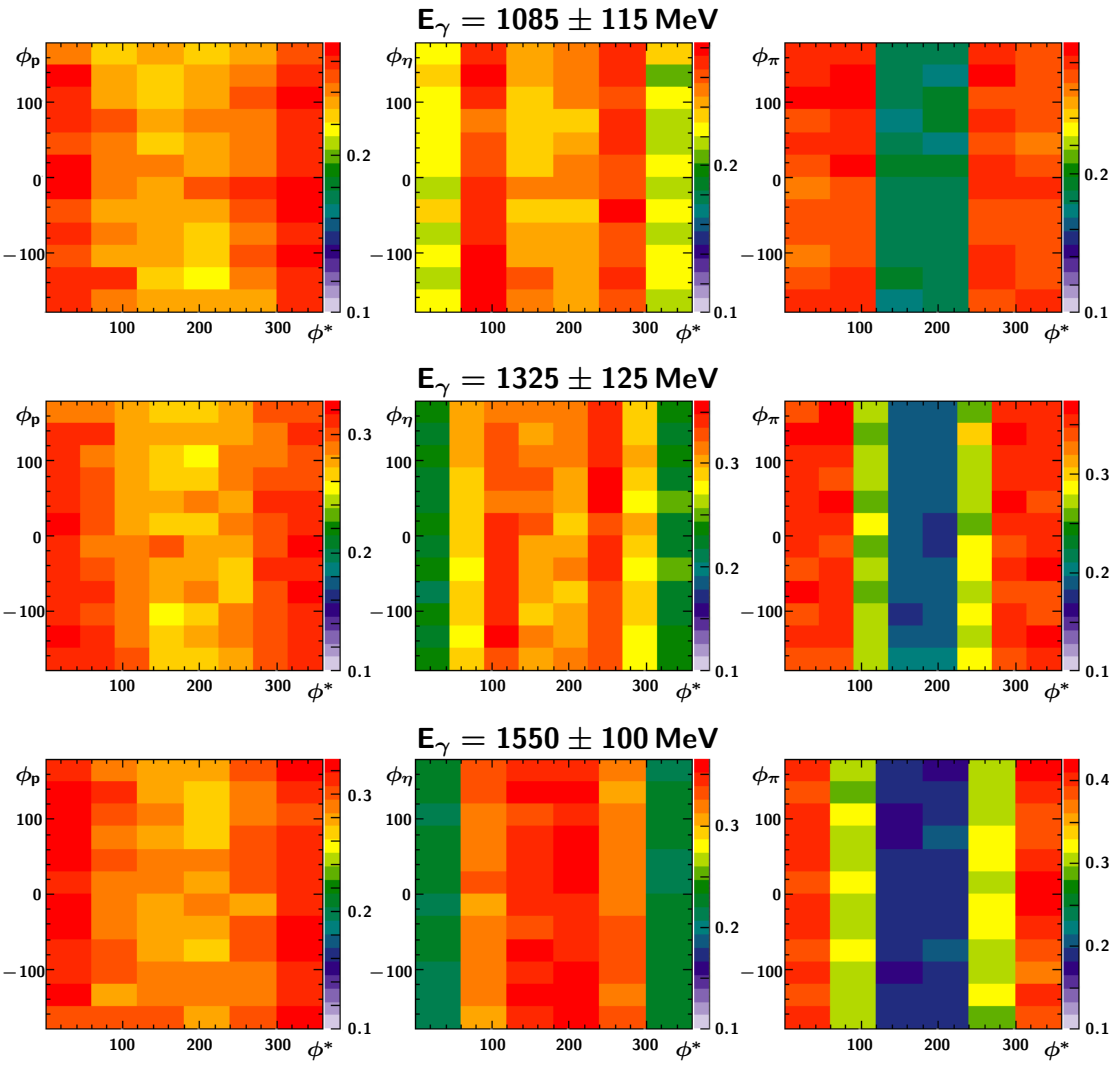

Figure 7.9: **Acceptance, ϕ versus ϕ^*.** Shown are the ratios of reconstructed to generated Monte Carlo events, binned in the azimuthal angle ϕ of each of the three recoiling particles (left to right: p, η, π^0) and corresponding angle ϕ^* for the three energy ranges used for the extraction of the polarization observables (top to bottom).

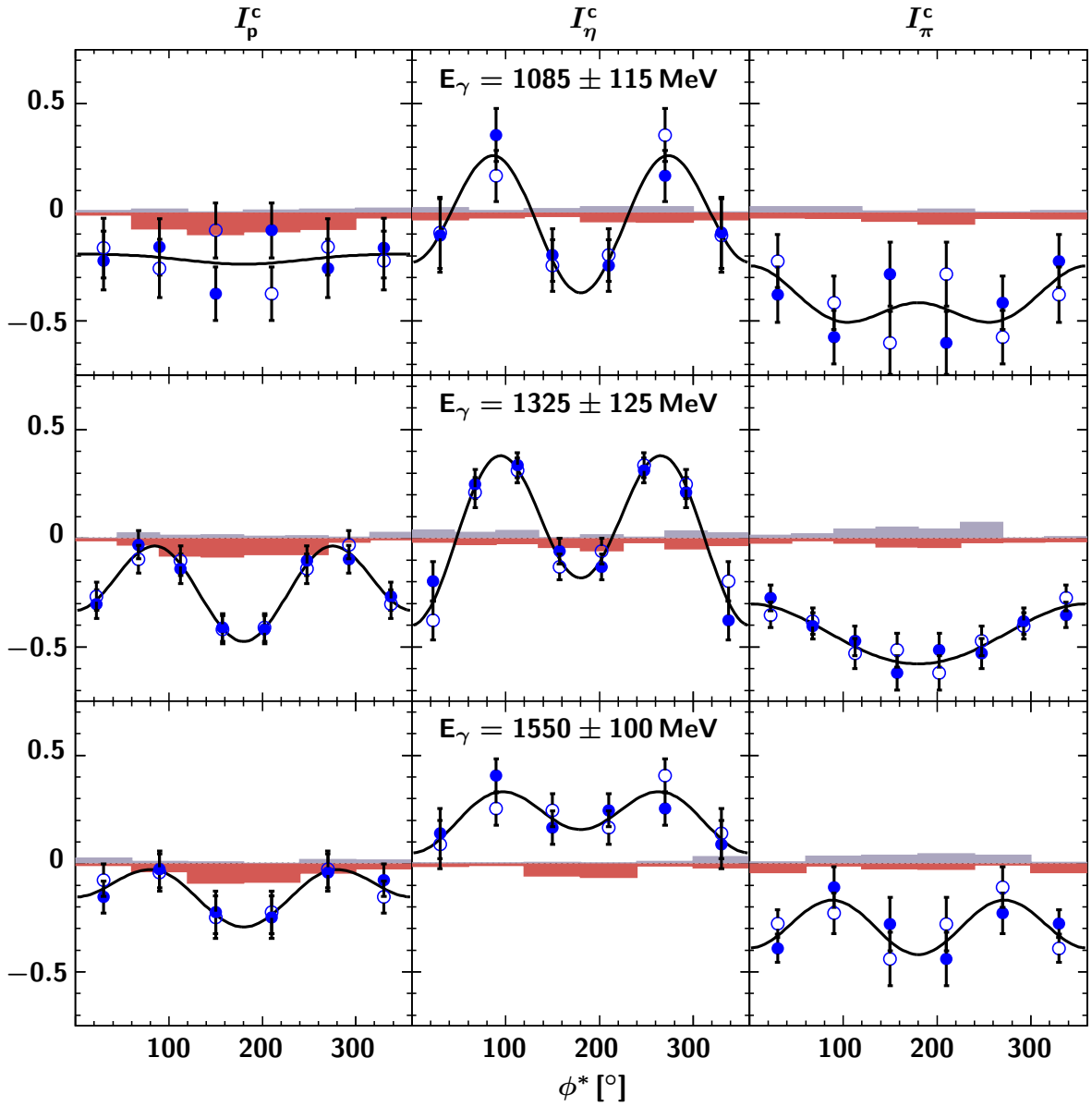

Figure 7.10: **The beam asymmetry I^c.** Left to right: Beam asymmetries derived from the ϕ-distribution of the final state proton, η and π^0, respectively, as functions of the angle ϕ^*. Filled symbols: Beam asymmetry $I^c(\phi^*)$ as derived from the data. Open symbols: $I^c(2\pi - \phi^*)$ (see (7.8)). Solid line: Second order cosine-series fit (see (7.10)). Bar graphs represent the systematic error estimate derived from acceptance correction ([BLUE], positive) and PWA phasespace-weighting ([RED], negative).

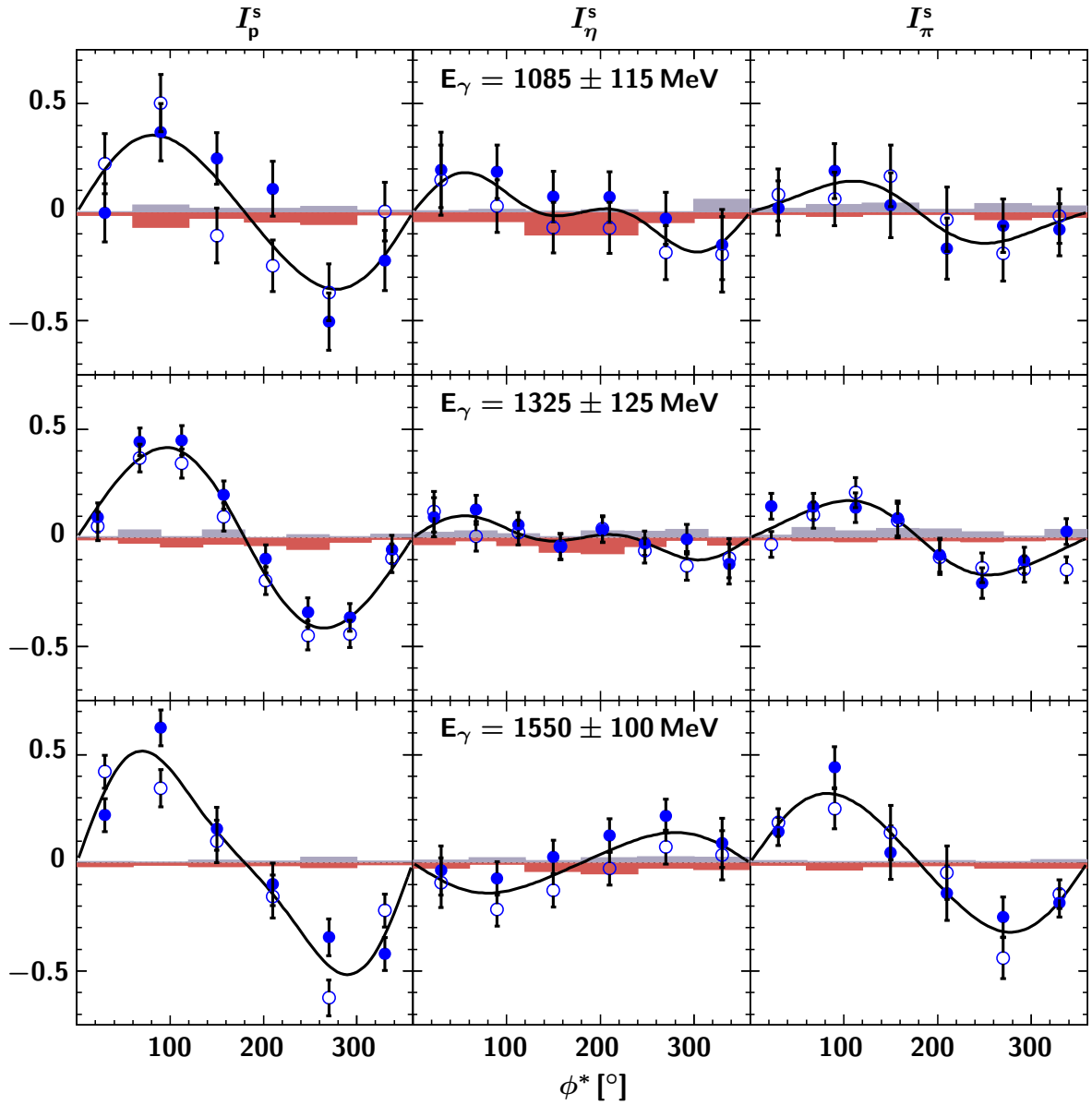

Figure 7.11: **The beam asymmetry I^s.** Left to right: Beam asymmetries derived from the ϕ-distribution of the final state proton, η and π^0, respectively, as functions of the angle ϕ^*. Filled symbols: Beam asymmetry $I^s(\phi^*)$ as derived from the data. Open symbols: $-I^s(2\pi - \phi^*)$ (see (7.7)). Solid line: Second order sine-series fit (see (7.9)). Bar graphs represent the systematic error estimate derived from acceptance correction ([BLUE], positive) and PWA phasespace-weighting ([RED], negative).

7.3 Invariant mass distributions and Dalitz plots

7.3.1 Invariant mass distributions

Figures 7.12 to 7.15 show the distributions for the three accessible two-body invariant masses in the reaction $\gamma p \rightarrow p\pi^0\eta$ for different ranges of incoming photon energy. They are compared with the according spectra resulting from reconstructed Monte Carlo events. Since no dynamical processes are simulated, these are pure phasespace distributions, including the detector acceptance and efficiency. Here the analysis is not restricted to the energy range used for the extraction of the polarization observables since the degree of polarization has no influence on the distributions shown. This has the advantage that structures appearing at the edge of the phase space covered by the polarization observables can be studied further towards higher energies and for example first indications for the intermediate states $\Delta\eta$, $S_{11}\pi^0$ and pa_0 (see chapter 3) can be obtained.

Figure 7.12 shows the $p\pi^0$ invariant mass distribution, once for the three energy ranges under consideration for the extraction of the polarization observables and additionally integrated over the full energy range from 900 MeV to 2500 MeV. A clear signal for the $\Delta(1232)P_{33}$ is observed beginning with the second energy bin, indicating the formation of an intermediate $\Delta\eta$ state. In the case of the $p\eta$ invariant mass (figure 7.13), the signal for the $N(1535)S_{11}$ resonance, indicating a $S_{11}\pi^0$ intermediate state, appears only on the very edge of the phasespace and is therefore less prominent. It is however clearly visible in a different representation, the Dalitz plot, introduced in the next section. In the $\pi^0\eta$ invariant mass shown in figure 7.14, no distinct features are visible in the energy regions selected for the extraction of the beam asymmetries. In the integrated spectrum however, a shoulder at the position of the scalar meson $a_0(980)$ can be observed. The invariant mass region of this signal is also covered in part in the third energy range from 1450 MeV to 1650 MeV, so intermediate pa_0 states might contribute to the reaction in this bin.

Figure 7.15 shows invariant mass distributions for the three, two-particle systems for three selected photon energy ranges of 100 MeV width each. Here the evolution of the signals for the intermediate $\Delta\eta$, $S_{11}\pi^0$, and pa_0 states becomes apparent. The lowest energy bin shown, $E_\gamma = 1650 \pm 50$ MeV partly overlaps with the high energy bin used for the extraction of the polarization observables, demonstrating the contributions of all of these intermediate states to the beam asymmetries extracted for this bin. This issue will be further discussed in chapter 8. For a full set of invariant mass distributions, see appendix C.

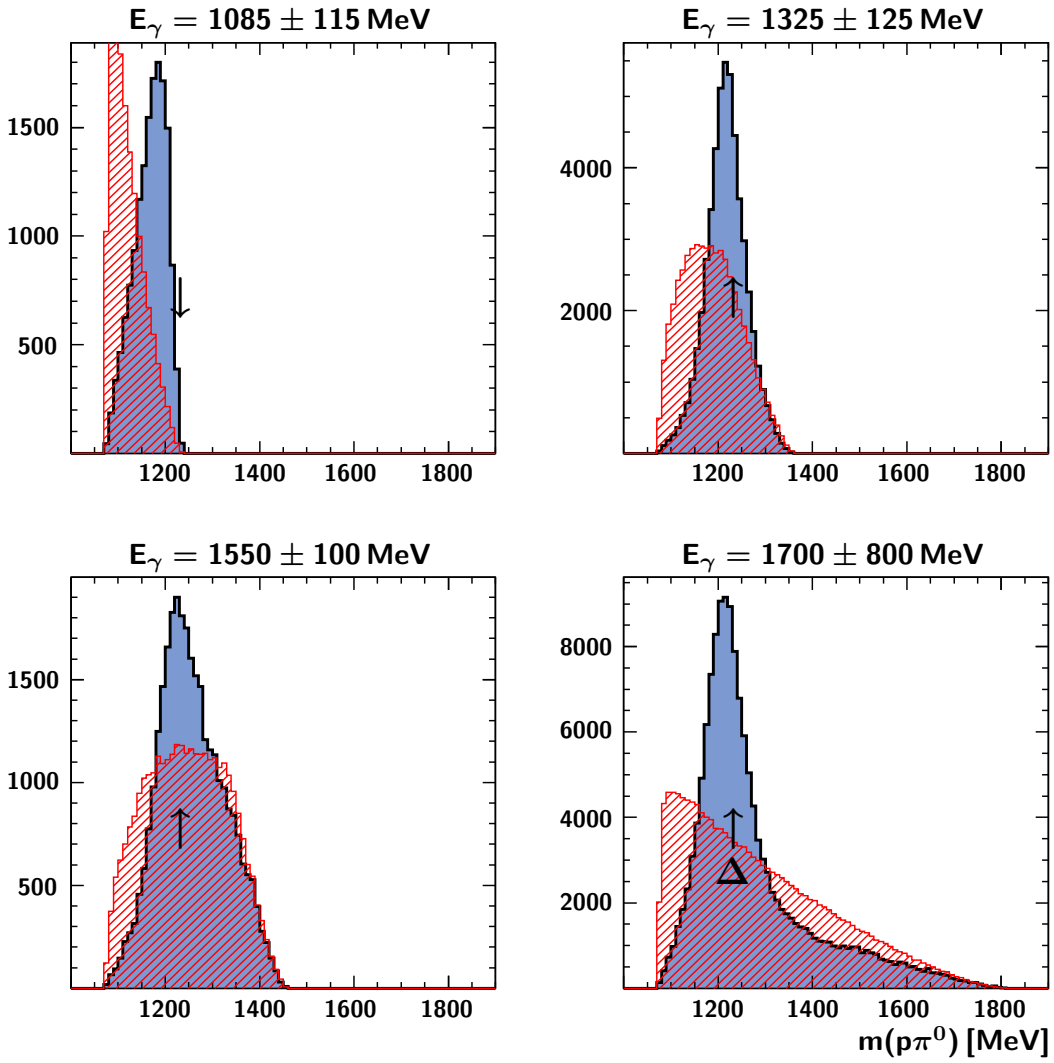

Figure 7.12: **Invariant mass distributions, $p\pi^0$-system.** The arrow indicates the position of the $\Delta(1232)P_{33}$ resonance. Hatched area ([RED]): Phasespace distribution, including detector acceptance.

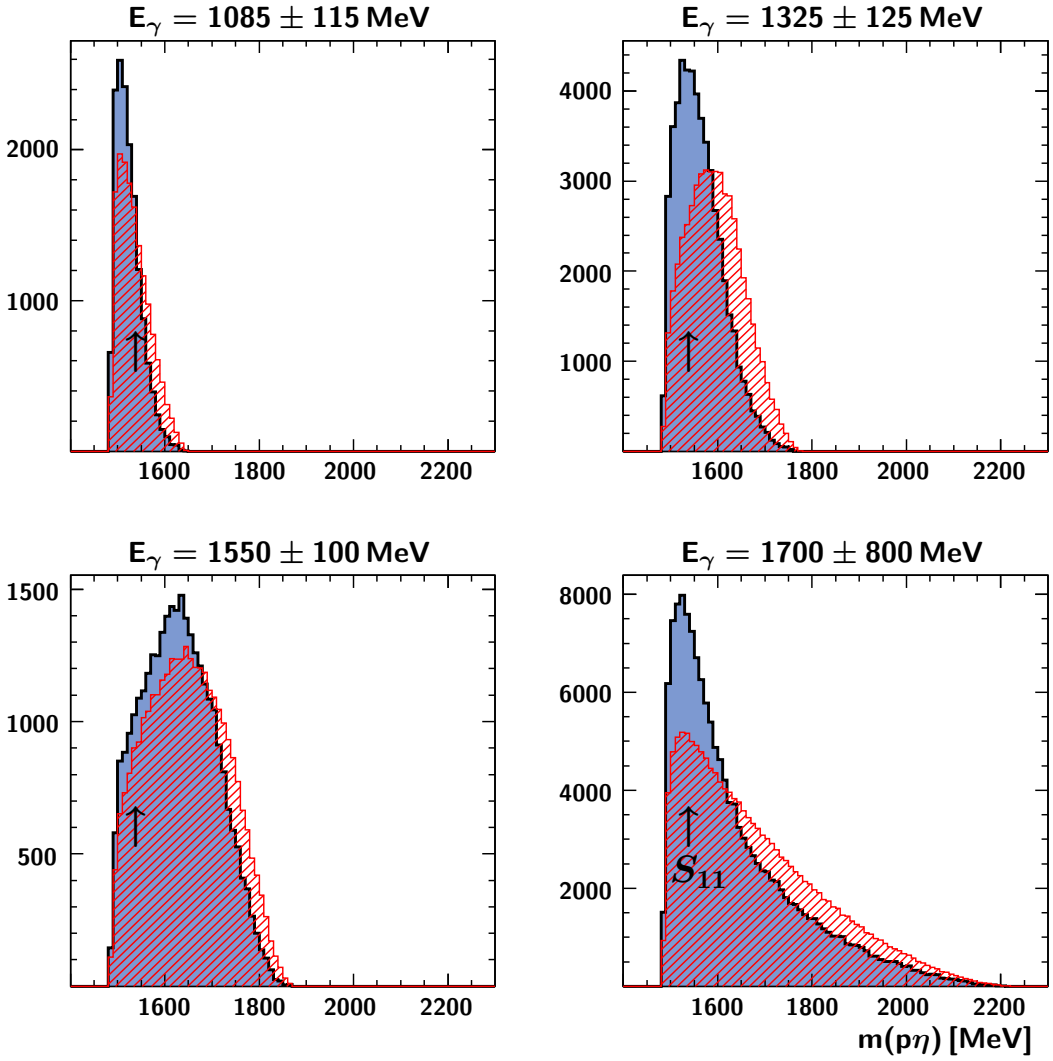

Figure 7.13: **Invariant mass distributions, pη-system.** The arrow indicates the position of the N(1535)S_{11} resonance. Hatched area ([RED]): Phasespace distribution, including detector acceptance.

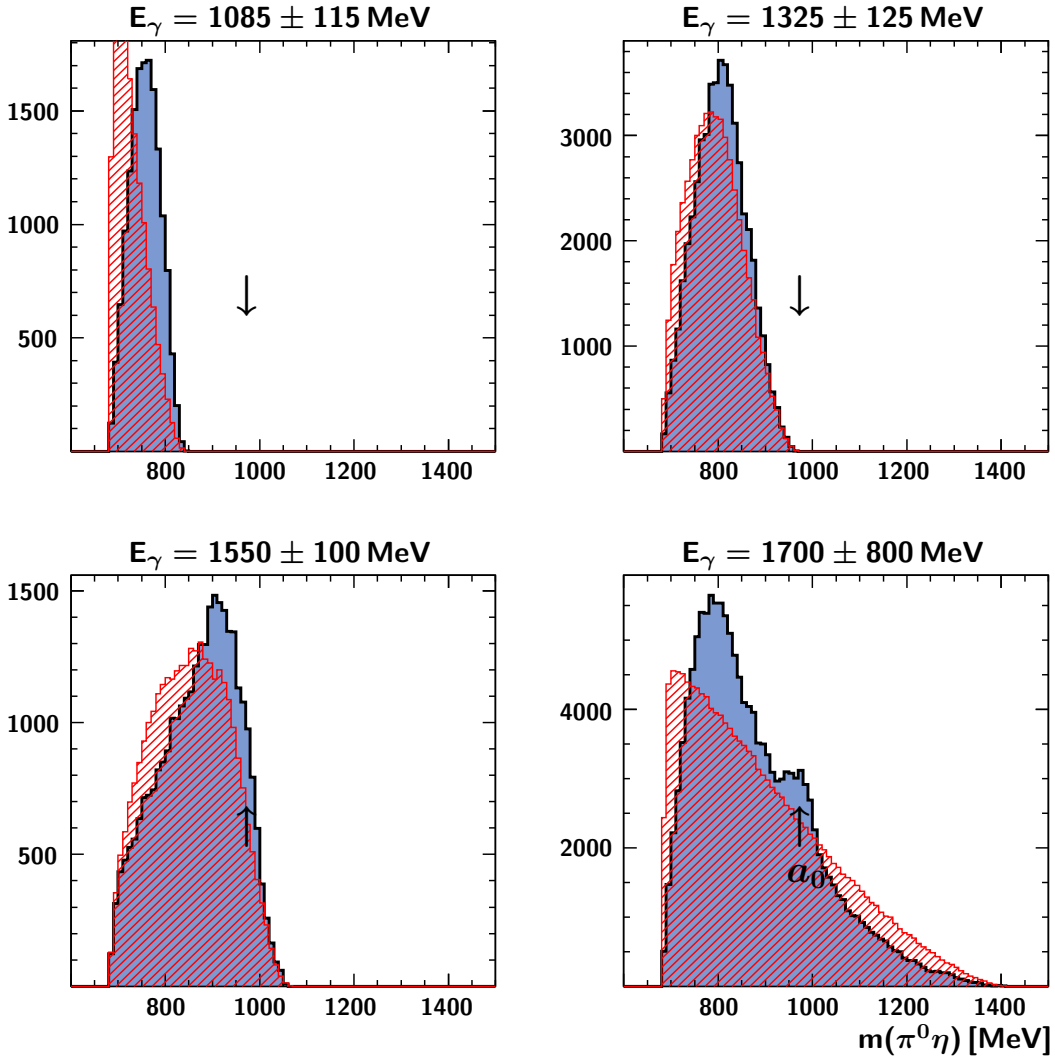

Figure 7.14: **Invariant mass distributions, $\pi^0\eta$-system.** The arrow indicates the position of the scalar meson $a_0(980)$. Hatched area ([RED]): Phasespace distribution, including detector acceptance.

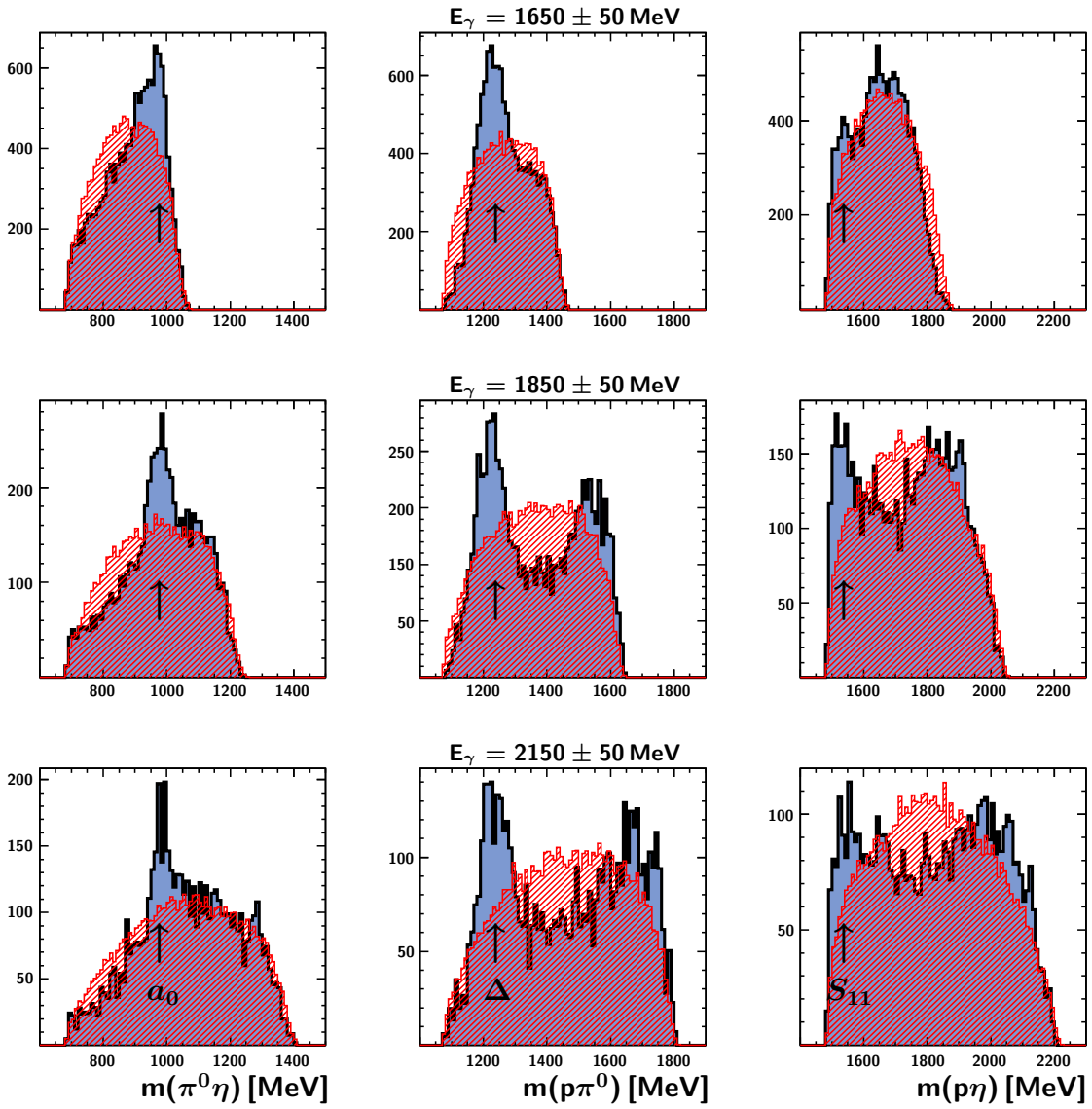

Figure 7.15: **Selected invariant mass distributions.** Left to right: Invariant masses calculated for the $\pi^0\eta$-, pπ^0-, and pη-system. Arrows indicate the positions of the $a_0(980)$, $\Delta(1232)P_{33}$, and $N(1535)S_{11}$, respectively. Structures arising towards higher invariant masses, particularly visible in the m(pπ^0)- and m(pη)-distributions are in fact reflections of resonances in the respective other invariant mass (see next section). Hatched area ([RED]): Phasespace distribution, including detector acceptance.

7.3.2 Dalitz plots

The Dalitz plot is a representation of a three-body system, commonly used to ascertain resonances contributing to a given reaction. For three final state particles, two squared invariant masses m_{12}^2 and m_{23}^2 are calculated and entered in a two-dimensional histogram. In the absence of dynamical processes in the reaction, the resulting intensity distribution exhibits no structures. Resonant contributions to the reaction however appear in the Dalitz plot as regions of increased intensity. Resonances in the invariant masses m_{12} and m_{23} can be seen as horizontal or vertical bands at their respective positions, resonances in the m_{13} invariant mass appear as diagonals. See for example the *Kinematics* section of [A$^+$08b] for details.

Figures 7.16 to 7.18 show Dalitz plots obtained from the data for four selected photon energy ranges, starting at the upper end of the high energy bin used for the extraction of the polarization observables. For a full set of plots covering the full energy range from 900 to 2500 MeV, see appendix C. Distinct bands indicating the formation of the three intermediate states mentioned above, $\Delta\eta$, $S_{11}\pi^0$, and pa_0 are visible throughout, supporting the interpretation of the linear invariant mass distributions in the previous section.

The comparison of these plots with the linear invariant masses, especially figure 7.15, also shows the origin of the peak-like structures at the upper end of the phasespace. In case of the pη-system for example, this structure is in fact the reflection of the $\Delta(1232)$-signal in the pπ^0 invariant mass, as can be clearly seen in figure 7.17. This demonstrates the advantage of this representation over one-dimensional mass spectra.

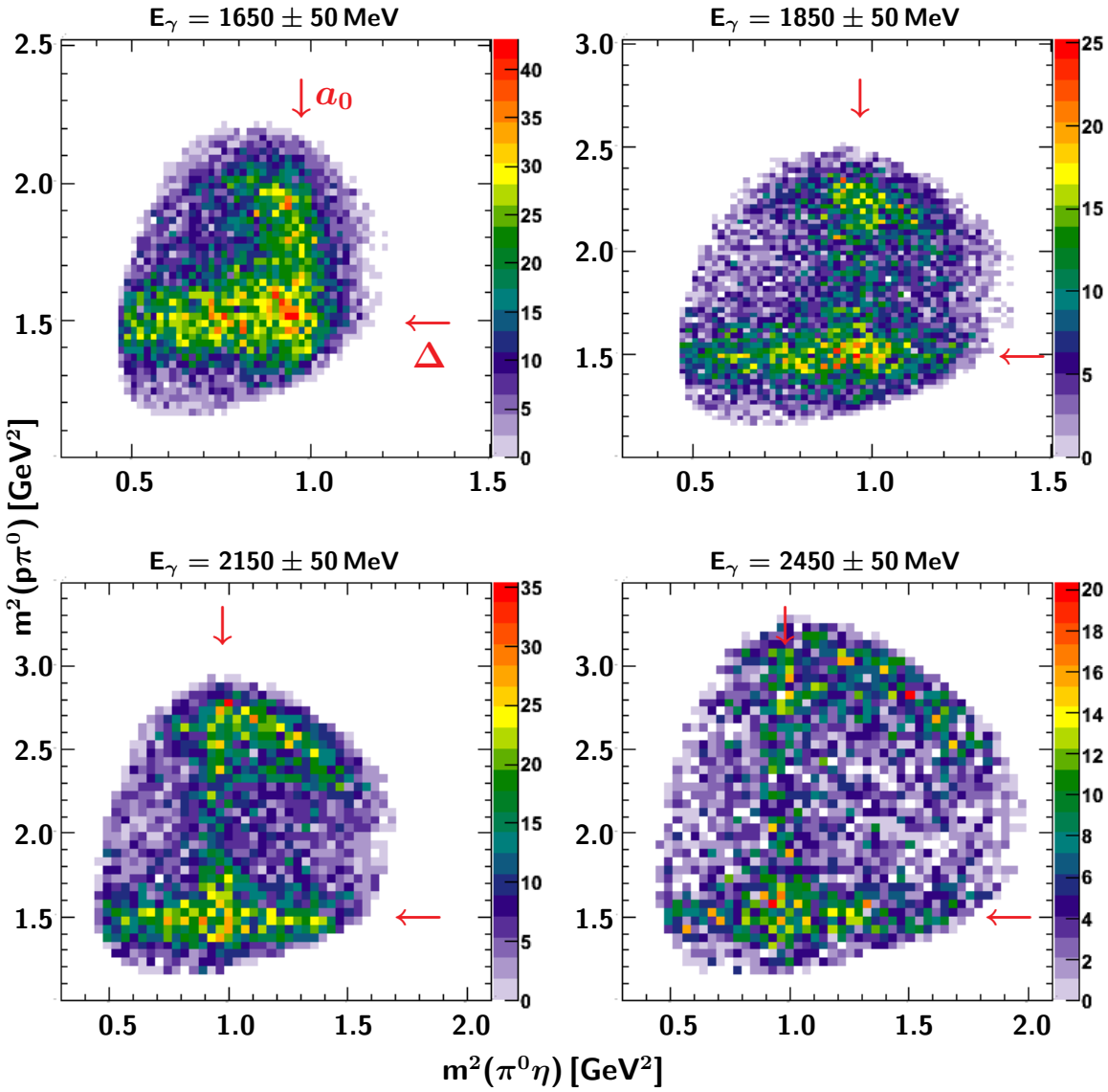

Figure 7.16: **Selected Dalitz plots, $m^2(p\pi^0)$ versus $m^2(\pi^0\eta)$.** Squared invariant masses calculated for four incoming photon energy ranges. Arrows indicate the positions of the scalar meson $a_0(980)$ and the $\Delta(1232)P_{33}$ resonance. Not indicated but clearly visible in the diagonal is the signal for the $N(1535)S_{11}$ resonance.

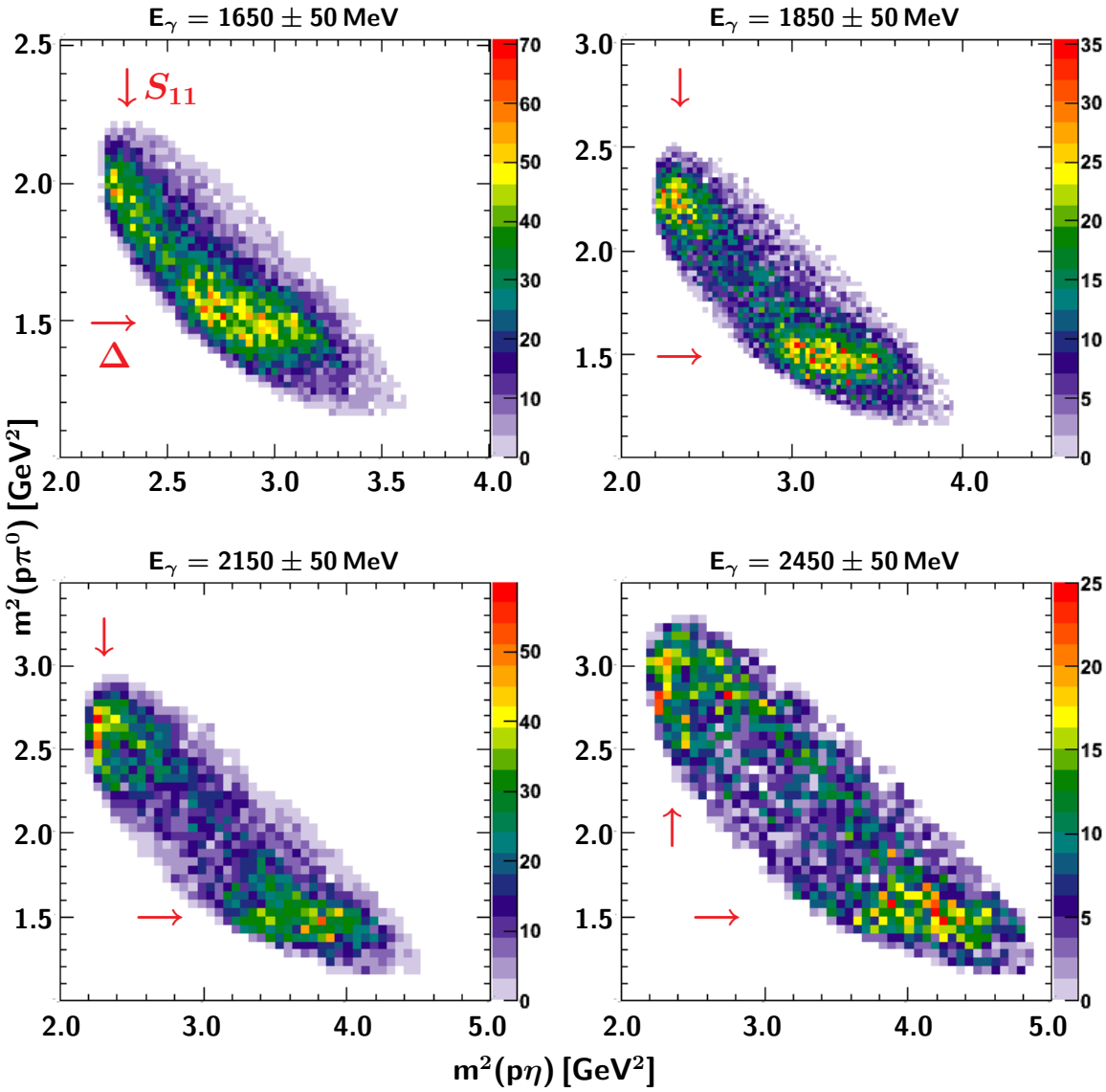

Figure 7.17: **Selected Dalitz plots, $m^2(p\pi^0)$ versus $m^2(p\eta)$.** Squared invariant masses calculated for four incoming photon energy ranges. Arrows indicate the positions of the $\Delta(1232)P_{33}$ and $N(1535)S_{11}$ resonances. Not indicated but visible in the diagonal is the signal for the scalar meson $a_0(980)$.

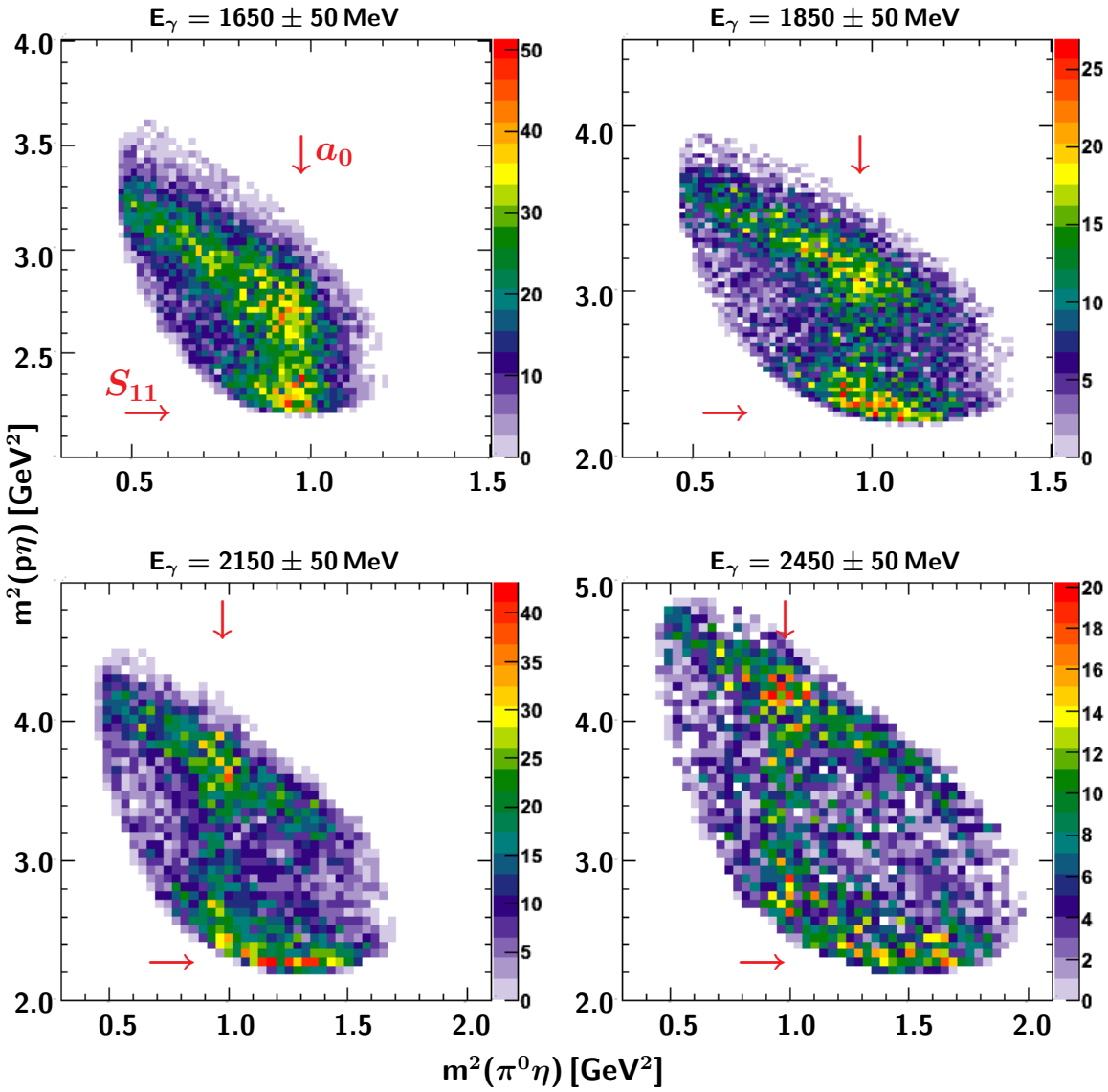

Figure 7.18: **Selected Dalitz plots, $m^2(p\eta)$ versus $m^2(\pi^0\eta)$.** Squared invariant masses calculated for four incoming photon energy ranges. Arrows indicate the positions of the scalar meson $a_0(980)$ and the N(1535)S_{11} resonance. Not indicated but clearly visible in the diagonal is the signal for the $\Delta(1232)P_{33}$ resonance.

8 Discussion

In chapter 3 the importance of the determination of polarization observables in general and the study of the reaction $\gamma p \rightarrow p\pi^0\eta$ in particular has been pointed out with respect to selected open questions in hadron physics. In this chapter the results of this work are compared to other available data.
Additionally, several frameworks to describe the photoproduction of $\pi^0\eta$-pairs are available [DOS06, KCL07, H$^+$08b, FKLO10] or in development [Rob10]. Attempts to describe the results of this work using three different theoretical approaches will be presented, after a brief introduction of the corresponding frameworks.

8.1 Comparison to other data

The first data on the quasi two-body beam asymmetry Σ in the reaction $\gamma p \rightarrow p\pi^0\eta$ has been published independently at about the same time by the CBELSA/TAPS collaboration (parts of the results presented in this work, [GSvP$^+$08]), and the GRAAL collaboration [A$^+$08a] (see 3.2.1). In the latter publication, the beam asymmetry has been extracted for all three recoiling particles as a function of invariant masses over an incoming photon energy range of $1100\,\text{MeV} \leq E_\gamma \leq 1500\,\text{MeV}$. In the GRAAL experiment, linearly polarized photons were produced by Compton-backscattering of polarized laser light (see 4.2), resulting in a high, constant degree of polarization, allowing for a finer energy-binning. The respective data obtained in this work has been rebinned accordingly for an energy range of $1000\,\text{MeV} \leq E_\gamma \leq 1700\,\text{MeV}$ to allow for a direct comparison of the results, as shown in figures 8.1 to 8.3.
The GRAAL data, shown as open (red) circles in the energy ranges covered by the experiment, is in excellent agreement with the results obtained in this analysis (closed blue circles). Especially the tendency towards positive asymmetries in case of the recoiling η (figure 8.2), starting at intermediate energies, is consistent in both experiments. It should be noted though that due to differences in the covered phase space because of the different geometrical acceptance of the two experiments, a perfect matching of the datapoints cannot be expected in general (see 7.1, [Sok10] for details).

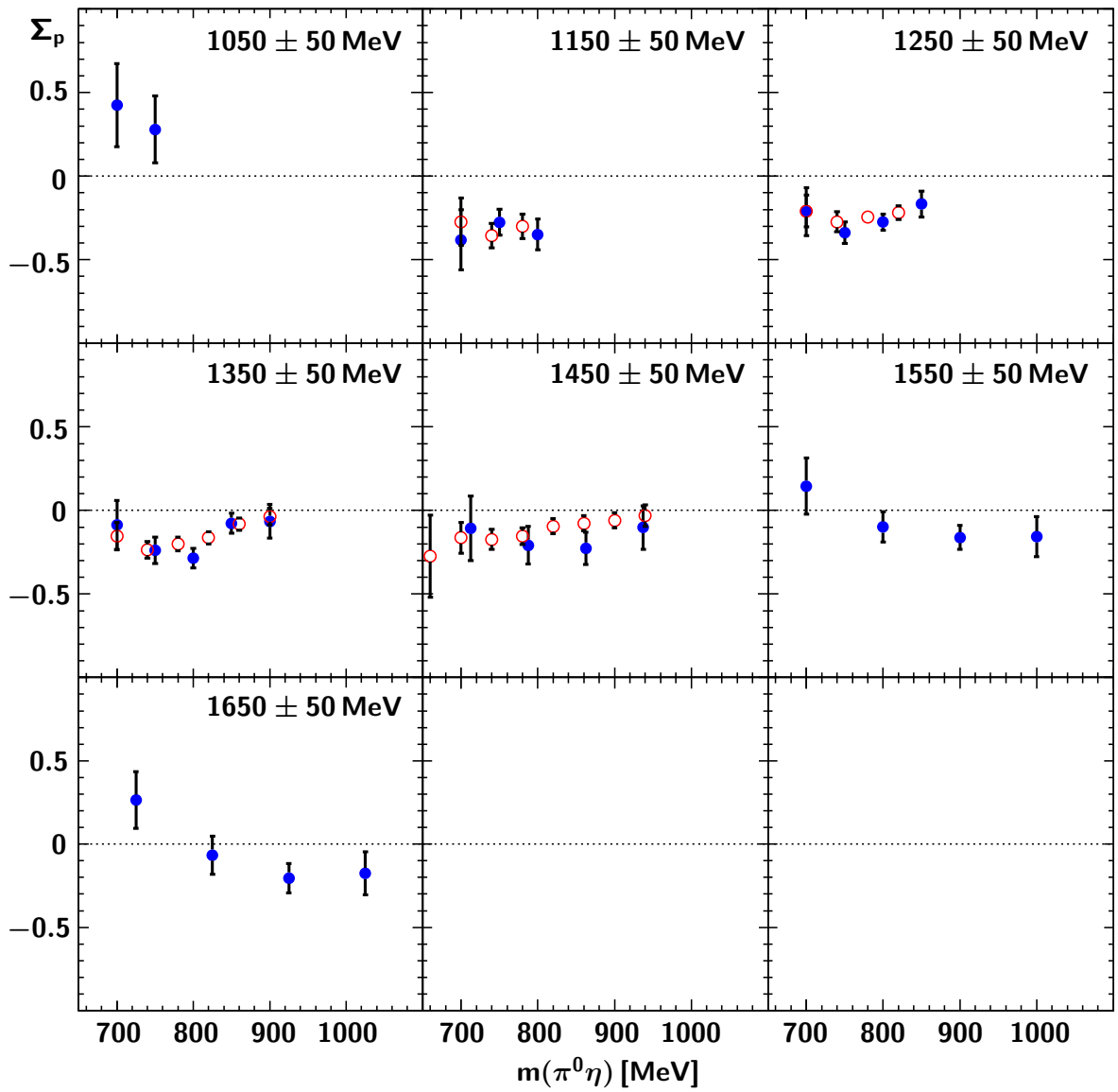

Figure 8.1: **Σ_p as function of the $\pi^0\eta$ invariant mass.** The beam asymmetries are given for seven bins in incoming photon energy, each of 100 MeV width. Open circles ([RED]): GRAAL [A$^+$08a], full circles ([BLUE]): This work. Only statistical errors are given.

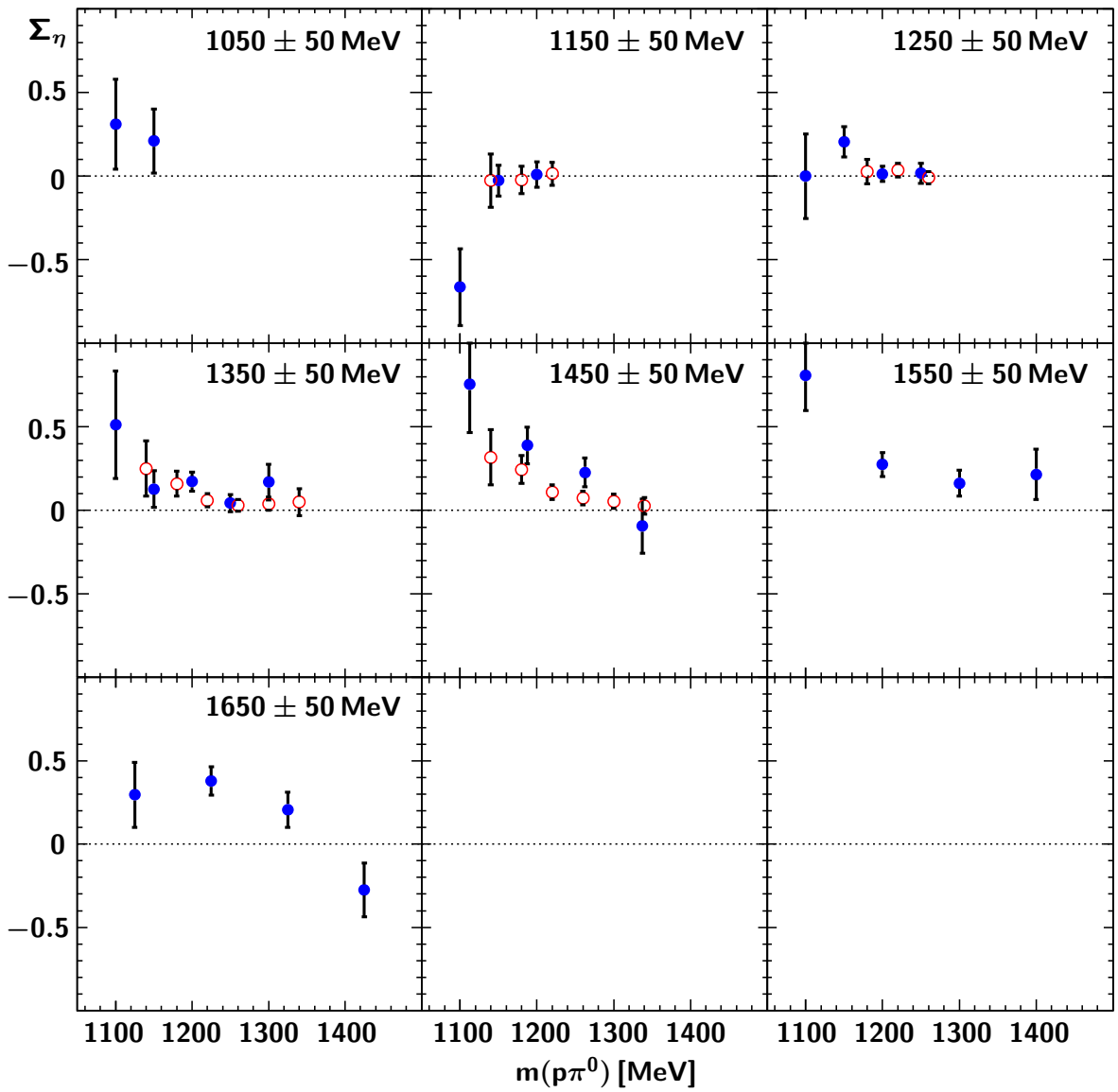

Figure 8.2: **Σ_η as function of the $p\pi^0$ invariant mass.** The beam asymmetries are given for seven bins in incoming photon energy, each of 100 MeV width. Open circles ([RED]): GRAAL [A$^+$08a], full circles ([BLUE]): This work. Only statistical errors are given.

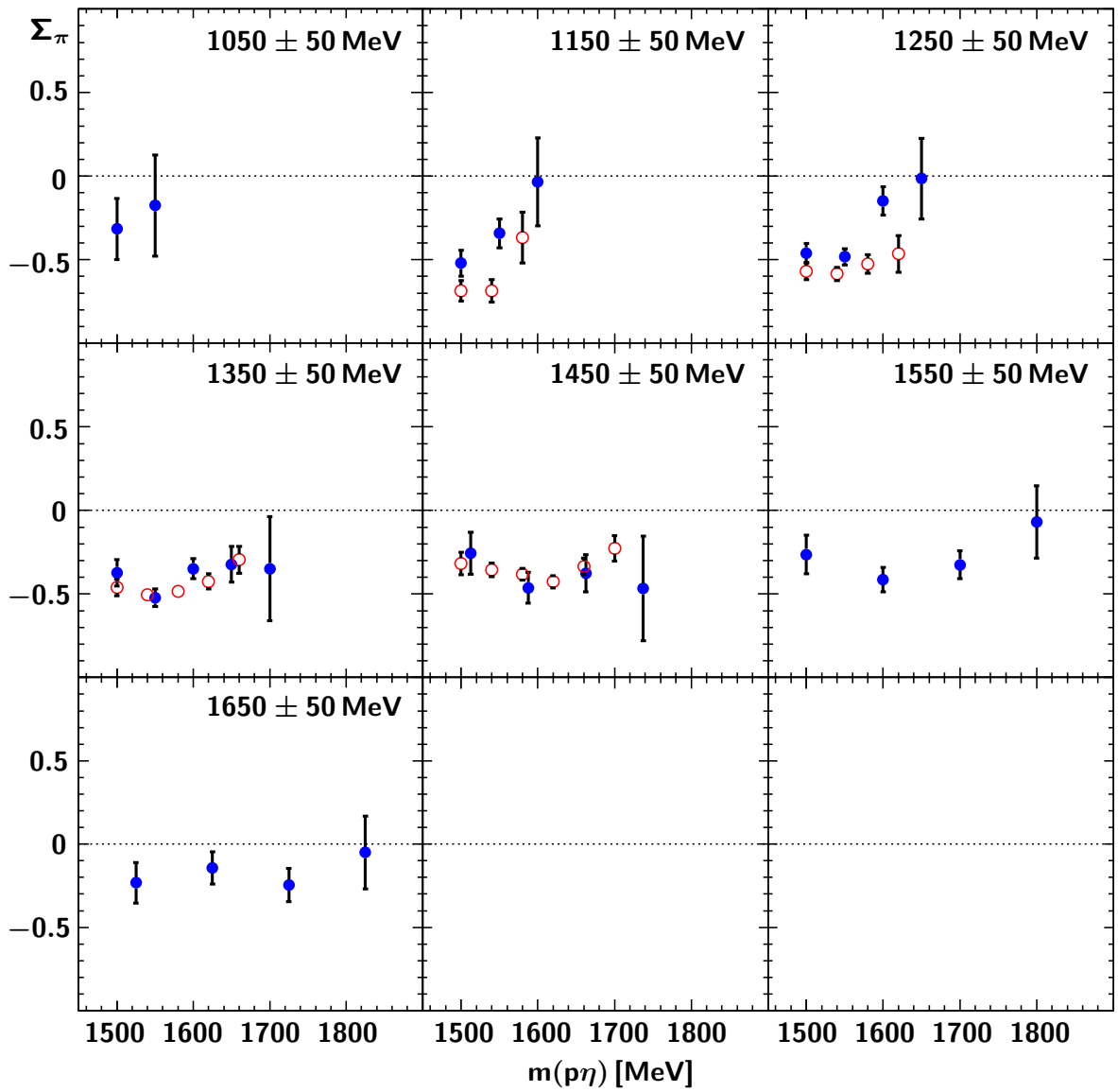

Figure 8.3: **Σ_π as function of the pη invariant mass.** The beam asymmetries are given for seven bins in incoming photon energy, each of 100 MeV width. Open circles ([RED]): GRAAL [A$^+$08a], full circles ([BLUE]): This work. Only statistical errors are given.

8.2 Comparison to theoretical results

The description of beam asymmetry data in the reaction $\gamma p \to p\pi^0\eta$ has, up to now, been addressed within three different theoretical frameworks, the Bonn-Gatchina partial wave analysis [GSvP$^+$08, GSvP$^+$10], the isobar model developed by Fix *et al.* [FKLO10] and the Valencia chiral unitary model [A$^+$08a, DOM10]. These frameworks differ considerably in their underlying methodology as well as the considered resonance contributions and their decay couplings. They are introduced briefly in the following and the latest results with respect to the beam asymmetries extracted within this work are discussed. The systematic error estimates shown in figures 8.4-8.7 were obtained by comparing the effects as derived from the two-dimensional acceptance correction and the PWA-weighting techique described in the previous chapter. For each bin, the larger of the two contributions is shown as grey bars. These are same values as the ones given in appendix A as systematic error.

Bonn-Gatchina partial wave analysis The main concepts of the partial wave analysis approach have already been given in chapter 2.2. The BnGa-PWA is a coupled-channel analysis incorporating data on about 40 observables in pion- and photoproduction, including single- and double-meson- as well as strangeness production. The partial wave fit itself is, in case of double-meson production, performed using an unbinned, event-based maximum likelihood method that takes the full correlations between all variables in the 5-dimensional phasespace into account. For a detailed introduction into the formalism, see [AKST05, AS06, AAK$^+$07], the application of the analysis with respect to the $p\pi^0\eta$ final state is described in [H$^+$08b]. For the results shown in figures 8.4-8.7 the data presented in this work has been incorporated into the fit along with data on other reactions as given in [H$^+$08b]. The resonances contributing to the solution and their decay modes are given in table 8.1. The solution derived in the BnGa-PWA framework describes the data very well and it should be kept in mind that the distributions presented here are only a fraction of the datasets that are described in parallel. Since the predictions for the beam asymmetries Σ [GSvP$^+$08] as well as I^c and I^s [GSvP$^+$10], obtained within this framework, already described the data considerably well, the solution shown barely differs from the one published in [H$^+$08b], confirming the results obtained from the partial wave analysis of the unpolarized data for the reaction $\gamma p \to p\pi^0\eta$ [Sar10]. This includes the necessity for a second D_{33}-resonance, $\Delta(1940)$, in addition to the $\Delta(1700)D_{33}$ dominating the reaction at threshold, as well as decay couplings of participating resonances to pa_0 and $N(1535)\pi^0$ (see table 8.1).

Fix isobar model Unlike the BnGa-PWA results shown in figures 8.4-8.7, where the presented data was included in the fit, the isobar model developed by Fix *et al.* provides predictions for the beam asymmetries. It is based on a single-resonance model developed in [KF$^+$09] for data on the unpolarized $\gamma p \to p\pi^0\eta$ cross section for low and intermediate energies [FKLO10]. In an isobar formalism the production of two mesons is described via successive two-body decays, the quasi two-body states being the isobars. In this model these are $N(1535)S_{11}\pi^0$ and $\Delta(1232)P_{33}\eta$, with these resonances subsequently decaying into $p\eta$ and $p\pi^0$, respectively. The $pa_0(980)$ isobar is assumed to not contribute [FKLO10]. Additionally, only the isospin $I = 3/2$ channel is considered for the initial resonance produced. It is to be noted that this model has been developed in order to describe data only up to an incoming photon energy of $E_\gamma = 1400\,\mathrm{MeV}$. The relevant resonant contributions and their decays are again given in table 8.1. For further information on the model and its theoretical basis, see [FOT08, FKLO10].
Especially in the low-energy bin but extending to the intermediate energies, the Fix-model describes the data quite well, further confirming the $\Delta(1700)D_{33}$-dominance at lower energies as first claimed by the Valencia group in [DOS06]. Going to the highest bin however, the agreement between model and data gets increasingly worse. This is most notable in the case of the η being treated as the recoiling particle, where the model fails to reproduce the large positive asymmetries in the quasi two-body case (figures 8.4, 8.5), leading to a wrong baseline for the asymmetry I^c (figure 8.6). This is also, to a lesser extend, true for the case of the proton recoiling. For I^s (figure 8.7), and here especially for the recoiling π^0, the model underestimates the amplitude of the asymmetry and seems out of phase in the η-recoil case.
In [FKLO10], the authors claim again the necessity for a second D_{33}-resonance, the $\Delta(1940)$, reported first by the Bonn-Gatchina-PWA group in [H$^+$08a], in order to describe the data. In their publication they also give alternative solutions with varied parameters, yielding a worse agreement with the data already at lower energies. The problem at higher energies is not addressed, and it is, at this point, difficult to predict the impact of for example the $pa_0(980)$ couplings or contributions from isospin $I = 1/2$ resonances within this framework [Fix10].

Valencia chiral unitary model The Valencia model is based on the assumption of certain resonances, for example the $N(1535)S_{11}$ and the $\Delta(1700)D_{33}$, being dynamically generated by meson-baryon interactions. These are treated in a unitarized chiral Lagrangian formalism [DOS06]. In this ansatz, only the excitation of the $\Delta(1700)D_{33}$ resonance is relevant for $\pi^0\eta$ photoproduction, however not only couplings of this resonance

to $\Delta\eta$ and $S_{11}\pi^0$ are considered, but also the intermediate formation of for example a $K\Sigma(1385)$ state, subsequently decaying to $S_{11}\pi^0$ is incorporated. The formation of a pa_0-state however is not included in this model. A comparison of the predictions to the results of this work has already been presented in [DOM10], illustrating the effects of for example the $\Delta(1700) - \eta\Delta$- and$\Delta(1700) - K\Sigma(1385)$-couplings on the beam asymmetries.
In the low-energy region, where the reaction $\gamma p \rightarrow p\pi^0\eta$ is dominated by the excitation of the $\Delta(1700)D_{33}$, the Valencia model shows very good agreement with the data for all observables. Beginning at intermediate energies two distinct features however become apparent. As for the Fix isobar model, the positive quasi two-body asymmetries in the case of the recoiling η are not reproduced (figures 8.4, 8.5), leading also to a shift in the baseline for I^c_η (figure 8.6). Additionally, while the description of Σ_π is widely satisfactory, the three-body asymmetries I^c_π and I^s_π do not exhibit any ϕ^*-dependence. For high energies the agreement between data and model becomes again somewhat worse, although, especially in the case of the recoiling proton, the main features are widely reproduced.
In [DOM10] the authors provide additional predictions, obtained by excluding certain $\Delta(1700)D_{33}$-couplings. A satisfactory description of the data can only be achieved by including couplings to $\Delta\eta$ and $K\Sigma(1385)$, both derived from their model based on the dynamical generation of the $\Delta(1700)D_{33}$. The poor agreement between the predictions and the data towards higher excitation-energies though proves that a full description of the process by just one dominating resonance is only sufficient in the threshold region.

Figures 8.4-8.7 show the beam asymmetries obtained in the analysis presented in this work in comparison to the latest BnGa-PWA fit and the recent predictions derived from the Fix and Valencia models.

Resonance	Decay modes	
	BnGa-PWA	Fix *et al.*
N(1880)P_{11}	pa_0(980), N(1535)π^0	not included
N(2200)P_{13}	pa_0(980), N(1535)π^0	not included
Δ(1750)P_{31}	not included	Δ(1232)η, N(1535)π^0
Δ(1600)P_{33}	Δ(1232)η	Δ(1232)η, N(1535)π^0
Δ(1920)P_{33}	pa_0(980), Δ(1232)η	Δ(1232)η, N(1535)π^0
Δ(1700)D_{33}	Δ(1232)η, N(1535)π^0	Δ(1232)η, N(1535)π^0
Δ(1940)D_{33}	pa_0(980), Δ(1232)η, N(1535)π^0	Δ(1232)η, N(1535)π^0
Δ(2360)D_{33}	pa_0(980), Δ(1232)η, N(1535)π^0	not included
Δ(1905)F_{35}	Δ(1232)η, N(1535)π^0	Δ(1232)η, N(1535)π^0
background contributions	t-channel ρ/ω-exchange u-channel p/Δ-exchange	Born terms

Table 8.1: **Resonant contributions to the p$\pi^0\eta$ final state within the BnGa-PWA and the isobar model developed by Fix *et al.*** Note that for the Fix-model, with the exception of the $\Delta(1600)P_{33}$ all resonances dominantly decay to $\Delta\eta$. For details see [H$^+$08b, FKLO10].

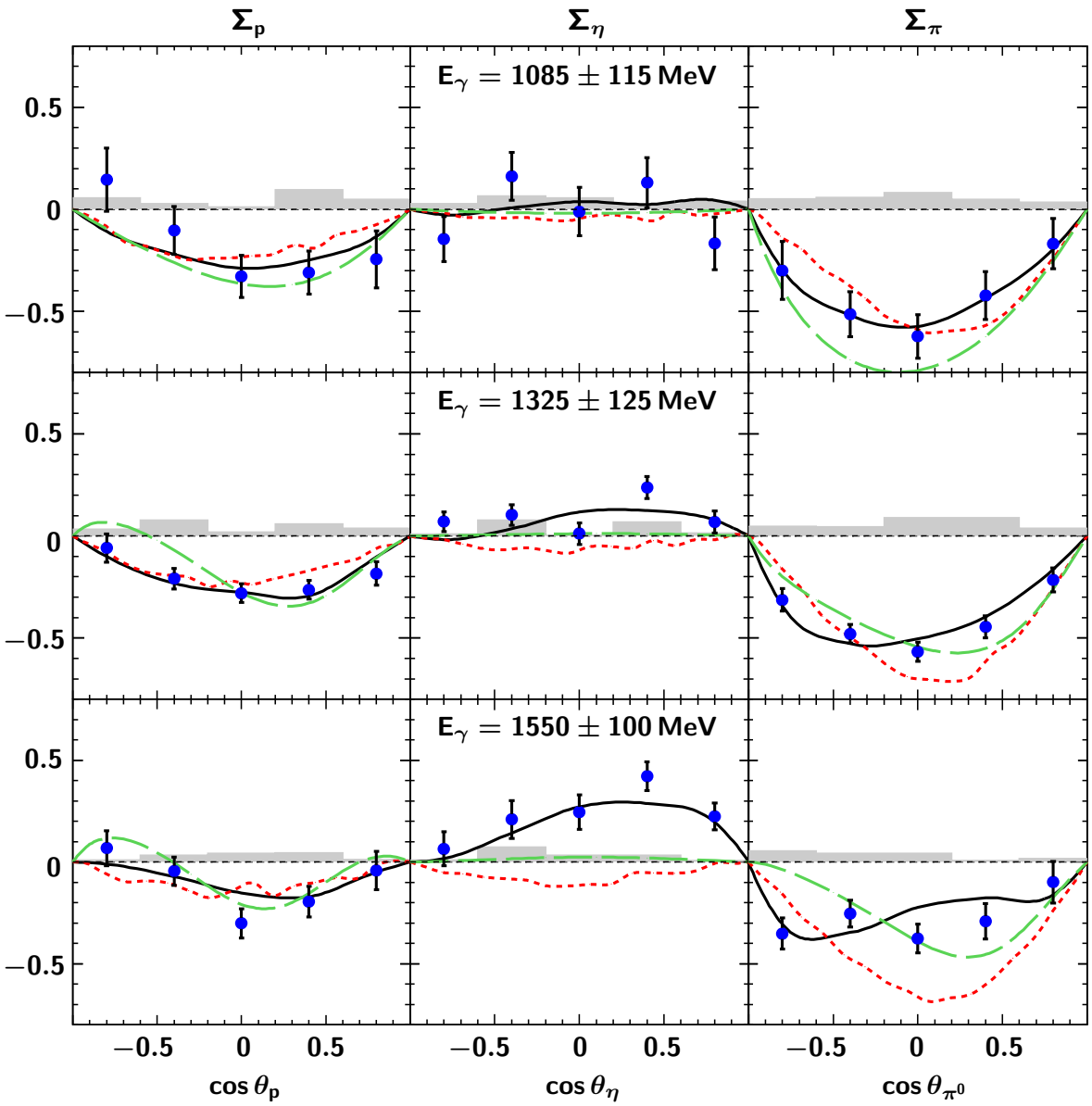

Figure 8.4: **The beam asymmetry Σ as function of $\cos\theta$.** Left to right: Beam asymmetries derived from the ϕ-distribution of the final state proton, η, and π^0, respectively, as functions of the corresponding $\cos\theta$ in the center-of-momentum frame. Grey bars: Estimate of systematic errors due to acceptance and efficiency. Solid ([BLACK]) line: BnGa-PWA, short-dashed ([RED]) line: Valencia chiral unitary model [DOM10], long-dashed ([GREEN]) line: Fix isobar model [FKLO10, Fix10].

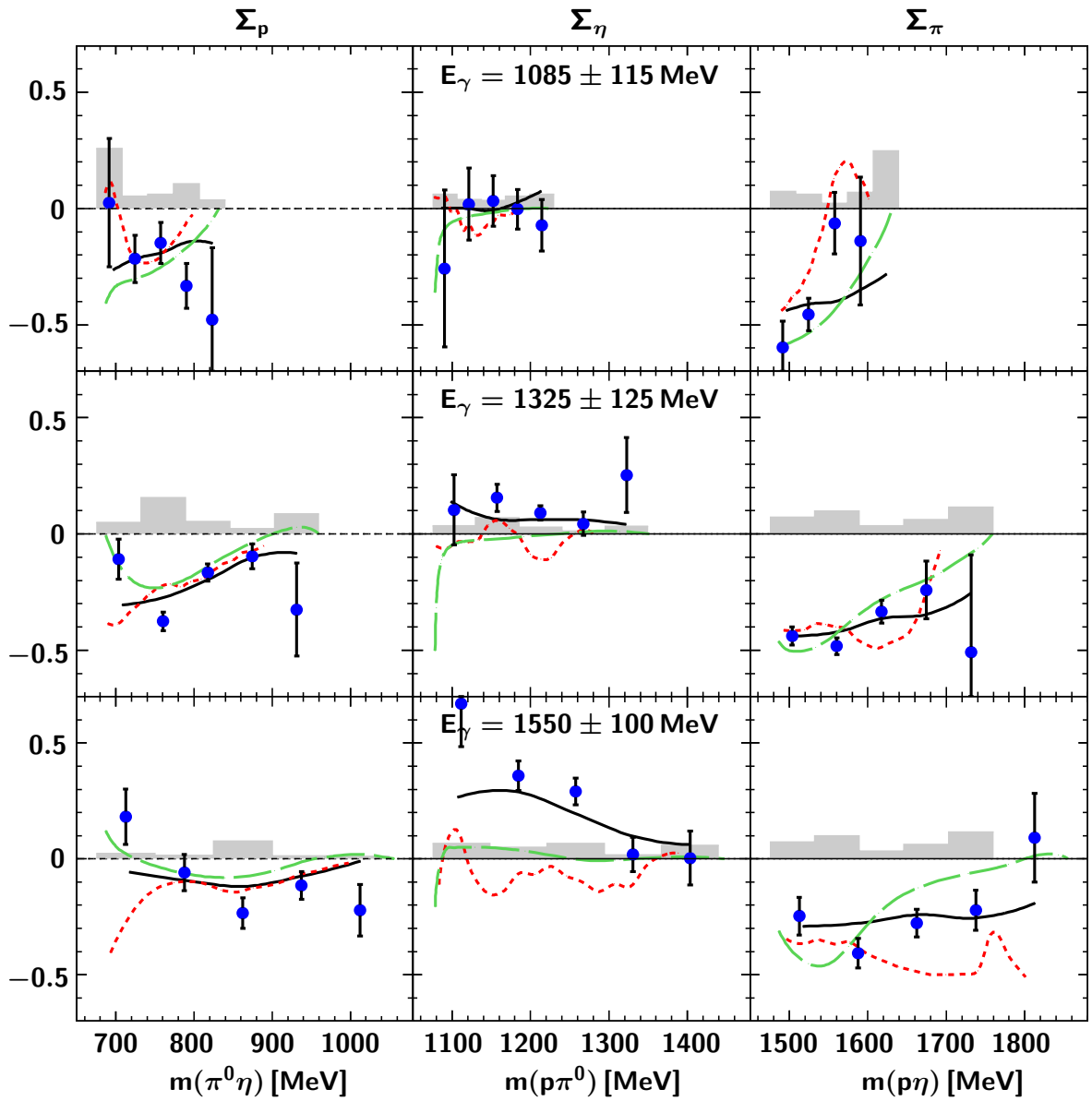

Figure 8.5: **The beam asymmetry Σ as function of invariant mass.** Left to right: Beam asymmetries derived from the ϕ-distribution of the final state proton, η and π^0, respectively, as functions of the invariant mass of the remaining two final state particles. Grey bars: Estimate of systematic errors due to acceptance and efficiency. Solid ([BLACK]) line: BnGa-PWA, short-dashed ([RED]) line: Valencia chiral unitary model [A^+08a, Dör10], long-dashed ([GREEN]) line: Fix isobar model [FKLO10, Fix10].

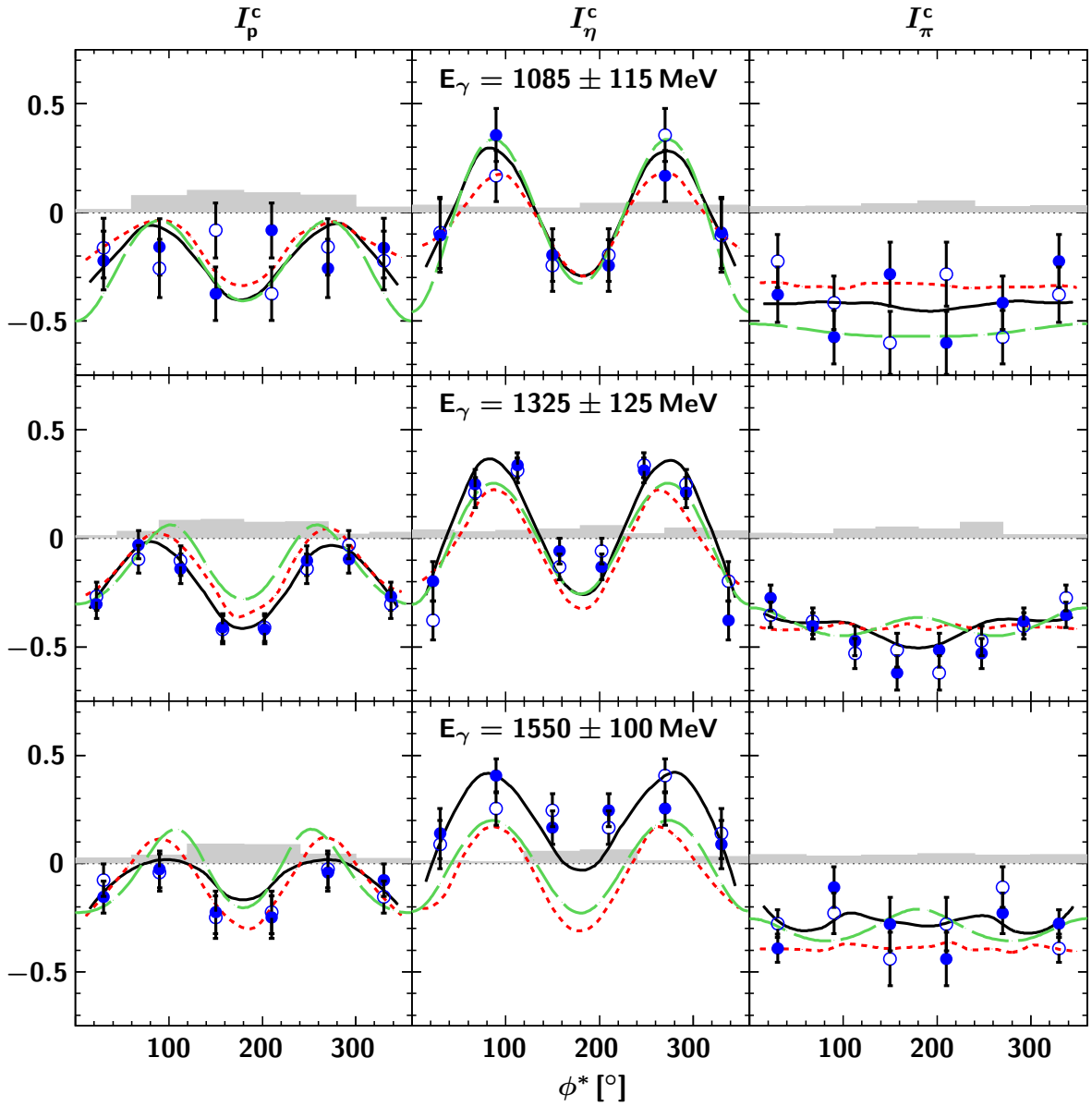

Figure 8.6: **The beam asymmetry I^c.** Left to right: Beam asymmetries derived from the ϕ-distribution of the final state proton, η and π^0, respectively, as functions of the angle ϕ^*. Filled symbols: Beam asymmetry $I^c(\phi^*)$ as derived from the data. Open symbols: $I^c(2\pi - \phi^*)$. Grey bars: Estimate of systematic errors due to acceptance and efficiency. Solid ([BLACK]) line: BnGa-PWA, short-dashed ([RED]) line: Valencia chiral unitary model [DOM10], long-dashed ([GREEN]) line: Fix isobar model [FKLO10, Fix10].

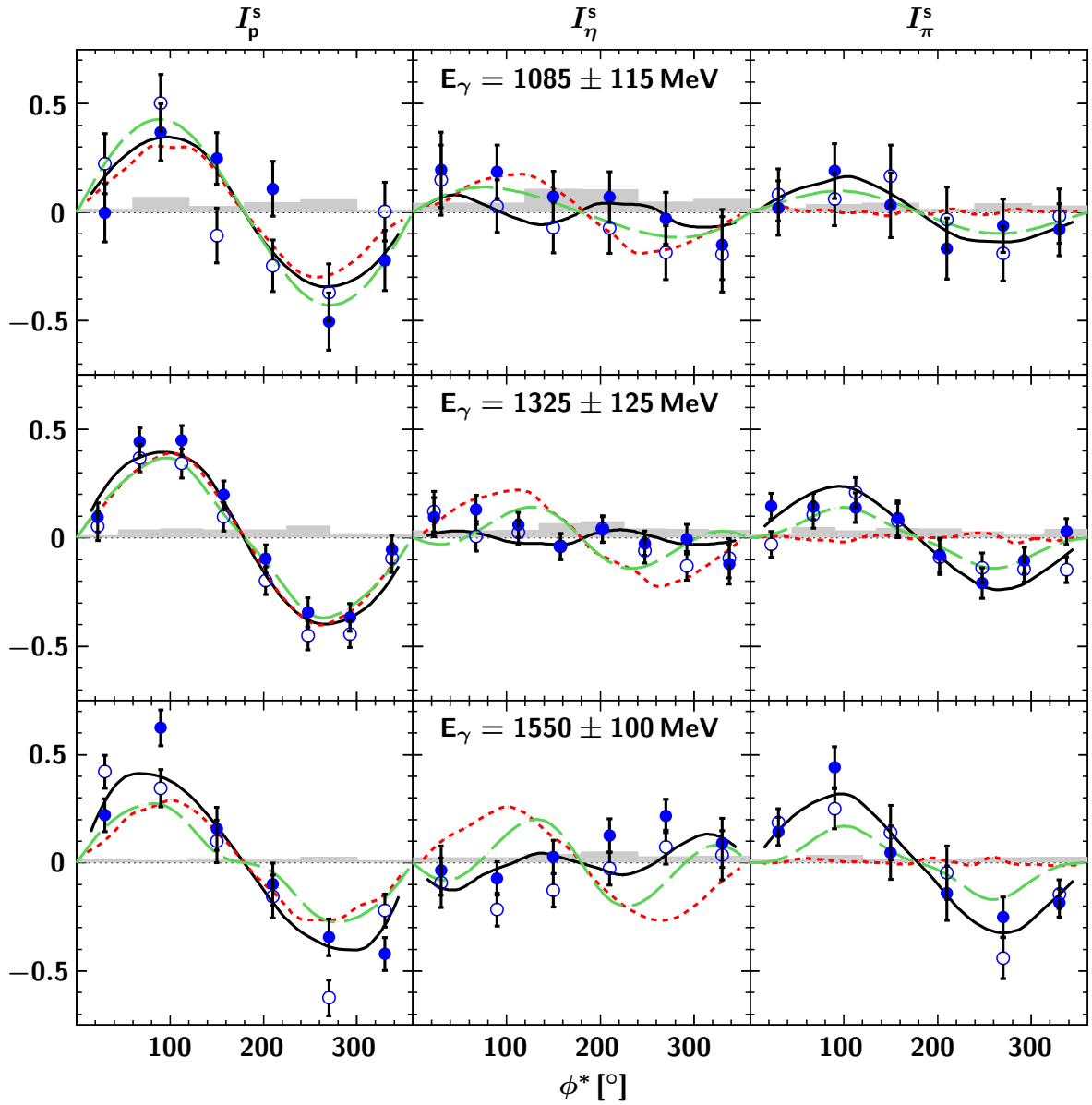

Figure 8.7: **The beam asymmetry I^s.** Left to right: Beam asymmetries derived from the ϕ-distribution of the final state proton, η and π^0, respectively, as functions of the angle ϕ^*. Filled symbols: Beam asymmetry $I^s(\phi^*)$ as derived from the data. Open symbols: $-I^s(2\pi - \phi^*)$. Grey bars: Estimate of systematic errors due to acceptance and efficiency. Solid ([BLACK]) line: BnGa-PWA, short-dashed ([RED]) line: Valencia chiral unitary model [DOM10], long-dashed ([GREEN]) line: Fix isobar model [FKLO10, Fix10].

The comparison of the theoretical approaches used for the interpretation of the data on the beam asymmetries shows the complexity of the reaction $\gamma p \rightarrow p\pi^0\eta$, once the incoming photon energy sufficiently exceeds the threshold energy for the process. A good description at low energies is already achieved by including just one resonant process, the excitation of the $\Delta(1700)D_{33}$, dominating the threshold region, as first introduced by the Valencia group in [DOS06]. The results are also consistent with the assumption that this resonance is in fact dynamically generated by meson-baryon interactions, as claimed by the same group. The further dominance of the D_{33} partial wave, at higher energies populated by the $\Delta(1940)D_{33}$, first claimed by the BnGa-PWA group in [H$^+$08a], is confirmed by the Fix-model. The poor agreement between the models, as opposed to the partial wave analysis, and the data in the high-energy bin however leads to the conclusion, that additional contributions have to be considered for the reaction. Those may include decay couplings of the participating resonances to $pa_0(980)$ as well as excited isospin $I = 1/2$ states.

9 Conclusions and outlook

In this work, the analysis of data taken with the Crystal Barrel/TAPS experiment at the ELSA accelerator facility in Bonn with respect to the photoproduction of $\pi^0\eta$-pairs off the proton has been presented. The data has been obtained, using linearly polarized photons produced from a primary electron beam with an energy of 3.2 GeV via the process of coherent bremsstrahlung. For the extraction of polarization observables, a data sample of approximately 65.000 events for the reaction $\gamma p \rightarrow p\pi^0\eta$ has been selected for an incoming photon energy range of $970\,\text{MeV} \leq E_\gamma \leq 1650\,\text{MeV}$.

The quasi two-body beam asymmetry Σ has been extracted for all three final state particles as a function of various angles and invariant masses. Data on this asymmetry as a function of invariant masses, published by the GRAAL collaboration for an incoming photon energy range of $1100\,\text{MeV} \leq E_\gamma \leq 1500\,\text{MeV}$, is in excellent agreement with the results presented here.
The full three-body final state beam asymmetries I^c and I^s have been determined for the first time for any two-meson final state. Thus, the complete set of polarization observables accessible for the reaction $\gamma p \rightarrow p\pi^0\eta$, using a linearly polarized photon beam and unpolarized target, has been measured.
Additionally, invariant mass distributions and Dalitz plots for an energy range from threshold up to 2500 MeV have been presented, illustrating the complex structure of the $p\pi^0\eta$ final state with respect to the contributing intermediate states $pa_0(980)$, $\Delta(1232)\pi^0$ and $S_{11}(1535)\eta$.

Some open questions in hadron physics accessible in two-meson photoproduction in general and the production of $\pi^0\eta$-pairs in particular could be addressed by comparing the data with the results of three different theoretical frameworks. Here, aspects like the D_{33} partial wave dominance in the reaction could be confirmed, which is manifest in the need for the $\Delta(1700)D_{33}$- and $\Delta(1940)D_{33}$-states. The problems of certain model-approaches to describe the data at higher excitation energies point to an even more complex structure of the processes involved. Here couplings of participating resonances to $pa_0(980)$ as well as the participation of isospin $I = 1/2$ resonances might have to be considered.

Continuing analyses within the theoretical frameworks presented here, for example the event-based inclusion of the presented data in the BnGa-PWA, as well as upcoming models will shed more light on these questions. Further experiments providing higher statistics on the reaction $\gamma p \to p\pi^0\eta$ are desirable to allow for a binning of the three-body asymmetries I^c and I^s in additional variables and to test the theoretical models even more thoroughly.

The topic of polarization observables and the photoproduction of meson pairs remains a fascinating field of research with a high potential for gaining a better understanding of the physics of hadrons. Experiments using linearly and circularly polarized beams and longitudinally and transversely polarized targets, like the Crystal Barrel/TAPS experiment in Bonn, now have access to a multitude of observables and will continue to provide valuable information to fix the spectrum and properies of baryon resonances.

A Beam asymmetry data points

$\cos\theta_{\mathrm{p}}$	Σ_{p}	$\Delta(\Sigma_{\mathrm{p}})_{\mathrm{stat}}$	$\Delta(\Sigma_{\mathrm{p}})_{\mathrm{sys}}$	$m(\pi^0\eta)$ [MeV]	Σ_{p}	$\Delta(\Sigma_{\mathrm{p}})_{\mathrm{stat}}$	$\Delta(\Sigma_{\mathrm{p}})_{\mathrm{sys}}$
$E_\gamma = 1085 \pm 115\,\mathrm{MeV}$							
-0.80	0.145228	0.154078	0.055593	691.5	0.024927	0.275407	0.258173
-0.40	-0.104341	0.117535	0.026900	724.5	-0.216493	0.101572	0.053900
0.00	-0.328174	0.103305	0.010300	757.5	-0.148796	0.088402	0.060638
0.40	-0.309937	0.104680	0.095649	790.5	-0.333239	0.096894	0.105825
0.80	-0.245332	0.138622	0.049891	823.5	-0.477480	0.308103	0.035530
$E_\gamma = 1325 \pm 125\,\mathrm{MeV}$							
-0.80	-0.058754	0.069327	0.032872	703.5	-0.108359	0.085554	0.049765
-0.40	-0.209271	0.050561	0.076766	760.5	-0.375685	0.040257	0.156056
0.00	-0.279997	0.045996	0.018045	817.5	-0.165783	0.036636	0.053458
0.40	-0.263880	0.045159	0.058139	874.5	-0.096327	0.053434	0.022892
0.80	-0.184049	0.057087	0.038400	931.5	-0.324845	0.199944	0.086288
$E_\gamma = 1550 \pm 100\,\mathrm{MeV}$							
-0.80	0.067833	0.085565	0.010622	712.5	0.181704	0.118926	0.023561
-0.40	-0.045094	0.068828	0.033830	787.5	-0.059312	0.078596	0.015980
0.00	-0.301180	0.071834	0.042992	862.5	-0.234193	0.065586	0.076317
0.40	-0.193844	0.075200	0.045953	937.5	-0.114146	0.059316	0.012697
0.80	-0.042320	0.094534	0.011630	1012.5	-0.221567	0.110483	0.010869

Table A.1: **Two-body beam asymmetry Σ_{p}.** The beam asymmetry values are given as a function of $\cos\theta_{\mathrm{p}}$ ([LEFT]) and the $\pi^0\eta$ invariant mass ([RIGHT]). See figures 7.4, 7.6.

$\cos\theta_\eta$	Σ_η	$\Delta(\Sigma_\eta)_{\text{stat}}$	$\Delta(\Sigma_\eta)_{\text{sys}}$	$m(\text{p}\pi)$ [MeV]	Σ_η	$\Delta(\Sigma_\eta)_{\text{stat}}$	$\Delta(\Sigma_{eta})_{\text{sys}}$
$E_\gamma = 1085 \pm 115\,\text{MeV}$							
-0.80	-0.146531	0.110365	0.027037	1090.5	-0.257881	0.337918	0.062098
-0.40	0.161170	0.116453	0.064667	1121.5	0.018701	0.154504	0.039601
0.00	-0.011704	0.118603	0.056724	1152.5	0.031734	0.108645	0.033652
0.40	0.130520	0.123281	0.026366	1183.5	-0.003187	0.085170	0.052603
0.80	-0.166730	0.129358	0.039335	1214.5	-0.072862	0.110594	0.061310
$E_\gamma = 1325 \pm 125\,\text{MeV}$							
-0.80	0.069591	0.048124	0.009158	1102.5	0.103913	0.150369	0.035222
-0.40	0.102427	0.051019	0.077080	1157.5	0.155323	0.057681	0.069500
0.00	0.011473	0.053250	0.002686	1212.5	0.090407	0.030284	0.029830
0.40	0.236442	0.054051	0.067600	1267.5	0.044191	0.050595	0.013190
0.80	0.067999	0.053660	0.014370	1322.5	0.253121	0.160869	0.033860
$E_\gamma = 1550 \pm 100\,\text{MeV}$							
-0.80	0.065273	0.083237	0.011170	1111.5	0.670868	0.185345	0.067004
-0.40	0.209445	0.093367	0.073393	1184.5	0.359683	0.063978	0.049309
0.00	0.244779	0.084511	0.033500	1257.5	0.290467	0.057297	0.066093
0.40	0.422241	0.070821	0.034600	1330.5	0.018965	0.074585	0.017550
0.80	0.224294	0.065418	0.008200	1403.5	0.003379	0.116248	0.057342

Table A.2: **Two-body beam asymmetry Σ_η.** The beam asymmetry values are given as a function of $\cos\theta_\eta$ ([LEFT]) and the $\text{p}\pi^0$ invariant mass ([RIGHT]). See figures 7.4, 7.6.

$\cos\theta_\pi$	Σ_π	$\Delta(\Sigma_\pi)_{\text{stat}}$	$\Delta(\Sigma_\pi)_{\text{sys}}$	$m(\text{p}\eta)$ [MeV]	Σ_π	$\Delta(\Sigma_\pi)_{\text{stat}}$	$\Delta(\Sigma_\pi)_{\text{sys}}$
$E_\gamma = 1085 \pm 115\,\text{MeV}$							
-0.80	-0.299940	0.141949	0.051487	1491.5	-0.597769	0.113034	0.072579
-0.40	-0.514620	0.110197	0.057576	1524.5	-0.456010	0.069288	0.060810
0.00	-0.622264	0.107054	0.080919	1557.5	-0.063295	0.132063	0.021200
0.40	-0.422171	0.117425	0.048000	1590.5	-0.139903	0.274024	0.069577
0.80	-0.168803	0.123038	0.034109	1623.5	0.720708	1.075660	0.247275
$E_\gamma = 1325 \pm 125\,\text{MeV}$							
-0.80	-0.313620	0.055179	0.046300	1503.5	-0.439144	0.038999	0.073087
-0.40	-0.479484	0.046310	0.044824	1560.5	-0.482071	0.036007	0.099859
0.00	-0.566781	0.047135	0.090380	1617.5	-0.334156	0.049729	0.034300
0.40	-0.445107	0.052955	0.090128	1674.5	-0.240763	0.123835	0.061700
0.80	-0.215775	0.058792	0.038530	1731.5	-0.508486	0.417589	0.115600
$E_\gamma = 1550 \pm 100\,\text{MeV}$							
-0.80	-0.351726	0.076090	0.054600	1512.5	-0.246747	0.081265	0.037711
-0.40	-0.253762	0.065984	0.043162	1587.5	-0.407502	0.064377	0.059657
0.00	-0.376694	0.070413	0.043272	1662.5	-0.277923	0.059726	0.031939
0.40	-0.291627	0.086808	0.008900	1737.5	-0.221801	0.087259	0.040806
0.80	-0.098437	0.102371	0.016727	1812.5	0.090842	0.191130	0.062436

Table A.3: **Two-body beam asymmetry Σ_{π^0}.** The beam asymmetry values are given as a function of $\cos\theta_{\pi^0}$ ([LEFT]) and the pη invariant mass ([RIGHT]). See figures 7.4, 7.6.

ϕ^* [°]	I_{p}^c	$\Delta(I_{\mathrm{p}}^c)_{\mathrm{stat}}$	$\Delta(I_{\mathrm{p}}^c)_{\mathrm{sys}}$	I_{p}^s	$\Delta(I_{\mathrm{p}}^s)_{\mathrm{stat}}$	$\Delta(I_{\mathrm{p}}^s)_{\mathrm{sys}}$
$E_\gamma = 1085 \pm 115\,\mathrm{MeV}$						
30.00	-0.221727	0.135888	0.011800	-0.002915	0.134390	0.013090
90.00	-0.158597	0.129852	0.075775	0.369107	0.131274	0.067550
150.0	-0.374261	0.122431	0.100800	0.247185	0.118447	0.026100
210.0	-0.082350	0.126153	0.089300	0.107738	0.126708	0.044600
270.0	-0.258322	0.134153	0.077720	-0.503513	0.132315	0.055900
330.0	-0.163854	0.136773	0.024700	-0.223122	0.138595	0.011300
$E_\gamma = 1325 \pm 125\,\mathrm{MeV}$						
22.5	-0.302428	0.065853	0.010850	0.094128	0.066461	0.009350
67.5	-0.029712	0.064383	0.030610	0.442825	0.063391	0.035623
112.5	-0.140093	0.068234	0.080815	0.449206	0.067686	0.040700
157.5	-0.410206	0.063465	0.085300	0.197607	0.064490	0.034705
202.5	-0.420373	0.064824	0.073400	-0.096702	0.064931	0.035800
247.5	-0.103309	0.067488	0.074630	-0.342822	0.067146	0.052150
292.5	-0.095431	0.063743	0.016935	-0.367220	0.064131	0.018750
337.5	-0.266949	0.065445	0.026112	-0.053497	0.065883	0.014733
$E_\gamma = 1550 \pm 100\,\mathrm{MeV}$						
30.00	-0.154556	0.074322	0.025926	0.220537	0.075981	0.016050
90.00	-0.026409	0.085522	0.037841	0.624019	0.083063	0.010300
150.0	-0.225029	0.097872	0.089860	0.156335	0.099358	0.017400
210.0	-0.247731	0.099015	0.086385	-0.098926	0.098100	0.012550
270.0	-0.041444	0.086590	0.042424	-0.344485	0.085878	0.024163
330.0	-0.076097	0.075455	0.022650	-0.421735	0.076019	0.008450

Table A.4: **Three-body beam asymmetry values, I_{p}^c, I_{p}^s as function of ϕ^*.** See figures 7.11, 7.10.

ϕ^* [°]	I_η^c	$\Delta(I_\eta^c)_{\text{stat}}$	$\Delta(I_\eta^c)_{\text{sys}}$	I_η^s	$\Delta(I_\eta^s)_{\text{stat}}$	$\Delta(I_\eta^s)_{\text{sys}}$
$E_\gamma = 1085 \pm 115\,\text{MeV}$						
30.00	-0.105113	0.169477	0.032800	0.194394	0.173727	0.041721
90.00	0.356798	0.122318	0.023500	0.185975	0.123551	0.041722
150.0	-0.196009	0.120246	0.018650	0.071901	0.117146	0.104220
210.0	-0.244845	0.118813	0.042131	0.070264	0.116259	0.103955
270.0	0.168357	0.117397	0.044950	-0.027924	0.120151	0.046750
330.0	-0.093466	0.163142	0.032596	-0.148949	0.161578	0.059741
$E_\gamma = 1325 \pm 125\,\text{MeV}$						
22.5	-0.197031	0.090500	0.038800	0.093916	0.090157	0.031454
67.5	0.249561	0.066301	0.029220	0.129065	0.066260	0.031298
112.5	0.336445	0.057260	0.035757	0.059553	0.057529	0.033704
157.5	-0.059403	0.059982	0.042180	-0.041265	0.059861	0.064984
202.5	-0.131917	0.059422	0.057805	0.038108	0.059346	0.072754
247.5	0.312824	0.057012	0.020105	-0.025102	0.056631	0.039012
292.5	0.210579	0.068614	0.047010	-0.006388	0.068093	0.037554
337.5	-0.377806	0.089007	0.032560	-0.120228	0.092815	0.033396
$E_\gamma = 1550 \pm 100\,\text{MeV}$						
30.00	0.139350	0.116099	0.011750	-0.035511	0.113440	0.023340
90.00	0.405572	0.077530	0.007800	-0.072681	0.077503	0.023134
150.0	0.166505	0.076727	0.055715	0.026650	0.076816	0.038010
210.0	0.246521	0.076165	0.062955	0.127413	0.077122	0.050006
270.0	0.254471	0.076501	0.011300	0.216573	0.076860	0.026546
330.0	0.088470	0.111377	0.030920	0.092033	0.113765	0.029105

Table A.5: **Three-body beam asymmetry values, I_η^c, I_η^s as function of ϕ^*.** See figures 7.11, 7.10.

ϕ^* [°]	I_π^c	$\Delta(I_\pi^c)_{\text{stat}}$	$\Delta(I_\pi^c)_{\text{sys}}$	I_π^s	$\Delta(I_\pi^s)_{\text{stat}}$	$\Delta(I_\pi^s)_{\text{sys}}$
$E_\gamma = 1085 \pm 115\,\text{MeV}$						
30.00	-0.378218	0.127208	0.025399	0.018822	0.125548	0.016438
90.00	-0.573893	0.123072	0.027200	0.189788	0.126656	0.034563
150.0	-0.283492	0.147437	0.039550	0.032843	0.148838	0.040461
210.0	-0.600361	0.144362	0.053000	-0.167537	0.141524	0.012854
270.0	-0.415358	0.122641	0.026650	-0.061376	0.122959	0.038975
330.0	-0.224247	0.122068	0.029500	-0.080252	0.120459	0.028156
$E_\gamma = 1325 \pm 125\,\text{MeV}$						
22.5	-0.274848	0.058958	0.022500	0.146172	0.059058,	0.010296
67.5	-0.403297	0.060477	0.019910	0.144098	0.060251	0.045615
112.5	-0.472535	0.067747	0.042329	0.138508	0.068206	0.030847
157.5	-0.619475	0.078324	0.050867	0.089502	0.080203	0.041104
202.5	-0.514680	0.078421	0.041953	-0.079809	0.078631	0.039828
247.5	-0.529680	0.069395	0.073265	-0.208225	0.069628	0.027637
292.5	-0.381028	0.059474	0.016600	-0.104856	0.060468	0.012050
337.5	-0.352699	0.058586	0.015500	0.029522	0.059249	0.038722
$E_\gamma = 1550 \pm 100\,\text{MeV}$						
30.00	-0.391084	0.065053	0.040950	0.145078	0.065380	0.011115
90.00	-0.108909	0.094063	0.033514	0.441145	0.094698	0.033200
150.0	-0.279185	0.122877	0.037693	0.046095	0.123411	0.016295
210.0	-0.440761	0.124220	0.043951	-0.140301	0.126098	0.013025
270.0	-0.229636	0.093707	0.038528	-0.250564	0.093039	0.023550
330.0	-0.276995	0.064157	0.041150	-0.185470	0.064361	0.024300

Table A.6: **Three-body beam asymmetry values, I_π^c, I_π^s as function of ϕ^*.** See figures 7.11, 7.10.

B ϕ-distributions

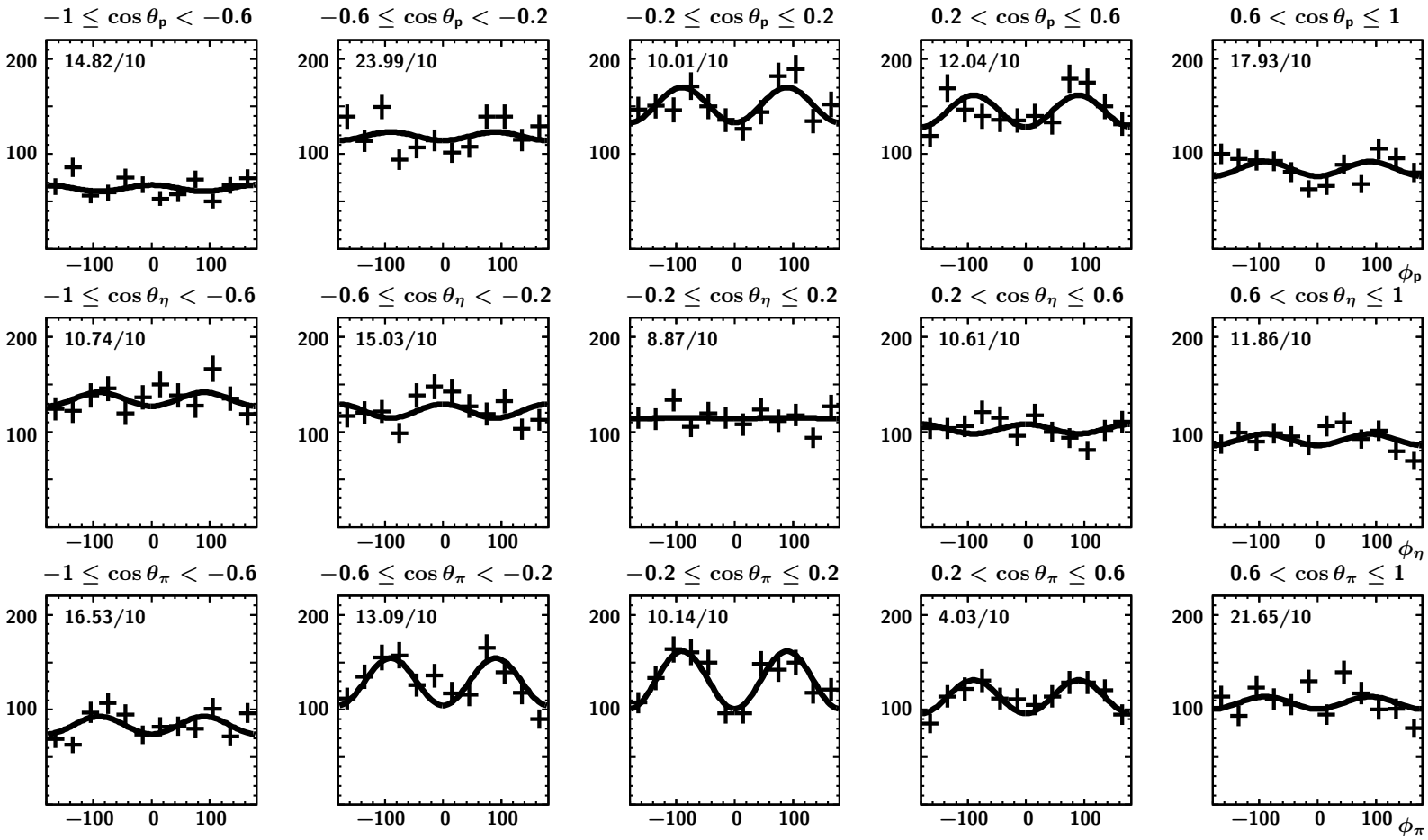

Figure B.1: **ϕ-distributions as function of $\cos\theta$, $E_\gamma = 1085 \pm 115$ MeV.** Top to bottom: ϕ-distributions of the final state proton, η, π^0, binned in $\cos\theta$ of the respective particle. Solid line: Fit according to (7.2). Numbers in each bin give the χ^2/NDF for each fit.

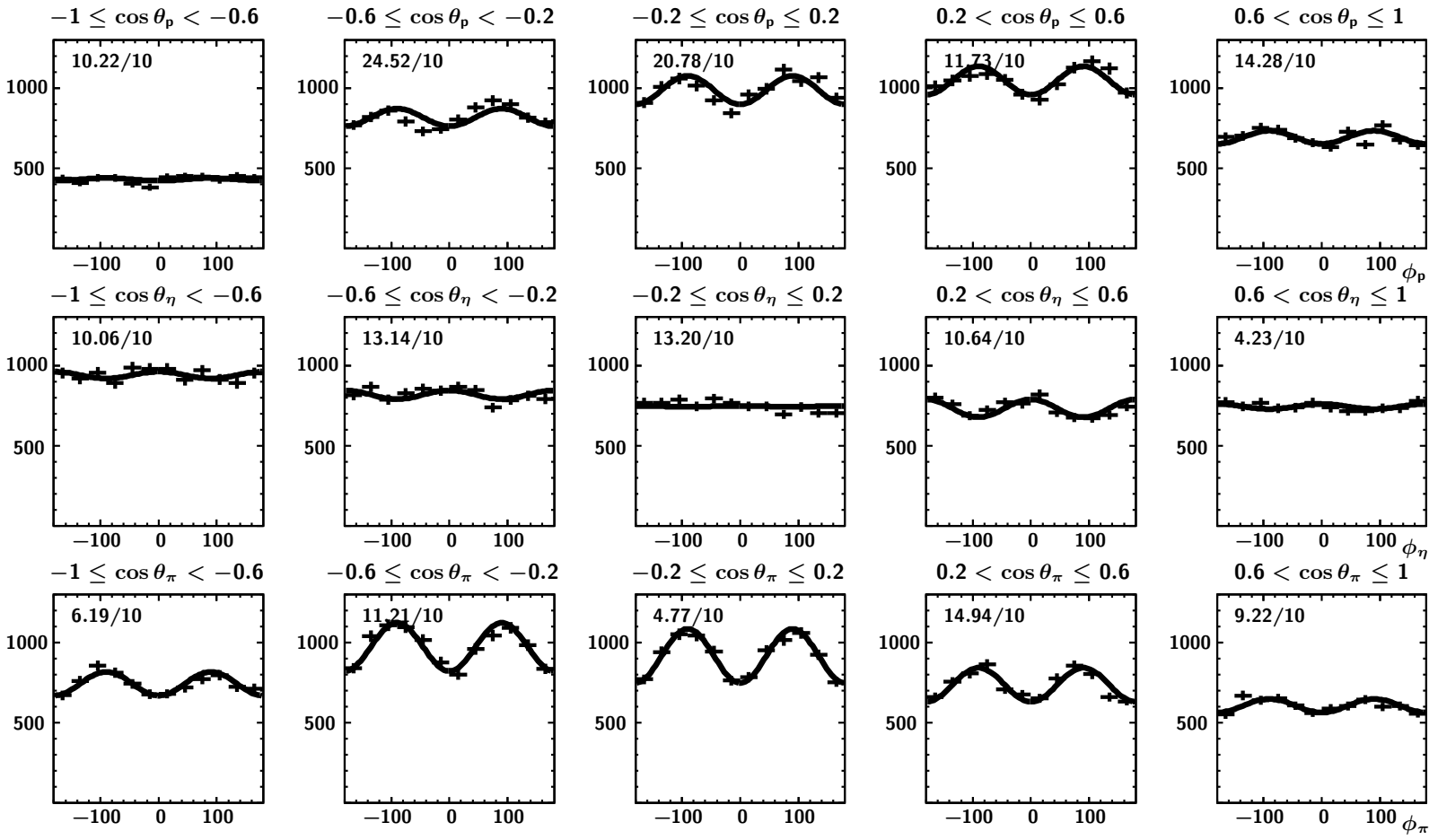

Figure B.2: **ϕ-distributions as function of $\cos\theta$, $E_\gamma = 1325 \pm 125$ MeV.** Top to bottom: ϕ-distributions of the final state proton, η, π^0, binned in $\cos\theta$ of the respective particle. Solid line: Fit according to (7.2). Numbers in each bin give the χ^2/NDF for each fit.

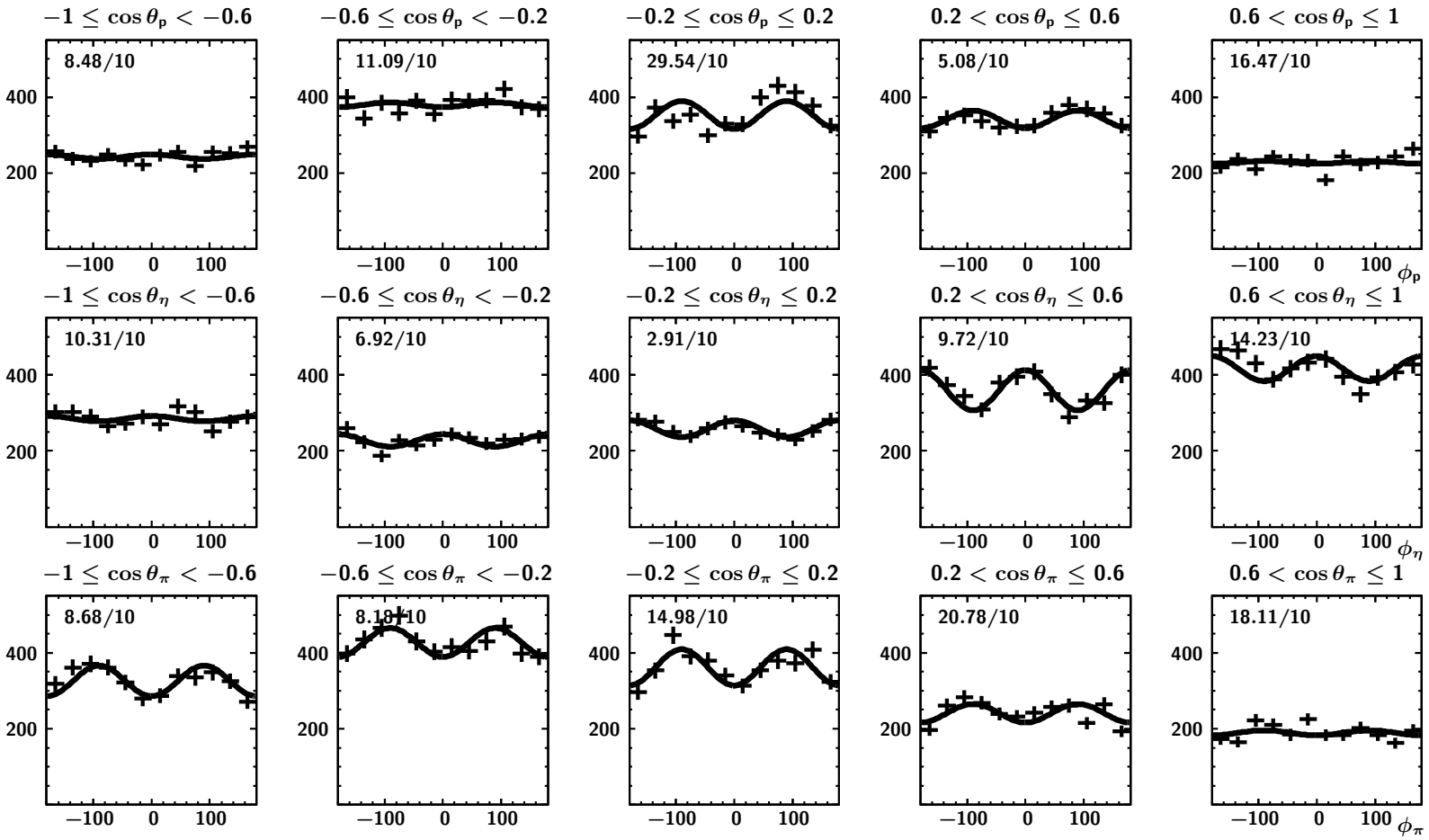

Figure B.3: **ϕ-distributions as function of $\cos\theta$, $E_\gamma = 1550 \pm 100\,\mathrm{MeV}$.** Top to bottom: ϕ-distributions of the final state proton, η, π^0, binned in $\cos\theta$ of the respective particle. Solid line: Fit according to (7.2). Numbers in each bin give the χ^2/NDF for each fit.

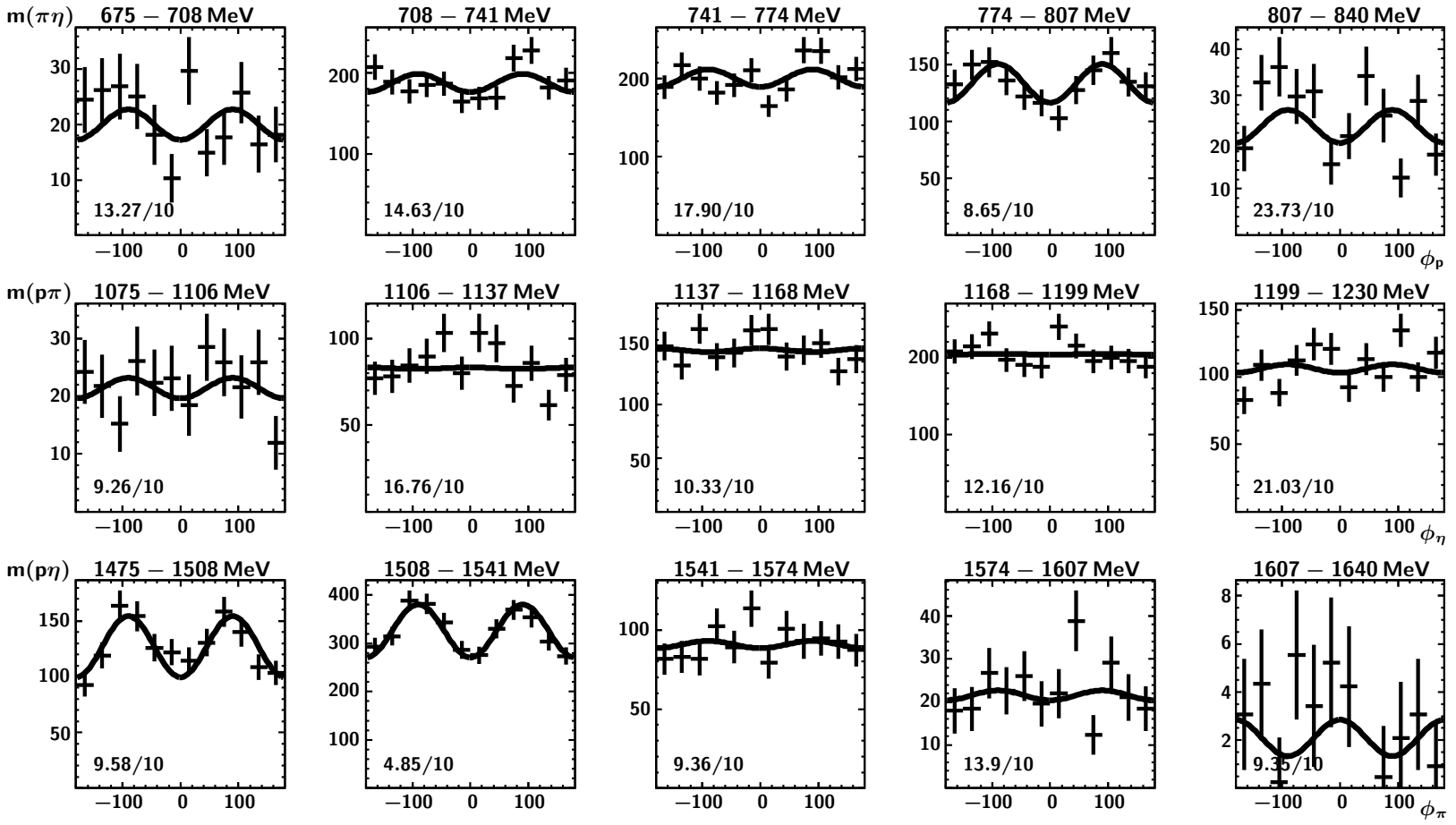

Figure B.4: **ϕ-distributions as function of invariant masses, $E_\gamma = 1085 \pm 115$ MeV.** Top to bottom: ϕ-distributions of the final state proton, η, π^0, binned in the invariant mass of the other pair. Mass ranges are given on top of each panel. Solid line: Fit according to (7.2). Numbers in each bin give the χ^2/NDF for each fit.

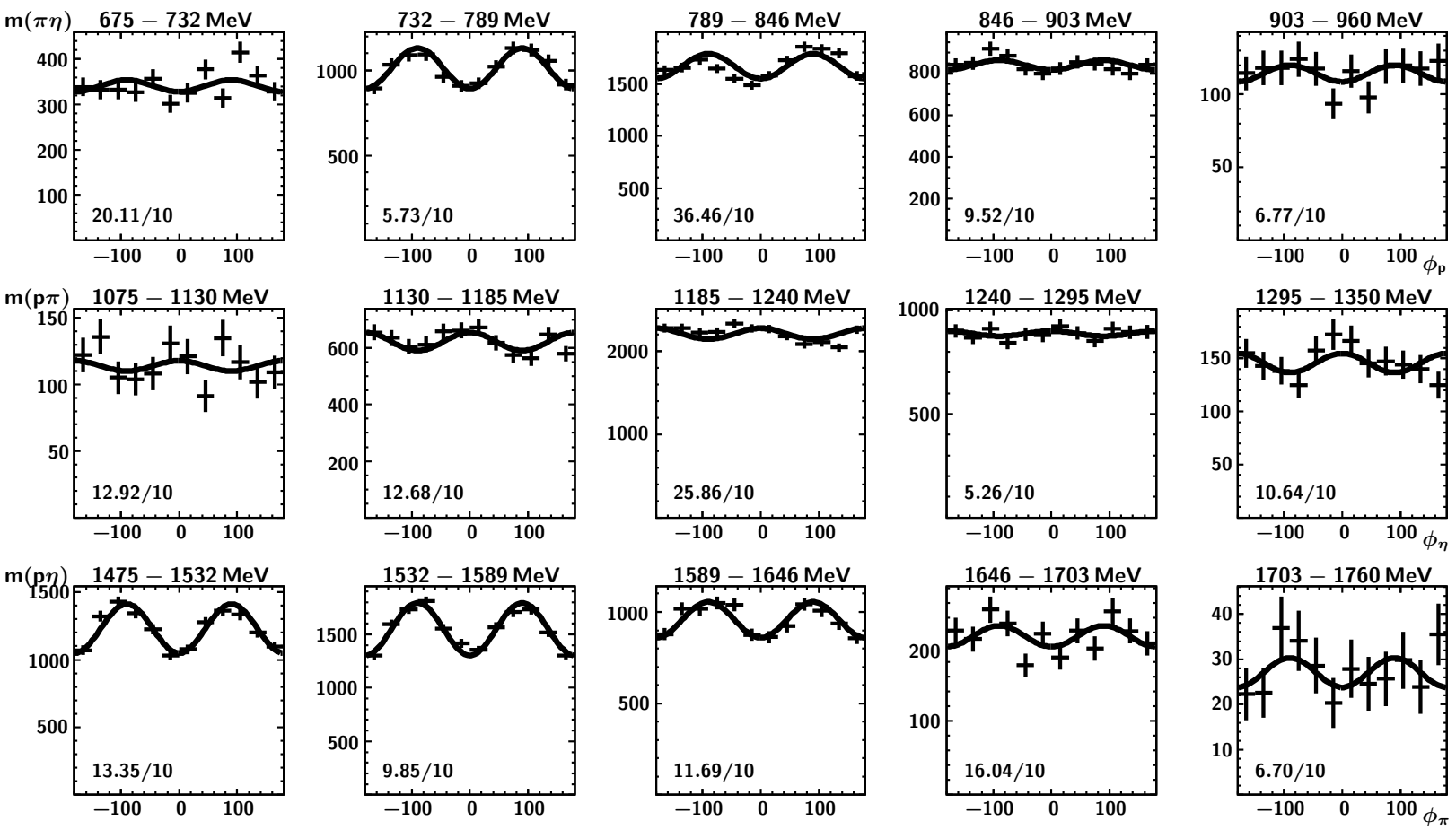

Figure B.5: **ϕ-distributions as function of invariant masses, $E_\gamma = 1325 \pm 125$ MeV.** Top to bottom: ϕ-distributions of the final state proton, η, π^0, binned in the invariant mass of the other pair. Mass ranges are given on top of each panel. Solid line: Fit according to (7.2). Numbers in each bin give the χ^2/NDF for each fit.

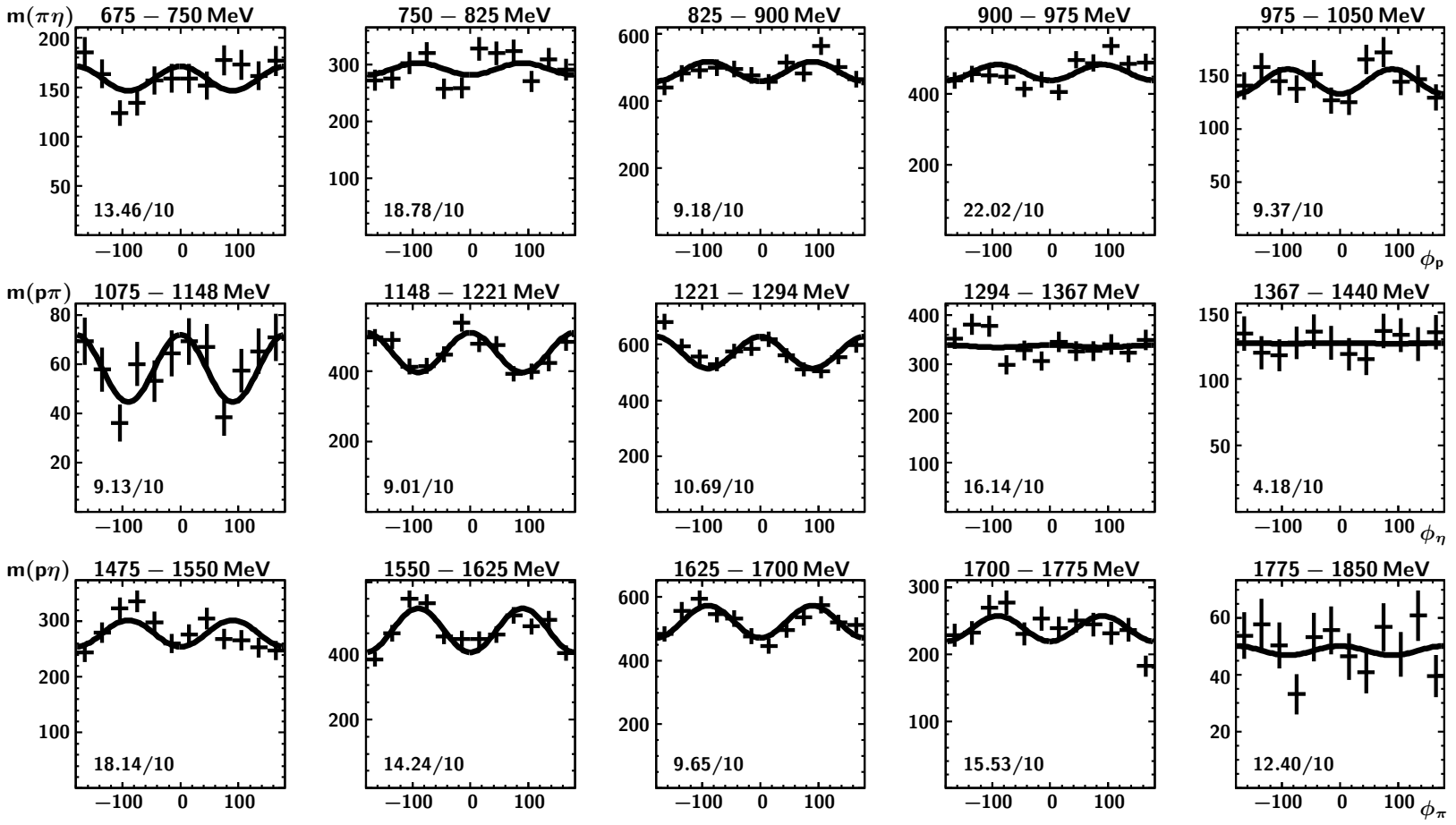

Figure B.6: **ϕ-distributions as function of invariant masses, $E_\gamma = 1550 \pm 100$ MeV.** Top to bottom: ϕ-distributions of the final state proton, η, π^0, binned in the invariant mass of the other pair. Mass ranges are given on top of each panel. Solid line: Fit according to (7.2). Numbers in each bin give the χ^2/NDF for each fit.

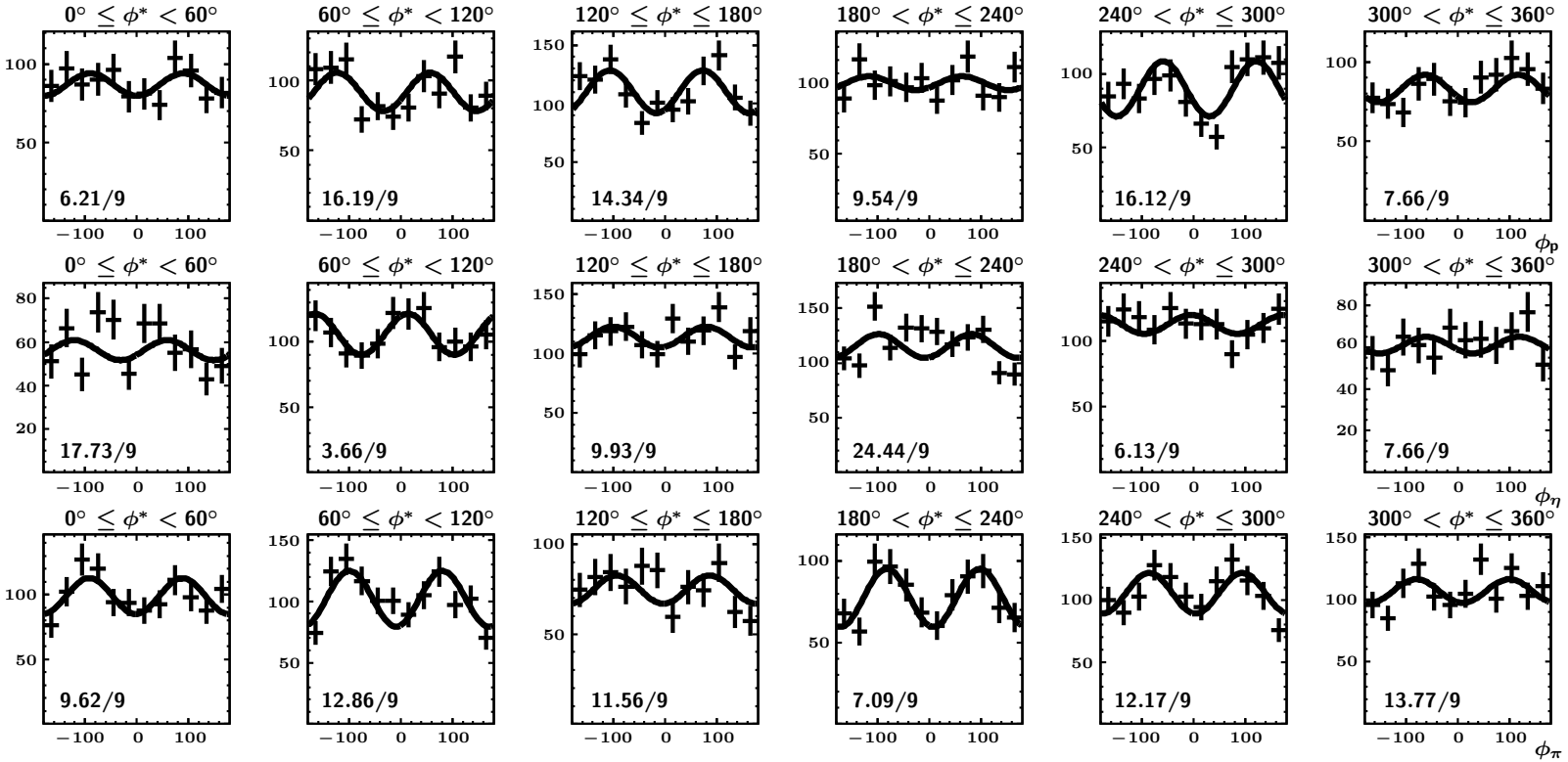

Figure B.7: **ϕ-distributions as function of ϕ^*, $E_\gamma = 1085 \pm 115$ MeV.** Top to bottom: ϕ-distributions of the final state proton, η, π^0. Solid line: Fit according to (7.11). Numbers in each bin give the χ^2/NDF for each fit.

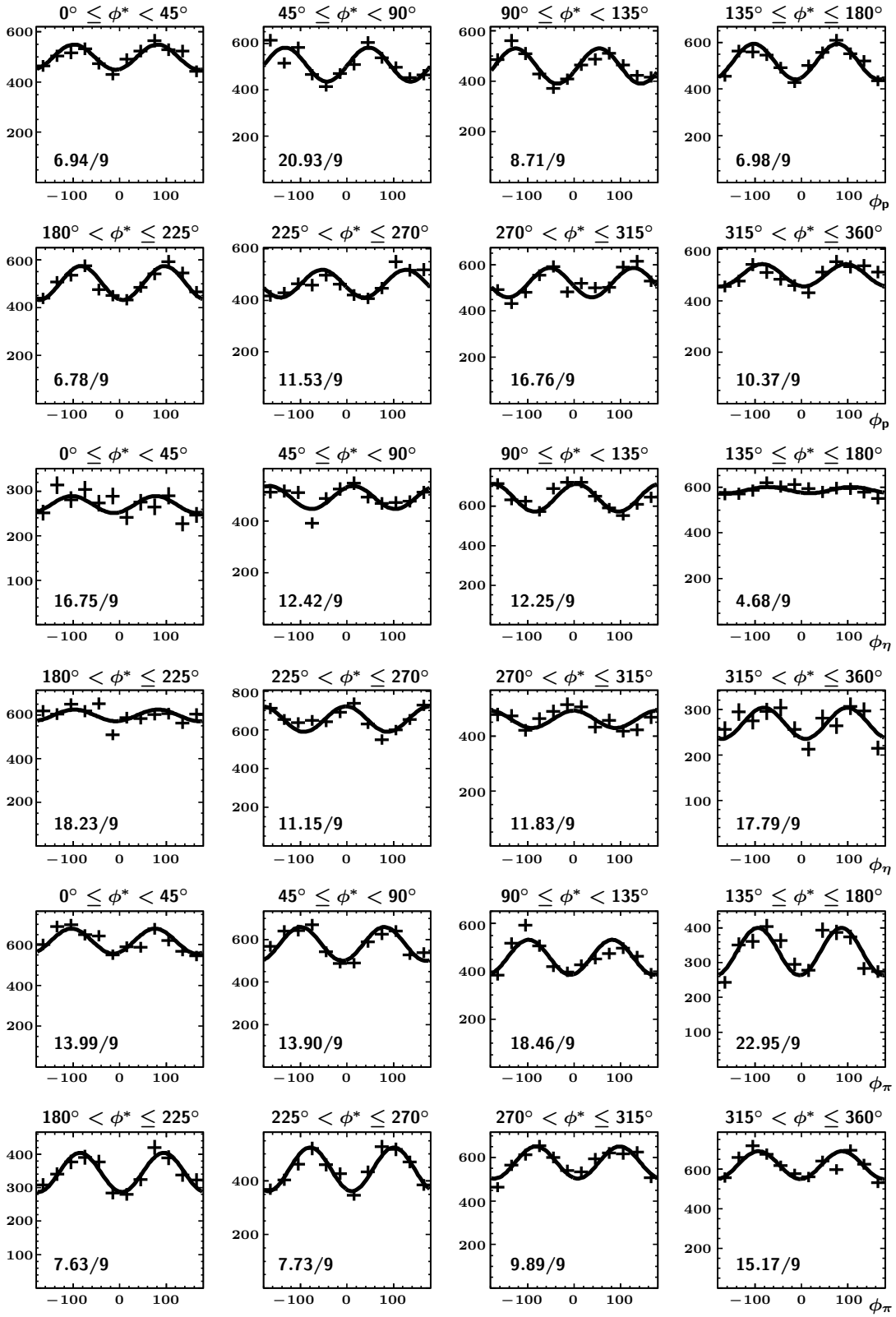

Figure B.8: **ϕ-distributions as function of ϕ^*, $E_\gamma = 1325 \pm 125$ MeV.** Top to bottom: ϕ-distributions of the final state proton, η, π^0. Solid line: Fit according to (7.11). Numbers in each bin give the χ^2/NDF for each fit.

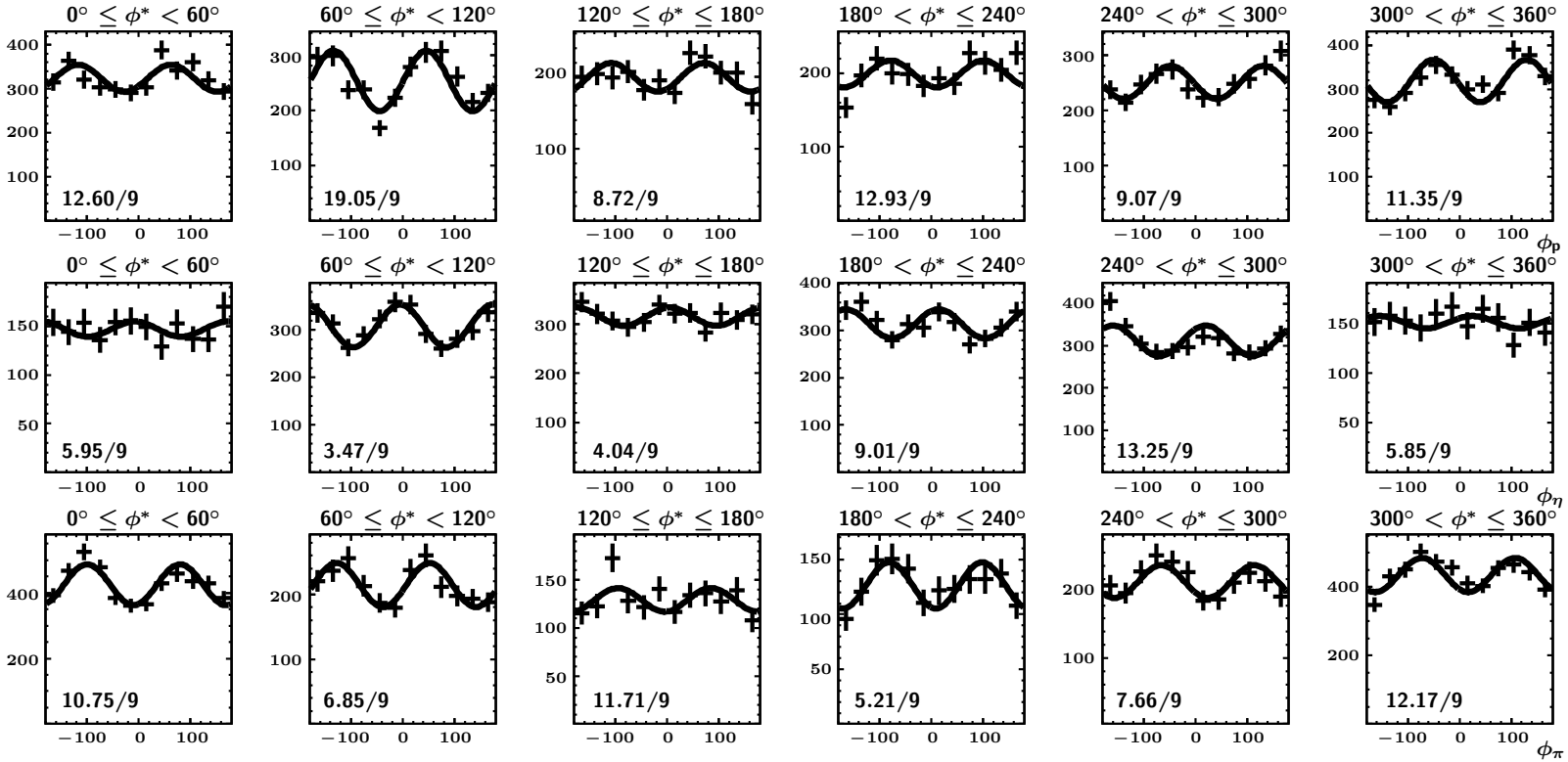

Figure B.9: **ϕ-distributions as function of ϕ^*, $E_\gamma = 1550 \pm 100\,\mathrm{MeV}$.** Top to bottom: ϕ-distributions of the final state proton, η, π^0. Solid line: Fit according to (7.11). Numbers in each bin give the χ^2/NDF for each fit.

C Invariant mass distributions and Dalitz plots

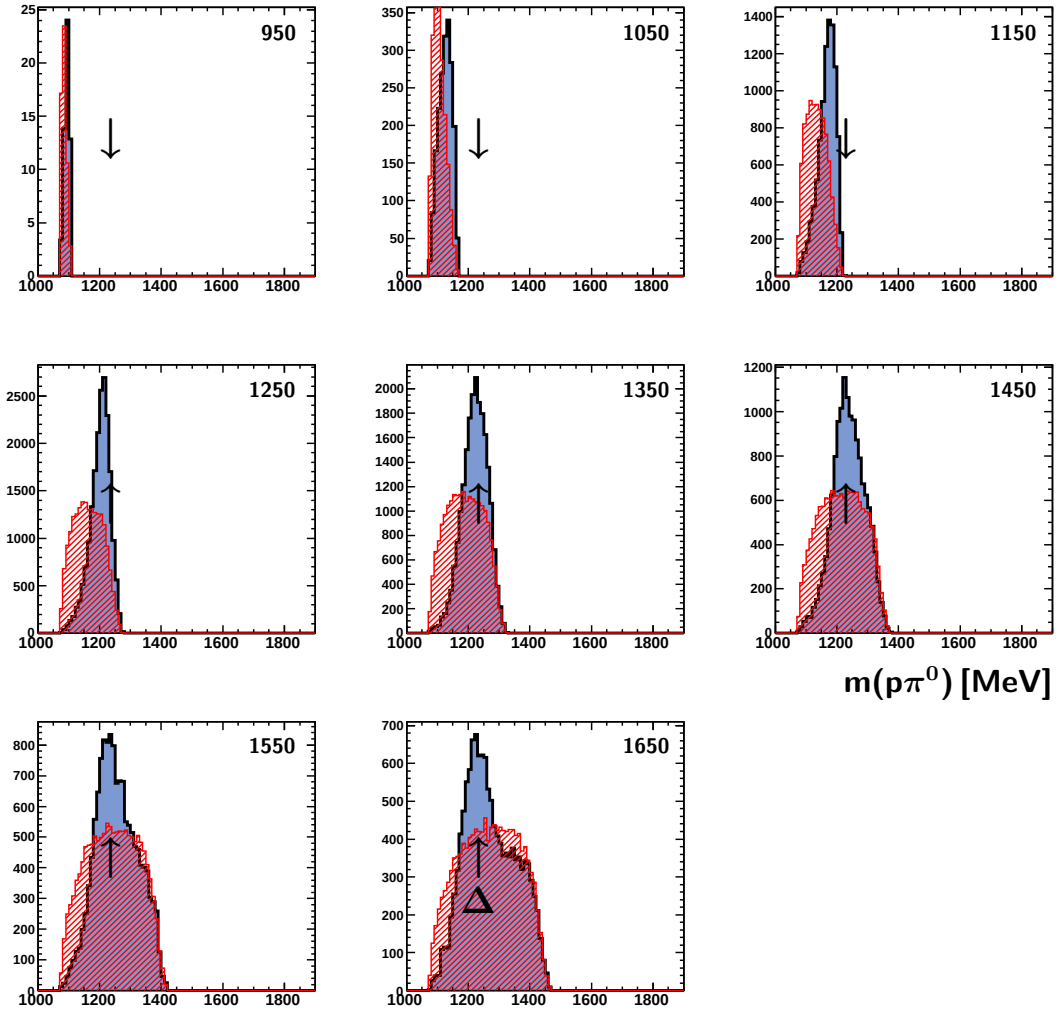

Figure C.1: **$p\pi^0$ invariant mass distributions, 900 MeV $\leq E_\gamma <$ 1700 MeV.** Numbers denote the bin center in E_γ, the arrow indicates the position of the $\Delta(1232)P_{33}$ resonance. Hatched area ([RED]): Phasespace distribution, including detector acceptance.

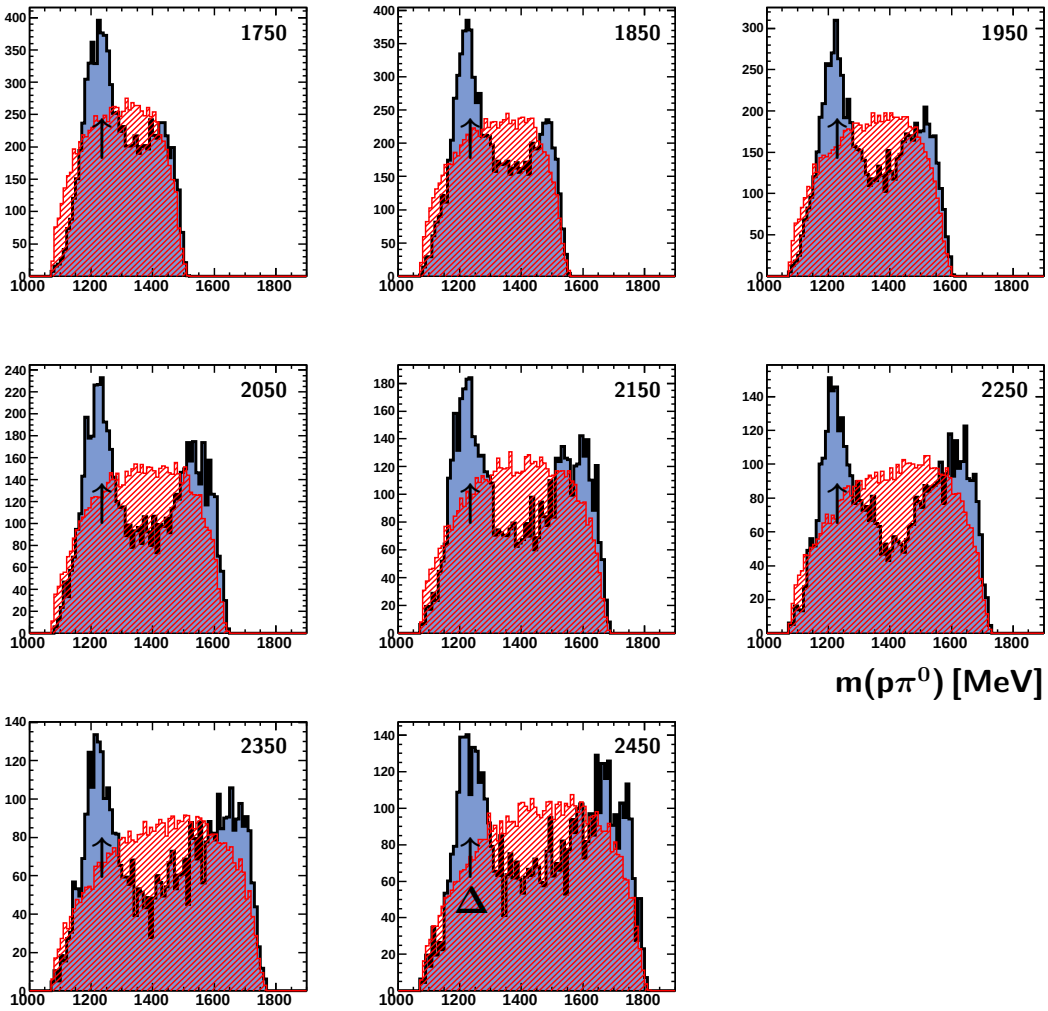

Figure C.2: **$p\pi^0$ invariant mass distributions, 1700 MeV $\leq E_\gamma \leq$ 2500 MeV.** Numbers denote the bin center in E_γ, the arrow indicates the position of the $\Delta(1232)P_{33}$ resonance. Hatched area ([RED]): Phasespace distribution, including detector acceptance.

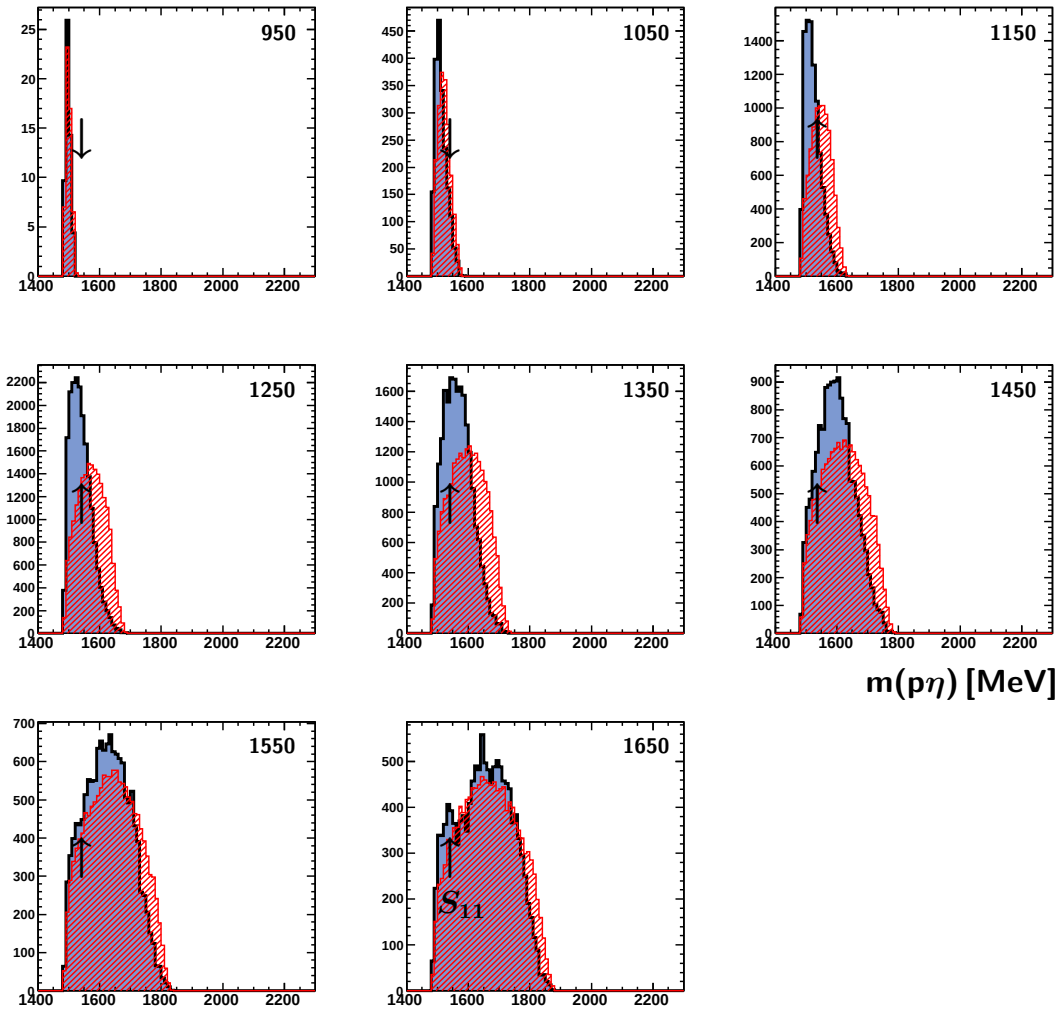

Figure C.3: **$p\eta$ invariant mass distributions, 900 MeV $\leq E_\gamma <$ 1700 MeV.** Numbers denote the bin center in E_γ, the arrow indicates the position of the N(1535)S_{11} resonance. Hatched area ([RED]): Phasespace distribution, including detector acceptance.

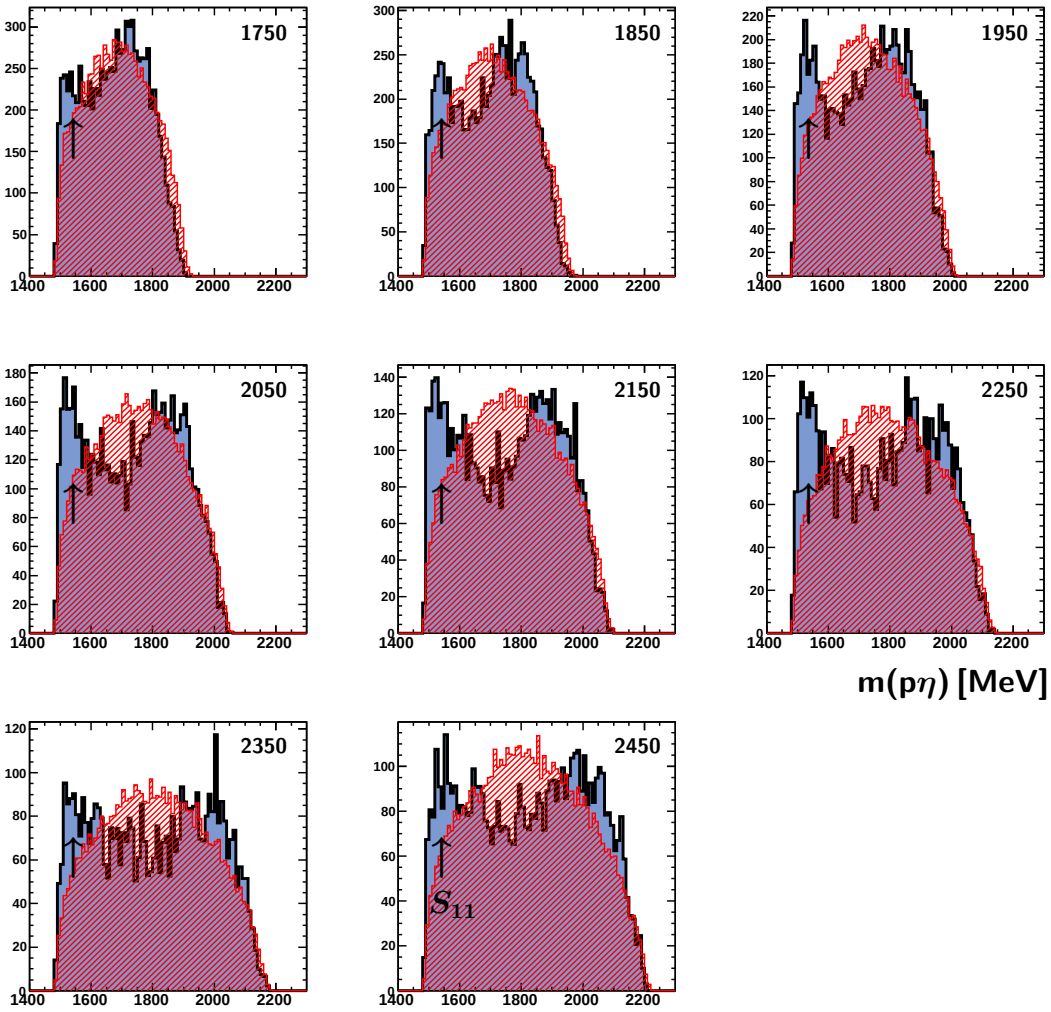

Figure C.4: **$p\eta$ invariant mass distributions, 1700 MeV $\leq E_\gamma \leq$ 2500 MeV.** Numbers denote the bin center in E_γ, the arrow indicates the position of the N(1535)S_{11} resonance. Hatched area ([RED]): Phasespace distribution, including detector acceptance.

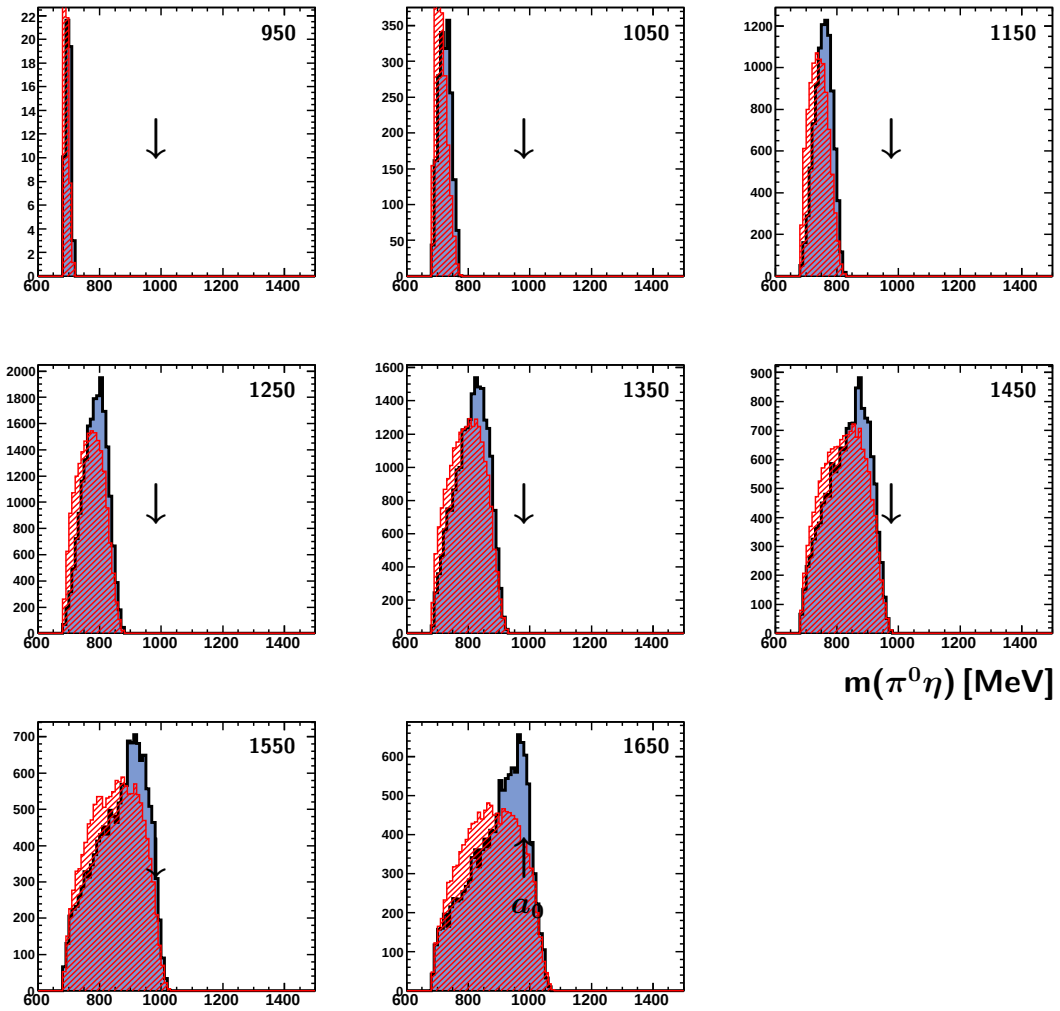

Figure C.5: **$\pi^0\eta$ invariant mass distributions, 900 MeV $\leq E_\gamma <$ 1700 MeV.** Numbers denote the bin center in E_γ, the arrow indicates the position of the scalar meson $a_0(980)$. Hatched area ([RED]): Phasespace distribution, including detector acceptance.

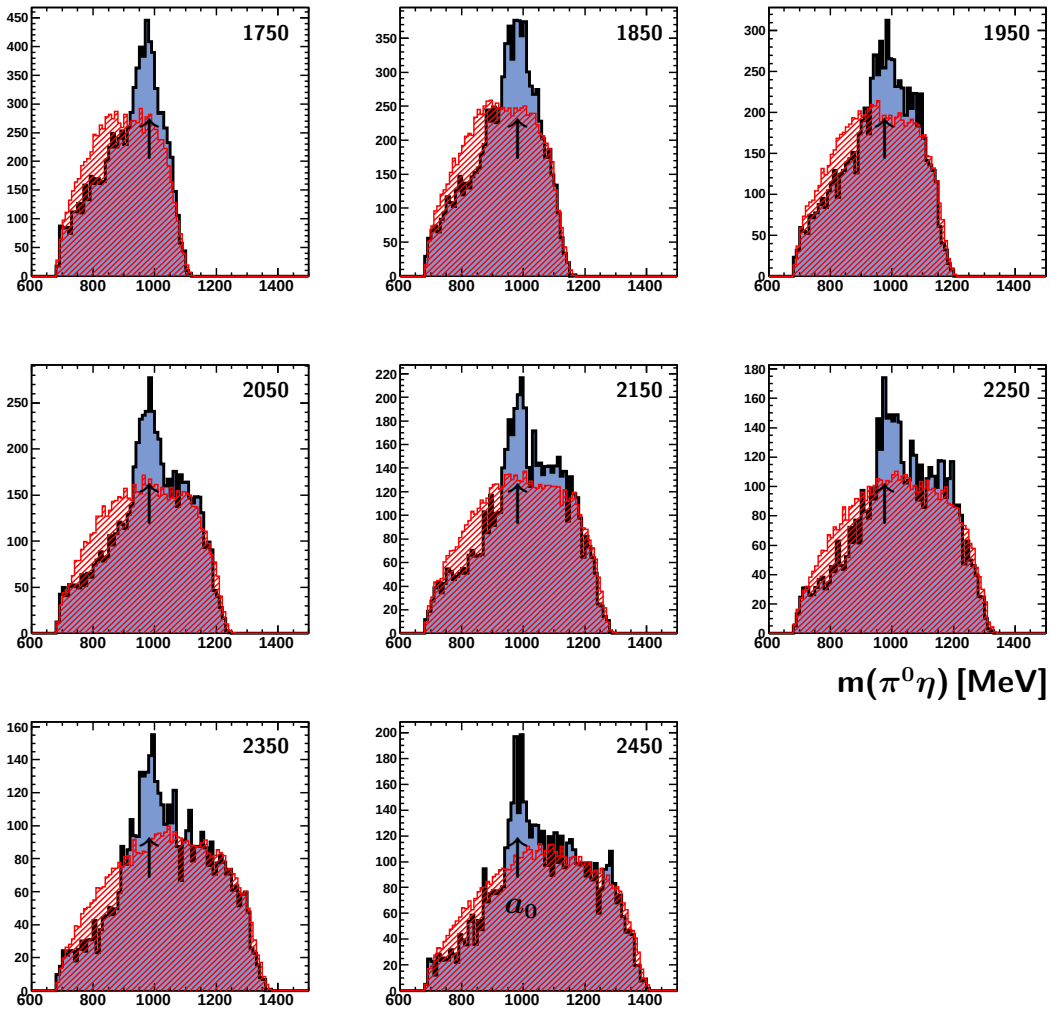

Figure C.6: **$\pi^0\eta$ invariant mass distributions, 1700 MeV $\leq E_\gamma \leq$ 2500 MeV.** Numbers denote the bin center in E_γ, the arrow indicates the position of the scalar meson $a_0(980)$. Hatched area ([RED]): Phasespace distribution, including detector acceptance.

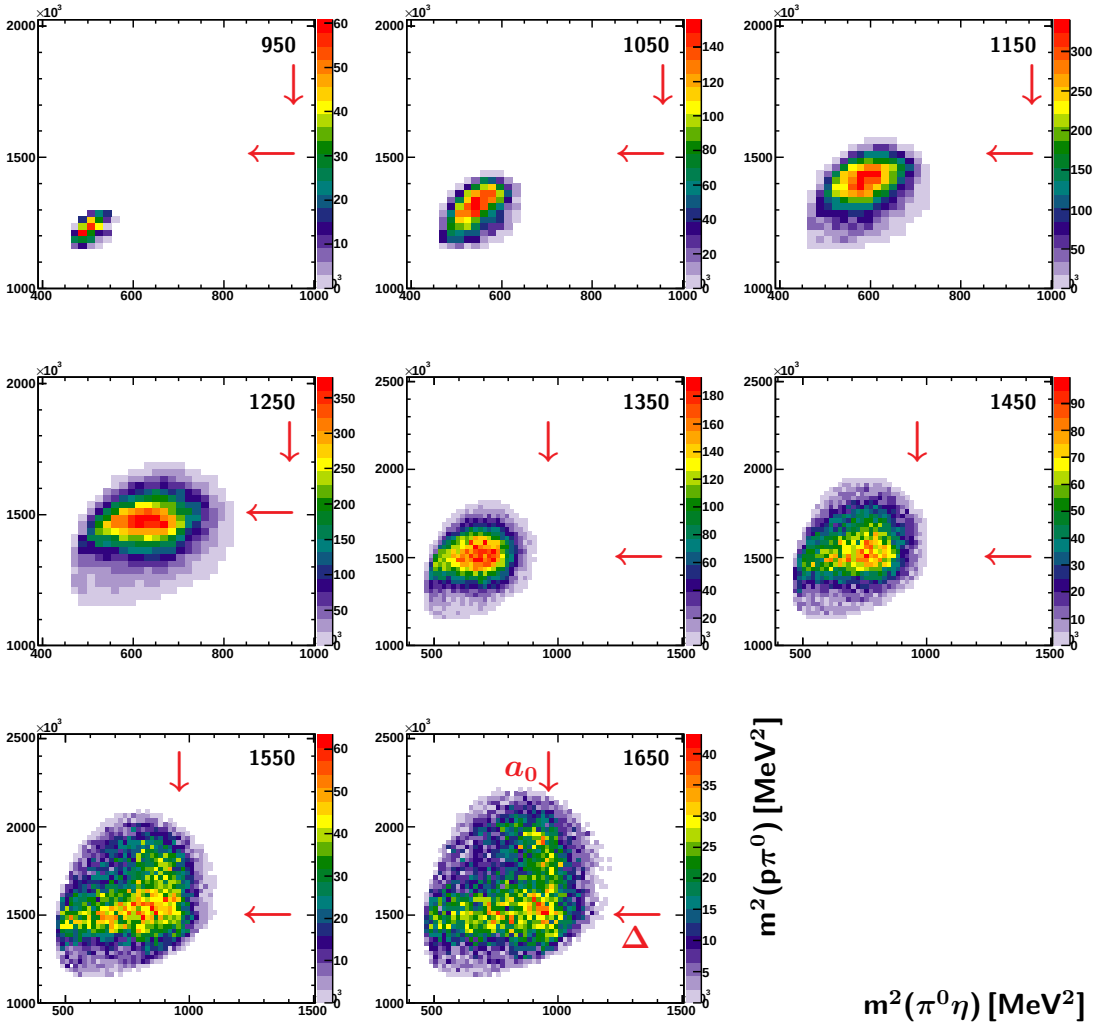

Figure C.7: **Dalitz plots, $m^2(\mathrm{p}\pi^0)$ vs. $m^2(\pi^0\eta)$, 900 MeV $\leq E_\gamma <$ 1700 MeV.** Numbers denote the bin center in E_γ, the arrows indicate the positions of the scalar meson $a_0(980)$ and the $\Delta(1232)P_{33}$ resonance. Not indicated but visible in the diagonal is the signal for the $N(1535)S_{11}$ resonance.

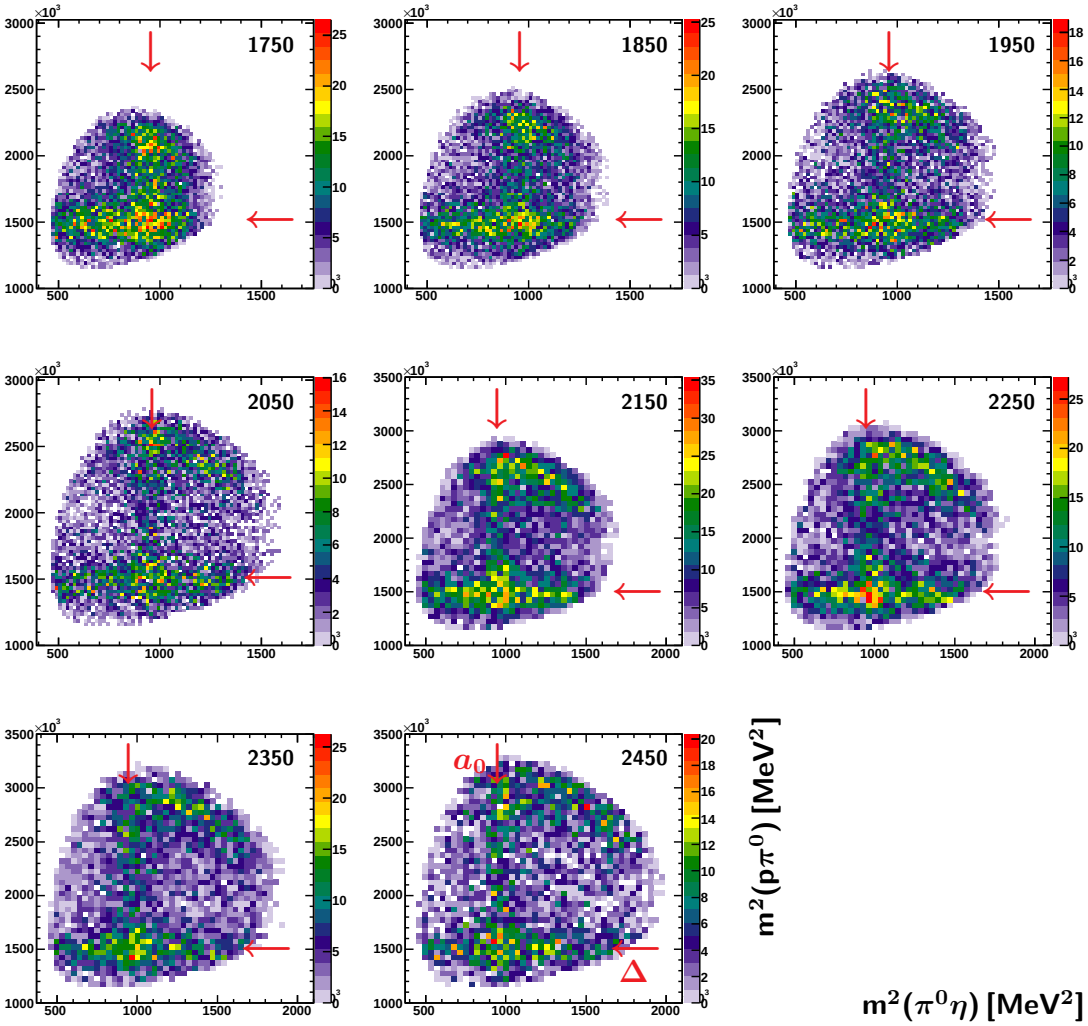

Figure C.8: **Dalitz plots, $m^2(\mathrm{p}\pi^0)$ vs. $m^2(\pi^0\eta)$, 1700 MeV $\leq E_\gamma \leq$ 2500 MeV.** Numbers denote the bin center in E_γ, the arrows indicate the positions of the scalar meson $\mathrm{a}_0(980)$ and the $\Delta(1232)P_{33}$ resonance. Not indicated but visible in the diagonal is the signal for the $\mathrm{N}(1535)S_{11}$ resonance.

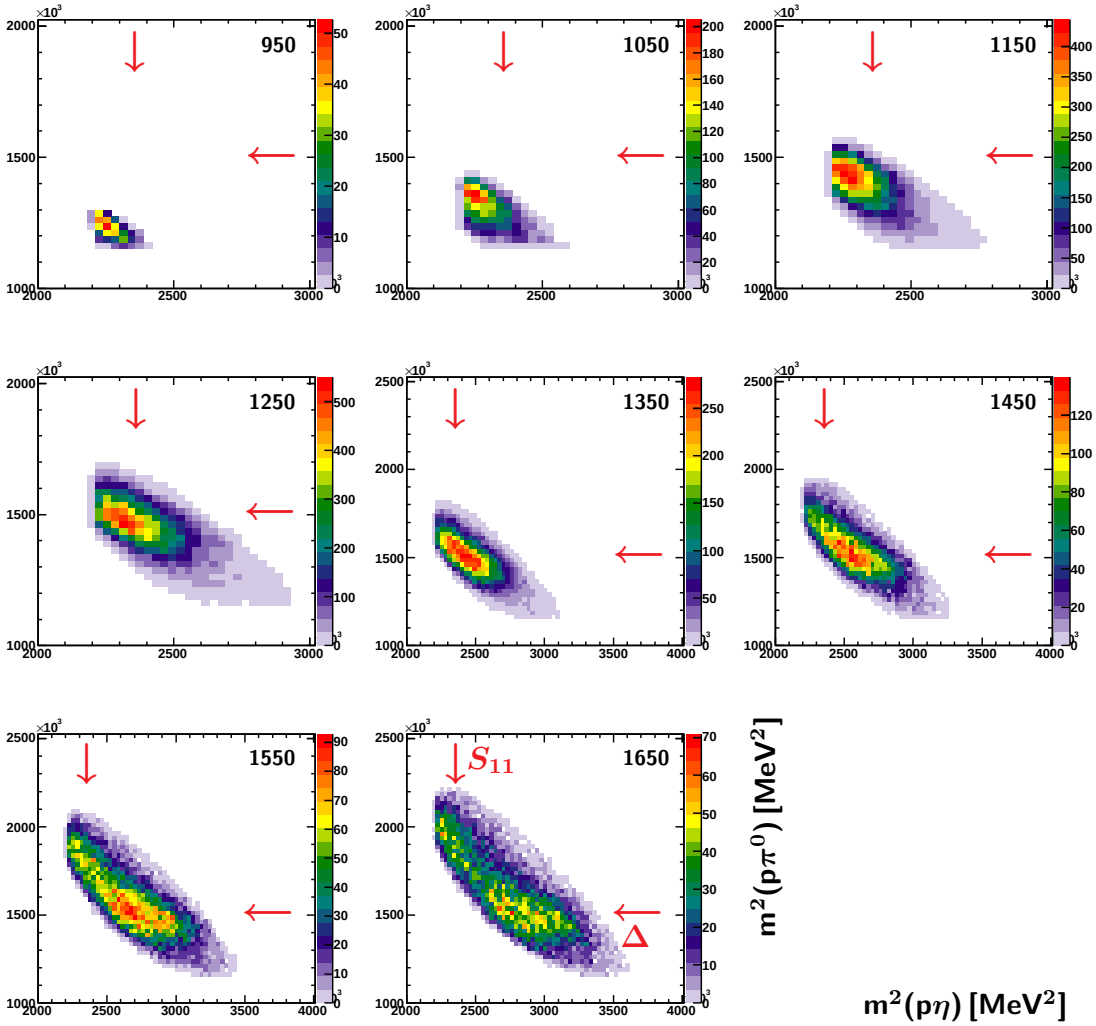

Figure C.9: **Dalitz plots, $m^2(p\pi^0)$ vs. $m^2(p\eta)$, 900 MeV $\leq E_\gamma <$ 1700 MeV.** Numbers denote the bin center in E_γ, the arrows indicate the positions of the $\Delta(1232)P_{33}$ and $N(1535)S_{11}$ resonances. Not indicated but visible in the diagonal is the signal for the scalar meson $a_0(980)$.

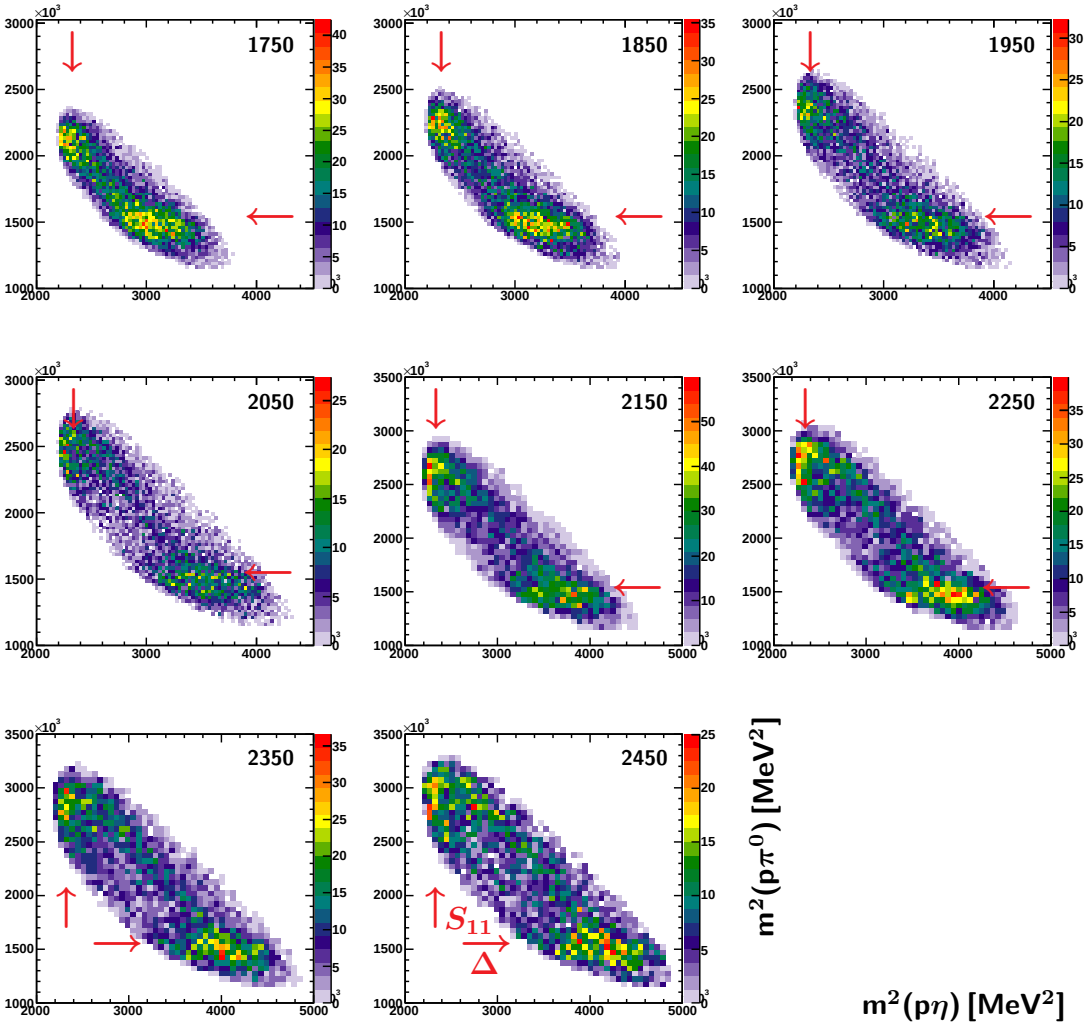

Figure C.10: **Dalitz plots, $m^2(p\pi^0)$ vs. $m^2(p\eta)$, 1700 MeV $\leq E_\gamma \leq$ 2500 MeV.** Numbers denote the bin center in E_γ, the arrows indicate the positions of the $\Delta(1232)P_{33}$ and N(1535)S_{11} resonances. Not indicated but visible in the diagonal is the signal for the scalar meson $a_0(980)$.

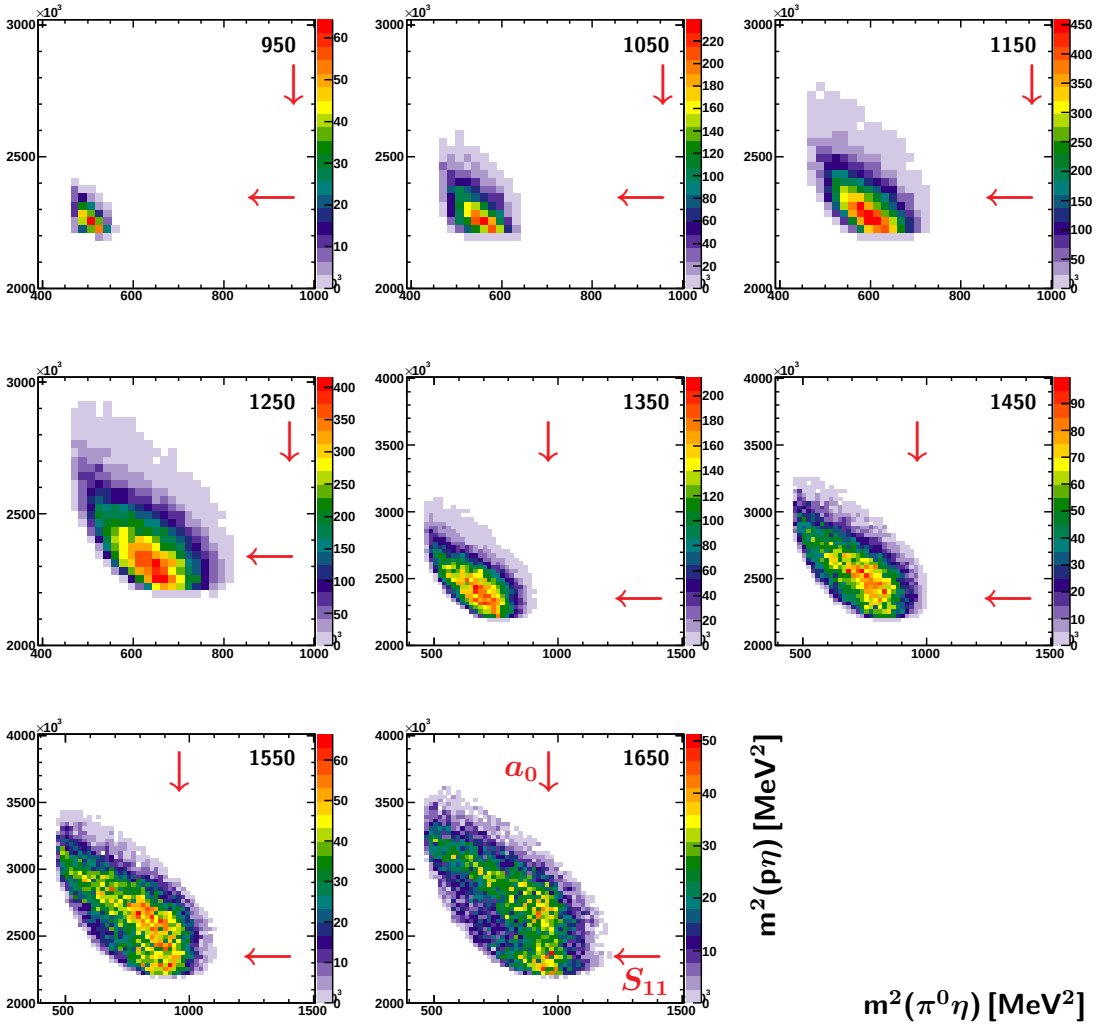

Figure C.11: **Dalitz plots, $m^2(p\eta)$ vs. $m^2(\pi^0\eta)$, 900 MeV $\leq E_\gamma <$ 1700 MeV.** Numbers denote the bin center in E_γ, the arrows indicate the positions of the scalar meson $a_0(980)$ and the N(1535)S_{11} resonance. Not indicated but visible in the diagonal is the signal for the $\Delta(1232)P_{33}$ resonance.

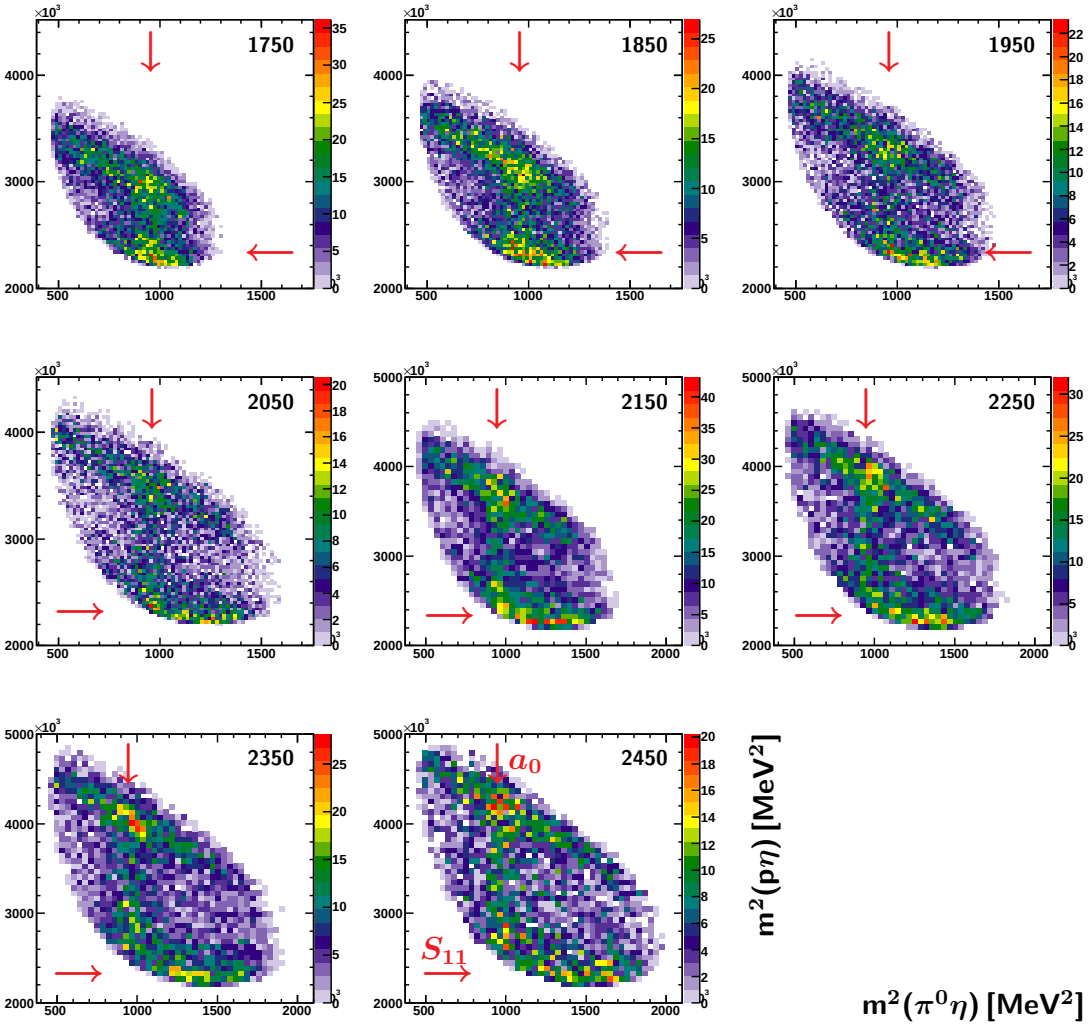

Figure C.12: **Dalitz plots, $m^2(p\eta)$ vs. $m^2(\pi^0\eta)$, 1700 MeV $\leq E_\gamma \leq$ 2500 MeV.** Numbers denote the bin center in E_γ, the arrows indicate the positions of the scalar meson $a_0(980)$ and the $N(1535)S_{11}$ resonance. Not indicated but visible in the diagonal is the signal for the $\Delta(1232)P_{33}$ resonance.

D TAPS LED threshold settings

Ring number	March 2003		May 2003	
	LED Low	LED High	LED Low	LED High
1	1107 MeV	1077 MeV	1118 MeV	1076 MeV
2	154 MeV	181 MeV	167 MeV	184 MeV
3	122 MeV	150 MeV	133 MeV	166 MeV
4	103 MeV	125 MeV	96 MeV	148 MeV
5	82 MeV	115 MeV	70 MeV	94 MeV
6	84 MeV	119 MeV	79 MeV	97 MeV
7	86 MeV	87 MeV	86 MeV	78 MeV
8	85 MeV	81 MeV	82 MeV	85 MeV
9	104 MeV	91 MeV	92 MeV	96 MeV
10	79 MeV	82 MeV	81 MeV	85 MeV
11	84 MeV	93 MeV	97 MeV	103 MeV
12	100 MeV	104 MeV	73 MeV	83 MeV

Table D.1: **TAPS LED threshold settings.** Given are the trigger thresholds for photons, protons see an effective threshold that is 20% higher.

E Publications and conference contributions

Publications in refereed journals

- E. Gutz, V. Sokhoyan, H. van Pee *et al.*, *Measurement of the beam asymmetry* Σ *in* $\pi^0\eta$ *production off the proton with the CBELSA/TAPS experiment.* European Physical Journal A **35**, 291 (2008).

- E. Gutz, V. Sokhoyan, H. van Pee *et al.*, *Photoproduction of meson pairs: First measurement of the polarization observable* I^s. Physics Letters B **687**, 11 (2010).

- E. Gutz, V. Sokhoyan, H. van Pee *et al.*, *Beam asymmetries in* $\pi^0\eta$*-photoproduction off the proton.* Publication in preparation (2010).

- V. Sokhoyan, E. Gutz, H. van Pee *et al.*, *First measurement of the polarization observables* I^s *and* I^c *in* $2\pi^0$*-photoproduction off the nucleon.* Publication in preparation (2010).

Proceedings

- E. Gutz, *Measurement of the beam asymmetry* Σ *in* $\pi^0\eta$ *production off the proton with the CBELSA/TAPS experiment.* Proceedings of the 11th Workshop on The Physics of Excited Nucleons (NSTAR2007), Bonn, Germany. Springer Berlin Heidelberg (2008).

- E. Gutz *Measurement of the single polarization observables* I^c *and* I^s *in* $\pi^0\eta$ *photoproduction.* Proceedings of the XIII International Conference on Hadron Spectroscopy (HADRON2009), Tallahassee, FL, USA. American Institute of Physics Conference Proceedings Volume 1257, 581 (2010).

Conference contributions

Talks

- E. Gutz, *Die Strahlasymmetrie Σ in der Reaktion $\vec{\gamma}p \rightarrow p\pi^0\eta$.* DPG Spring Meeting, Gießen, Germany (2007).
- E. Gutz, *Measurement of the beam asymmetry Σ in two-meson production off the proton with the CBELSA/TAPS experiment.* Invited talk, 11th Workshop on The Physics of Excited Nucleons (NSTAR), Bonn, Germany (2007).
- E. Gutz, *Measurement of the Beam Asymmetry Σ in the Reaction $\vec{\gamma}p \rightarrow p\pi^0\eta$.* DPG Spring Meeting, Darmstadt, Germany (2008).
- E. Gutz, *Single polarization observables in two-meson production.* Invited talk, XIII International Conference on Hadron Spectroscopy (HADRON), Tallahassee, FL, USA (2009).
- E. Gutz, *Messung der Polarisationsobservablen I^s und I^c in $\pi^0\eta$ Photoproduktion mit dem CBELSA/TAPS Experiment.* Group report, DPG Spring Meeting, Bonn, Germany (2010).

Other contributions

- E. Gutz, *Perspectives of double polarization experiments.* Poster presentation, DPG Spring Meeting, Cologne, Germany (2004).

Workshops

- E. Gutz, *The beam asymmetry Σ in the reaction $\vec{\gamma}p \rightarrow p\pi^0\eta$.* 24^{th} Students' Workshop on Electromagnetic Interactions, Bosen, Germany (2007).

List of Figures

List of Tables

Bibliography

[A+68] Althoff, K.-H. et al.: *The 2.5 GeV Electron Synchrotron of the University of Bonn.* Nuclear Instruments and Methods in Physics Research, (61):1–30, 1968.

[A+92] Aker, E. et al.: *The Crystal Barrel Spectrometer at LEAR.* Nuclear Instruments and Methods in Physics Research, A(321):69–109, 1992.

[A+08a] Ajaka, J. et al.: *Simultaneous Photoproduction of η and π^0 Mesons on the Proton.* Physical Review Letters, (100):052003, 2008.

[A+08b] Amsler, C. et al.: *Review of Particle Physics.* Physics Letters, B(667):1ff, 2008.

[AAK+07] Anisovich, A.V., V.V. Anisovich, E. Klempt, V.A. Nikonov and A.V. Sarantsev: *Baryon-baryon and baryon-antibaryon interaction amplitudes in the spin-momentum operator expansion method.* European Physical Journal, A(34):129–152, 2007.

[AKST05] Anisovich, A.V., E. Klempt, A.V. Sarantsev and U. Thoma: *Partial wave decomposition of pion and photoproduction amplitudes.* European Physical Journal, A(24):111–128, 2005.

[AOP+92] Awes, T.C., F.E. Obenshain, F. Plasil, S. Saini, S.P. Sorensen and G.R. Young: *A simple method of shower localization and identification in laterally segmented calorimeters.* Nuclear Instruments and Methods in Physics Research, A(311):130–138, 1992.

[AS06] Anisovich, A.V. and A.V. Sarantsev: *Partial decay widths of baryons in the spin-momentum operator expansion method.* European Physical Journal, A(30):427–441, 2006.

[ASB+05] Anisovich, A.V., A.V. Sarantsev, O. Bartholomy, E. Klempt, V.A. Nikonov and U. Thoma: *Photoproduction of baryons decaying into $N\pi$ and $N\eta$.* European Physical Journal, A(25):427–439, 2005.

[Bar00] Bartholomy, O.: *Test und Modifikation des Lichtpulsersystems für den CB-ELSA-Detektor.* Diploma thesis, Helmholtz-Institut für Strahlen- und Kernphysik, Universität Bonn, 2000.

[BDS75] Barker, I.S., A. Donnachie and J.K. Storrow: *Complete experiments in pseudoscalar photoproduction.* Nuclear Physics B, 95(2):347–356, 1975.

[Bog02] Bogendörfer, R.: *Effizienzbestimmung für den Innendetektor des Crystal-Barrel-Experiments an ELSA.* Diploma thesis, Physikalisches Institut, Universität Erlangen, 2002.

[Bös06] Böse, S.: *Modifikation und Test des Lichtpulsersystems für den Crystal Barrel Aufbau an ELSA.* Diploma thesis, Helmholtz-Institut für Strahlen- und Kernphysik, Universität Bonn, 2006.

[BS64] Berger, M.J. and S.M. Seltzer: *Tables of Energy Losses and Ranges of Electrons and Positrons.* National Aeronautics and Space Administration Report, 1964.

[Cas06] Castelijns, R.: *Photoproduction of strange mesons and hyperons in the proton.* PhD thesis, Rijksuniversiteit Groningen, 2006.

[CG98] Cano, F. and P. Gonzáles: *A consistent explanation of the Roper phenomenology.* Physics Letters, B(431):270–276, 1998.

[CR93] Capstick, S. and W. Roberts: *$N\pi$ decays of baryons in a relativized model.* Physical Review, D(47):1994–2010, 1993.

[CR94] Capstick, S. and W. Roberts: *Quasi-two-body decays of nonstrange baryons.* Physical Review, D(49):4570–4586, 1994.

[Cre01] Crede, V.: *CBGEANT 1.08/01.* CB-Note, October 2001.

[CT97] Chiang, W.-T. and F. Tabakin: *Completeness rules for spin observables in pseudoscalar meson photoproduction.* Physical Review, C(55):2054–2066, 1997.

[D$^+$00] D'Angelo, A. et al.: *Generation of Compton backscattering γ-ray beams.* Nuclear Instruments and Methods in Physics Research, A(455):1–6, 2000.

[DOM10] Döring, M., E. Oset and U.-G. Meissner: *Evaluation of the polarization observables I^S and I^C in the reaction $\gamma p \to \pi^0 \eta p$.* arXiv:1003.0097 [nucl-th], 2010.

[Dör10] Döring, M.: *private communication*, 2010.

[DOS06] Döring, M., E. Oset and D. Strottman: *Chiral dynamics in the $\gamma p \to \pi^0 \eta p$ and $\gamma p \to \pi^0 K^0 \Sigma^+$ reactions.* Physical Review, C(73):045209, 2006.

[E+07] Elsner, D. et al.: *Measurement of the beam asymmetry in η photoproduction off the proton.* European Physical Journal, A(33):147–155, 2007.

[E+09] Elsner, D. et al.: *Linearly polarised photon beams at ELSA and measurement of the beam asymmetry in π^0 photoproduction off the proton.* European Physical Journal, A(39):373–381, 2009.

[Els07] Elsner, D.: *Untersuchung kleiner Partialwellenbeiträge in der Nähe dominierender Resonanzbeiträge des Protons mit linear polarisierten Photonen.* PhD thesis, Physikalisches Institut, Universität Bonn, 2007.

[Fix10] Fix, A.: *private communication*, 2010.

[FK09] Forkel, H. and E. Klempt: *Diquark correlations in baryon spectroscopy and holographic QCD.* Physics Letters, B(679):77–80, 2009.

[FKLO10] Fix, A., V.L. Kashevarov, A. Lee and M. Ostrick: *Isobar model analysis of $\pi^0\eta$ photoproduction on protons.* arXiv:1004.5240 [nucl-th], 2010.

[Fle01] Flemming, H.: *Entwurf und Aufbau eines Zellularlogik-Triggers für das Crystal-Barrel-Experiment an der Elektronenbeschleunigeranlage ELSA.* PhD thesis, Institut für Experimentalphysik I, Ruhr-Universität Bochum, 2001.

[Fös01] Fösel, A.: *Entwicklung und Bau des Innendetektors für das Crystal Barrel Experiment an ELSA/Bonn.* PhD thesis, Physikalisches Institut, Universität Erlangen, 2001.

[FOT08] Fix, A., M. Ostrick and L. Tiator: *Analysis of angular distributions in $\gamma N \to \pi^0 \eta N$.* European Physical Journal, A(36):61–72, 2008.

[Fuc05] Fuchs, M.: *Photoproduktion neutraler Pionpaare mit dem Crystal Barrel Detektor an ELSA.* PhD thesis, Helmholtz-Institut für Strahlen- und Kernphysik, Universität Bonn, 2005.

[G+94] Gabler, A. et al.: *Response of TAPS to monochromatic photons with energies between 45 and 790 MeV.* Nuclear Intruments and Methods in Physics Research, A(346):168–176, 1994.

[Glo00] GLOTZMANN, L.YA.: *Parity doublets and chiral symmetry restoration in baryon spectrum.* Physics Letters, B(475):329–334, 2000.

[Gri08] GRIFFITHS, D.: *Introduction to Elementary Particles.* Wiley, 2nd edition, 2008.

[GSvP+08] GUTZ, E., V. SOKHOYAN, H. VAN PEE et al.: *Measurement of the beam asymmetry Σ in $\pi^0\eta$ production off the proton with the CBELSA/TAPS experiment.* European Physical Journal, A(35):291–293, 2008.

[GSvP+10] GUTZ, E., V. SOKHOYAN, H. VAN PEE et al.: *Photoproduction of meson pairs: First measurement of the polarization observable I^s.* Physics Letters, B(687):11–15, 2010.

[H+08a] HORN, I. et al.: *Evidence for a Parity Doublet $\Delta(1920)P_{33}$ and $\Delta(1940)D_{33}$ from $\gamma p \to p\pi^0\eta$.* Physical Review Letters, (101):202002, 2008.

[H+08b] HORN, I. et al.: *Study of the reaction γp $\to$ p$\pi^0\eta$.* European Physical Journal, A(38):173–186, 2008.

[Hei54] HEITLER, W.: *The Quantum Theory of Radiation.* Oxford University Press, 1954.

[Hej98] HEJNY, V.: *Photoproduktion von η-Mesonen an Helium 4.* PhD thesis, II. Physikalisches Institut, Universität Giessen, 1998.

[Hil06] HILLERT, W.: *The Bonn Electron Stretcher Accelerator ELSA: Past and future.* European Physical Journal, A(28):139–148, 2006.

[Hof01] HOFFMANN, M.: *Beschleunigung polarisierter Elektronen in der Bonner Elektronen-Beschleunigeranlage ELSA.* PhD thesis, Physikalisches Institut, Universität Bonn, 2001.

[Hor04] HORN, I.: *The decay of the γp system into the $p\pi^0\eta$ final state.* PhD thesis, Helmholtz-Institut für Strahlen- und Kernphysik, Universität Bonn, 2004.

[Jac98] JACKSON, J.D.: *Classical Electrodynamics.* Wiley, 3rd edition, 1998.

[Jae06] JAEGLÉ, I.: *private communication*, 2006.

[Jan98] JANSSEN, S.: *Entwicklung eines CPV-Systems für TAPS.* Diploma thesis, II. Physikalisches Institut, Universität Giessen, 1998.

[JG04] JUNKERSFELD, J. and E. GUTZ: *Simulation of the Trigger of the CBELSA/TAPS experiment.* CBELSA/TAPS-Note, August 2004.

[Jun00] Junkersfeld, J.: *Kalibration des Crystal-Barrel-ELSA Detektors mit Hilfe der Reaktion* $\gamma p \rightarrow p\pi^0$. Diploma thesis, Helmholtz-Institut für Strahlen- und Kernphysik, Universität Bonn, 2000.

[Jun05] Junkersfeld, J.: *Photoproduktion von* $\pi^0\omega$ *am Proton bei Energien bis zu 3 GeV*. PhD thesis, Helmholtz-Institut für Strahlen- und Kernphysik, Universität Bonn, 2005.

[KCL07] Kiswandhi, A., S. Capstick and T.-S. H. Lee: *A unitary and relativistic model for* $\pi\eta$ *and* $\pi\pi$ *photoproduction*. Journal of Physics: Conference Series, 69:012018, 2007.

[KF+09] Kashevarov, V.L., A. Fix et al.: *Photoproduction of* $\pi^0\eta$ *on protons and the* $\Delta(1700)D_{33}$ *resonance*. European Physical Journal, A(42):141–149, 2009.

[Kit04] Kittel, Ch.: *Introduction to Solid State Physics*. Wiley, 8th edition, 2004.

[Kle03] Klempt, E.: *Do parity doublets in the baryon spectrum reflect restoration of chiral symmetry ?* Physics Letters, B(559):114–152, 2003.

[Kle10] Klein, F.: *(in preparation)*. PhD thesis, Physikalisches Institut, Universität Bonn, 2010.

[Kon01] Konrad, M.: *Ortssensitiver Detektor für hochenergetische Photonen bei höchsten Raten*. Diploma thesis, Physikalisches Institut, Universität Bonn, 2001.

[Kop02] Kopf, B.: *Untersuchung der photoinduzierten Reaktionen* $\gamma p \rightarrow p\pi^0\pi^0$ *und* $\gamma p \rightarrow p\pi^0\eta$. PhD thesis, Institut für Kern- und Teilchenphysik, Technische Universität Dresden, 2002.

[Kot01] Kotulla, M.: *Experiment zur Bestimmung des magnetischen Moments der* $\Delta^+(1232)$ *Resonanz*. PhD thesis, II. Physikalisches Institut, Universität Giessen, 2001.

[KZF+09] Krambrich, D., F. Zehr, A. Fix, L. Roca et al.: *Beam-Helicity Asymmetries in Double-Pion Photoproduction off the Proton*. Physical Review Letters, 103(5):052002, 2009.

[LBP82] Lifshitz, E.M., V.B. Berestetskii and L.P. Pitaevskii: *Landau and Lifshitz Course of Theoretical Physics*, volume 4. Butterworth-Heinemann, 2nd edition, 1982.

[LKMP01] Löring, U., K. Kretschmar, B.C. Metsch and H.R. Petry: *Relativistic quark models of baryons with instananeous forces.* European Physical Journal, A(10):309–346, 2001.

[LMP01] Löring, U., B.C. Metsch and H.R. Petry: *The light baryon spectrum in a relativistic quark model with instanton-induced quark forces: The non-strange baryon spectrum and ground-states.* European Physical Journal, A(10):395–446, 2001.

[N+06] Nakabayashi, T. et al.: *Photoproduction of η mesons off protons for $E_\gamma \leq$ 1.15 GeV.* Physical Review, C(74):035202, 2006.

[Nan06] Nanova, M.: *private communication*, 2006.

[NGH+03] Natter, F.A., P. Grabmayr, T. Hehla, R.O. Owens and S. Wunderlich: *Monte Carlo simulation and analytical calculation of coherent bremsstrahlung and its polarisation.* Nuclear Instruments and Methods in Physics Research, B(211):465–486, 2003.

[NST08] *NSTAR 2007, Proceedings of The 11th Workshop on The Physics of Excited Nucleons.* Springer Berlin Heidelberg, 2008.

[Pal68] Palazzi, G.D.: *High-Energy Bremsstrahlung and Electron Pair Production in Thin Crystals.* Reviews of Modern Physics, (40):611–631, 1968.

[RO05] Roberts, W. and T. Oed: *Polarization Observables for Two-Pion Production off the Nucleon.* Physical Review, C(71):052002, 2005.

[Rob10] Roberts, W.: *private communication*, 2010.

[Roc05] Roca, L.: *Helicity asymmetries in double pion photoproduction on the proton.* Nuclear Physics, A(748):192–205, 2005.

[S+05a] Strauch, S. et al.: *Beam-Helicity Asymmetries in Double-Charged-Pion Photoproduction on the Proton.* Physical Review Letters, 95(16):162003, 2005.

[S+05b] Suft, G. et al.: *A scintillating fibre detector for the Crystal Barrel experiment at ELSA.* Nuclear Instruments and Methods in Physics Research, A(531):416–424, 2005.

[San95] Sandorfi, A.M.: *Polarized Photon Facilities - Windows to New Physics.* Plenary talk, Baryons'95, October 1995.

[Sar10] SARANTSEV, A.: *private communication*, 2010.

[Sch92] SCHAERF, C.: *The Graal project: A polarized and tagged gamma-ray beam.* Nuclear Physics News, 2:7–8, 1992.

[SHKL09] SANDORFI, A.M., S. HOBLIT, H. KAMANO and T.-S.H. LEE: *Calculations of Polarization Observables in Pseudoscalar Meson Photo-production Reactions.* arXiv:0912.3505 [nucl-th], 2009.

[Sok10] SOKHOYAN, V.: *Measurement of polarization observables in the reaction $\gamma p \to p\pi^0\pi^0$ with the CBELSA/TAPS experiment.* PhD thesis, Helmholtz-Institut für Strahlen- und Kernphysik, Universität Bonn, 2010. (in preparation).

[Ü56] ÜBERALL, H.: *High-Energy Interference Effect of Bremsstrahlung and Pair Production in Crystals.* Physical Review, 103(4):1055–1067, 1956.

[vP03] PEE, H. VAN: *Untersuchung der Reaktion $\gamma p \to p\pi^0$ für Photonenergien von 0.45 bis 1.3 GeV mit dem Crystal Barrel-Detektor an ELSA.* PhD thesis, Helmholtz-Institut für Strahlen- und Kernphysik, Universität Bonn, 2003.

[Wal10] WALTHER, D.: *private communication*, 2010.

[Wor72] WORDEN, R.P.: *Regge models of forward pion and eta photoproduction.* Nuclear Physics, B(37):253–312, 1972.

Acknowledgement

The frontpage of this thesis has only room for one name, but this work would not have been possible without the help and support, be it scientific, financial or personal, by many, many people. To name a few:

Ulrike Thoma, Christian Weinheimer, Eberhard Klempt, Reinhard Beck, Ulf-G. Meißner and Klaus Lehnertz, thank you for giving me the opportunity to start, continue and finish my work supervised, financed and, in the end, read and examined.

Vahe Sokhoyan, Harald van Pee and Winston Roberts, without your input, this would have been a very different thesis.

Michael Döring, Eulogio Oset, Alexander Fix, Victor Kashevarov, Andrey Sarantsev, Victor Nikonov and Alexey Anisovich, thank you for broadening my views on the subjects discussed in this work and backing it theoretically.

Mariana Nanova, Igal Jaeglé, Volker Metag, Bernd Krusche, Ralph Castelijns, David Trnka and Jörg Junkersfeld, without whom the analysis of the data would have been way more tedious, well-nigh impossible.

Aaron McVeigh, Karoly Makonyi, Susanne Kammer, Hartmut Kalinowsky, Frank Klein, Andre Süle, Daniel Elsner, Olivia Bartholomy and Volker Credé, for too many things over the course of the past years to mention here.

And most of all, here's to you, my friends:
Annika, Krishna, Christoph, Russell, Tom, Simon, Michael, Ralf, Damian, Sabine.
Regine.

When you can't run, you crawl... and when you can't crawl, when you can't do that... you find someone to carry you.

Firefly, *The Message*